UNIVERSITY OF SOUTHAMPTON

ABSTRACT

FACULTY OF SCIENCE

OCEANOGRAPHY

Doctor of Philosophy

THROUGHFLOW FROM THE PACIFIC TO THE INDIAN OCEAN THROUGH SOUTH EAST ASIAN WATERS

by Michael Paul Dearnaley

The South East Asian Waters form the only tropical latitude link between the world's ocean basins. The region has an important role in the circulation of the Pacific and Indian Oceans. In the Indian Ocean the area is the source of the South Equatorial current and the polewards flowing Leeuwin Current off Western Australia.

The throughflow from the Pacific to the Indian Ocean is investigated using a model driven by a forcing term representing the difference in sea level between the Pacific and Indian Oceans. Initially steady forcing is used in a cross equatorial channel model. The transient motions are controlled by the width of the channel. No evidence for westward propagating Rossby waves is found in a channel of width 560km. At steady state southward flow occurs throughout the channel in a western boundary layer where the required change in planetary vorticity is balanced by dissipation of vorticity. Meridional flow through the channel at steady state is found to be largely due (>80%) to the geostrophic balance with the cross channel sea level gradient. Results are presented for linear and non linear baroclinic models and a linear two layer model.

The effects of islands, sills and continental shelves are included in the channel models and lead to the development of a linear baroclinic 'realistic' model (20km grid) covering the region 110°E-140°E, 20°S-10°N. Forcing this model by the seasonal difference in sea level between the Pacific and Indian Oceans gives a mean throughflow of 7.5Sv with a seasonal oscillation of +/-7.9Sv. Maximum throughflow occurred in August and minimum in January. Flow through the Lombok Strait accounted for 50% of the total transport into the Indian Ocean. The seasonal forcing produces a pulse of outflow through the Timor Sea confined to the North West Australian Shelf during March-July (in phase with the observed development of the Leeuwin Current). During the remainder of the year outflow turned westwards along 10°S south of Java. Changes in the Pacific sea level reached the North West Australian Shelf by Kelvin waves. Changes in the Indian Ocean sea level south of Java occur only after Rossby waves have had time to propagate offshore from the North West Australian Shelf.

UNIVERSITY OF SOUTHAMPTON

THROUGHFLOW FROM THE PACIFIC TO THE INDIAN OCEAN THROUGH SOUTH EAST ASIAN WATERS

By
Michael Paul Dearnaley

A Dissertation submitted in candidature for the degree of
Doctor of Philosophy at the University of Southampton

August 1990

To my parents

Acknowledgments

This work was funded by a studentship from the Natural Environment Research Council and carried out under the joint supervision of Dr. N.C. Wells of the Oceanography Department at Southampton University and Dr. D.J. Webb of the Institute of Oceanographic Sciences Deacon Laboratory. I wish to thank both Neil and Dave for their patience, interest and guidance throughout the last four years. I also wish to thank the many other members of the department who have helped make this work possible. Thanks also to Sue Ganney for typing the text and figure headings.

Finally I wish to thank my family and friends who have provided support, and diversions over the last four years. Without them the finished product would not have been attained.

Michael Dearnaley

CONTENTS

INTRODUCTION

1.1 INTRODUCTION

In developing an understanding of the role of the world ocean in global climate, increasing attention is being given to the interconnections between the ocean basins (Semtner and Chervin, 1988). Changes in local forcing in one part of the world ocean may influence atmosphere-ocean interaction in a distant region. The cycle for formation and replenishment of North Atlantic Deep Water is an example of this interocean circulation. Gordon (1986) proposed a global circulation cell in which upper layer water flowed towards the northern North Atlantic to feed North Atlantic Deep Water formation.

Tropical oceans play a particularly important part in determining the global climate for two reasons. Firstly, the atmosphere has been found to be particularly sensitive to low latitude sea surface temperature anomalies. Weather systems over much of the globe have been found to be strongly correlated with equatorial sea surface temperature variations (eg. Horel and Wallace, 1981). Secondly, the vanishing of the Coriolis Force at the equator permits fast zonal propagation of long equatorial waves. Thus a localized forcing in one particular region can lead to changes in the ocean across the whole of an equatorial ocean basin.

International effort in these areas is seen in two major research programs. The ongoing Tropical Ocean, Global Atmosphere (TOGA) program (1985-1995) seeks understanding and prediction of interannual climate variability (TOGA Scientific Steering Group, 1985). The planned World Ocean Circulation Experiment (WOCE). (1990s) aims to achieve a global understanding of ocean circulation in order to predict long term climate change. (WOCE Scientific Steering Group, 1986). Both programs combine the use of observations and numerical models of the ocean-atmosphere system.

The South East Asian waters form the only tropical latitude link between the world's ocean basins. The region also has an important role in the circulation of the Pacific and Indian Oceans. In the

Pacific the region is the source of the Kuroshio, the North Equatorial Counter Current and the Equatorial Under Current. In the Indian Ocean the area is the source of the South Equatorial Current and the Leeuwin Current (Cresswell and Golding, 1980).

The geometry of the region is complex (figure 1.1.1) and comprises a system of islands, sills and basins. In some early global models (Veronis, 1973, 1976 and Andreyev et al, 1976) the region was considered closed, in other models (see section 1.4.1), the link was represented by one or two grid points. In all finite difference modelling, processes with scales that cannot be resolved have to be parameterized in some way. Thus with the coarse resolution of these early models (typically $2\frac{1}{2}°\times2\frac{1}{2}°$) there is very poor representation of the physics of the Pacific to Indian Ocean throughflow.

Present day modelling and understanding of the world ocean is still in the formative stages compared to that of the atmosphere. This has been because of the lack of computational power for running global ocean models with horizontal resolution comparable to the Rossby radius of deformation and also to the relative lack of observational data with which to verify the models. In the near future the predicted increase in computing power of 1-2 orders of magnitude and the availability of global synoptic data from ocean sensing satellites, with which to constrain the better models, make global ocean modelling and climate prediction realistic aims.

Semtner and Chervin (1988) presented the first global ocean simulation with resolution fine enough ($\frac{1}{2}°$ grid, 20 vertical levels) to allow for the formation of synoptic eddies, the oceanic equivalent to synoptic weather systems, and the resolution of features such as the equatorial under current region. The model includes only three islands; Australia-New Guinea, New Zealand and Antarctica. The complex geometry of the South East Asian Waters has been smoothed and the islands of the region submerged. The smallest scale feature that can be resolved in this region is 100km wide. The model shows transport from the tropical Pacific, through the Indonesian

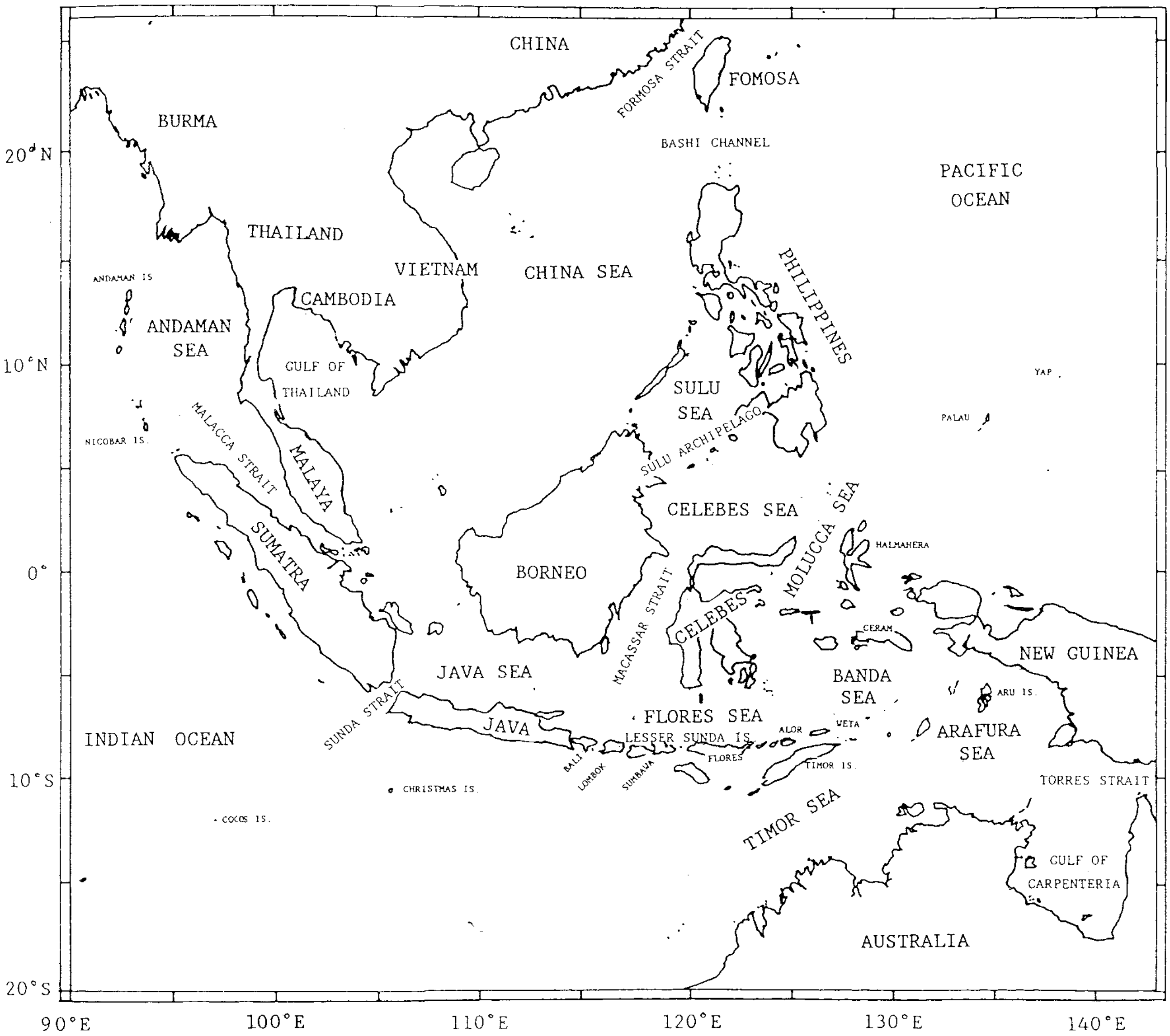

Figure 1.1.1 : The South East Asian Waters.

Archipelago and across the Indian Ocean. The magnitude of the flow through the Archipelago (15-18 Sv) appears to be over estimated because of the poor resolution there. Recent estimates (section 1.3.3, table 1.3.1) suggest a throughflow of 6-8Sv. Semtner and Chervin suggest that increasing the resolution of the model in the region of the Indonesian seas would give better representation of the physics of the throughflow. They also discuss the prospects of the predicted increase in computational power for carrying out longer simulations at finer resolutions.

In the present study a numerical model is developed to investigate the throughflow from the Pacific to the Indian Ocean in more detail than previous studies, (e.g. Kindle et al, 1987). Initially the flow through a cross equatorial channel is investigated. Then the effects of islands, sills and shelves on this flow are studied. The use of a many layered primitive equation model was considered but because of the computational cost it was regarded unsuitable for the preliminary studies proposed. Numerical models derived from the two layer shallow water equations are used for the initial studies. The final realistic model of the Eastern Archipelago of the South East Asian Waters (chosen from the initial models) is a reduced gravity single layer model that achieves a resolution of 40km (20km grid).

A description of the circulation of South East Asian Waters and the external forcing on the region, form the first part of this chapter. In the following sections an overview of the observations and estimates of the throughflow is given and relevant analytic theory is presented. The Chapter concludes with a statement on the approach and aims of this study. In subsequent chapters the shallow water models are developed (chapter 2) and initial results of the open channel presented (chapter 3). The effects of islands, sills and shelves on the flow in the open channel are given in chapter 4. The development and results of the final realistic model are described in Chapter 5. In the final chapter the model results are discussed with respect to observational and other theoretical studies.

1.2 PHYSICAL OCEANOGRAPHY OF SOUTH EAST ASIAN WATERS

1.2.1 Introduction

There have been two detailed studies of the South East Asian Waters. The data from the 1929-1930 Snellius Expedition was analysed by Postma (1958) and this and other data was further analysed by Wyrtki (1961). These studies showed that all the water masses within the South East Asian Waters came from the Pacific Ocean. In this section a description of the South East Asian Waters and the circulation associated with the forcing in the region are given.

1.2.2 Description of region

The South East Asian Waters are shown in figure 1.1.1. In the west the Sunda Shelf comprising the Java Sea west of the Macassar Strait, the Gulf of Thailand, the Southern China Sea and the shallower parts of the Malacca Strait has a maximum depth of 100m. The shelf is bounded by coastlines or steep slopes leading to deep oceanic areas. The currents over the shelf are everywhere affected by bottom friction resulting in a homogeneous water column (Wyrtki, 1961).

The northern part of the China Sea is a deep basin with maximum depth of 5000m. There is exchange with the Pacific at all levels through the deep Bashai channel. The Sulu Sea to the south is unusual because of the height of the sill (420m) compared to the depth of the basin (5600m). Direct exchange with the waters of the South China Sea can occur only at levels above 420m. Through the shallow straits (<100m) between the Phillipine islands and the Sulu Sea a strong exchange of surface waters with the Pacific ocean occurs.

The Eastern Archipelago is used to denote the region of islands and channels bounded by the Sunda Shelf in the west, the Arafura Shelf in the east, the Phillipines in the north and the Indian Ocean in the south. The Archipelago thus contains the Flores, Banda, Celebes, Molucca and Timor Seas and the Macassar Strait. The Eastern Archipelago is the only deep connection (>500m) between the Pacific and Indian Oceans (or between any two major oceans) at low latitudes. The bathymetry of the Eastern Archipelago is shown in figure 1.2.1. The deepest direct pathway between the two oceans is 1500m and is via the Molucca, Banda and Timor Seas. There are numerous sills in the Archipelago but the shallowest (~500m) and most important for this study occur in the Lombok Strait and at the southern end of the Macassar Strait. The islands within the Archipelago do not have extensive surrounding shelves but steep slopes leading to the deep oceanic areas.

The Eastern Archipelago is partially bounded to the south by the Lesser Sunda Islands that extend eastwards from Java. The islands create a number of straits connecting the Flores Sea to the Indian Ocean. The two deepest straits, where the main throughflow will be, are the Lombok Strait (~350m) and channels in the Timor Sea (~1900m and 1200m) north and south of Timor Island. In the north between Mindanao and Halmahera the Molucca Sea is closed by a sill with a depth of 2300m. In the east, exchange with the Pacific also occurs between the island groups of Halmahera and Ceram. The Arafura Shelf connecting New Guinea and Australia is 30-70m deep. The Torres Strait further to the east is shallower, 15-20m deep, and has strong tidal exchange with the Pacific but only a small (<0.01Sv) residual transport (Wolanski et al, 1988). The seasonal variation of flow through the Strait is larger (~ 1.0Sv) and affects the upper layer circulation (Wyrtki, 1961).

Evidence for the water masses of the South East Asian Waters originating from the Pacific Ocean is seen in two core layers, a salinity maximum and a salinity minimum at depths of 100m and 300m respectively. These two layers originate from waters of the Northern Pacific. Hydrographic evidence (Wyrtki, 1961) shows the water flows through the Celebes Sea and the Macassar Strait and into the Indian Ocean via the Lombok Strait or via the Flores, Banda and Timor Seas. A salinity maximum associated with waters of the Southern Pacific Sea is found at 100-200m throughout the waters to the east of the Celebes. Deeper Pacific waters also travel south through the deep channels of the region and evidence of an oxygen minimum associated with Pacific Intermediate Water is found at 800m in the Banda Sea.

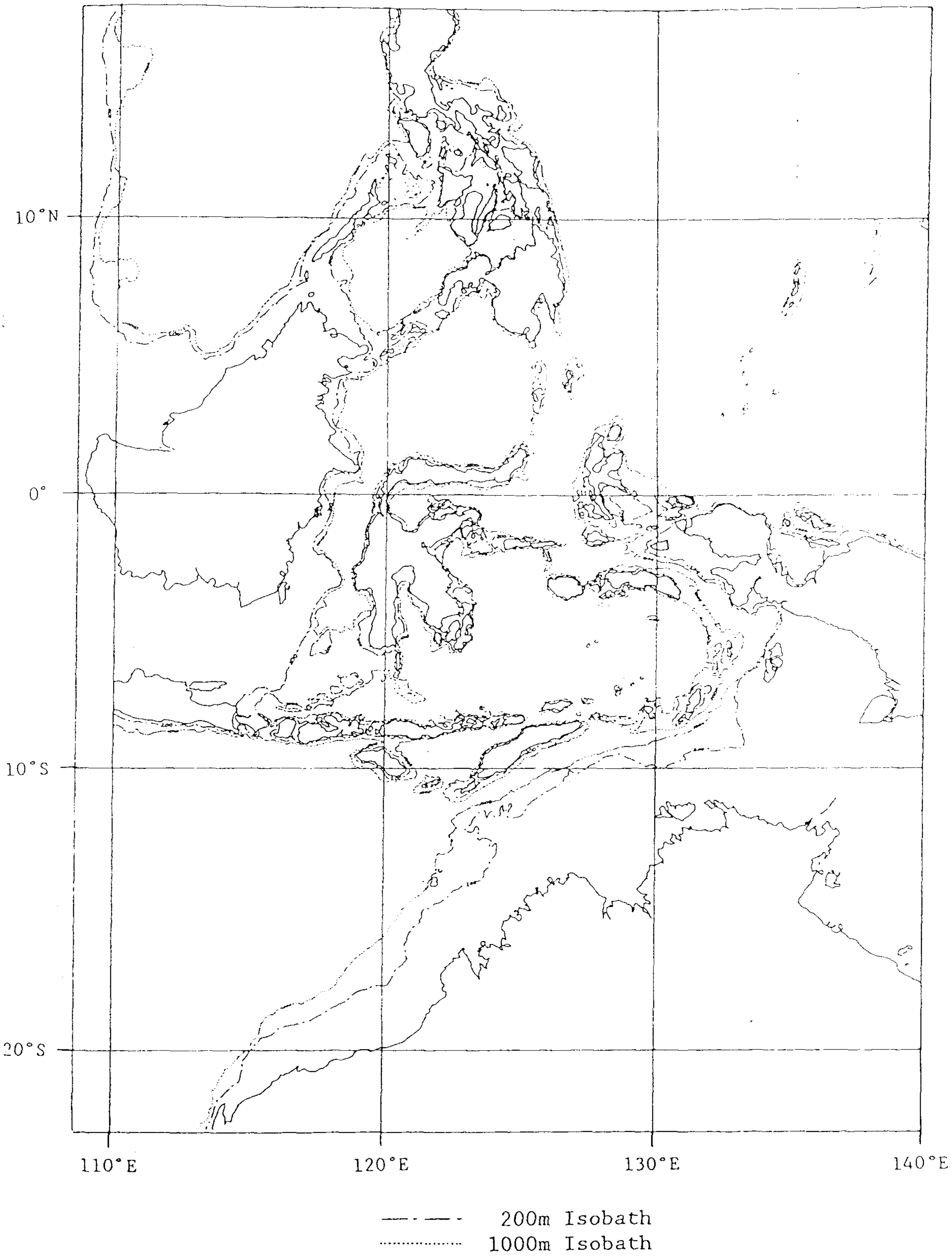

Figure 1.2.1 : Bathymetry of the Eastern Archipelago showing 200m and 1000m isobaths.

This oxygen minimum lies below another minimum which is the only known indication of Indian Ocean water entering the Eastern Archipelago (Wyrtki, 1961). A number of studies of the water masses after they have entered the Indian Ocean have been carried out by Rochford (1964, 1966, 1969).

1.2.3 Surface layer circulation

The circulation of the surface layer of the South East Asian Waters is largely governed by the monsoon wind system. The equatorial pressure trough moves with the sun and crosses the equator twice each year. In the northern summer winds are from the south east in the seas south of the equator and from the south west in those north of the equator. The monsoon winds are not strong (typically $6ms^{-1}$) (Wyrtki, 1961) but are steady and thus have the effect of driving surface water westward through the Banda, Flores and Java seas into the South China sea. Currents up to $1ms^{-1}$ are observed in the Java Sea at this time (Wyrtki, 1961). The depth to which the monsoon winds act is typically 50m in the Banda, Flores and Java Seas (Wyrtki, 1961).

In the northern winter the wind directions reverse and surface water is driven south from the Pacific via the shallow seas and eastwards into the Banda Sea. The seasonal transport due to the wind system is quite large (3-4.5Sv in the Java Sea) but does not cause a large annual transport of surface water through the region (Wyrtki, 1961).

1.2.4 Lower layer forcing and circulation

The prevailing trade winds over a tropical ocean cause an increase of sea level on the western side of the ocean and a lowering on the eastern side. Assuming that the deep connection between the Indian and Pacific Oceans south of Australia implies that the mean sea levels of the two oceans remain roughly equal, the effect of the trade winds will be to produce a sea level difference between the Western Pacific and the Eastern Indian Ocean.

Wyrtki (1987) used sea level records from the Pacific and Indian Oceans to determine the difference in sea level between the two oceans. In the Pacific, records started in 1948, exist at Davao and Julo in the Phillipines and at Guam and Truk. In the Indian Ocean observations along the northwest coast of Australia have been made for approximately 50 years at Dampier, Port Hedland, Broome, Wyndham and Darwin. Unfortunately no sea level records have been made in Indonesian Waters since 1940. A seven year record between 1925-1931 made by the Dutch exists at many locations.

Although little Indonesian data is available there is a good correlation between the sea levels at Cilacap (south Java) and Darwin (figure 1.2.2). Wyrtki (1987) considered sea level at Darwin to be representative of sea level in the Eastern Indian Ocean and sea level at Davao in the Phillipines to be representative of the Western Pacific.

The absolute value of the sea level difference between the Western Pacific and Eastern Indian Ocean was determined from the difference of dynamic height between the two areas (Wyrtki, 1987). Using dynamic height differences calculated from the data prepared by Levitus (1982) and the Indian Ocean Atlas (Wyrtki et al, 1971) it was found the pressure difference decreased from the surface to a minimum at 500m. Below the minimum a weak pressure gradient from the Pacific to the Indian Ocean is again present. The mean pressure difference at the sea surface relative to the minimum at 500m is 16.3 dyn cm. (Wyrtki, 1987). Thus the mean sea level at Davao is 16.3cm greater than that at Darwin. The sea level difference has an approximately sinusoidal annual variation with a maximum of 33cm during July and August and a minimum of zero in January and February (see figure 1.2.3). The pressure difference is concentrated in the upper 200m (Wyrtki, 1987).

Inter annual variations in the sea level in the Pacific and Indian Oceans correlate and show lowering of sea level throughout the region during El Nino events (Wyrtki, 1987).

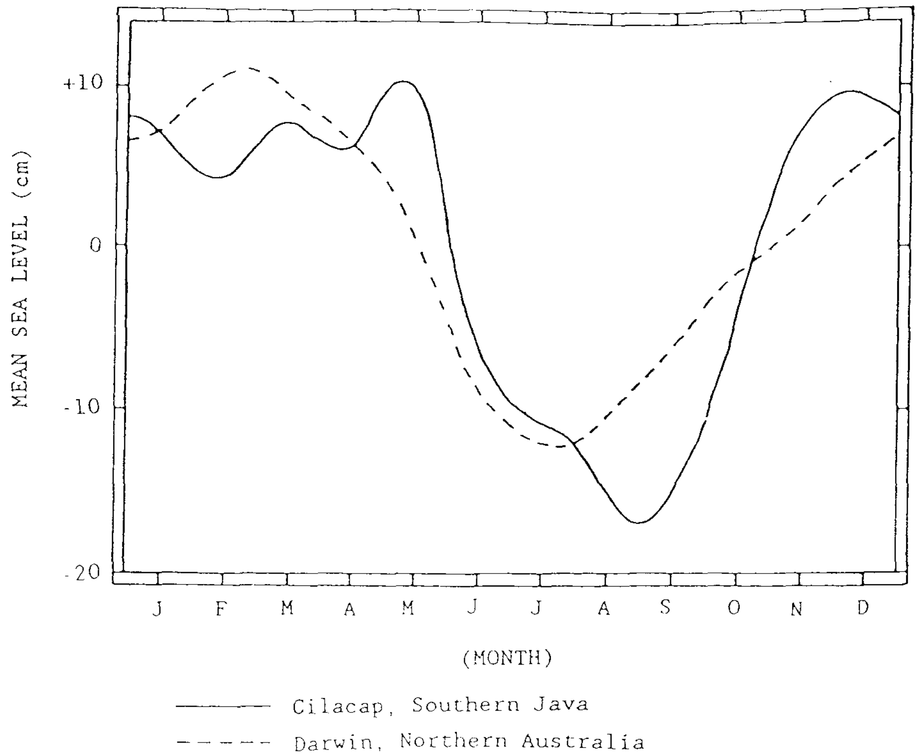

Figure 1.2.2 : Sea level elevation at Cilacap (South Java) and Darwin (N. Australia) (after Wyrtki, 1987).

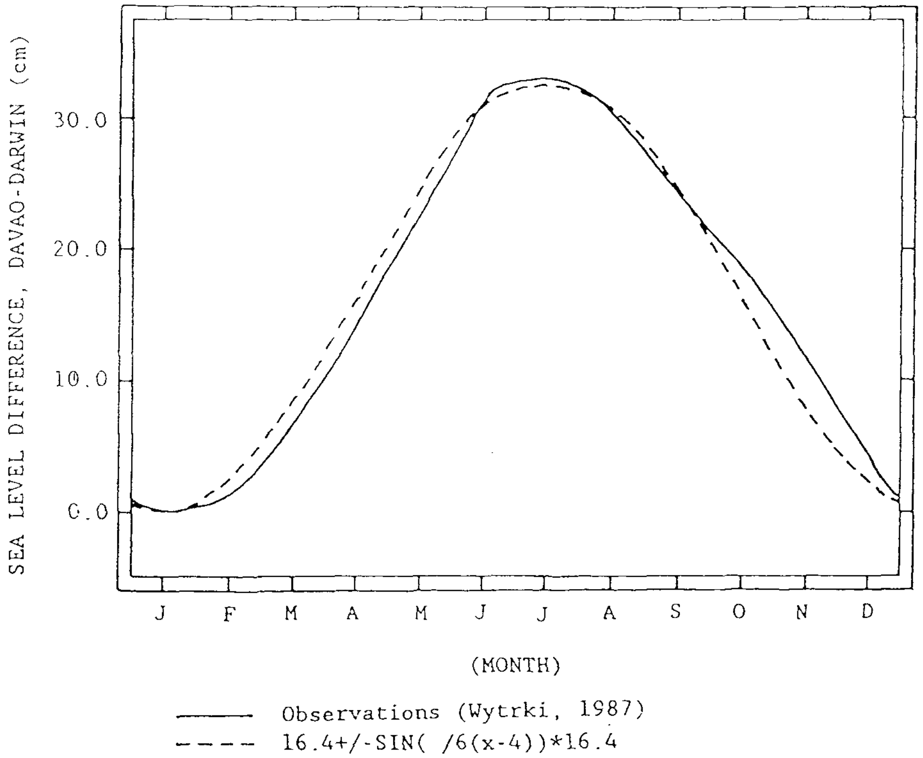

Figure 1.2.3 : Sea level difference between Davao (Phillipines) and Darwin (N. Australia) after Wyrtki, 1987).

Below the surface layer the southward spreading of the Subtropical Lower Water (100-200m) and the Northern Intermediate Water (300m) occurs due to the pressure gradient from the Pacific to the Indian Ocean. The strength of the transport decreases with depth (Wyrtki, 1961) associated with the decreasing pressure gradient. At 500m where the north-south pressure gradient is zero (Wyrtki, 1987) there is weak inflow from the Indian Ocean (section 1.2.2). Below 700m the pressure gradient is again present and weak southward flow of Pacific water through the deep channels to the east of the Celebes occurs.

1.2.5 Effects of throughflow on South Eastern Indian Ocean

Godfrey and Golding (1981) showed that if the throughflow did not occur, the Sverdrup circulation pattern in the Southern Indian Ocean would become similar to that in other tropical oceans, namely that the flow would be directed to the northwest over most of the ocean. Godfrey and Golding proposed that closure of the passages through the Indonesian waters would lower temperatures off Western Australia. Thus the throughflow might be responsible for the observed lack of upwelling along the coast of Western Australia.

The problem of upwelling off Western Australia was raised earlier by cores taken during the Deep Sea Drilling Program (The Shipboard Scientific Party, 1974). The cores were found to contain high values of organic carbon at levels that suggested in recent times (0-10^6 years before present) there had been periods of high levels of ocean productivity in the waters off Western Australia. Webb and Morris (1984) suggested that the high productivity may have arisen during the recent ice ages. The CLIMAP study (Prell et al, 1980) also found evidence of cool surface water flowing north off Western Australia at a period 18,000 years before present. This indicates that the circulation of the Southern Indian Ocean was more normal and like that of Southern Atlantic and Pacific during the last ice age. Sea level would have been about 100m lower and thus many of the shallow passages through the Indonesian islands would have been blocked during an ice age.

Godfrey and Golding (1981) also suggested that long internal waves might propagate south from the equatorial Pacific through Indonesian waters and along the Western Australian coast. This disturbance would broaden westward with time because of the propagation of long Rossby waves from the eastern boundary. Thus the propagation of a Kelvin wave along the coast of Western Australia would eventually produces changes throughout the whole of the Southern Indian Ocean. Data was not available to test the hypothesis that fluctuations of the mass transport relation north of New Guinea induced changes in the mass transport throughout the Indian Ocean. However, there was evidence that the interannual El Nino related fluctuations in the mean sea level of the Western Pacific induced corresponding changes in mean sea level along the coast of Western and Southern Australia.

The most important observation of the work of Godfrey and Ridgway (1985) is that they found that the latitudinal change of mean dynamic height along the western Australian coast is very similar to that along the eastern coast. This implies that Australia is acting as if it were an island in a larger Indian-South Pacific Ocean.

Godfrey (1989) used a Sverdrup model of depth integrated flow for the world ocean that allowed for island circulations and determined the circulation around Australasia (Australia-New Guinea as 16+/-4Sv. This circulation is just the transport through Indonesian waters. Using Levitus (1982) data for a section between Sumatra and North Western Australia Godfrey repeated the calculation of the throughflow and obtained a valve of 10-13Sv, closer to that of the other recent estimates (see section 1.3.3).

The model calculations were repeated with the Indonesian passages closed. It was found that the model predicted an increase in the strength of the Eastern Australian Current in the Pacific by 16Sv and removed the westward zonal jet at 10°S in the Indian Ocean. The effect on the Indian Ocean if no salinity changes occurred was to cause a 6°C decrease in the temperatures of the upper 500m throughout the Southern Indian Ocean.

Kundu and McCreary (1986) investigated the circulation forced by a steady inflow (taken to be 7.3Sv) of water through the eastern boundary of an ocean using two linear, viscid, continuously stratified models. Without vertical mixing they found all the inflow eventually turned westward across the ocean due to Rossby wave propagation. With vertical mixing included in the model a part of the inflow remained as a coastal current. From this solution they suggested that the throughflow from the Pacific to the Indian Ocean may contribute to the Leeuwin Current but that the throughflow was not the dominant mechanism for driving the circulation along the western coast of Australia.

1.3 OBSERVATIONS

1.3.1 Introduction

Major observational sources are Postma's (1958) analysis of the 1929-1930 Snellius Expedition and Wyrtki's (1961) report. More recently realisation of the importance of the throughflow in determining global climate and the transport of heat and freshwater has provoked experimental interest in the area.

1.3.2 Early observational evidence for throughflow

Direct evidence for the vertical extent of the throughflow is found from current meter data at anchor stations during the Snellius Expedition (Lek, 1938). In the Macassar Strait a strong southward flow (50-60cms^{-1}) was found concentrated in the upper 200m in August. The flow reached a maximum of 84cms^{-1} at a depth of 50m. Observations in September in the Halmahera Sea found the current to be weaker ($\sim$30cms^{-1}) and not as deep (upper 100m). At both stations the currents at 400m are southward and between 5-10cms^{-1}. In the Halmahera Sea there is northward flow ($\sim$5-10cms^{-1}) between 100m and 150m.

Some hydrographic evidence for the throughflow based on water mass movements has been described in section 1.2.2. Further data in the Atlas of the Indian Ocean Expedition (Wyrtki et al, 1971) shows a tongue of low salinity water originating from the South East Asian Waters extending westwards into the Indian Ocean at depths up to 400m. Rochford (1966) shows that much of the water in the South Equatorial Current appears to be supplied from the intermediate waters of the Banda Sea.

Wyrtki (1961) calculated geostrophic currents from the available hydrographic data to estimate the mass transports through the different basins of the Eastern Archipelago. Some of the transports are large for individual basins and seas. Eastwards transport through the Flores Sea was calculated to be 6.0Sv in February. However, Wyrtki's estimate of the throughflow from the Pacific to the Indian Ocean was 1.0–2.5Sv, with the maximum throughflow occurring in August and the minimum in December to February.

1.3.3 Recent Observational estimates of throughflow

Godfrey and Golding (1981) carried out computations of mass transport in the South Eastern Indian Ocean using the observed distribution of depth integrated dynamic height. They concluded that an annual mean throughflow of 10Sv was required to produce a mass balance in the region.

Godfrey and Ridgeway (1985) continued working with the observations of integrated dynamic heights and found that south of Java the South Equatorial Current had a strength of 5Sv. The Leeuwin Current which also transports water away from the Indonesian region had a strength of 5Sv and might be connected with the throughflow. Thus the throughflow was estimated to be 5–10Sv.

Piola and Gordon (1984) used conservation of mass and salinity arguments to investigate the freshwater balance in the upper layers of the Pacific and Indian Oceans. A box model was used together with estimates of freshwater input and upwelling of deep waters into the upper layers at a rate required to balance the formation of North Atlantic Deep Water. The salinity of the model upper layer was found to be lower than observed in the Pacific and higher than observed in the Indian Ocean. This discrepancy was avoided if a Pacific to Indian Ocean throughflow of 14Sv at a salinity of 33.6 ppt was taken into account.

Fine (1985) used a tritium box model (upper 300m only) to investigate the throughflow. An anomalously high maximum of tritium was observed in the South Equatorial Current of the Indian Ocean. This had to be due to a combination of throughflow from the Pacific and precipitation. Using estimates of the sources of bomb produced tritium and the rates of input from precipitation compared to molecular exchange, Fine estimated the throughflow to be 5.1Sv (upper 300m only).

Fu (1986) used data from six sections of the Indian Ocean Expedition to examine the circulation and property fluxes in the Southern Indian Ocean from 10°S to 32°S. Temperature and salinity observations were interpolated to a set of standard depths. Geostrophic velocities relative to an initial chosen reference level were then computed for each standard depth at all station points. Finally the inverse method of Wunsch (1978) was applied to the geostrophic velocities to estimate an absolute velocity at the initial reference level. The basis of the inverse method is a mathematical statement of the fundamental principles (conservation of mass, momentum, energy) upon which previous descriptions of ocean circulation have been based. The absolute velocities so determined at the reference level satisfy, to a certain degree, the fundamental principles. Fu found that the throughflow was dependent upon the choice of initial reference level and estimated the transport to be 6-7Sv.

Gordon (1986) proposed that the main thermoclines of the world ocean are linked in a global circulation cell involving North Atlantic Deep Water (NADW) formation. Formation of NADW represents a transfer of upper layer water to abyssal depths at a rate of 15-20Sv (Gordon, 1986). NADW spreads throughout the Atlantic Ocean and into the Indian and Pacific Oceans via the Antartic Circumpolar Current and the deep western boundary currents. There is a compensating flow of upper layer water towards the areas of NADW formation. The path of this return flow was suggested to be from the Pacific to the Indian Ocean via Indonesian waters, westward flow across the Indian Ocean then occurs at 10-15°S. Southwards flow into the Atlantic is via the Mozambique channel and the Agulhas Current.

Gordon (1986) showed the magnitude of the return flow increasing along its path as more NADW is incorporated into the upper layer of the oceans. Gordon also suggested that the Indonesian waters might be particularly important in controlling the rate of formation of NADW since the surface layer circulation is strongly affected by the monsoon wind forcing. Using values of 6-10Sv for the Agulhars Current entering the Atlantic an upper limit of 6-10Sv is placed on the throughflow from the Pacific to the Indian Ocean. Gordon chose a value of 8•5Sv for the throughflow but notes the value would be halved if the NADW entering the South Pacific thermocline returns to the Atlantic by way of the Drake Passage.

The results of the first direct measurement of part of the Pacific to Indian Ocean throughflow have been presented by Murray and Arief (1988). A series of current meter arrays were set up in the Lombok Strait in 1985. The current meter data indicates continuous southward flow into the Indian Ocean with velocities up to 85cms^{-1}. The flow is interrupted by bursts of northward current associated with tropical cyclone activity. The vertical structure of the flow is similar to that observed in the Snellius data. With a rapid decrease from 75-300m, most (~75%) of the flow being baroclinic. None of the data from stations in the Lombok Strait shows evidence of a deep northward return flow caused by reflection from the shallow sill (350m) in the strait (Murray and Arief, 1988).

Calculations based on the observations from the five current meter arrays determined a mean transport through the Lombok Strait of 1.7Sv with a maximum of 4.0Sv in August and a minimum of 1.0Sv from February to May. 80% of the transport was found to be through the upper 200m. Determination of the transport was based on rotational effects in the strait being negligible due to the narrow width of the strait. At its narrowest the Lombok Strait is 30km wide and has an internal Rossby radius (the fundamental horizontal length scale that appears in problems adjusting under gravity in a rotating flow) of 90km. A comparison of the transport through the Lombok Strait with other recent estimates suggests that at least 20% of the total throughflow occurs through the Strait.

Other observations have been made on an opportunity basis and are not widely reported. In 1988 the RVS Charles Darwin made an Acoustic Doppler Current Profiler (ADCP) section in the upper 200m from the Phillipines to New Guinea (Webb et al, 1989). Analysis of this data should give an estimate of the inflow from the Pacific to the region during August. The CSIRO at Hobart, Tasmania are presently installing a set of stations throughout the region to monitor sea level variability (Lennon, personal communication). The forthcoming Indonesian Seas throughflow Experiment (INSTEP) is intended to make direct measurements of the throughflow (Wyrtki, 1987).

The observations of the throughflow are summarized in table 1.3.1.

TABLE 1.3.1 Observational estimates of Pacific to Indian Ocean throughflow.

		MEAN (Sv)	SEASONAL (Sv)	METHOD
Wyrtki	(1961)	1.7	1.0-2.5	Dynamic calculation
Godfrey & Golding	(1981)	10		Mass transport
Godfrey & Ridgeway	(1985)	5-10		Mass transport
Piola & Gordon	(1984)	14		Freshwater box model
Fine	(1985)	5.1		Tritium box model (upper 300m)
Fu	(1986)	6-7		Inverse method
Murray & Arief	(1988)	1.7	1.0-4.0	Direct measurement
Godfrey	(1989)	10-13		Sverdup model

1.4 MODELS

1.4.1 Early model estimates of throughflow

The multi level global circulation models of Cox (1975), Bryan et al (1975) and Takano (1975) were the first to include a tropical latitude link between the Pacific and Indian Oceans. The resolution of these models are summarized in table 1.4.1. The models were forced by observed mean wind fields and the effects of observed temperature and salinity fields were included in some of the model experiments. Of these early modelling studies that of Cox had the greatest resolution. Cox (1975) reports a Pacific to Indian Ocean throughflow of 18Sv.

MODEL	**HORIZONTAL RESOLUTION*** **(km)**	**VERTICAL RESOLUTION** **(Levels)**
Cox (1975)	~ 200x200	9
Bryan et al (1975)	~ 500x500	12
Takano (1975)	~ 400x250	5

***Of South East Asian Waters**

The results of the many global circulation models of the past decade are not presented here. Instead in the next section results of the two most relevant recent studies are described.

1.4.2 Recent model estimates of throughflow

The single layer, reduced gravity, global model of the Naval Ocean Research and Development Activity (NORDA) was used by Kindle et al (1987) to examine the Pacific to Indian Ocean throughflow and its seasonal and inter annual variability. The model equations are the non linear shallow water equations for a single layer with reduced gravity on a spherical grid. The resolution is $1\frac{1}{4}°$ in the meridional direction and 1½° in the zonal. The model is forced by the observed wind fields from the Fleet Numerical Oceanographic Centre (FNOC).

In the initial model (Kindle et al, 1987) the region representing the Eastern Archipelago did not include the Macassar or Lombok Straits. Pacific to Indian Ocean throughflow occurred via the Molucca, Halmahera and Timor Seas. The mean transport was found to be 7Sv in the period 1977-1981. The maximum transport occurred in July and August (~11Sv) and the minimum (~3Sv) in January. Inter annual variability of the transport (3.0-4.5Sv) was comparable to the seasonal variations.

Later results of the NORDA model, reported by Wyrtki (1987), are in agreement with the observations of seasonal and interannual variability of the sea level difference between Davao and Darwin. The model was adopted to include the Macassar Strait and Wyrtki (1987) states that the throughflow occurred in a strong western boundary layer that separated from the Mindanao Current and flowed through the Celebes Sea, the Macassar Strait, eastwards through the Flores Sea and finally into the Indian Ocean through the Timor Sea.

Murray and Arief (1988) compared the results of the NORDA model for 1985 with their observations of transport through the Lombok Strait. They found the model results and the observations were in phase. The NORDA model is being adapted to include the Lombok Strait.

As described in section 1.1, to date the finest resolution global model is that of Semtner and Chervin (1988). This model was able to include some of the major topographic features of the Eastern Archipelago, although all islands in the region were submerged. The Lombok Strait was represented as being 100km wide (two ½° grid spaces) and 710m deep. The model showed the chain of thermocline transport suggested by Gordon (1986). Transport through the Indonesian Waters was 15-18Sv.

Semtner and Chervin (1988) do not report any details of the pathway of the throughflow from the Pacific to the Indian Ocean.

However they do show eddies from the Pacific Ocean turning west into the Indian Ocean after passage through the Macassar and Lombok Straits. The eddies are of 30 day period.

The preliminary experiment reported by Semtner and Chervin (1988) was forced by annual mean wind stresses and was intended to investigate the intrinsic variability due to dynamical instabilities. In the future it is expected to force the model with seasonal wind stresses to investigate the seasonal and interannual variability of the world ocean.

1.5 ANALYTIC THEORY

1.5.1 Introduction

In this section a variety of analytic theories relevant to the problem of flow through a cross equatorial channel are presented. These theories will be frequently referred to in later chapters.

In any problem many important properties of the transient response are determined by the free waves of the system. In a linear system of waves there is always a complete set of waves that can be used as an expansion in describing the system. At the equator the natural set of waves (section 1.5.4) is different to that at high latitudes because the Coriolis parameter, f, is zero at the equator. In a narrow channel because the waves become mixed by the boundary conditions at the east and west boundaries the problem is complicated (section 1.5.5).

In understanding the long term response of the channel the conservation of potential vorticity of the flow as the water travels south is important (section 1.5.3).

No adequate analytic solution exists to investigate the flow forced through a cross equatorial channel by a north south difference in sea level. The purpose of this section is to allow a clear understanding of the important processes revealed by later numerical models.

1.5.2 Dynamics of Channel flow

The rotation of the earth has a major influence on the way the ocean responds to imposed changes. The dynamic response is caused by the Coriolis acceleration, which is the product of the Coriolis parameter, f, and the horizontal velocity. When f=0 the response is made up of inertia-gravity (Poincare) waves and a steady current (Gill, 1982). With rotation included coastal Kelvin waves can exist.

When f is large but varying the steady current becomes planetary (Rossby) waves (Gill, 1976). If f is varying but at some point (the equator) is zero the response is composed of equatorial Kelvin waves plus equatorial Rossby and Poincare waves and the mixed Rossby-gravity (Yanai) wave (Cane and Sarachik, 1976, 77, 79).

At meridional or zonal boundaries the longshore component of the Coriolis acceleration must vanish. The offshore scale, L, at which the longshore component is small with respect to other terms is the Rossby radius of deformation given by

$$L = \frac{c}{|f|} \qquad (1.5.2.1)$$

At the equator both components of the Coriolis acceleration vanish and the important scale is the equatorial radius of deformation given by

$$L_e = \left(\frac{c}{2\beta}\right)^{\frac{1}{2}} \qquad (1.5.2.2)$$

Using a value of $\beta = 2.3\mathrm{x}10^{-11}m^{-1}s^{-1}$ and $c = 2.4ms^{-1}$, as an estimate of the first baroclinic phase speed in the Eastern Archipelago (section 2.6.2) the radius of deformation at different latitudes have been calculated and are given in table 1.5.1.

In a narrow channel where the channel width, W, is small compared with L, rotation effects in the along channel direction can be neglected (to a first approximation) because the cross channel velocity must be small. At the next order of approximation rotation gives rise to a cross-channel pressure gradient in order to

TABLE 1.5.1 Rossby radius at different latitudes in the Eastern Archipelago

Latitude (degrees)	f $x10^{-5}s^{-1}$	Radius of deformation (Km)
30	7.35	33
15	3.75	64
10	2.5	96
8	2.0	120
6	1.5	160
5	1.25	192
<4		228*

*** (1.5.2.2) applies, $\beta = 2.3 \times 10^{-11} m^{-1} s^{-1}$.**

geostrophically balance the longshore flow and produces a shear in order to conserve potential vorticity in response to any departure from the equilibrium position of the free surface (Pedlosky, 1979). This balance also holds near the boundaries of wide channels.

1.5.3 Conservation of Potential Vorticity

The fundamental physical problem that affects the long term flow through a cross equatorial north south channel is the enforced change in relative vorticity, ζ, that water flowing south must undergo to conserve potential vorticity, PV.

$$PV = \frac{\zeta + f}{H} \qquad (1.5.3.1)$$

where $\zeta = \frac{\partial v}{\partial x} - \frac{\partial u}{\partial y}$ and H is the depth of the fluid column. The theory states that if the fluid is inviscid the throughflow will follow f/H contours to conserve potential vorticity (Gill, 1982).

In the absence of bottom topography the southward movement of the fluid column requires an increase in the relative vorticity ζ

(ie. the generation of positive or cyclonic vorticity) to balance the decrease in f. Mechanisms that can provide this vorticity are bottom dissipation of vorticity and viscous dissipation of vorticity.

In the case of the throughflow from the Pacific to the Indian Ocean through South East Asian Waters bottom dissipation of vorticity may be important in the shallow seas. The deeper water can gain cyclonic vorticity through horizontal viscosity acting on the sides of the channel. Alternatively by the action of eddying a transfer of potential vorticity to the surface waters might occur. The surface waters can then lose the vorticity in the shelf seas. An example of an ocean current where eddy formation is used to transfer vorticity is the East Australian Current (Boland and Hamon, 1970). Reports by Wyrtki (1961) of the effect of 'internal tides and waves' on some of the bottle station measurements in the Macassar Strait may also have been due to eddies associated with vorticity transfer in the strait.

1.5.4 Equatorial wave motions

Determining the dynamic response in the equatorial region is carried out by using an approximation called the equatorial beta plane. The Coriolis parameter is taken to be the product of a constant, β and the distance from the equator

$$f = \beta y \qquad (1.5.4.1)$$

where $\beta = 2.3 \times 10^{-11} m^{-1} s^{-1}$.

Within 15° of the equator the maximum percentage error in this approximation compared to the use of spherical polar co-ordinates is less than 4%.

The linear shallow water equations take the form

$$\frac{\partial u}{\partial t} = -\beta y v - g\frac{\partial \eta}{\partial x} \qquad (1.5.4.2)$$

$$\frac{\partial v}{\partial t} = \beta y u - g\frac{\partial \eta}{\partial y} \qquad (1.5.4.3)$$

$$\frac{\partial \eta}{\partial t} = -H\left(\frac{\partial u}{\partial x} + \frac{\partial v}{\partial y}\right) \qquad (1.5.4.4)$$

where x and y are the eastward and northward co-ordinates respectively and t is the time, u and v are the x and y components of the horizontal velocity, η is the sea surface elevation and g the acceleration due to gravity.

An equation for v alone can be formed from (1.5.4.2)-(1.5.4.4).

$$\frac{\partial}{\partial t}\left[\frac{1}{c^2}\left(\frac{\partial^2 v}{\partial t^2} + \beta^2 y^2 v\right) - \left(\frac{\partial^2 v}{\partial x^2} + \frac{\partial^2 v}{\partial y^2}\right)\right] - \beta\frac{\partial v}{\partial x} = 0 \qquad (1.5.4.5)$$

where $c = (gH)^{\frac{1}{2}}$

Looking for free wave solutions, which have $v \propto \exp i(kx-\omega t)$ to (1.5.4.5) leads to the ordinary differential equation

$$\frac{d^2 v}{dy^2} + \left(\frac{\omega^2}{c^2} - k^2 \;\; \frac{\beta k}{\omega} - \frac{\beta^2 y^2}{c^2}\right) v = 0 \qquad (1.5.4.6)$$

The important feature of the solutions of (1.5.4.6) is the equatorial trapping due to the variation of the Coriolis parameter with latitude. For a wave of fixed frequency ω and fixed east-west wavenumber k the co-efficient of v in (1.5.4.6) may be positive at the equator giving wavelike behaviour, but as $|y|$ increases $f=\beta y$ increases and the co-efficient of v decreases until it becomes zero at the 'turning point' or critical latitude, y_c, given by

$$f_c^2 = \beta^2 y_c^2 = \omega^2 - k^2 c^2 - \frac{\beta k c^2}{\omega} = (2n+1)\beta c \qquad (1.5.4.7)$$

At latitudes higher than the critical one the co-efficient of v becomes negative and solutions of (1.5.4.6) are exponential in character giving wave trapping. With the value of $c=2.4\,\mathrm{ms}^{-1}$ the critical distances for $n = 0,1$ and 2 are 323,560 and 722km respectively (2.9°, 5.0° and 6.0°).

The solutions of (1.5.4.6) that vanish as $y \to \pm\infty$ are given (eg. Gill, 1982)

$$V_n = 2^{-n/2} H_n\left[\left(\frac{\beta}{c}\right)^{\frac{1}{2}} y\right] \exp\left(\frac{-\beta y^2}{2c}\right) \cos(kx-\omega t) \qquad (1.5.4.8)$$

where n is the order of the Hermite polynomial H_n. The corresponding dispersion relation is

$$\left(\frac{\omega}{c}\right)^2 - k^2 - \frac{\beta k}{\omega} = \frac{(2n+1)}{\beta c} \quad n = 0,1,2,... \qquad (1.5.4.9)$$

and the dispersion curves are shown in figure 1.5.1.

For n > 1 the wave solutions divide into two classes, for one class the term $\frac{\beta k}{\omega}$ is small so the dispersion relation is approximated

$$\omega_n{}^2 = (2n+1)\ \beta c + k^2c^2 \quad n = 1,2,3,... \qquad (1.5.4.10)$$

These waves are called equatorially trapped Poincare waves. The group velocity $\partial\omega/\partial k$ can be to the east or west. For long waves (with $k \to 0$) the frequency is given by

$$\omega_n{}^2 = (2n+1)\beta c \qquad n = 1,2,3,... \qquad (1.5.4.11)$$

Hence the minimum frequency of the Poincare waves is $\omega_1 = (3\beta c)^{\frac{1}{2}}$ which for a phase speed of $2.4 ms^{-1}$ is $1.29 \times 10^{-5} s^{-1}$ equivalent to a 5½ day period.

The other class of wave solution for n >1 comes from the term ω^2/c^2 being small, then the dispersion relation is given approximately by

$$\omega_n = \frac{-\ \beta k}{(k^2+(2n+1)\beta/c)} \qquad n = 1,2,3,... \qquad (1.5.4.12)$$

The corresponding waves are called equatorically trapped planetary or equatorially trapped Rossby waves.

Long Rossby waves ($k \to 0$) are essentially non dispersive with wave speed (both phase and group)

$$\frac{\omega_n}{k} = \frac{\partial\omega_n}{\partial k} = Cg_{xn} = -\frac{c}{(2n+1)} \qquad n = 1,2,3,... \qquad (1.5.4.13)$$

The group velocity is thus westward with speeds 0.8, 0.48, 0.34ms^{-1}, ..., when c = 2.4ms^{-1}

Short Rossby waves have eastwards group velocity in the direction opposite to the phase velocity. The maximum value is (Gill, 1982),

$$\frac{\partial\omega_n}{\partial k} = Cg_{xn} = -\frac{c}{8(2n+1)} \qquad n = 1,2,3,... \tag{1.5.4.14}$$

which for a phase speed of 2.4ms^{-1} is 0.1ms^{-1}. For very short waves ($k \to \infty$) the approximate dispersion relation is

$$\omega = -\frac{\beta}{k} \text{ and } \frac{\partial\omega}{\partial k} = \frac{\beta}{k^2} \tag{1.5.4.15}$$

and the phase and group velocities are equal and opposite.

The maximum frequency of the Rossby wave occurs when the group velocity is zero and is given by

$$\omega_n = \frac{1}{2}\left(\frac{\beta c}{(2n+1)}\right)^{\frac{1}{2}} = \frac{\frac{1}{2}f_c}{(2n+1)} = \frac{1}{2}\frac{\beta c}{f_c} \tag{1.5.4.16}$$

Thus the maximum frequency Rossby wave with a phase speed of 2.4ms^{-1} is 2.1×10^{-6}s^{-1}, corresponding to a period of 34 days.

The Yanai wave labelled by n=0 in figure 1.5.1 has the dispersion relation

$$\frac{\omega}{c} - k - \frac{\beta}{\omega} = 0 \tag{1.5.4.17}$$

For large positive k the Yanai wave behaves like a Poincare wave whilst for large negative k the wave behaves like a Rossby wave. The phase velocity can be to the east or west but the group velocity is always eastward.

The case k = 0 corresponds to a standing wave for which the surface moves sinusoidally up and down on opposite sides of the equator. Particles move anticyclonically with eastward phase when the free surface is elevated and westward phase when it is depressed. The frequency of the standing wave is given by

$$\omega = (\beta c)^{\frac{1}{2}} \tag{1.5.4.18}$$

which for a baroclinic phase speed of 2.4ms^{-1} is $7.4\text{x}10^{-6}\text{s}^{-1}$ and corresponds to a period of about 10 days.

The final type of equatorial wave is the equatorial Kelvin wave that exists due to the vanishing of the Coriolis acceleration at the equator. The motion is everywhere parallel to the equator

$$u = \left(\frac{g}{H}\right)^{\frac{1}{2}} e^{-y}/L_e \; G(kx-\omega t) \tag{1.5.4.19}$$

showing decay in a distance, L_e, the equatorial radius of deformation (equation 1.5.2.2).

The dispersion relation for the equatorial Kelvin wave is

$$\omega = kc \tag{1.5.4.20}$$

and shows that the equatorial Kelvin wave propagates eastward without dispersion at the same speed, c, as in the non rotating case

$$\frac{\omega}{k} = \frac{\partial\omega}{\partial k} = C_{gx} = c \tag{1.5.4.21}$$

The equatorial Kelvin wave is sometimes called the n=-1 wave because (1.5.4.21) satisfies (1.5.4.9) when n=-1.

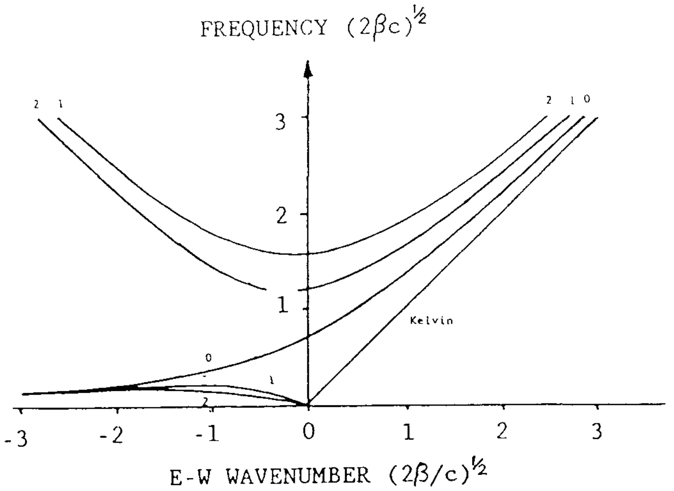

Figure 1.5.1 : Dispersion curves for equatorial waves.

1.5.5 Effect of Meridional boundaries

The equatorial modes of section 1.5.4 are required to understand the short term response of the channel. However these modes are not a good set in a narrow channel because they become mixed by the boundary conditions at the east and west boundaries. Some aspects of the flow are better thought of as a boundary trapped Kelvin wave, which can also be expanded as a sum of equatorial modes (Moore, 1968 referenced in Cane and Sarachik, 1977).

The coastal Kelvin wave solution can be found by setting the cross shore velocity equal to zero in the linear shallow water equations (1.5.4.2) - (1.5.4.4). Hence in an ocean of constant depth in any vertical plane parallel to the boundary the motion is exactly the same as in the non rotating case, namely a shallow water gravity wave. The longshore velocity must also be in geostrophic balance. Thus for a north-south boundary the complete coastal Kelvin wave solution is

$$\eta = \eta_0 . e^{-x/L} \cos(ly-\omega t) \tag{1.5.5.1}$$

$$v = \left(\frac{g}{H}\right)^{\frac{1}{2}} \eta_0 e^{-x/L} \cos(ly-\omega t) \tag{1.5.5.2}$$

where l is the north-south wave number and η_0 some constant. the dispersion relation for the coastal Kelvin wave is

$$\omega = lc \tag{1.5.5.3}$$

the same as that of the equatorial kelvin wave (1.5.4.20). Kelvin waves propagate equatorwards on a western boundary and polewards on an eastern boundary. Examples of the decay scale, L, the Rossby radius of deformation, are given in table 1.5.1. This shows that on an eastern boundary the Kelvin wave becomes more confined to the boundary as it travels polewards and that the opposite occurs on a western boundary as it moves towards the equator.

In the low frequency region of the dispersion relation (1.5.4.9) (figure 1.5.1) the only westward propagating wave is the long Rossby wave. When this wave impinges on a western boundary the reflected (eastward propagating) waves are the Kelvin wave, the Yanai wave, and a finite series of short Rossby waves. All these reflected waves will be at the same frequency as the incident wave. The finite series of short Rossby waves is generated because a mode incident on a western boundary excites a response which is as equatorially confined as itself (Cane and Sarachik, 1977). Hence energy tends to become equatorially trapped at a western boundary.

At an eastern boundary the reflection process can only involve long Rossby waves. Thus the response is less equatorially confined than the incident mode. A Kelvin wave incident on the eastern boundary produces a set of long Rossby modes that asymptote to a coastal Kelvin wave away from the equator.

Cane and Sarachik (1977) give details of the reflection of long Poincare waves. The net effect is that the initial waves are reflected back and forth between the boundaries. On reflection at the eastern boundary there is a loss of incident energy to boundary trapped motions.

The initial response of a narrow channel is the generation of all wavelength equatorial modes. However after the waves have been reflected by the boundaries a few times destructive and constructive interference occurs and the set of solutions are the equatorial modes with east-west wave number k given by

$$k = \frac{m\pi}{W} \qquad m = 1,2,3,.. \qquad (1.5.5.3)$$

where W is the width of the channel. The dispersion curves appropriate to the first six channel modes are shown in figures 1.5.2a,b and the group and phase velocities are shown in figures 1.5.3a,b. (calculated using $c = 2.4\text{ms}^{-1}$).

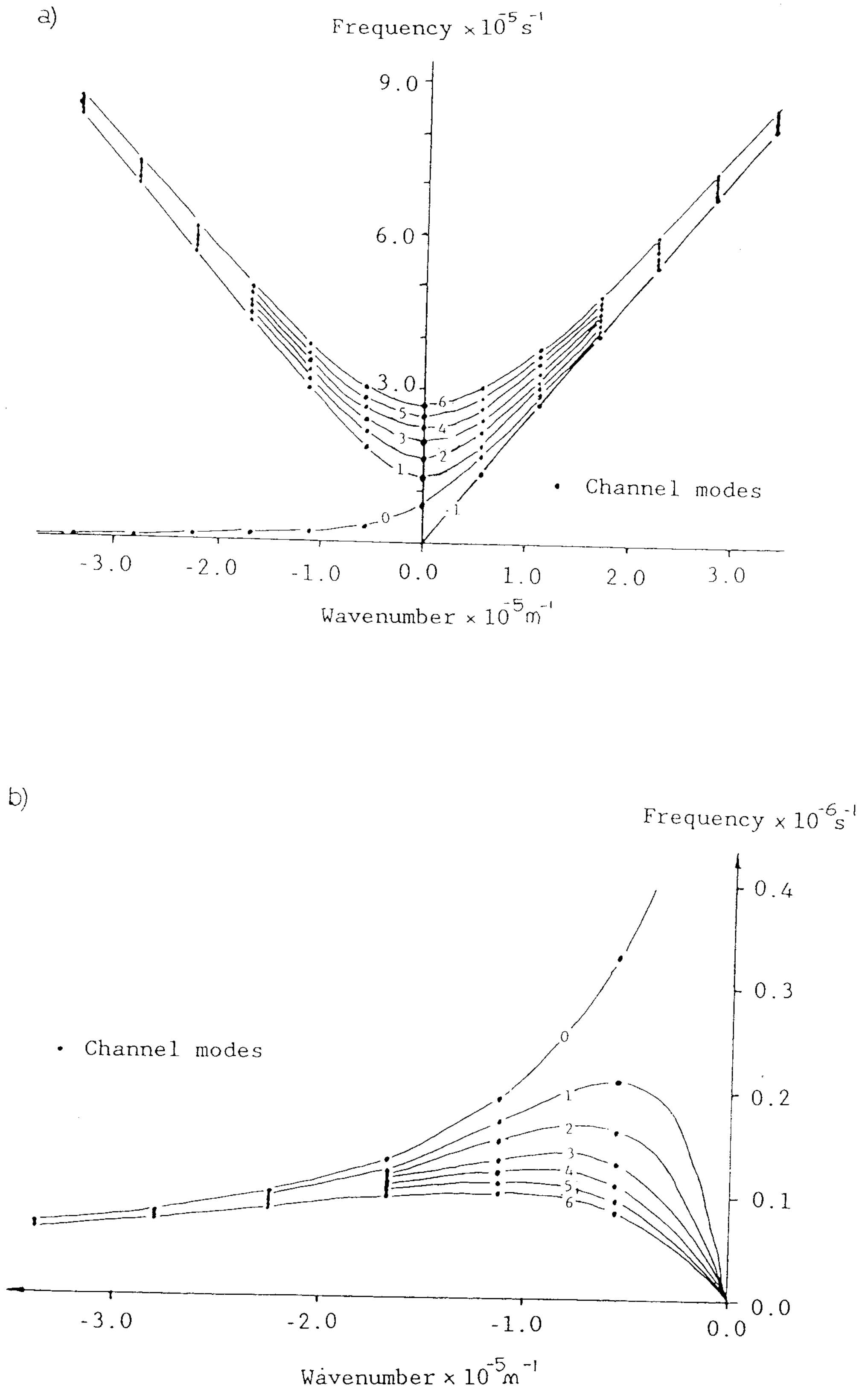

Figure 1.5.2 : Dispersion curve of first six channel modes; a) Inertia-gravity, b) Planetary.

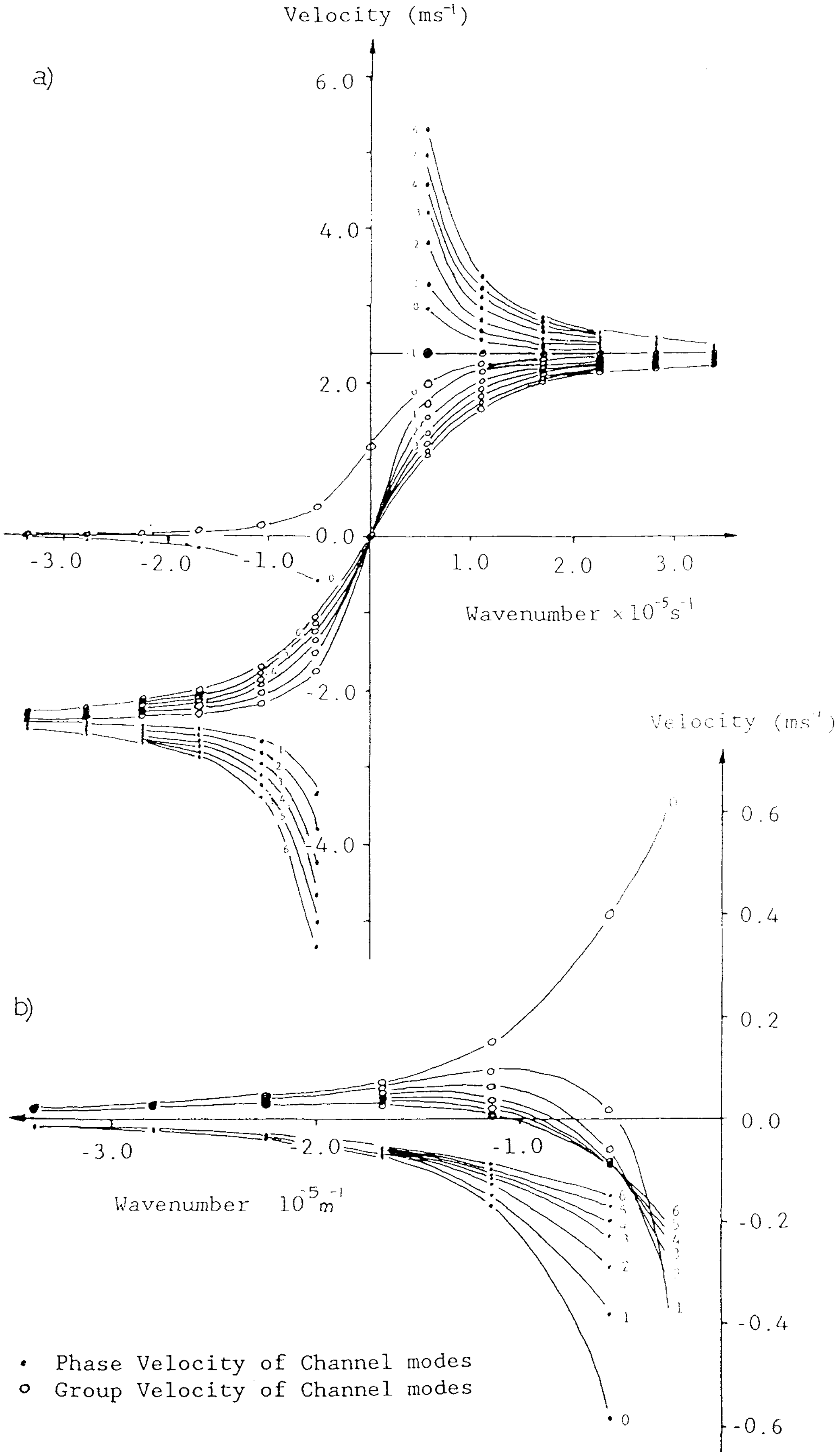

Figure 1.5.3: Phase and Group Velocity of first six channel modes; a) Inertia-gravity, b) Planetary.

1.5.6 Development of a western boundary layer

In section 1.5.4 the difference in the transmission properties of the eastward and westward travelling Rossby waves was shown. The eastward travelling waves having a shorter wavelength than the westward propagating waves. The western boundary can thus be thought of as a source of small scale energy (Pedlosky, 1979).

Small scale wave energy will be trapped at the western boundary when the distance D, moved eastward by the energy in a time t_d given by

$$D = Cg_x t_d = \frac{\beta}{k^2} t_d \tag{1.5.6.1}$$

is of the same order as the wavelength (k^{-1}). t_d is the characteristic time for the decay of small scale energy by lateral friction, nonlinear advection or bottom friction.

In Munk's (1950) model lateral friction dominates and

$$t_d = \frac{1}{A_H k^2} \tag{1.5.6.2}$$

Combining (1.5.6.1) and (1.5.6.2) leads to the estimate for the scale of trapping

$$Dm = \left(\frac{A_H}{\beta} \right)^{1/3} \tag{1.5.6.3}$$

Munk's solution for a flat bottomed rectangular ocean extending from x=0 to x=r in the east west direction with u=v=0 at x=0 and x=r gives the east-west variation in meridional velocity as

$$\frac{x'}{k} = Ke^{-\frac{1}{2}kx} \sin\left(\frac{\sqrt{3}}{2}kx + \frac{\sqrt{3}}{2kr} \right) - \frac{1}{kr}(1-e^{-k(r-x)}) \tag{1.5.6.4}$$

where $K = \frac{2}{\sqrt{3}} - \frac{\sqrt{3}}{kr}$ and $k = \left(\frac{\beta}{A_H} \right)^{1/3}$

Munk's solution, from x=0 to x=1000km, is plotted in Figure 1.5.4. For an ocean basin where r=6000km and $A_H = 5{,}600 m^2 s^{-1}$. The important features are the counter current east of the main boundary current and the width of the main current. In figure 1.5.4 the

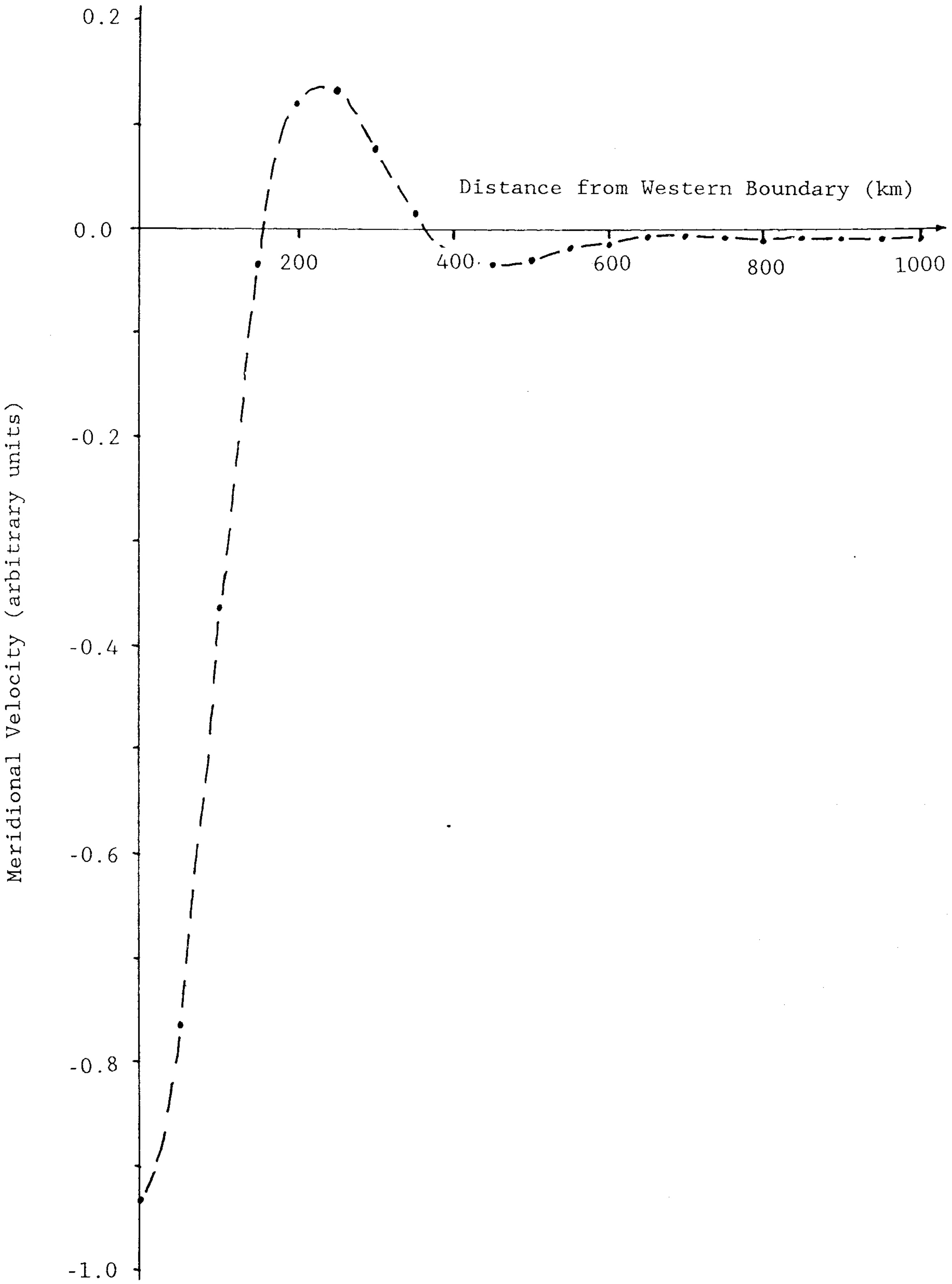

Figure 1.5.4 : Munk's solution from x = 0–1000km for a 6000km wide ocean basin.

magnitude of the counter current is 17% ($\exp^{-\pi}/\sqrt{3}$) of that of the main current and the width of the main current and the counter are

$$D_m = \frac{2\pi}{\sqrt{3}} \left(\frac{A_H}{\beta}\right)^{1/3} \qquad (1.5.6.5)$$

Maximum velocities occurred at $^1/3\ D_m$ and $^4/3\ D_m$ from the western boundary.

In this study the interest is in the western boundary currents that may develop in the deep channels of the Eastern Archipelago. These channels have widths < 250km. The entire region through which the throughflow can occur is less than 1000km in width (Halmahera-Borneo).

The magnitude of the counter current compared to that of the boundary current in channels of various widths with $A_H = 100 m^2 s^{-1}$ is given in table 1.5.2.

TABLE 1.5.2 Ratio of counter current to boundary current for channels of different widths

Channel width (km)	**ratio of maximum current valves (%)**
280	29
560	23
1120	19
6000	17

Using the channel of width 560km (used in later experiments) the effect of variations in the horizontal viscosity is shown in table 1.5.3. The boundary layer width determined from (1.5.6.5) is shown for comparison with that calculated from (1.5.6.4). The ratio of maximum currents is also given.

TABLE 1.5.3 Effect of variations in the horizontal viscosity on Munk's solution for a narrow channel (560km)

A_H (m^2s^{-1})	$Dm(f(A_H,\beta))$ (km)	Munk's solution (km)	ratio of max. currents (%)
10	28	27	19
50	47	45	21
100	59	56	23
500	101	92	27
1000	128	113	32
5000	218	177	41
10000	275	188	65

Munks (1950) solution is for the circulation in an ocean basin caused by zonal wind forcing. There is no net transport through the basin. A strong poleward boundary current exists with a weaker equatorward counter current adjacent and weak equatorward flow throughout the remainder of the basin.

In Munk's linear model the boundary layer exists as a balance between the relative vorticity produced in a column of water as it is moved polewards at the western boundary and the lateral diffusion of this relative vorticity into the western wall. A fluid element entering the western boundary layer has negligible relative vorticity and therefore possesses only planetary vorticity. The movement of the particle southward would decrease the planetary vorticity. Frictional forces must add this vorticity to the fluid element by diffusing vorticity through the boundary over the time t_d so that the fluid element can rejoin the region of weak interior flow where fluid elements have negligible relative vorticity.

1.5.7. Summary

The analytic solution for the adjustment to a steady state of an equatorial basin forced by zonal winds is well understood (eg. Cane and Sarachik, 1976, 77, 79). Similarly Munk (1950) has developed an analytic solution for the steady western boundary layer that develops in an ocean basin by the action of zonal wind forcing. In both these cases the forcing is via the momentum equations. No analytic solutions have been found for the adjustment problem when the forcing is via the continuity equation.

The investigations into channel flow have not looked at cross equatorial flow (eg. Gill, 1976) except for one case (Hughes, 1981) where wind forcing was the driving mechanism. Thus the problem of investigating the throughflow forced by a north-south pressure gradient through a narrow channel crossing the equator cannot be solved analytically and a numerical approach is required.

1.6 APPROACH AND AIMS

1.6.1 Approach

The reviews presented in section 1.2 and 1.3 suggest that the driving force for the throughflow from the Pacific to the Indian Ocean is the north-south difference in sea level across South East Asian Waters (Wyrtki, 1987). In the present study it is recognised that it is not necessary to use a global model to study the throughflow. The observed north-south pressure difference is a means of parameterizing the circulation of the world ocean that drives the throughflow. The pressure difference is due to the dynamic effects of monsoonal and global wind forcing. Thus a regional model can be developed to investigate the throughflow.

Primitive equation global models driven by observed wind fields are computationally costly. Simpler single level reduced gravity global models such as the NORDA model (Kindle et al, 1987) are also computationally costly if a fine resolution (~40km) is to be achieved. The propagation of coastal Kelvin waves throughout the region may be important (Godfrey and Golding, 1981) and needs to be included in any model. Hence a Quasi Geostrophic model is not appropriate. Two layer models are a possibility for use given the two layer nature of the observed flow in the deep channels (Wyrtki, 1961, Murray and Arief, 1988).

In this study the two layer shallow water equations (section 2.2) are used as the basis for investigating the throughflow. Linearization of the equations and the use of a rigid lid to filter out surface waves are approximations that can be made to develop simpler computationally faster models. In chapter 2 a series of models are developed from the two layer shallow water equations.

The initial problem studied is the flow forced through a narrow cross equatorial channel by a north-south pressure gradient. The results of the models developed in Chapter 2 are compared and presented in Chapter 3. The study then investigates the effects of sills, shelves and islands on the transport through the open channel as a preliminary to developing a realistic model of the Eastern Archipelago. In this study (Chapter 4) attention is limited to sills, shelves and islands of similar dimensions to those occurring in the Eastern Archipelago.

In Chapter 5 a realistic model is developed to investigate the forced flow through the Eastern Archipelago. The choice of model used for the realistic model is based upon the results of Chapter 3 and 4. It was decided to use the linear baroclinic model, the simplest of the models developed in Chapter 2. The use of this model is justified by the observed weak lower layer flows (Wyrtki, 1961 and Murray and Arief, 1988) and the fact that for experiments with seasonal forcing requiring lengthy integrations computational cost was a minimum.

Throughout this study the approach has been to start with a simple model, that is computationally fast and can thus be used for a series of integrations in order to understand the underlying ocean physics. The model can then be built upon to increase the complexity of the model physics.

1.6.2 Aims

(1) The development of shallow water models to investigate the flow in a north-south cross equatorial channel forced by a north-south difference in sea level.

(2) An investigation of the effects of islands, sills and shelves on the flow predicted by the initial models.

(3) The development of a realistic regional model from the initial models to investigate the throughflow from the Pacific to the Indian Ocean through South East Asian Waters.

2. THE MODEL

2.1 INTRODUCTION

In this chapter a series of models are developed that describe the circulation in a narrow north-south cross equatorial channel forced by a north-south pressure gradient. There are many different approaches to this type of problem (reviewed by McCreary, 1985). However the initial models are preliminary to the development of a regional model to investigate the throughflow form the Pacific to the Indian Ocean. In the process of developing the regional model the importance of islands, sills and shelves on the throughflow is investigated. Thus the initial models must be capable of including some or all of these features.

The lack of observational data, other modelling studies and an analytic solution to the problem all suggested that the development of a sophisticated, nonlinear, continuously stratified regional model was impractical. The required model is one that can represent the physics of the initial problem and that can be used in a variety of ways so that faith in the predictions of the model come from the models ability to repeat results across a wide parameter range.

The two layer shallow water equations were thus used as the basis of the model. The approximations that can be made to these equations are described in section 2.2 and lead to the development of the linear and nonlinear baroclinic equations. These predictive equations can then be expressed in a finite difference form (section 2.3) to form the basis of four numerical models. By applying appropriate forcing and boundary conditions (section 2.4) a time stepping procedure is implemented that updates the model variable fields to simulate the real ocean. Within a model the energy, momentum and vorticity balances are calculated providing useful information about the transient processes that occur as the model is forced towards a final steady state.

In the last section of this chapter the parameter space and limitations of the four initial models in simulating sills, shelves and islands are discussed.

2.2 THE PREDICTIVE EQUATIONS

2.2.1 Introduction

A set of time dependent partial differential equations describing the evolution of the velocity and height fields of a two layer ocean are given. Linearization and the rigid lid approximation lead to the formulation of three systems of predictive equations that form the basis of the models used in the series of experiments presented in chapters 3,4 and 5.

2.2.2 The two layer equations

The physical model is a rectangular channel of constant depth H_0. The vertical structure is modelled with a density contrast $\Delta\rho = \rho_2 - \rho_1$ between two homogeneous layers of initial thicknesses H_1 and H_2 $(H_1+H_2=H_0)$.

In the model the equatorial beta plane approximation (equation 1.5.4.1) is made, taking x and y as the eastward and northward co-ordinates respectively and t as the time. The forcing in the model is through the north-south gradient in sea level discussed later in section 2.4.2.

The hydrostatic approximation is made in which the pressure at any point in the channel is regarded as being due to the sum of the static head of the column of water above that point. The Boussinesq approximation is also made in which the density is regarded as constant when computing rates of change of momentum from accelerations and as a variable when giving rise to bouyancy forces (ie. when multiplied by g).

The model system is closed by a horizontal viscosity A_H, which is used to parameterize processes not included in the model (ie. turbulent transfer of energy to scales smaller than the grid size).

Bottom friction is incorporated into the model at a later stage (see section 4.4).

The reduced gravity g', is defined

$$g' = \frac{g(\rho_2 - \rho_1)}{\rho_2} \qquad (2.2.2.1)$$

Assuming that the motion in each layer is independent of the depth the equations of motion are:

$$\frac{\partial u_1}{\partial t} + u_1\frac{\partial u_1}{\partial x} + v_1\frac{\partial u_1}{\partial y} = -g\frac{\partial \eta}{\partial x} + A_H\nabla^2 u_1 + \beta y v_1 \qquad (2.2.2.2)$$

$$\frac{\partial v_1}{\partial t} + u_1\frac{\partial v_1}{\partial x} + v_1\frac{\partial v_1}{\partial y} = -g\frac{\partial \eta}{\partial y} + A_H\nabla^2 v_1 - \beta y u_1 \qquad (2.2.2.3)$$

$$\frac{\partial u_2}{\partial t} + u_2\frac{\partial u_2}{\partial x} + v_2\frac{\partial u_2}{\partial y} = -g\frac{\partial \eta}{\partial x} - g'\frac{\partial h}{\partial x} + A_H\nabla^2\ {}_2 + \beta y v_2 \qquad (2.2.2.4)$$

$$\frac{\partial v_2}{\partial t} + u_2\frac{\partial v_2}{\partial x} + v_2\frac{\partial v_2}{\partial y} = -g\frac{\partial \eta}{\partial y} - g'\frac{\partial h}{\partial y} + A_H\nabla^2 v_2 - \beta y v_2 \qquad (2.2.2.5)$$

$$\frac{\partial}{\partial t}(H_1 + \eta - h) = -(H_1 + \eta - h)\left(\frac{\partial u_1}{\partial x} + \frac{\partial v_1}{\partial y}\right) + \alpha_1(\eta_0 - \eta) \qquad (2.2.2.6)$$

$$\frac{\partial}{\partial t}(H_2 + h) = -(H_2 + h)\left(\frac{\partial u_2}{\partial x} + \frac{\partial v_2}{\partial y}\right) + \alpha_2(h_0 - h) \qquad (2.2.2.7)$$

Equations (2.2.2.2) - (2.2.2.5) are the momentum equations and (2.2.2.6) - (2.2.2.7) are the continuity equations for the two layers. The subscripts 1 and 2 refer to the upper and lower layers respectively. u_1, u_2 and v_1, v_2 are the eastward and northward horizontal velocity components in each layer. η and h are the perturbations from their initial levels of the free surface and the interface respectively.

This set of equations can be rewritten in a depth averaged or flux form with

$$U_1 = u_1(H_1+\eta-h) \;,\quad V_1 = v_1(H_1+\eta-h) \text{ and}$$

$$U_2 = u_2(H_2+h) \;,\quad V_2 = v_2(H_2+h)$$

thus the continuity equations (2.2.2.6) - (2.2.2.7) become

$$\frac{\partial\eta}{\partial t} = -\left(\frac{\partial U_1}{\partial x} + \frac{\partial V_1}{\partial y}\right) - \left(\frac{\partial U_2}{\partial x} + \frac{\partial V_2}{\partial y}\right) + \alpha_1(\eta_o-\eta) + \alpha_2(h_o-h) \qquad (2.2.2.8)$$

$$\frac{\partial h}{\partial t} = -\left(\frac{\partial U_2}{\partial x} + \frac{\partial V_2}{\partial y}\right) + \alpha_2(h_o-h) \qquad (2.2.2.9)$$

and the momentum equations are written

$$\frac{\partial U_1}{\partial t} + \frac{\partial}{\partial x}(u_1U_1) + \frac{\partial}{\partial y}(u_1V_1) = (H_1+\eta-h)\left[-g\frac{\partial\eta}{\partial x} + A_H\nabla^2 u_1\right]$$
$$+\beta yV_1 + u_1\alpha_1(\eta_o-\eta) - u_1\alpha_2(h_o-h) \qquad (2.2.2.10)$$

$$\frac{\partial V_1}{\partial t} + \frac{\partial}{\partial x}(v_1U_1) + \frac{\partial}{\partial y}(v_1V_1) = (H_1+\eta-h)\left[-g\frac{\partial\eta}{\partial x} + A_H\nabla^2 v_1\right]$$
$$-\beta yU_1 + v_1\alpha_1(\eta_o-\eta) - v_1\alpha_2(h_o-h) \qquad (2.2.2.11)$$

$$\frac{\partial U_2}{\partial t} + \frac{\partial}{\partial x}(u_2U_2) + \frac{\partial}{\partial y}(u_2V_2) = (H_2+h)\left[-g\frac{\partial\eta}{\partial x} - g'\frac{\partial h}{\partial x} + A_H\nabla^2 u_2\right]$$
$$+\beta yV_2 + u_2\alpha_2(h_o-h) \qquad (2.2.2.12)$$

$$\frac{\partial V_2}{\partial t} + \frac{\partial}{\partial x}(v_{2}U_{2}) + \frac{\partial}{\partial y}(v_2V_2) = (H_2+h)\left[-g\frac{\partial\eta}{\partial y} - g'\frac{\partial h}{\partial y} + A_H\nabla^2 v_2\right]$$
$$-\beta yU_2 + v_2\alpha_2(h_o-h) \qquad (2.2.2.13)$$

U_1, U_2 and V_1, V_2 are the eastward and northward components of the momentum in the upper layer and lower layer respectively.

2.2.3 Approximations to the two layer equations

The flux form of the two layer equations (2.2.2.8) - (2.2.2.13) may be represented in a finite difference form (developed in section 2.3, shown in Appendix A) and used as the basis of a numerical model. Computationally this model is relatively slow to integrate because it includes the nonlinear terms and the free surface. In this section the approximations that can be made to the two layer equations and thus form the basis of computationally faster models are discussed.

The two layer equations (2.2.2.2) - (2.2.2.7) can be linearized by considering motion of infinitesimal amplitude, thus terms of the form $\mathbf{u} \nabla \mathbf{u}$, $\eta \nabla \mathbf{u}$ and $h \nabla \mathbf{u}$ can be neglected. For any particular class of wave motions implied by equations (2.2.2.2) - (2.2.2.7) the validity of the linearization will depend upon the characteristic length, L, and velocity, U, scales with which that motion is associated.

The Rossby number R_o is a measure of the ratio of the nonlinear acceleration terms to the Coriolis term, thus

$$R_o = \frac{U}{fL} \ll 1 \quad \text{where } f = \beta y \tag{2.2.3.1}$$

The condition is only a local condition on the validity of linearization. Practically it is very difficult to obtain a global condition over a wide range of length and velocity scales. In table 2.2.1, Rossby numbers are given for the interior and the western boundary layer of the channel presented in chapters 3 and 4. The Rossby number decreases with increasing latitude.

Another nondimensional number that can be defined from the characteristic scales of motion is the Reynolds number

$$Re = \frac{UL}{A_H} \tag{2.2.3.2}$$

In most cases of geophysical interest Re>>1. The Reynolds number is the ratio of the inertial acceleration to the frictional term. In the ocean A_H is typically in the range $10\text{-}10^4 m^2 s^{-1}$ (Gill, 1982). As Re increases the effects of nonlinearity become increasingly evident in the boundary layer.

TABLE 2.2.1 ROSSBY AND REYNOLDS NUMBERS OF CHANNEL USED IN CHAPTERS 3 AND 4 (560km WIDE).

	U (ms^{-1})	L (km)	A_H (m^2s^{-1})	Ro (at 4°S)	Re
interior	0.02	100	$10\text{-}10^4$	0.02	0.2-200
w. boundary	1.7	30	10	5.7	5100
layer	1.2	37	10^2	3.2	444
(table 3.3.3)	0.6	90	10^3	0.7	54
	0.3	180	10^4	0.2	5

It can be seen that linearization of the equations is only inappropriate with small viscosities when it can be expected that nonlinear effects at the boundary layer might become important.

The second simplification that can be made to the two layer equations is to filter out the long surface waves to obtain the baroclinic (or internal mode). Long internal waves are the same as long surface gravity waves would be if the acceleration due to gravity were the reduced gravity g' (given by equation 2.2.2.1) instead of g. Because g'<<g the speed of the internal waves is very much slower than that of the surface waves. The numerical integration process is speeded up by an order of magnitude or more when the surface waves are not included.

The approximation used to filter out surface waves is called the rigid lid approximation. The pressure gradients in the upper layer which would have been caused by displacements in the free surface now exist due to pressure acting against the lid.

The linear two layer equations are given in section 2.2.4 and the non linear and linear baroclinic equations are developed in sections 2.2.5 and 2.2.6 respectively.

2.2.4 The linear two layer equations

By neglecting the nonlinear terms in the momentum and continuity equations the linear equations can be derived from (2.2.2.2) - (2.2.2.7).

$$\frac{\partial u_1}{\partial t} = - g\frac{\partial \eta}{\partial x} + A_H \nabla^2 u_1 + \beta y v_1 \qquad (2.2.4.1)$$

$$\frac{\partial v_1}{\partial t} = - g\frac{\partial \eta}{\partial y} + A_H \nabla^2 v_1 - \beta y u_1 \qquad (2.2.4.2)$$

$$\frac{\partial u_2}{\partial t} = - g\frac{\partial \eta}{\partial x} - g'\frac{\partial h}{\partial x} + A_H \nabla^2 u_2 + \beta y v_2 \qquad (2.2.4.3)$$

$$\frac{\partial v_2}{\partial t} = - g\frac{\partial \eta}{\partial y} - g'\frac{\partial h}{\partial y} + A_H \nabla^2 v_2 - \beta y U_2 \qquad (2.2.4.4)$$

$$\frac{\partial \eta}{\partial t} = -H_1\left(\frac{\partial u}{\partial x} + \frac{\partial v_1}{\partial y}\right) -H_2\left(\frac{\partial u_2}{\partial x} + \frac{\partial v_2}{\partial y}\right) + \alpha_1(\eta_o - \eta) + \alpha_2(h_o - h) \qquad (2.2.4.5)$$

$$\frac{\partial h}{\partial t} = -H_2\left(\frac{\partial u_2}{\partial x} + \frac{\partial v_2}{\partial y}\right) + \alpha_2(h_o - h) \qquad (2.2.4.6)$$

where the notation is the same as in section 2.2.2.

2.2.5 The non-linear baroclinic equations

When the rigid lid approximation is made (2.2.2.6) becomes;

$$\frac{\partial}{\partial t}(H_1-h) = -(H_1-h)\left(\frac{\partial u_1}{\partial x} + \frac{\partial v_1}{\partial y}\right) \qquad (2.2.5.1)$$

The remaining equations (2.2.2.2)-(2.2.2.5) and (2.2.2.7) are unaltered. Since the continuity equations now do not involve η a combination of the momentum equations that does not involve η is made.

$$\frac{\partial u}{\partial t} + \frac{(H_2-H_1)}{H_1+H_2}\left[\frac{u\partial u}{\partial x} + \frac{v\partial u}{\partial y}\right] \quad \frac{g'\partial h}{\partial x} + A_H\nabla^2 u + \beta yv \qquad (2.2.5.2)$$

$$\frac{\partial v}{\partial t} + \frac{(H_2-H_1)}{H_1+H_2}\left[\frac{u\partial v}{\partial x} + \frac{v\partial v}{\partial y}\right] = \frac{g'\partial h}{\partial y} + A_H\nabla^2 v - \beta yu \qquad (2.2.5.3)$$

where $u = u_1-u_2$, $v = v_1-v_2$ and $u_1(H_1-h)=-u_2(H_2+h)$,
$v_1(H_1-h)=-v_2(H_2+h)$.

The two continuity equations can be combined.

$$\frac{\partial h}{\partial t} = \frac{(H_1-h)(H_2+h)}{H_1+H_2}\left(\frac{\partial u}{\partial x} + \frac{\partial v}{\partial y}\right) - \alpha_2(h_o-h) \qquad (2.2.5.4)$$

which can be written in flux form

$$\frac{\partial h}{\partial t} = \frac{\partial U}{\partial x} + \frac{\partial V}{\partial y} - \alpha_2(h_o-h) \qquad (2.2.5.5)$$

where $U = \dfrac{(H_1-h)(H_2+h)}{H_1+H_2}\,u$ and $V = \dfrac{(H_1-h)(H_2+h)}{H_1+H_2}\,v$

similarly the depth averaged momentum equations can be derived,

$$\frac{\partial U}{\partial t} = \frac{(H_2+h)(H_1-h)}{H_1+H_2}\left[\frac{g'\partial h}{\partial x} + A_H\nabla^2 u\right] + \frac{H_1-H_2}{H_1+H_2}\left[\frac{\partial}{\partial x}(uU)+\frac{\partial}{\partial y}(uV)\right]$$

$$+ \beta yV - \frac{2hu}{H_1+\;2}\left[\frac{-\partial U}{\partial x} + \frac{\partial V}{\partial y}\right] - \frac{u(H_1-2h-H_2)\alpha_2(h_o-h)}{H_1+H_2} \qquad (2.2.5.6)$$

$$\frac{\partial V}{\partial t} = \frac{(H_2+h)(H_1-h)}{H_1+H_2}\left[\frac{g'\partial h}{\partial y} + A_H\nabla^2 v\right] + \frac{H_1-H_2}{H_1+H_2}\left[\frac{\partial}{\partial x}(vU)+\frac{\partial}{\partial y}(vV)\right]$$

$$- \beta yV - \frac{2hv}{H_1+H_2}\left[\frac{-\partial U}{\partial x} + \frac{\partial V}{\partial y}\right] - \frac{v(H_1-2h-H_2)\alpha_2(h_o-h)}{H_1+H_2} \qquad (2.2.5.7)$$

2.2.6 The linear baroclinic equations

In the same manner that equations (2.2.4.1) - (2.2.4.6) were derived from the two layer equations (2.2.2.2) - (2.2.2.7) a set of linear equations may be derived from (2.2.5.2) - (2.2.5.4). These equations form the linear baroclinic equations.

$$\frac{\partial u}{\partial t} = \frac{g'\partial h}{\partial x} + A_H\nabla^2 u + \beta yv \qquad (2.2.6.1)$$

$$\frac{\partial v}{\partial t} = \frac{g'\partial h}{\partial y} + A_H\nabla^2 v - \beta yu \qquad (2.2.6.2)$$

$$\frac{\partial h}{\partial t} = \frac{H_1H_2}{H_1+H_2}\left(\frac{\partial u}{\partial x} + \frac{\partial v}{\partial y}\right) - \alpha_2(h_o-h) \qquad (2.2.6.3)$$

2.3 THE NUMERICAL METHOD

2.3.1 Introduction

The predictive equations of section 2.2 are solved by integrating forward in time the finite difference equations which approximate them. Details of the difference forms for the different approximations to the predictive equations of section 2.2 are given in Appendix A. In this section the spatial and temporal differencing schemes used in the models and the associated stability criteria are considered. There are numerous arrangements of the variables u,v and h on a finite difference grid. In this study the Arakawa C-grid is used because it is considered the best lattice for simulating the geostrophic adjustment process (Messinger and Arakawa, 1976). (See figure A.1. for arrangement of variables on the C-grid).

2.3.2 Temporal difference schemes

Equations (2.3.2.1)-(2.3.2.3) are the time differencing schemes used in this study,

$$\frac{\phi^{(n+1)} - \phi^{(n-1)}}{2\Delta t} = f^{(n)}(x,y,t) \quad \text{centred scheme} \qquad (2.3.2.1)$$

$$\frac{\phi^{(n+1)} - \phi^{(n-1)}}{2\Delta t} = f^{(n-1)}(x,y,t) \quad \text{forward scheme} \qquad (2.3.2.2)$$

$$\frac{\phi^{(n+1)} - \phi^{(n)}}{\Delta t} = f^{(n)}(x,y,t) \quad \text{forward scheme} \qquad (2.3.2.3)$$

The variable ϕ represents any of the components of velocity or perturbation of the surface or interface. The function f(x,y,t) takes the form of the advection, diffusion or coriolis term in the predictive equation. The time t is given by

$$t = (n-1)\Delta t \qquad (2.3.2.4)$$

where Δt is the timestep duration.

The three level schemes (2.3.2.1) and (2.3.2.2) are widely used in geophysical modelling as they are both second order accurate and stable provided that the function f(x,y,t) is correctly initialised (Messinger and Arakawa, 1976). To initiate a three level scheme the initial value of the function at n=0 is required as well as the value of the function at n=1. The value of the function at n=1 cannot be calculated using a three level scheme and therefore is calculated from the two level forward scheme (2.3.2.3).

In this study (2.3.2.2) is used to approximate the diffusion term of the predictive equations and (2.3.2.1) is used for the remaining terms. The use of (2.3.2.2) is widely adopted in this manner in order to avoid linear numerical instability (Bryan, 1969). The three level schemes give rise to a computational mode, the usual method for suppression of this instability is the occasional insertion of a step made by a two level scheme which eliminates the computational mode (Messinger and Arakawa, 1976). The forward scheme (2.3.2.3) is used at regular intervals in all the models to overcome this instability.

2.3.3 Spatial difference schemes

The spatial arrangement of variables on the Arakawa c-grid is shown in figure A.1. It is convenient if the boundaries of the region to be modelled are chosen so that the north-south boundaries coincide with a line of u points and east-west boundaries coincide with a line of v points. This permits a simple way of specifying the kinematic boundary condition of having no normal flow across lateral boundaries. An additional array of points is introduced outside each boundary to allow the same computing algorithm to be used for points adjacent to the boundary as for points of the interior. These additional points allow the specification of the dynamic boundary condition (section 2.4.2).

The spatial differencing scheme used is similar to that of Lilly (1965) for single layer problems. It is a scheme which conserves total energy of the system in the absence of truncation errors.

Following Lilly (1965) four operators $\delta_x(\ )$, $\delta_y(\ )$, $(\bar{\ })^x$ and $(\bar{\ })^y$ are defined such that

$$\delta_x\phi(x,y) = \frac{1}{\Delta x}(\phi_{i+1,j} - \phi_{i,j}) \qquad (2.3.3.1)$$

$$\delta_y\phi(x,y) = \frac{1}{\Delta y}(\phi_{i,j+1} - \phi_{i,j}) \qquad (2.3.3.2)$$

$$\overline{\phi}^x(x,y) = \frac{1}{2}(\phi_{i+1,j} + \phi_{i,j}) \qquad (2.3.3.3)$$

$$\overline{\phi}^y(x,y) = \frac{1}{2}(\phi_{i,j+1} + \phi_{i,j}) \qquad (2.3.3.4)$$

where $\phi(x,y)$ is a function of the discrete variables x and y. The subscripts i and j refer to the x and y co-ordinates respectively of the location of the variable ϕ on the grid. The finite difference Laplacian is defined as

$$\nabla^2(\ ) = \delta_x{}^2(\ ) + \delta_y{}^2(\ ) \qquad (2.3.3.5)$$

The finite difference forms of the four systems of predictive equations are given in Appendix A. The u-momentum equations are written with reference to a u-point. The v-momentum equations are written with reference to a v-point and the continuity equations with reference to an h point (see figure A.1).

2.3.4 Stability Criteria

The stability criteria for the advection, diffusion and coriolis terms when the temporal and spatial differencing schemes of sections 2.3.2 and 2.3.3 apply are now presented.

For a linear advection equation

$$\frac{\partial\phi}{\partial t} = -u\frac{\partial\phi}{\partial x} - v\frac{\partial\phi}{\partial y} \qquad (2.3.4.1)$$

using spatial derivatives given by (2.3.3.3) and (2.3.3.4) and a temporal derivative given by (2.3.2.1) the finite difference approximation requires

$$\Delta t < \frac{1}{\frac{u}{\Delta x} + \frac{v}{\Delta y}} \qquad (2.3.4.2)$$

for stable integration.

For the diffusion equations

$$\frac{\partial \phi}{\partial t} = A_H \nabla^2 \phi \qquad (2.3.4.3)$$

using spatial derivatives given by (2.3.3.5) and a temporal derivative given by (2.3.2.2) the finite difference approximation requires

$$\Delta t < \frac{1}{\frac{4A_H}{\Delta x^2} + \frac{4A_H}{\Delta y^2}} \qquad (2.3.4.4)$$

The explicit treatment of the coriolis term requires,

$$\Delta t < \frac{1}{\beta y} \qquad (2.3.4.5)$$

Stability criteria that arise because of the channel dynamics are due to the need to resolve any boundary layer that might exist. Thus to resolve a coastal Kelvin wave,

$$\Delta x < \frac{c}{|f|} \quad \text{or} \quad \Delta x < \frac{c}{|\beta y|} \qquad (2.3.4.6)$$

In the case of a Munk type western boundary layer (section 1.5.6) the constraint on the grid spacing becomes,

$$\Delta x < \frac{2\pi}{\sqrt{3}} \left(\frac{A_H}{\beta} \right)^{1/3} \qquad (2.3.4.7)$$

The timescale of the forcing described in section 2.4.3 is also constrained

$$\alpha < \frac{1}{2\Delta t} \qquad (2.3.4.8)$$

2.4. BOUNDARY CONDITIONS AND FORCING

2.4.1 Solid wall boundaries

Lateral boundary conditions can be either free slip or no slip conditions.

For free slip boundaries

$$u_i = 0, \quad \frac{\partial v_i}{\partial x} = 0 \quad \text{on meridional boundaries} \qquad (2.4.2.1)$$

and $$\frac{\partial u_i}{\partial y} = 0, \quad v_j = 0 \quad \text{on zonal boundaries} \qquad (2.4.2.2)$$

For no slip boundaries

$$u = 0, \ v = 0 \text{ on all boundaries} \qquad (2.4.2.3)$$

In section 2.3.3 the arrangement of variables on the Arakawa C-grid (figure A.1) was discussed and it was noted that an additional array of grid points was introduced outside each boundary, these points provide a way for specifying the conditions (2.4.2.1) - (2.4.2.3). For a free slip boundary condition, the tangential velocity outside the boundary is set equal to that of its adjacent counterpart inside the boundary. For a no slip boundary condition the tangential velocity outside the boundary is set equal to but opposite in sign to that of its adjacent counterpart inside the boundary.

2.4.2 Forcing in the Model

The region being modelled can be thought of as connecting two infinite ocean basins whose only important characteristics are their respective sea levels. The basin to the north of the region (Pacific Ocean) has a sea level elevation η_p. The basin to the south of the region (Indian Ocean) has a sea level elevation η_I. Geographically the sea level difference $\eta_p - \eta_I$ occurs between 3°N and 10°S and has a mean value of 16cm (Wyrtki, 1987).

A simple relaxation condition in the region of the model extending from 3°N-5°N is used to relax the sea level elevation to η_p.

$$\frac{\partial \eta}{\partial t} = \alpha_1 \, (\eta_p - \eta) \qquad (2.4.3.1)$$

Similarly in the region 12°S - 14°S the condition,

$$\frac{\partial \eta}{\partial t} = \alpha_1 \, (\eta_I - \eta) \qquad (2.4.3.2)$$

is applied.

In a two layer ocean there is a balance between the sea surface perturbation and the interface perturbation. Hence the relaxation conditions,

$$\frac{\partial h}{\partial t} = \alpha_2 (h_p - h) \quad \text{and} \quad \frac{\partial h}{\partial t} = \alpha_2 (h_I - h) \qquad (2.4.3.3)$$

apply to the north and south respectively. The timescales α_1 and α_2 can be thought of as the barotropic and baroclinic rates of relaxation respectively. Typical values used in the models are $\alpha_1 = (6 \text{ minutes})^{-1}$ and $\alpha_2 = (18 \text{ hours})^{-1}$, thus $\alpha_2 << \alpha_1$.

Forcing in the baroclinic models is via the interface alone, the hydrostatic balance given by

$$\rho_2 g' h = -\rho_1 g \eta \qquad (2.4.3.4)$$

implies that a 10cm surface elevation is balanced by a 28m depression of the interface (when $\rho_2 = 1060$ and $\rho_1 = 1025$ Kgm^{-3}).

Forcing in the model is investigated in section 3.3.2.

2.4.3 Open boundary conditions

Numerical models of finite regions inevitably involve the treatment of open boundaries where the numerical grid ends but where the fluid motion should continue to be unrestricted. An ideal open boundary is one which is transparent to motions (waves, mean flows, eddies etc.) generated within the computational region.

Unfortunately there is no numerical treatment of open boundaries which achieves this ideal for general models that include two (or three) dimensions, rotation, variable depth, bottom friction and forcing terms. It has been suggested (Bennet and McIntosh, 1982) that approximate, ad hoc, open boundary conditions may be the most reasonable approach to the problem.

Forcing flow through a region representing the South East Asian Waters essentially prescribes inflow and outflow conditions. This means that when the sea level elevation in the Pacific is greater than that in the Indian Ocean an outflow condition is required at the southern boundary, whilst in the north an inflow condition is needed.

The relaxation conditions of section 2.4.3 are a form of open boundary condition known as a 'sponge' boundary condition. This form of open boundary condition creates a discontinuity at the boundary of the forcing region that may produce some reflection (Chapman, 1985). Waves travelling tangential to the boundary may be distorted by spatial variation of the damping. Another disadvantage of this type of condition is that a significant number of grid points close to the boundary are wasted, as flow associated with this region is not of interest but has to be computed nevertheless. One positive aspect of a simple relaxation boundary condition is that it is certain to maintain the required north-south pressure gradient if similar conditions are prescribed to the north and south.

The shallow water equations (section 2.2) are hyperbolic in nature and therefore the most accurate way to prescribe the outflow at an open boundary is to use the Sommerfeld radiation condition (Sommerfeld, 1949),

$$\frac{\partial \phi}{\partial t} + c\frac{\partial \phi}{\partial y} = 0 \qquad (2.4.4.1)$$

where ϕ is any variable and c the phase speed, y is in the cross boundary direction. There are many methods for implementing

(2.4.4.1) reviewed by Chapman (1985). Discussion will be limited to the most sophisticated of these implementations, due to Orlanski (1976).

Instead of fixing a constant value for the phase velocity in (2.4.4.1) an estimate of ci,j is made from values of the variables at previous times close to the boundary. Writing (2.4.4.1) in the finite difference form of sections 2.3.2 and 2.3.3.

$$\frac{\phi^{n}_{i,j+1}-\phi^{n-2}_{i,j+1}}{2\Delta t} + C\phi\left[\frac{\phi^{n}_{i,j+1}-\phi^{n-2}_{i,j+1}-2\phi^{n-1}_{i,j+2}}{2}\right]\frac{1}{\Delta y} = 0 \qquad (2.4.4.2)$$

where i,j denotes a point on the boundary and subscripts j+1, j+2 refer to the first and second interior points in the y-direction.

Manipulation yields.

$$C_{\phi} = \frac{-(\phi^{n}_{i,j+1} - \phi^{n-2}_{i,j+1})}{(\phi^{n}_{i,j+1}-\phi^{n-2}_{i,j+1} - 2\phi^{n-1}_{i,j+2})} \qquad \frac{\Delta y}{\Delta t} \qquad (2.4.4.3)$$

To determine the variable at the boundary point at the next timestep substitution of (2.4.4.3) into (2.4.4.1) gives,

$$\phi^{n+1}_{1,j} = \frac{[1-(\Delta t/\Delta y)C\phi]}{[1+(\Delta t/\Delta y)C_{\phi}]}\,\phi^{n-1}_{i,j} + \frac{2(\Delta t/\Delta y)}{[1+(\Delta t/\Delta y)C_{\phi}]}\,C\phi\,\phi^{n}_{i,j+1} \qquad (2.4.4.4)$$

in this expression it is required that

$$0 < C_{\phi} < \Delta y/\Delta t \qquad (2.4.4.5)$$

Thus the limiting outflow condition where $C_{\phi} = \Delta y/\Delta t$ in (2.4.4.4.) gives

$$\phi^{n+1}_{i,j} = \phi^{n}_{i,j+1} \qquad (2.4.4.6)$$

which is the condition for the phase speed in (2.4.4.1) to be equal to the numerical maximum of the grid spacing divided by the timestep. In the limit $C_\phi = 0$ then

$$\phi^{n+1}_{i,j} = \phi^{n-1}_{i,j} \tag{2.4.4.7}$$

Here no information has come from the interior so this is regarded as an inflow condition, the variable is prescribed at the boundary by a value at a previous timestep or by some external value. It would be possible to set up the forcing by means of this inflow condition.

Since each variable u_1, u_2, v_1, v_2, η and h are determined by different predictive equations the numerical propagation velocities C_ϕ can be different for each variable and thus must be calculated separately.

Open boundary conditions in the model are investigated in section 3.3.3.

2.5 ENERGY, MOMENTUM AND VORTICITY BALANCES IN THE MODELS

2.5.1 Introduction

The energy, momentum and vorticity balances within a model provide a useful insight into the fundamental mechanisms of the model circulation. These balances may be globally averaged over the entire model region or at individual locations on the model grid, both approaches being useful. A comparison of the energy, momentum and vorticity balances of the linear two layer and baroclinic models is made in sections 3.4.3 - 3.4.5. Elsewhere throughout the results chapters the energetics are constantly referred to.

The momentum balance can be studied by calculating the value of the different terms in the momentum equations at each point on the grid. Similarly the energy and vorticity balances are found by computing the values of the different terms in the energy and vorticity equations at each point on the grid. The four different sets of predictive equations given in section 2.2. give rise to four different sets of energy equations (Appendix B) and vorticity equations (Appendix C).

The predictive equations and their finite difference counterparts, given in Appendix A, conserve mass and total energy when viscosity and forcing are set to zero.

2.5.2 **Energetics of the models**

In this section equations for the rates of change of potential and kinetic energy as a function of time and the work done on each layer by the various forces acting are discussed. Let the available potential energy and the kinetic energy for each layer be PE_i and KE_i. For the two layer model the energy equations can be written as

$$\langle \partial/\partial t(PE_1)\rangle = \langle P_1+N_1+S_1\rangle \tag{2.5.2.1}$$

$$\langle \partial/\partial t(PE_2)\rangle = \langle P_2+N_2+S_2\rangle \tag{2.5.2.2}$$

$$\langle \partial/\partial t(KE_1)\rangle = \langle P_3+F_1+O_1\rangle \tag{2.5.2.3}$$

$$\langle \partial/\partial t(KE_2)\rangle = \langle -(P_1+P_2+P_3) + F_2 + O_2\rangle \tag{2.5.2.4}$$

where the angled brackets denote a horizontal average. The terms P_i redistribute the energy between the kinetic and potential energy of the two layers. The terms N_i and S_i are associated with the forcing conditions at the north and south. F_i is due to the effects of lateral viscosity and O_i is due to nonlinear effects in the forcing regions.

Similar equations can be produced for the linear two layer model (the terms O_i are now absent) and the baroclinic models. These equations and the terms P_i, N_i, S_i, F_i and O_i are given in Appendix B for the four models.

There are two other ways in which the rates of change of energy can be calculated from the model. Numerically from the evaluation of the derivatives thus

$$\langle \frac{\partial}{\partial t}(PE_1)\rangle = \langle \tfrac{1}{2}\rho g\eta \frac{\partial\eta}{\partial t} \rangle \tag{2.5.2.5}$$

$$\langle \frac{\partial}{\partial t}(PE_2) \rangle = \langle \tfrac{1}{2}\rho g' h \frac{\partial h}{\partial t} \rangle \qquad (2.5.2.6)$$

$$\langle \frac{\partial}{\partial t}(KE_1) \rangle = \langle \tfrac{1}{2}\rho(u_1\frac{\partial u_1}{\partial t} + v_1\frac{\partial v_1}{\partial t} \rangle \qquad (2.5.2.7)$$

$$\langle \frac{\partial}{\partial t}(KE_2) \rangle = \langle \tfrac{1}{2}\rho(u_2\frac{\partial u_2}{\partial t} + v_2\frac{\partial v_2}{\partial t} \rangle \qquad (2.5.2.8)$$

The values of the variables calculated by the model can be substituted into the expressions for kinetic and potential energy and averaged in time giving (in the two layer case)

$$\langle \partial/\partial t(PE_1) \rangle = ((\langle \tfrac{1}{2}\rho g\eta^2 \rangle^{n+1} - \langle \tfrac{1}{2}\rho g\eta^2 \rangle^{n-1}) \frac{1}{2\Delta t} \qquad (2.5.2.9)$$

$$\langle \partial/\partial t(PE_2) \rangle = ((\langle \tfrac{1}{2}\rho g' h^2 \rangle^{n+1} - \langle \tfrac{1}{2}\rho g' h^2 \rangle^{n-1}) \frac{1}{2\Delta t} \qquad (2.5.2.10)$$

$$\langle \partial/\partial t(KE_1) \rangle = ((\langle \tfrac{1}{2}\rho_1 H_1(u_1{}^2+v_1{}^2) \rangle^{n+1} - \langle \tfrac{1}{2}\rho_1 H_1(u_1{}^2+v_1{}^2) \rangle^{n-1}) \frac{1}{2\Delta t} \qquad (2.5.2.11)$$

$$\langle \partial/\partial t(KE_2) \rangle = ((\langle \tfrac{1}{2}\rho_2 H_2(u_2{}^2+v_2{}^2) \rangle^{n+1} - \langle \tfrac{1}{2}\rho_2 H_2(u_2{}^2+v_2{}^2) \rangle^{n-1}) \frac{1}{2\Delta t} \qquad (2.5.2.12)$$

The three methods for determining the rates of change of energy should all give the same result.

2.5.3 Vorticity balances in the models

The equations for vorticity balances for the flow are now discussed.

The vorticity equation for the upper layer of the two layer equations (2.2.2.8) - (2.2.2.13) is

$$\frac{\partial\zeta_1}{\partial t} = \underbrace{-\frac{\partial^2(v_1U_1)}{\partial x^2}-\frac{\partial^2(v_1V_1-u_1U_1)}{\partial x\partial y}+\frac{\partial^2(u_1V_1)}{\partial y^2}}_{}\underbrace{-\beta V_1}_{}\underbrace{-\beta y\left(\frac{\partial U_1}{\partial x}+\frac{\partial V_1}{\partial y}\right)}_{}$$
$$\underbrace{+(H_1+\eta-h)A_H\nabla^2\left(\frac{\partial v_1}{\partial x}-\frac{\partial u_1}{\partial y}\right)+A_H\nabla^2v_1\left(\frac{\partial\eta}{\partial x}-\frac{\partial h}{\partial x}\right)-A_H\nabla^2u_1\left(\frac{\partial\eta}{\partial y}-\frac{\partial h}{\partial y}\right)}_{} \qquad (2.5.3.1)$$

For the lower layer ζ is given by

$$\frac{\partial\zeta_2}{\partial t} = \underbrace{-\frac{\partial^2(v_2U_2)}{\partial x^2}-\frac{\partial^2(v_2V_2-u_2U_2)}{\partial x\partial y}+\frac{\partial^2(u_2V_2)}{\partial y^2}}_{}\underbrace{-\beta V_2}_{}\underbrace{-\beta y\left(\frac{\partial U_2}{\partial x}+\frac{\partial V_2}{\partial y}\right)}_{}$$
$$\underbrace{+(H_2+h)A_H\nabla^2\left(\frac{\partial v_2}{\partial x}-\frac{\partial u_2}{\partial y}\right)+A_H\nabla^2v_2\frac{\partial h}{\partial x}-A_H\nabla^2u_2\frac{\partial h}{\partial y}}_{} \qquad (2.5.3.2)$$

The first term on the right hand sides of (2.5.3.1) and (2.5.3.2) comes from the advection terms of the momentum equations and is zero in the linear models and will be referred to as the advection of the vorticity by the flow. The second term is the planetary vorticity tendency, the third term is the relative vorticity due to stretching or compressing a fluid column within the layer. The last term represents the dissipation of the vorticity due to the viscosity.

Thus the vorticity equation for each layer in any of the four models can be written

$$\frac{\partial\zeta_i}{\partial t} = \text{ADVECTION} + \text{BETA} + \text{DIVERGENCE} + \text{VISCOSITY} \qquad (2.5.3.3)$$

where $\zeta_i = \left(\frac{\partial v_i}{\partial x} - \frac{\partial u_i}{\partial y}\right)$

At the steady state $\partial\zeta/\partial t = 0$ and a balance exists between the terms on the right hand side of (2.5.3.3). In Appendix C the four terms on the right hand side of (2.5.3.3) are given for the four models.

2.6 MODEL EXPERIMENTS

2.6.1 Introduction

The four numerical models developed from the two layer shallow water equations of section 2.2 are computationally and mathematically very similar in their structure. It is also comparatively easy to make changes to the models to test phenomena as and when required. Accordingly there are essentially four models to choose from to carry out numerical experiments. These will range from sensitivity studies and investigations into the forcing terms and representations of open boundaries to including the effects of islands, sills and shelves on the throughflow in a cross equatorial channel.

In this section the parameter space that the models can operate in is discussed and the types of numerical experiment that can be carried out with each of the models is examined.

2.6.2 Channel parameters

The channel is 2160km in the north-south direction corresponding to the region 5°N - 14°S across which the pressure gradient from the Pacific Ocean to the Indian Ocean occurs. The channel is 560km wide, in order that rotational effects are of importance, away from the equatorial region (±2°).

An upper layer thickness of $H_1 = 200$m is chosen following Wyrtki (1987) who states that most of the north-south pressure gradient is contained within the upper 200m of the region. The total water depth $H_0 = H_1+H_2$ is taken to be 1500m, the depth of the deepest direct pathway between the Pacific and Indian Oceans. The total depth H_0 determines the barotropic phase speed, C_0 within the channel

$$C_0 = (gH_0)^{\frac{1}{2}} = 121.3\text{ms}^{-1} \qquad (2.6.2.1)$$

The vertical structure of the channel is represented by a density contrast $\Delta\rho = \rho_2 - \rho_1$ between the two layers. The density contrast is chosen to give a baroclinic phase speed, c_1, equal to the speed of the first baroclinic mode calculated from observed data (Postma, 1958).

Thus for a baroclinic phase speed of 2.4ms^{-1} the reduced gravity required is

$$g' = \frac{c_1{}^2 H_0}{H_1 H_2} = 0.0332\text{ms}^{-2} \qquad (2.6.2.2)$$

The equatorial beta plane approximation (1.5.4.1) is made with $\beta = 2.3 \times 10^{-11}\text{m}^{-1}\text{s}^{-1}$.

2.6.3 Model parameters

A regular grid spacing of $\Delta x = \Delta y = 20\text{km}$ is used in all the models. Thus the grid is 2200km in north-south extent with the equator 600km from the northern boundary and 600km in the east-west direction (110x30 points). The grid spacing is much less than the baroclinic radii of deformation given in table 1.5.1 and the stability criteria (2.3.4.6) is obeyed.

The timestep Δt used in the models must satisfy (2.3.4.2), (2.3.4.4) and (2.3.4.5). The strongest constraint on the timestep length comes from (2.3.4.2) which reduces to the CFL condition.

$$\Delta t < \frac{\Delta x}{c} \qquad (2.6.3.1)$$

where c is the appropriate barotropic or baroclinic phase speed. For the two layer models a timestep less than 165 seconds is required and for the baroclinic models a timestep less than 8,300 seconds is required. Since the stability criteria are developed from linear theory these values are used only as a reference for determining the timestep length. In practice a timestep of $\Delta t = 50$s was used for the two layer models and $\Delta t = 1800$s for the baroclinic models. There are severe implications on computational time due to timestep length and these are discussed in the following sections.

Using the values for Δx, Δy and Δt the lower limit for the horizontal viscosity in the models can be determined from (2.3.4.7). An upper limit on the horizontal viscosity can be determined by rearrangement of (2.3.4.4) but since this limit is greater than the physically realistic range $10 - 10^4 m^2 s^{-1}$ given by Gill (1982) it is not of importance. The lower limit for the horizontal viscosity with the 20km grid is

$$A_H > \left(\frac{\sqrt{3}}{2\pi} \Delta x \right)^3 \qquad = 4 m^2 s^{-1} \qquad (2.6.3.2)$$

In practice it was found that in the baroclinic models horizontal viscosities of $10 m^2 s^{-1}$ could be used but in the two layer models the horizontal viscosity used had to be greater for stable integration (discussed in sections 2.6.6 - 2.6.7). The values for $\Delta x, \Delta y, \Delta t$ and A_H used in the models for the experiments of chapters 3,4, and 5 are given in table 2.6.1.

TABLE 2.6.1. **Range of Model parameters used in this study**

Model		Δt (s)	$\Delta x = \Delta y$ (km)	A_H ($m^2 s^{-1}$)
Two layer	non linear	50	20	$>10^4$
	linear	50	20	>500
Baroclinic	non linear	1800	20	>10
	linear	1800	20	>10

2.6.4 **The linear baroclinic model**

The linear baroclinic model is computationally and mathematically the simplest of the four models. In cases where the linear baroclinic model is suitable for use the model is the first choice and provides an initial understanding and basis for comparison with the more complex models. There are two main problems with the baroclinic models, i) determining the transport in the model and ii) including sills and shelves in the model.

As noted in section 2.2.5 the meridional transport in the two layers of the nonlinear baroclinic model are equal and opposite

$$v_1(H_1-h) = -v_2(H_2+h) \qquad (2.6.3.1)$$

Similarly in the linear baroclinic model

$$v_1H_1 = -v_2H_2 \qquad (2.6.3.2)$$

Thus there is no net transport through the channel. However in the case where $H_2 >> H_1$ the lower layer velocity can be neglected and an estimate of the transport in the upper layer can be obtained. With the two layer models the exact transport in the upper and lower layers can be determined.

In the baroclinic models topographic features that extend into the upper layer cannot be included. Thus the baroclinic models cannot be used to investigate the effects of shallow shelf seas adjacent to the deep channel. The barotropic mode is required when large scale topographic features are included in the models. The free surface is required to allow interaction between the baroclinic and barotropic modes. Thus the baroclinic models are not suitable for investigating the effects of sills in the channel.

The lateral boundary conditions (section 2.4.1) may be applied in all the models to produce an irregular coastline or an island. The smallest feature that can be resolved with the treatment of boundary conditions as described in section 2.4.2 is a square island

$2\Delta x$ by $2\Delta y$. This resolution is due to the need to include separate interior u and v points for all the adjacent exterior points. Accordingly an irregular coastline resolution of two grid point inlets and promontories can be achieved.

The linear baroclinic model is approximately 70 times faster to integrate than the linear two layer model thus for sensitivity studies and preliminary work this model is the most useful.

2.6.5 The non-linear baroclinic model

In the nonlinear baroclinic model non-linear terms are included in the momentum and continuity equations and the model is written in flux form. The non-linear model is more realistic than the linear model, advection of vorticity by the mean flow can become important. The range of horizontal viscosities that can be used ($10-10^4 m^2 s^{-1}$) suggests that eddies may be formed in the non-linear model. Holland and Lin (1975a,b) produced eddies with horizontal viscosities $< 330 m^2 s^{-1}$ when viscous dissipation of vorticity did not dominate.

The non-linear baroclinic model is more complex than its linear counterpart but this presents no significant computational problems. However, interpretation of the non-linear model result is complicated when eddies are produced. Non-linear effects will also complicate the forcing terms. Thus the non-linear baroclinic model is only used after an initial understanding has been gained from the linear baroclinic model.

2.6.6 The linear two layer model

The linear two layer model allows the effects of sills and shelves to be included in the model and transports at all times can be determined exactly. In the case of including regions of shallow shelf seas the effects of bottom friction over the shelves are included by the addition of the terms (2.6.5.1) - (2.6.5.2) in the upper layer momentum equations over the shelf.

$$\frac{c_D\, u_1(u_1^2+v_1^2)^{\frac{1}{2}}}{D} \qquad (2.6.5.1)$$

$$\frac{c_D\, v_1(u_1^2+v_1^2)^{\frac{1}{2}}}{D} \qquad (2.6.5.2)$$

where c_D is the coefficient of bottom friction and D is the depth of water over the shelf. The value of c_D used is based on the order of magnitude estimate of $c_D = 2\text{x}10^{-3}$ (Csanady, 1982).

The two layer models also produce effects due to the faster barotropic mode which is not included in the baroclinic models. Thus the two layer models appear to be the best models to use for all experiments. However computationally the two layer models are very slow and repeated experiments with different parameters are not practical.

Additionally the range of horizontal viscosities that can be used is reduced ($>500\text{m}^2\text{s}^{-1}$) compared with the baroclinic model ($>10\text{m}^2\text{s}^{-1}$). The instability that develops with the use of lower viscosities in the linear two layer model appears to be related to the forcing terms used. Thus the linear two layer model is used where necessary rather than where possible.

2.6.7 The non-linear two layer model

The non-linear two layer model should be the most realistic of the models available for use. However an instability develops in this model when horizontal viscosities in the realistic range (10–$10^4\text{m}^2\text{s}^{-1}$) are used. Hence this model is not used in this study.

It was decided that the additional benefits that might be gained by further development and investigation of the non-linear two layer model could not be justified in the time available for this study. The use of the non-linear two layer model was not foreseen as a major part of the study.

3. RESULTS: THE CROSS EQUATORIAL CHANNEL

3.1 INTRODUCTION

In this chapter a variety of analysis methods are applied to the results of the models developed in chapter 2. The model results are compared and contrasted with a view to understanding the model physics and the differences between the models. An important aim of these initial experiments is to find the most practical model for use in the further experiments described in chapter 4 and 5.

The model results consist of a large data set containing the predicted values of the model variables at each point on the finite difference grid. Contour and vector plots give an instantaneous view of these variable fields. Quantitative interpretation is achieved by the use of sections in time and space throughout the data set. Studies of the energetics and the balance of terms in the momentum and vorticity equations are also useful approaches to understanding the physical processes that occur in the model.

3.2 THE LINEAR BAROCLINIC MODEL

3.2.1 Introduction

In this section the results of the linear baroclinic model are compared with the theory of section 1.5. These results provide a reference frame for later sensitivity studies (Section 3.3) and comparison with the more complex models (section 3.4 and 3.5).

The parameters used for this experiment are those given in section 2.6.2 and table 2.6.1. For this initial experiment a horizontal viscosity of $A_H = 100 m^2 s^{-1}$ is used. In the northernmost 200km of the numerical grid the relaxation forcing condition (2.4.3.3) is used with the interface between the two layers being forced to -30m, equivalent to a sea surface elevation of +11cm. In the southernmost 200km of the grid the interface is forced back to its unperturbed state. The relaxation time of this forcing is taken to be $\alpha = (18 \text{ hours})^{-1}$. At all lateral boundaries the free slip boundary condition is applied.

In this model tests were carried out to be certain that both potential vorticity and energy integrated over the domain of the model were conserved in the absence of dissipation and continued forcing. The conservation of potential vorticity of tracked particles was also established.

3.2.2 Transition to steady state

Figures 3.2.1.a) - g) show a time series of contour plots of the interface perturbation and vector plots of the horizontal velocity fields. The vector plots show the interpolated horizontal velocity of the currents every 40km. The point at the north western corner of the plot is 20km from the lateral boundaries of the channel. The vector plots are of the upper layer velocities, the lower layer velocities are determined from the baroclinic relation.

$H_2u_2 = -H_1u_1$ therefore, $u_2 = -0.154u_1$ (3.2.2.1)

Figure 3.2.1.a) shows the fields after 5 days. North of 3°N the interface has attained a level of -20m, which is equivalent to a sea surface elevation of ~7cms. The zonal gradient on the interface is seen to change sign at the equator. The flow from the forcing region reaches the equator on the western boundary but south of the equator the flow is turning towards the eastern boundary to form a coastal Kelvin wave. There is strong southward flow across the entire channel to approximately 4°S.

The fields after 7½ days are shown in figure 3.2.1.b) and clearly show the trapping of the coastal Kelvin wave to the eastern boundary due to the decrease in Rossby radius away from the equator (see also section 3.2.3). Maximum currents associated with this wave are less than 50cms^{-1}. The region of southward flow across the equator is narrower than that after 5 days and a weak ($<20\text{cms}^{-1}$) return flow is seen to develop at the eastern boundary. The region of southward flow at the western boundary has not significantly moved from its position after 5 days which suggests it is equatorially trapped.

After 12½ days (figure 3.2.1.c) the coastal Kelvin wave has propagated the length of the channel and is in the process of being damped out in the southern boundary region. The southward flow ($\sim 1\text{ms}^{-1}$) is becoming more confined to the western boundary and has extended to 6°S. The region of northward flow has moved slowly westward and increased in magnitude. Associated with this motion the

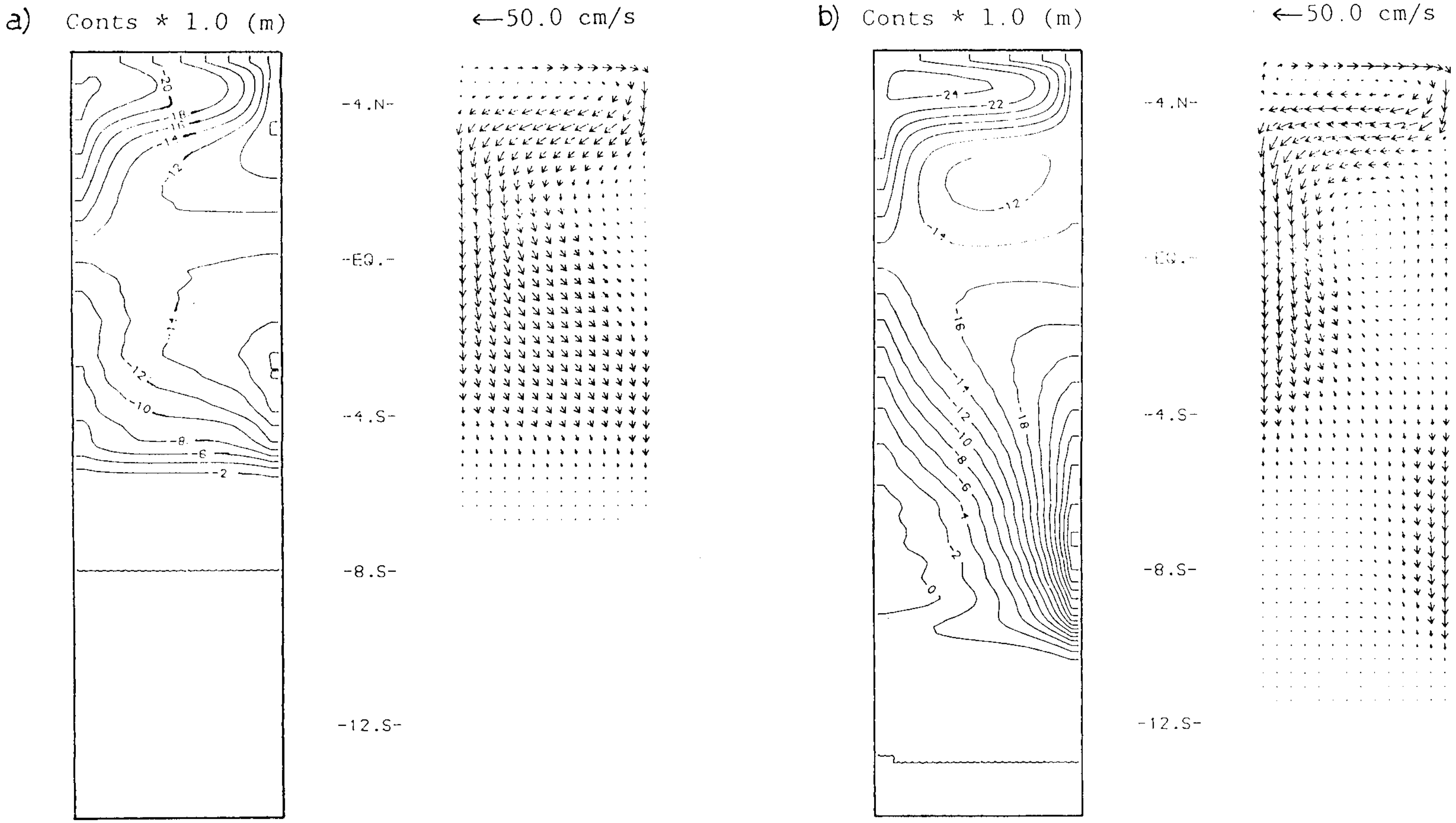

Figure 3.2.1 : Linear Baroclinic Model, $A_H=100m^2s^{-1}$, Interface Perturbation and Upper Layer Velocity Field after a) 5 days and b) 7½ days.

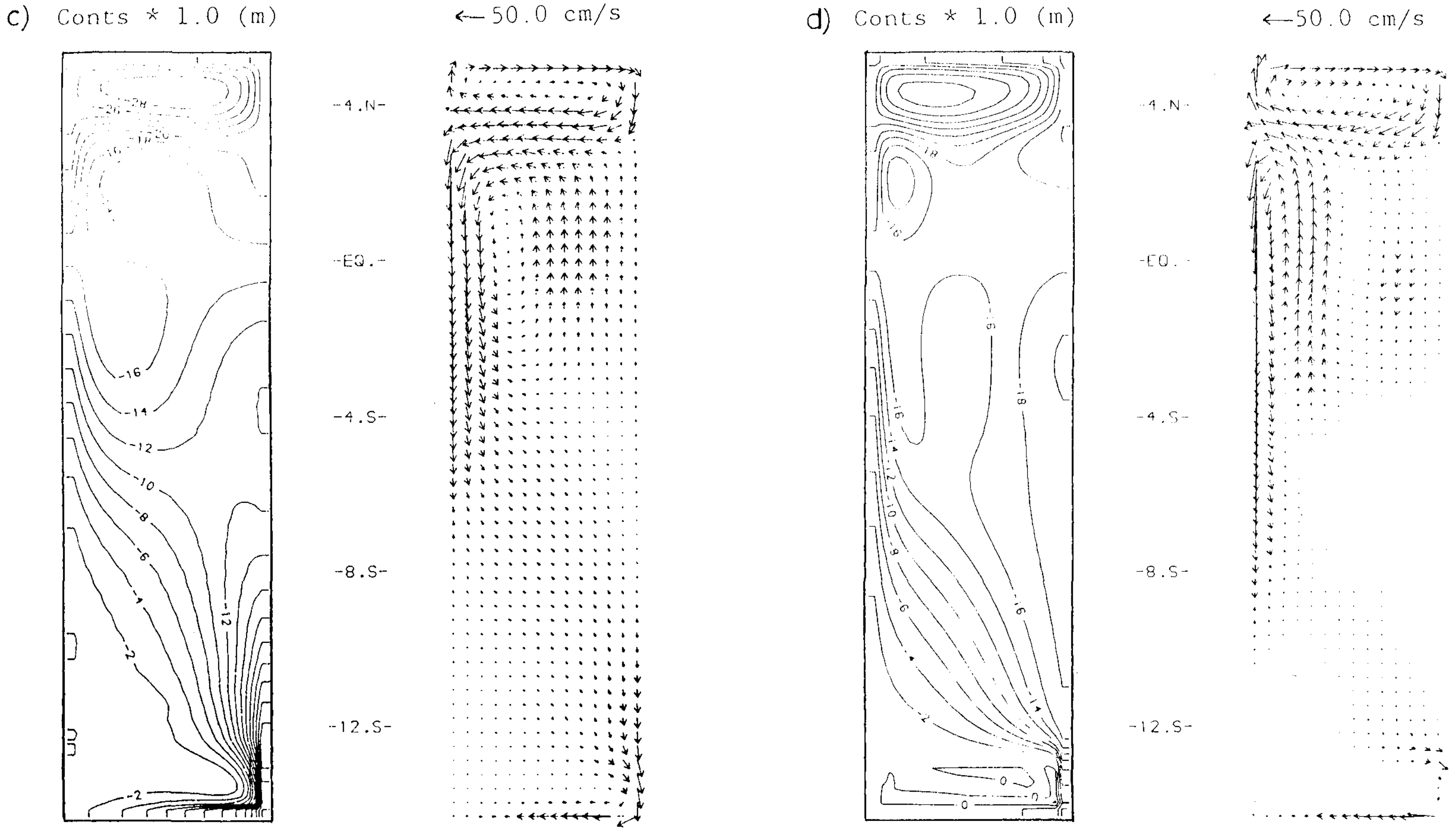

Figure 3.2.1 : Linear Baroclinic Model, $A_H=100m^2s^{-1}$, Interface Perturbation and Upper Layer Velocity Field after c) 12½ days and d) 25 days.

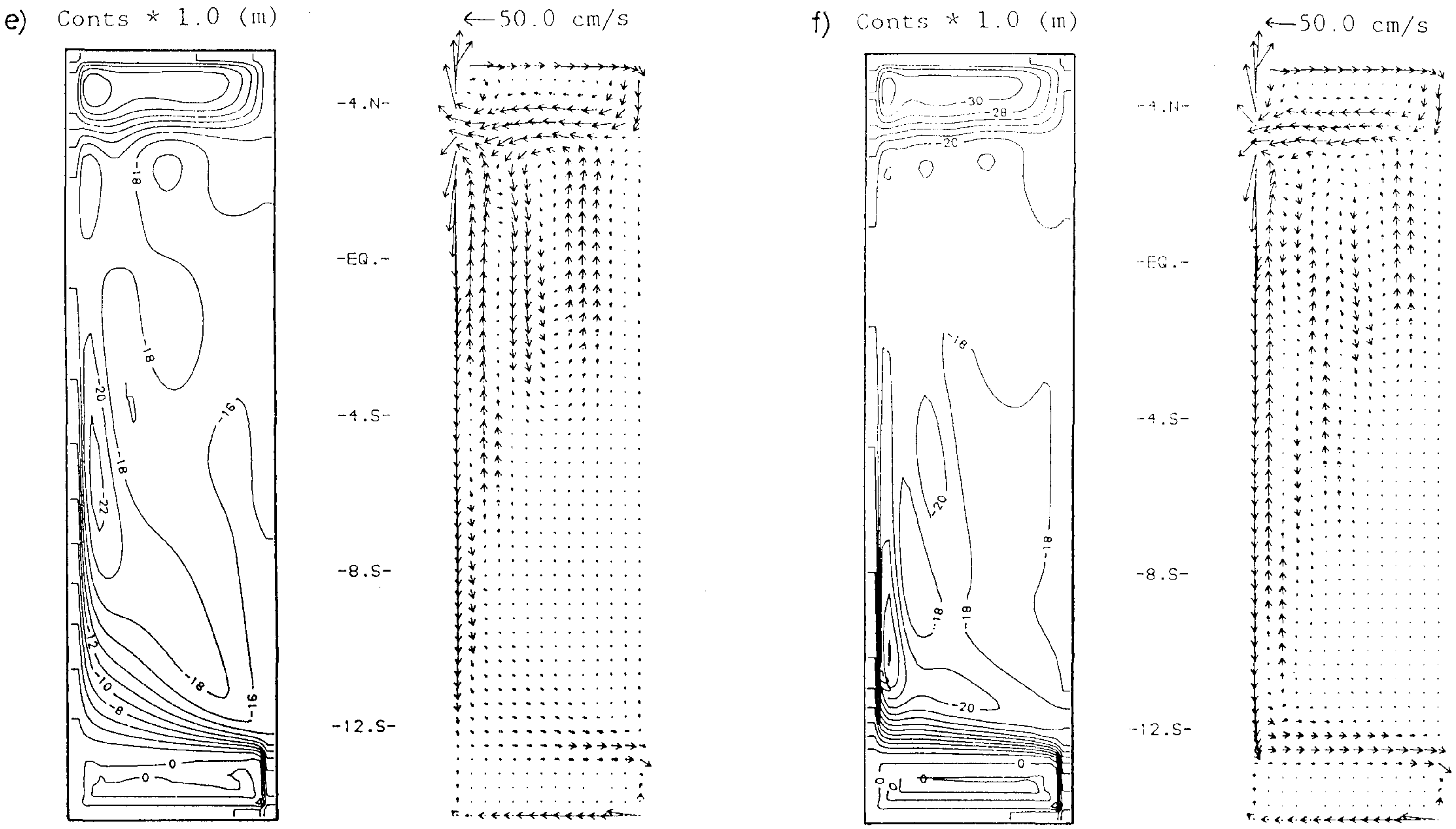

Figure 3.2.1 : Linear Baroclinic Model, $A_H=100m^2s^{-1}$, Interface Perturbation and Upper Layer Velocity Field after e) 50 days and f) 100 days.

g)

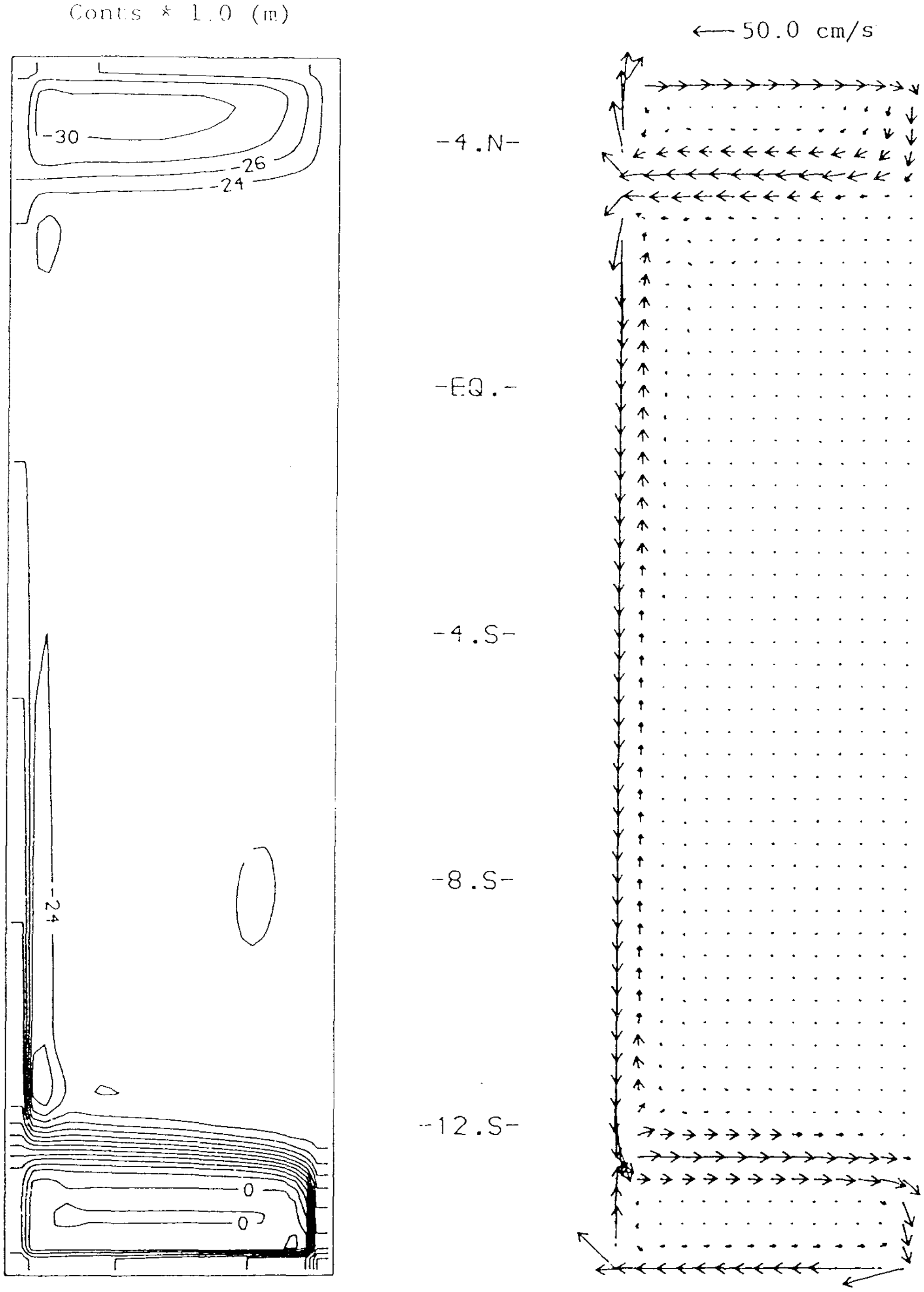

Figure 3.2.1 : Linear Baroclinic Model, $A_H = 100 m^2 s^{-1}$, Interface Perturbation and Upper Layer Velocity Field after g) 400 days.

interface is developing a maxima (>-14m) and a minima (<-16m) on either side of the equator. This motion is evidence of low frequency Planetary waves.

Figures 3.2.1.d) shows the fields after 25 days. The coastal Kelvin wave has been absorbed by the southern boundary condition, the currents existing in this region are now associated with the development of a cyclonic gyre needed to geostrophically balance the raised interface. The north-south pressure gradient of -30m prescribed by the forcing terms has now been attained. At the equator the strong southward flow (~1·2ms^{-1}) is confined to a region 80km wide and extends to 10°S. The northward counterflow has maximum currents of 40cms^{-1} and is 200km wide. A second pair of maxima and minima has developed at the interface on either side of the equator and the eastern half of the channel is occupied by a weak (~20cms^{-1}) southward flow. This series of flow and counterflow extend from the northern forcing region to 4°S.

In figure 3.2.1.e), fields at 50 days , the western boundary current extends to 12°S and is wider at the higher latitudes than at the equator where the current now occupies about 40km. The adjacent regions of northward and southward flow are now more strongly developed. There are four pairs of maxima and minima on the interface associated with two regions of northward flow and two regions of southward flow. The width of these currents increases away from the western boundary whilst the magnitudes of the currents increase towards the western boundary.

After 100 days, figure 3.2.1.f), Planetary waves have created four regions of southward flow and three regions of northward flow at the equator. The first three of these interior flows and the interface minima and maxima associated with them extend to 11°S, 8°S and 6°S respectively. The remaining flows are trapped north of 4°S. The maximum western boundary current occurs at the equator and remains approximately 1.2ms^{-1}. The interior flows have approximately equal magnitudes of 20cms^{-1}. The entire north-south pressure gradient occupies the region of the western boundary current, elsewhere the interface between the two forcing regions is maintained at approximately -20m.

Beyond 300 days of integration there is no further change to the variable fields. Figure 3.2.1.g) shows the fields after 400 days, a strong southward flowing western boundary current ($\sim 0{\cdot}75\text{ms}^{-1}$) and an adjacent weaker ($\sim 0{\cdot}15\text{ms}^{-1}$) return flow are the dominant features of the flow away from the forcing regions. Currents in the interior are very small ($< 1\text{ cms}^{-1}$). The entire north-south pressure gradient (24m) occurs across the western boundary current. This final state agrees well with the solution predicted by Munk (1950) for a system where horizontal viscosity is the dominant dissipative mechanism (discussed further in section 3.3.4). The difference between this solution and Munk's (1950) solution is that Munk required an interior Sverdup flow to balance his western boundary current. In this solution there is no such interior flow and there is a net transport through the upper layer.

3.2.2 Kelvin Waves

Figures 3.2.1.a) - c) show the southwards progression of a baroclinic Kelvin wave along the eastern boundary of the channel south of the equator. The fields do not show the Kelvin wave travelling southwards along the western boundary of the channel north of the equator or crossing from west to east at the equator. This is due to the proximity of the forcing region to the equator and to the narrowness of the channel compared to the equatorial radius of deformation (560km and 228km respectively). The position of the maximum amplitude of the Kelvin wave at 5 days and 7½ days gives an estimate of the speed of propagation as 2.4ms^{-1}.

Sections in time of the meridional component of velocity at the eastern and western boundaries are shown in figures 3.2.2.a) and b). The speed of the Kelvin wave can be calculated from the gradient of the initial disturbance and is found to be 2.35ms^{-1}, in good agreement with the prescribed baroclinic phase speed of 2.4ms^{-1}.

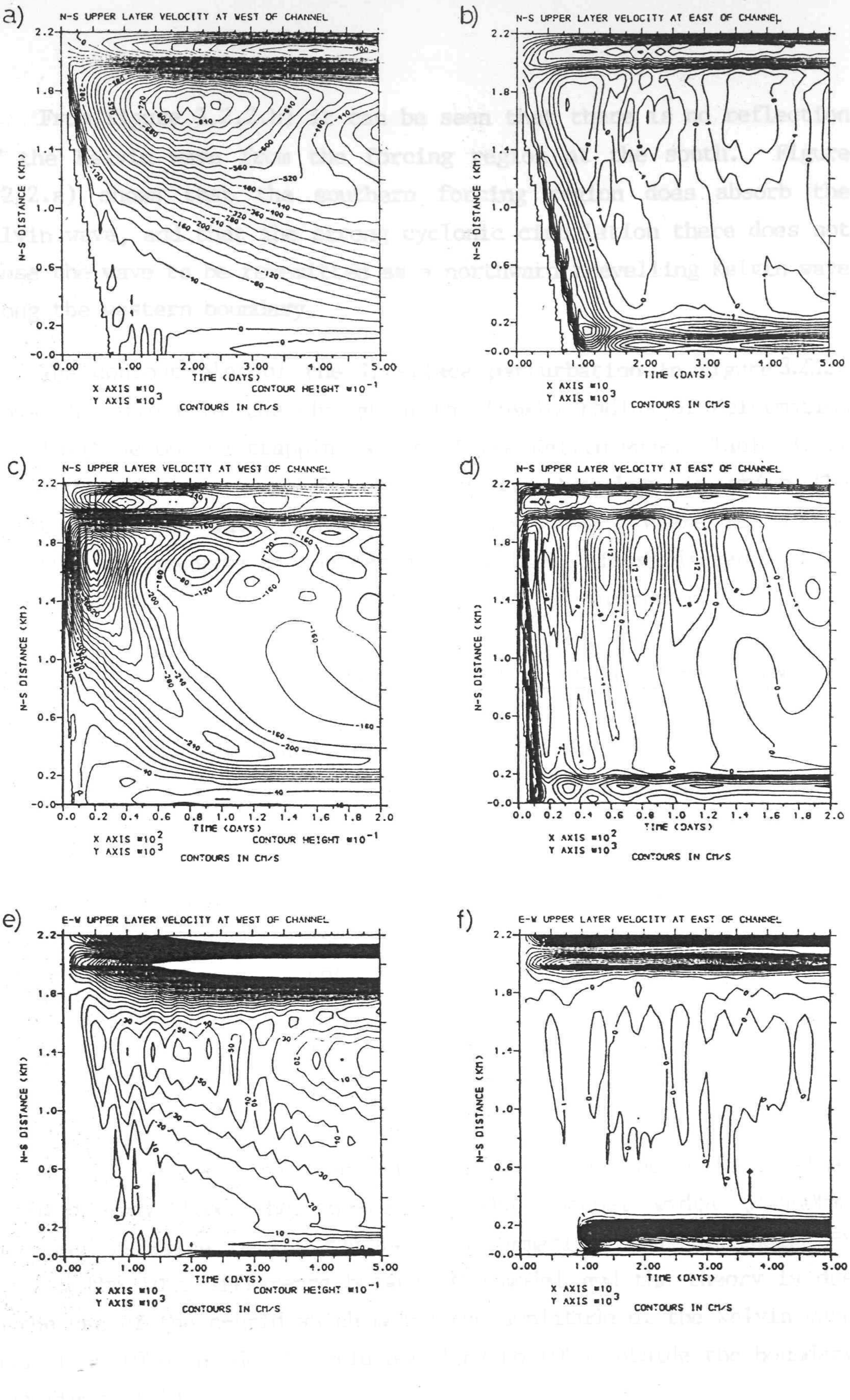

Figure 3.2.2 : North - South sections in time through the Meridional a) - d) and Zonal e) - f) components of Velocity.

From figure 3.2.2.b) it can be seen that there is no reflection of the Kelvin wave from the forcing region at the south. Figure 3.2.2.a) shows that the southern forcing region does absorb the Kelvin wave, and that the strong cyclonic circulation there does not cause the wave to be re-emitted as a northward travelling Kelvin wave along the western boundary.

The contour plot of the interface perturbation in figure 3.2.1.b) shows the effect of the change in the Rossby radius of deformation with latitude on the trapping scale of the Kelvin wave. Table 3.2.1 gives the distance away from the eastern boundary in which the amplitude of the wave decays from A_0 to $0.37A_0$, where A_0 is the amplitude of the wave at the eastern boundary. These distances were determined by interpolation of the interface perturbation field.

TABLE 3.2.1 **Effect of latitude on width of coastal Kelvin wave**

Latitude	Distance for decay A_0 to $0.37A_0$ (km)	Radius of deformation (from table 1.5.1) (km)
4°S	397	228
5°S	264	192
6°S	206	160
7°S	155	137
8°S	130	120
9°S	117	107

It can be seen that the agreement with the theoretical values improves away from the equator as the channel width (W=560km) increases relative to the radius of deformation. At latitudes 8°S and 9°S the 10km difference between the model and the theory is due to the use of the c-grid which makes the amplitude of the Kelvin wave equal from 10km inside the grid boundary to 10km outside the boundary (see figure A.1).

3.2.4 Inertial - Gravity Waves

Figures 3.2.2.e) and f) show inertial type oscillations (periods < 120 hours) in the zonal velocity fields. The frequency of these waves can be seen to increase away from the equator. The east-west sections in time of the zonal velocity at different latitudes (figures 3.2.3.a) and b)) also show these high frequency waves. The largest amplitude occurs in the interior of the channel. Initially the zonal velocity fields are dominated by the high frequency oscillations but after 20 days the slow formation of regions of northward and southward flow due to the Rossby wave motion can clearly be seen. Even after 100 days the background of inertial oscillations is apparent.

In table 3.2.2 the mean frequency and period of the observed oscillations at different latitudes are given.

TABLE 3.2.2 Period and Frequency of Inertial-Gravity Waves

Latitude	Period (hours)	Frequency ($\times 10^{-5} s^{-1}$)
2°N	110+/-4	1.59+/-0.05
0°	107+/-2	1.63+/-0.03
2°S	105+/-3	1.66+/-0.04
4°S	86+/-3	2.03+/-0.04
6°S	74+/-2	2.36+/-0.03
8°S	65+/-2	2.69+/-0.03
10°S	60+/-2	2.91+/-0.03

It is clear that the mean frequency of the waves increases with latitude and that within 2° of the equator the frequency is approximately constant 1.63 +/- 0.05 x $10^{-5} s^{-1}$. These observed frequencies agree well with the values of the m=1 inertial - gravity waves given in figure 1.5.2.a). The Yanai wave is the dominant

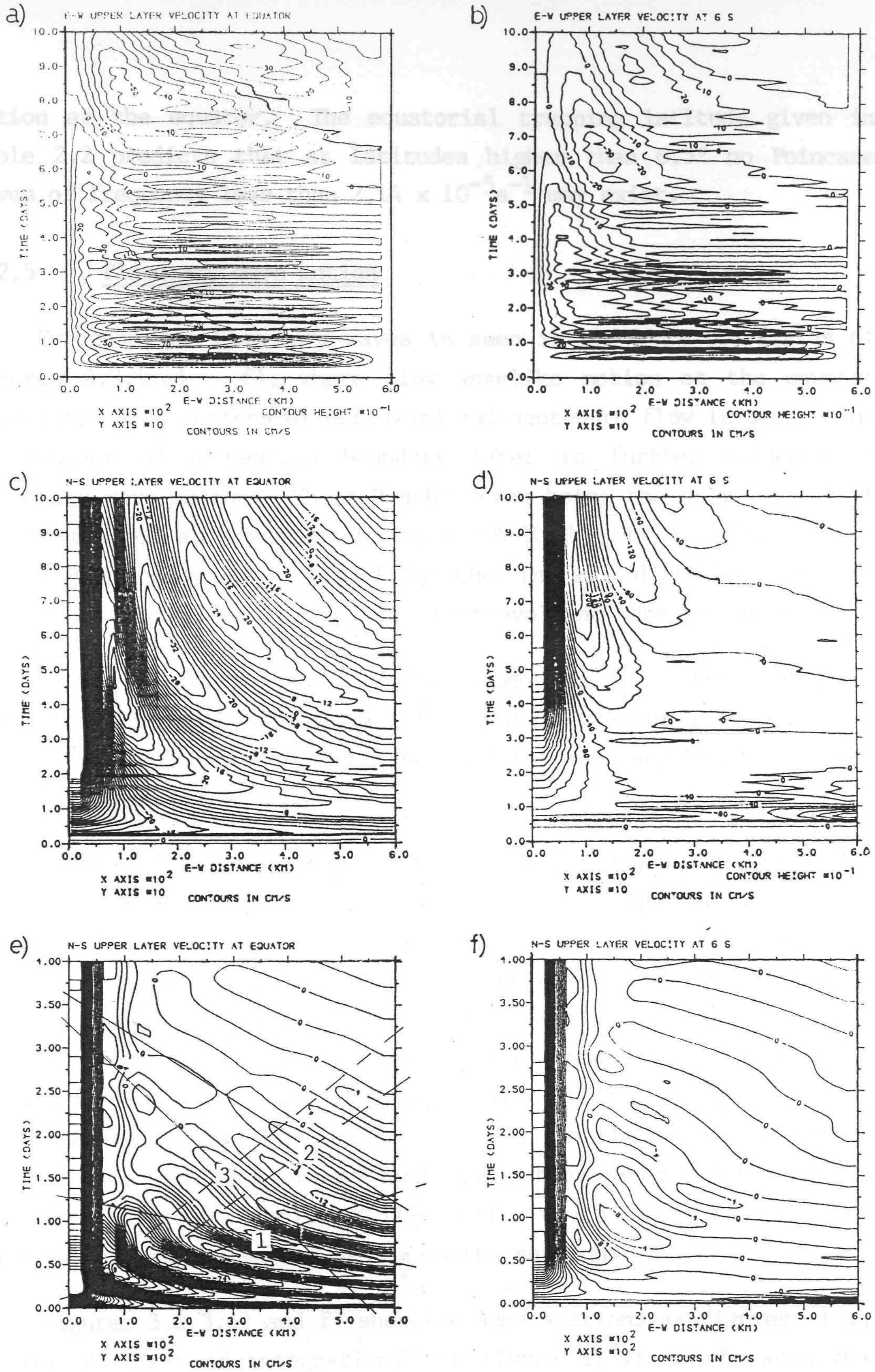

Figure 3.2.3 : East - West Sections in time through the Zonal a) - b) and Meridional c) - f) Components of Velocity.

motion at the equator. The equatorial trapping latitude given in table 2.2 predicts that at latitudes higher than 6.5° no Poincare waves of frequency less than $2.14 \times 10^{-5} s^{-1}$ may exist.

3.2.5 Planetary wave motion

Evidence for Planetary waves is seen in the velocity fields of figures 3.2.1.c) - f), where slow wavelike motion at the equator associated with regions of northward and southward flow is seen. The development of a western boundary layer is further evidence of Planetary wave motion. Short Rossby waves being the only waves that can be trapped at a western boundary (Pedlosky, 1979). These short Rossby waves may be produced by the initial disturbance or by reflection of incident long, westward travelling, Rossby waves.

Figure 3.2.2.c) shows the development of the western boundary current with time. The parabolic nature of the curve on which the maximum boundary current lies shows that the boundary layer is formed more slowly at higher latitudes.

Figures 3.2.3.c) and d) show sections through the meridional velocity with time for the first 100 days of the integration. At the equator, figure 3.2.3.c), the westward phase velocity of the long Rossby waves is clear. A decrease in the phase velocity of the long Rossby waves with time can also be seen. The initial phase and hence group velocity of the long Rossby wave is found to be $0.8ms^{-1}$. In good agreement with the theoretical value ($0.8ms^{-1}$ from 1.5.4.13). The decrease in velocity westwards across the channel may be due to interference with shorter eastward propagating waves. After 30 days the eastward group velocity of the shorter waves can be seen from the position of the maxima and minima in the sections.

Figures 3.2.3.e) and f) show the same sections as figures c) and f) for 400 days of integration. In figure e) it can be seen that after an initial period of approximately 100 days the eastward group velocity and westward phase velocity of the short waves becomes steady. Wave motion ceases after approximately 300 days. In figure e), which is representative of sections within 2° of the equator, various eastward propagating waves are clearly seen and numbered (1)-(3) in figure e). The properties of these waves are determined and summarized in table 3.2.3.

TABLE 3.2.3 **Wave properties determined from figure 3.2.3.e)**

Wave number	Phase Velocity (ms^{-1})	Group Velocity (ms^{-1})	Wavenumber $x10^{-5}(m^{-1})$	Frequency $x10^{-6}(s^{-1})$
1	-0.07	0.07	1.6	1.2
2	-0.03	0.03	2.8	0.8
3	-0.02	0.02	3.6	0.6

These waves have properties that correspond to the m = 3,5 and 7 channel modes given in section 1.5.5 figures 1.5.2.b) and 1.5.3.b). The m = 1 mode has a higher frequency $\sim 2.2x1^{-6}s^{-1}$, a phase velocity of $-0.38ms^{-1}$ and a group velocity of $0.02ms^{-1}$. Thus the m = 1 mode might exist initially but clear evidence is not found in figure 3.2.3.e). From figures 1.5.2.b) and 1.5.3.b) it can be seen that these short waves are either Yanai or Rossby waves. For the higher channel modes m > 4 there is little difference between the zonal properties of these waves. From figure 3.2.11.d) the meridional structure of the equatorial motion can be determined. It can be seen that there is decay on a scale approximately equal to the equatorial radius of deformation which indicates that Yanai waves are important. The decay scale of the n=1 Rossby wave is given by equation 1.5.4.7 and is ~560km.

At 6°S, figures 3.2.3.d) and f), the wave motion is much less pronounced suggesting that it is the Yanai and n=1 modes that are dominant. Initially at 6°S there is no evidence for long Rossby waves in figure 3.2.3.d).

In summary it is seen that initially all wavelengths of Rossby wave are generated. However after reflection at the boundaries of the channel interference occurs and the only modes that can then occur are those with east-west wavenumber $^{m\pi}/W$. The meridional structure of these modes is dominated by the equatorially trapped Yanai wave and to a lesser extent the n=1 Rossby mode. The channel modes the dominate are the m=3,5 and 7 modes.

3.2.6 Western boundary layer

The Western boundary current is produced by the trapping of short Rossby waves at the eastern boundary. These waves are generated by the passage of the initial trout southwards through the channel that excites all possible waves. No evidence has been found that propagation and reflection of long Rossby waves are an important part of this boundary current generation.

With the value of $100m^2s^{-1}$ for the horizontal viscosity used in this initial experiment the boundary layer width with no slip boundary conditions would be expected to be 56km (table 1.5.3). Reference to figures 3.2.3.e) and f) shows that the boundary layer width is 36+/-2km after 400 days. Due to the use of the c-grid the first point shown in the meridional contour plot is 10km outside the lateral boundary of the channel. It can be seen that the width of the counter current is 59+/-2km. The magnitude of the northward counter current is approximately 18% of the southward flow, in agreement with the value of 23% in table 1.5.3. The effect of no slip and free slip boundary conditions on the western boundary current is investigated in section 3.3.4.

3.3 PARAMETER STUDIES

3.3.1 Introduction

A series of experiments are now described that look at the sensitivity of the results to varying the basic parameters of the model ocean within physically realistic ranges. In particular, the effects of varying the co-efficient of lateral viscosity, the forcing timescale, the boundary conditions and the location of the channel on the equatorial Beta plane are discussed. The experiments are based on the linear baroclinic model but in most cases the results are relevant for the whole of this study.

3.3.2 The forcing conditions

In the baroclinic model two variables are involved in the forcing condition. The relaxation timescale α and the difference in height between the interface at the north and the south of the channel. One set of results for the linear case has been reported in section 3.2 and will scale linearly for changes in the height difference. The intention here is to investigate the effect of changing the relaxation timescale α. The choice of α must be such that the prescribed north-south height difference is attained without reflection occurring at the boundaries of the forcing regions.

In the preliminary experiment the value of α in the northern forcing region was $1.54 \times 10^{-5} s^{-1}$ equivalent to a timescale of 18 hours. In the southern forcing region a linearly increasing condition was used to reduce the possibility of reflection from the boundary, α rising from $3.08 \times 10^{-6} s^{-1}$ to $3.08 \times 10^{-5} s^{-1}$ over the southern most 10 grid points. Two further experiments were also carried out using order of magnitude changes from the initial experiment. As in the initial experiment the height difference to be maintained is -30m. The main features of the results are described below and summarized in table 3.3.1.

TABLE 3.3.1 Effects of varying relaxation timescale.

Relaxation Rate (hours)$^{-1}$	W.bdry Current (at 0°) (ms^{-1})	Interface gradient across W. bndry (10°S) (m).	Interface in N. Forcing Region
180	-0.6	-12	-24
18	-1.2	-20	-30
1.8	-1.5	-23	-30

With α^{-1} = 180 hours the steady state gives the same flow pattern as the initial experiment but the currents are much reduced. The maximum velocity that occurs at the western boundary after 25 days is now 60cms^{-1} compared with 120cms^{-1} in the initial experiment (section 3.2.2), zonal velocities are similarly reduced by 50%. The reason for this reduction in Kinetic energy is that α is not able to maintain the interface in the north at -30m but reaches a minimum of -24m. This smaller north-south height difference results in a weaker gradient across the boundary current. A geostrophic balance would then predict currents to be 60% of those in the initial experiment.

When α^{-1} is decreased to 1.8 hours the effect is to increase the currents because of the increased pressure gradient across the boundary current. These results are again explained by the geostrophic balance. From the stability criteria for α (equation 2.3.4.8) it can be shown that this lower value of α^{-1} lies just within the upper limit for stability. No reflection occurs at the edge of the forcing region in this case.

The major effect of increasing α was found to be in the amplitude of the Poincare waves. With large α the initial front is stronger and more sharply defined, more energy is thus transferred to the high frequency Poincare waves. Planetary waves and the initial Kelvin wave are not significantly affected by the choice of α.

It would appear that to achieve a height difference of -30m across the western boundary current at steady state the interface in the northern forcing region must be forced below -30m. The choice of relaxation timescale α, can then be made to reduce the high frequency Poincare waves if necessary. Throughout this study a relaxation timescale of α^{-1} = 18 hours is used (for the baroclinic models).

3.3.3 Open boundary conditions

In section 2.4.4. the problem of the treatment of open boundary conditions was discussed. In this section the aim is to compare the relaxation or 'sponge' boundary condition used in the preliminary experiment and an Orlanski open boundary condition (see section 2.4.3) in order that in further experiments the most suitable boundary condition is used.

The baroclinic model is computationally a quick model to integrate because of the length of timestep. It is thus possible to create perfect open boundaries at 3°N and 12°S by extending the channel to the north and south. The model can be integrated for 25 days if the channel covers the region ~30°N-40°S. The Kelvin waves generated in the northern forcing region propagate around the boundaries of the channel but in 25 days have not had sufficient time to re-enter the region of interest (3°N-12°S). For a free surface model with the barotropic mode this formulation would be impractical. The β plane approximation over the whole region is a poor assumption but does not affect the solution in the region of interest for the first 25 days.

The horizontal velocity and interface perturbation fields of the perfect open boundary version of the model are presented in figure 3.3.1.a). The forcing condition to the north is the same as that in the initial experiment,north of 3°N the interface is forced to -30m, other parameters are also unchanged. A comparison with figure 3.2.1.d) shows that in the region of interest the two versions produce similar results. The differences between the fields are due to circulation in the forcing regions. The use of the perfect open boundary version of the model suggests that the initial model is satisfactorily reproducing the physics that occurs in an open channel.

Implementing an Orlanski open boundary condition at the southern boundary of the channel of the form given in section 2.4.4 is straight forward. The fields after 25 days of integration are shown in figure 3.3.1.b) for comparison with figures 3.3.1.a) and 3.2.1.d). In figure 3.3.1.b) the western boundary current south of 8°S has developed much faster than in the other two versions. North-south sections in time of the meridional velocity at the western boundary of the perfect open boundary and the Orlanski boundary condition versions of the model are shown in figures 3.3.2 and 3.3.3. The effect of the Orlanski boundary condition on the developing western boundary current is very obvious.

Various authors (e.g. Camerlengo and O'Brien, (1980), Miller and Thorpe, (1981) and Chapman (1985)) have had success using Orlanski type boundary conditions to allow waves (Rossby or Kelvin) to propagate through a boundary. However, few authors have had success

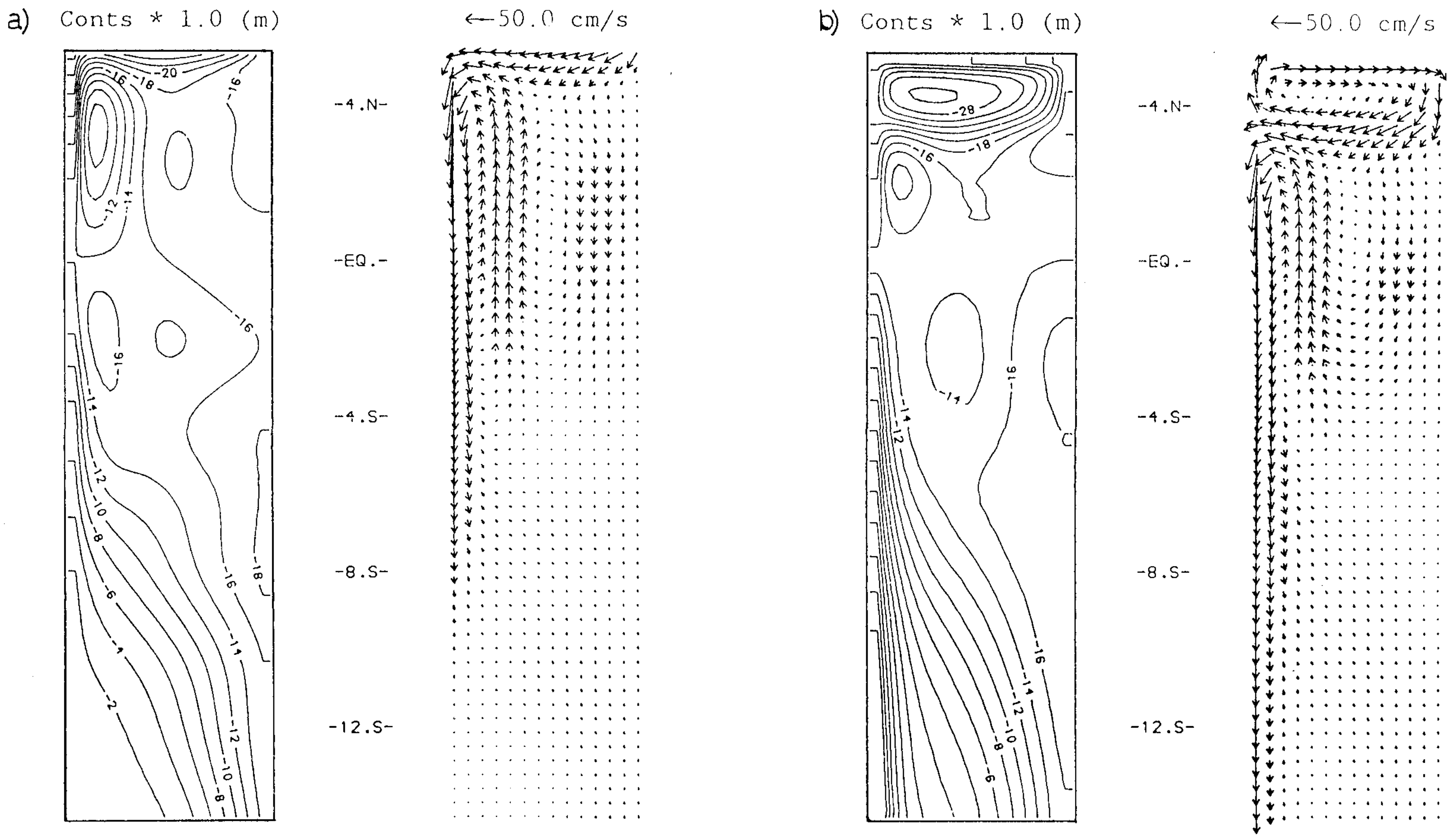

Figure 3.3.1 : Linear Baroclinic Model, $A_H = 100 m^2 s^{-1}$, Fields after 25 days a) 'Perfect' Open Boundaries b) Orlanski Boundary Condition at South (Compare with figure 3.2.1 d)).

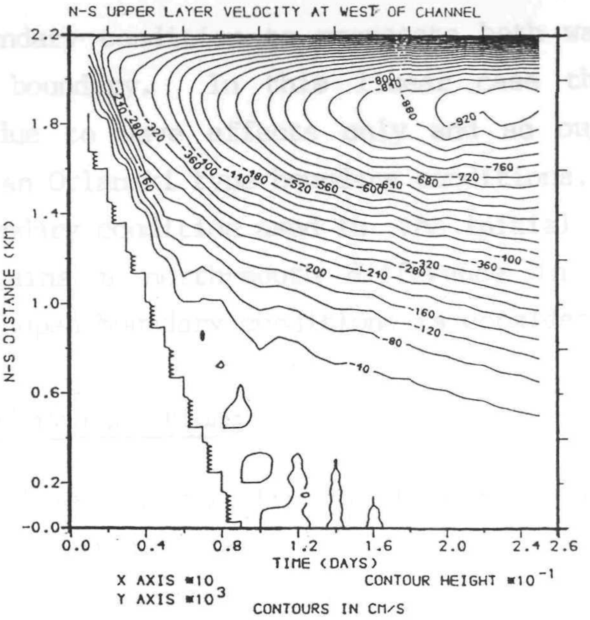

Figure 3.3.2 : North - South Section in time of Meridional Velocity at Western Boundary, Perfect Open Boundary Conditions at North and South.

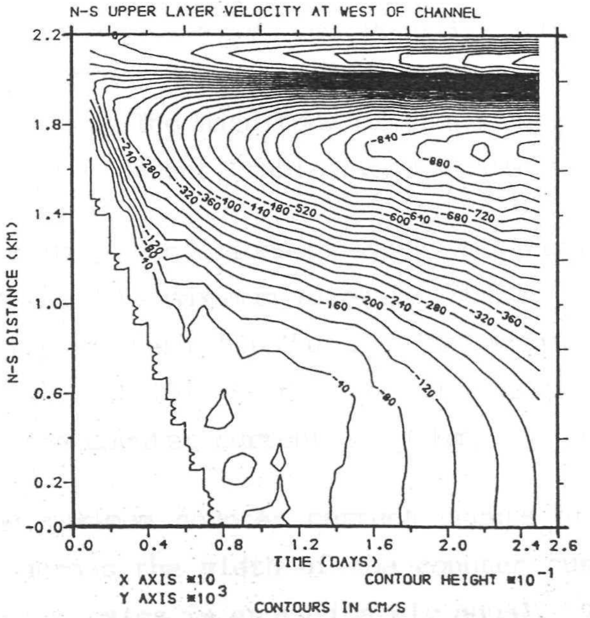

Figure 3.3.3 North -South Section in time of Meridional Velocity at Western Boundary, Orlanski Boundary Conditions at South.

using a radiation boundary condition to propagate both waves and a mean flow through a boundary. In this linear case the western boundary current is due to wave effects only and so ought to be suitable for use with an Orlanski type boundary conditions. However, since the 'sponge' boundary condition used in the initial experiment works well and maintains a north-south difference in height no further development of open boundary conditions is considered here.

3.3.4 Lateral boundary conditions

The effect of implementing no slip boundary conditions is now investigated. All other physical parameters are the same as in the preliminary experiment. Figures 3.3.4.a) and b) show the instantaneous fields after 400 days for the cases of free slip and no slip boundary conditions respectively. The main difference between the fields is at the western boundary. The meridional velocity at the western boundary is shown in figure 3.3.5.

The no slip boundary conditions produce a western boundary layer of thickness 56km in good agreement with the theory of table 1.5.3 for $A_H=100m^2s^{-1}$. The maximum southward velocity is $0.6ms^{-1}$ and occurs at one third of the width of the boundary layer from the boundary. The counter current has a maximum northward velocity of $0.1ms^{-1}$ and a width of 58km. The magnitude of the counter current is 17% of that of the boundary current (table 1.5.3 predicts 23%).

The free slip boundary conditions produce a narrower western boundary layer (~37km) with the maximum velocity ($0.82ms^{-1}$) occurring 10km either side of the western boundary. The magnitude of the counter current ($0.15ms^{-1}$) is 18% of that of the western boundary current. The width of the counter current is 60km.

In both cases the maximum counter current occurs at one third the distance (~ 20km) across the width of the counter current. The total transport in the two cases is approximately equal. The greater velocity in the free slip case offsetting the narrower width of the flow. The western boundary current formed by the use of free slip

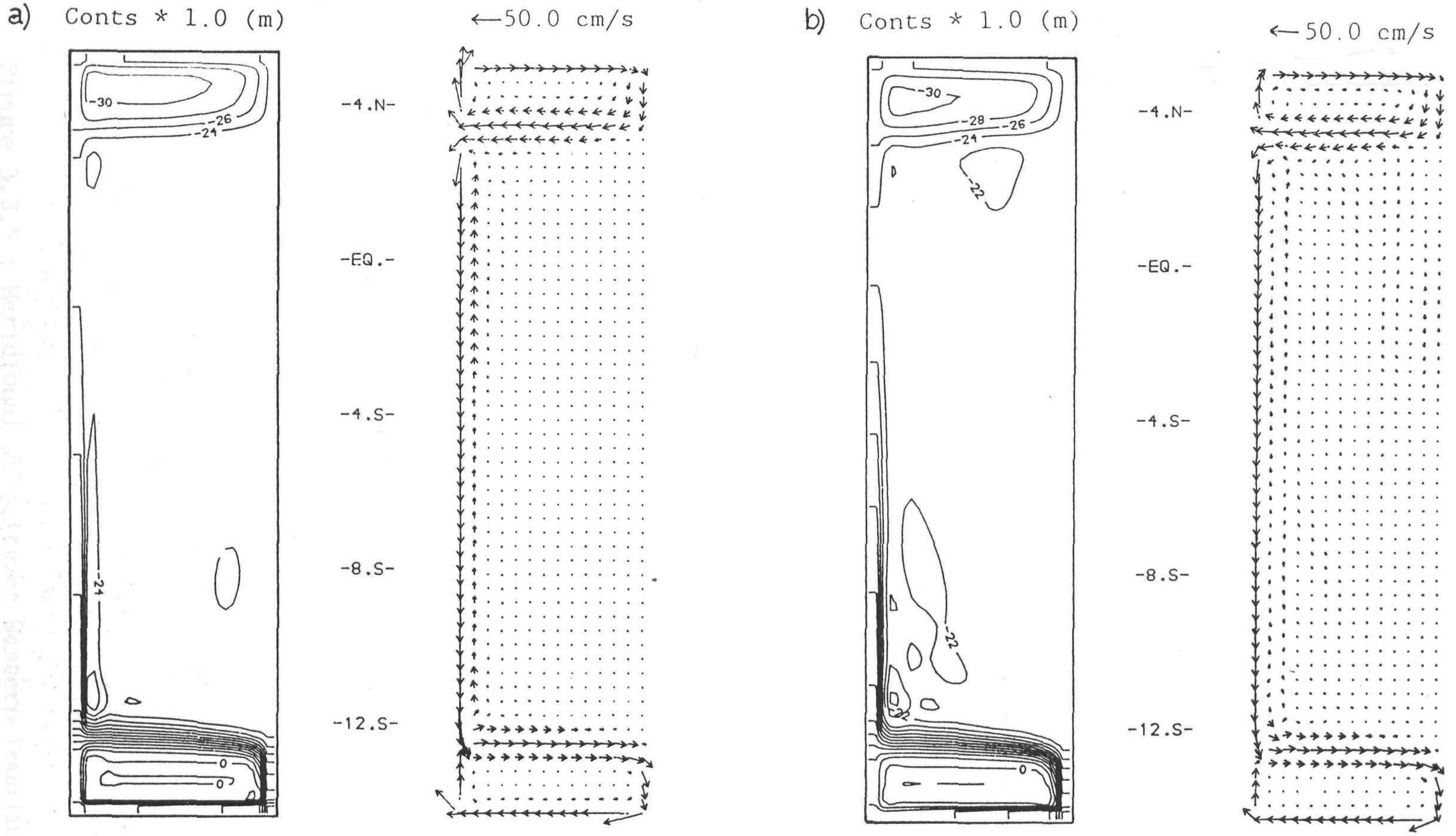

Figure 3.3.4. : Linear Baroclinic Model, $A_H = 100m^2s^{-1}$, fields after 400 days a) Free slip b) No slip Boundary conditions.

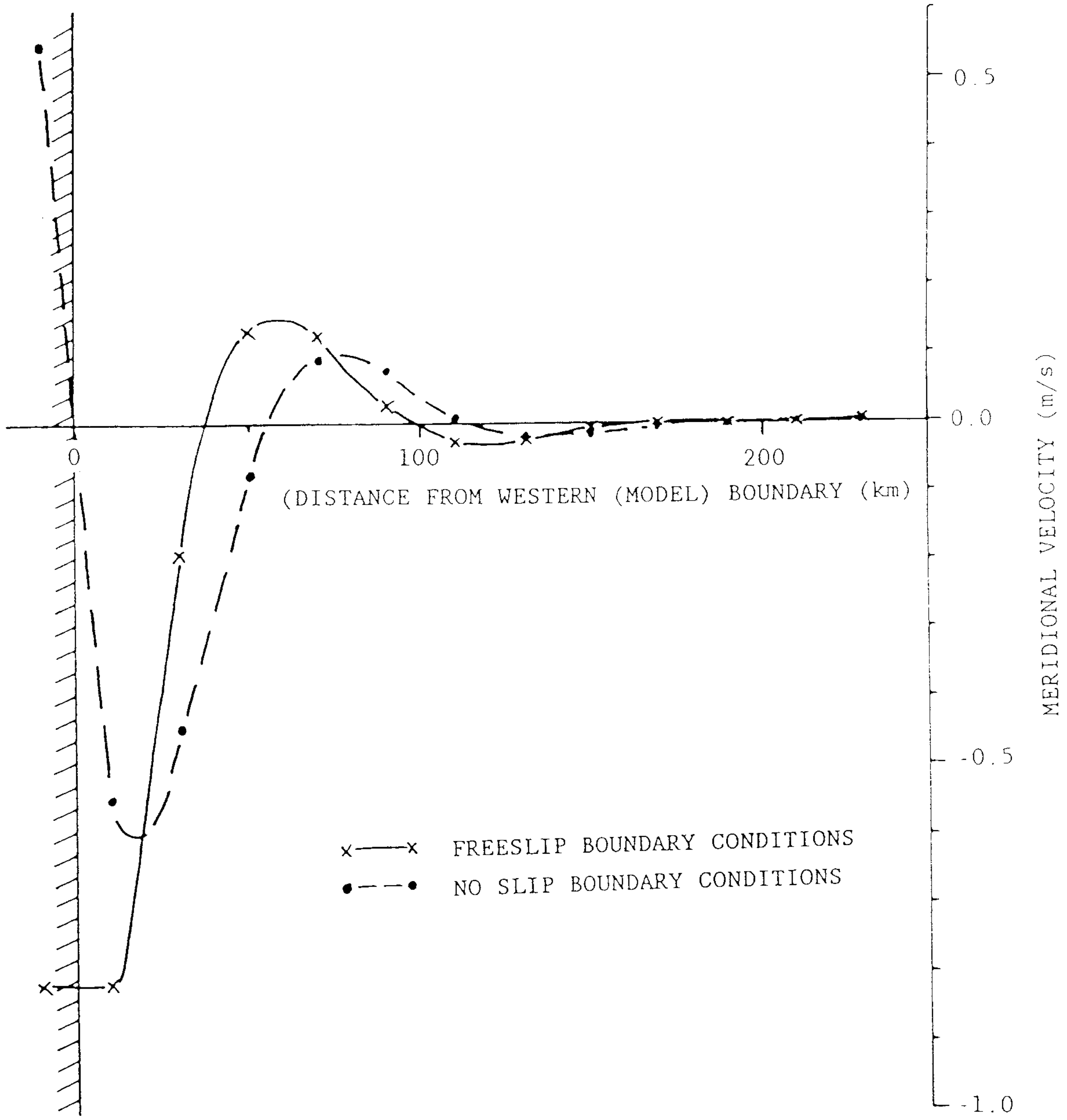

Figure 3.3.5 : Meridional Velocity at Western Boundary at the Equator (from figures 3.3.4 a), b)).

boundary conditions is approximately two thirds the width of that produced by no slip boundary conditions and that predicted by Munk's solution (section 1.5.6).

In the interior of the channel the fields are very similar, and in the initial part of the integration the transitory wave motions are largely unaffected by the nature of the solid wall boundary conditions.

The explanation for the difference caused by the boundary conditions is that the no-slip condition causes an input of positive vorticity at the western boundary. Since the lateral viscosity is unchanged between the two cases the region where the extra positive vorticity is lost by lateral diffusion has to be larger in the no slip case.

3.3.5 Location of Channel on the β-plane

The initial implementation of the model with the forcing in the region 3°N-5°N and 12°S-14°S is representative of the forcing across the South East Asian Waters. It is of interest to investigate whether the channel is sensitive to the latitude of the forcing and whether any forced southward flow in the channel results in the same steady state and transitional waves. The results of two experiments using the same parameters as in the initial experiment of section 3.2 but moving the position of the channel (and hence the forcing) on the equatorial β-plane are presented here.

The first experiment places the equator in the middle of the channel, the forcing then being between 8°N and 10°N. The velocity fields and interface perturbation are shown in figure 3.3.6.a) comparison with figure 3.2.1.e) (the initial experiment) shows that the planetary waves at the equator have developed to the same extent. However in figure 3.3.6.a) it can be seen that the regions of northward and southward flow extend further to the north of the equator than to the south and that the first region of northward flow extends to 5°S whereas in the initial experiment this region has reached $6\frac{1}{2}$°S. These differences are summarised in table 3.3.2.

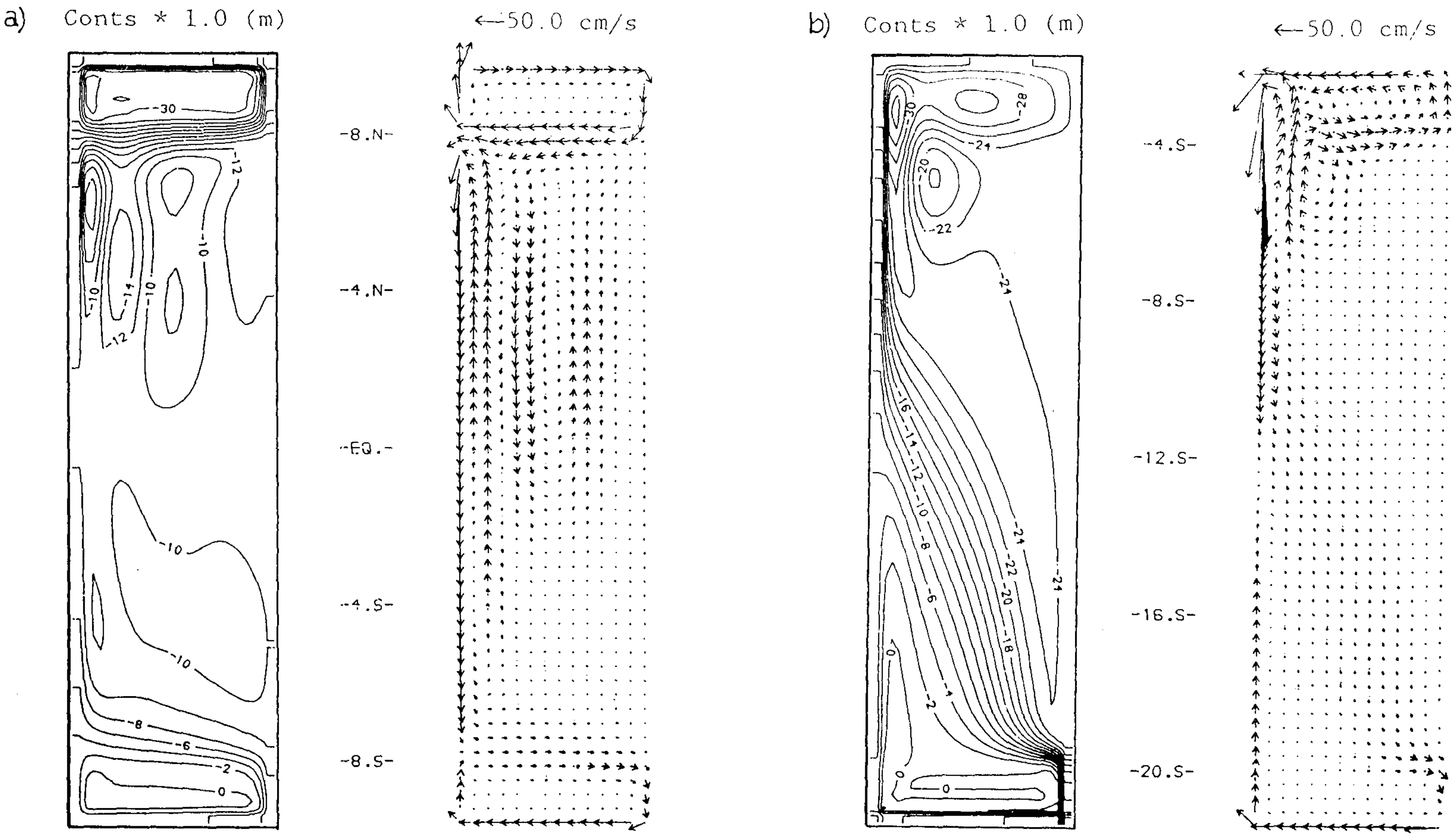

Figure 3.3.6 : Linear Baroclinic Model, $A_H = 100m^2s^{-1}$, Fields after 50 days. Channel location a) 10°N - 10°S, b) 2°S - 22°S.

The second experiment (figure 3.3.6.b) places the entire channel south of the equator and the forcing is in the region 2°S - 4°S. The initial coastal Kelvin wave is now only confined to the eastern boundary. The western boundary current and the counter current have developed to a similar extent as in the initial experiment (figure 3.2.1.e).

TABLE 3.3.2 **Summary of figures 3.2.1.e), 3.3.6.a) and b)**

Latitude of Forcing	Western Boundary Current Max Velocity	 Southern Extent	Counter Current Southern Extent
3°- 5°N	$1.2ms^{-1}$	12°S	6.5°S
8°-10°N	$1.0ms^{-1}$	>8°S	5.0°S.
4°- 2°S	$2.0ms^{-1}$	11°S	6.5°S

These experiments show that the development of the cross equatorial flow is independent of the latitude of the northern forcing. The only difference arising between figures 3.2.1.e) and 3.2.6.a) being due to the proximity of the forcing region. The experiments also support the theory that long westward propagating Rossby waves are not important in the development of the western boundary current.

3.3.6 Lateral viscosity in the channel

In this section the effect of the magnitude of the lateral viscosity term, A_H, in the model is examined. Table 3.3.3 summarizes the results of a series of experiments using horizontal viscosities in the typical ocean range $10m^2s^{-1}$ - $10000m^2s^{-1}$ (Gill, 1982). The integrations use identical parameters to the initial experiment with the exception of the lateral viscosity. The theoretical value of the width of the western boundary current calculated from table 1.5.3 is compared with the model western boundary layer width. The maximum western boundary current at steady state is also shown.

TABLE 3.3.3 **Effect of varying lateral viscosity on western boundary currents**

Lateral Viscosity (m^2s^{-1})	Theoretical Munk boundary Layer width (km)	Model Western boundary Layer width (km)	Max boundary Current at 0° (ms^{-1})
10	27	30	1.70
100	56	37	1.20
500	92	75	0.70
1000	113	90	0.60
5000	177	150	0.40
10000	188	180	0.30

Changing the lateral viscosity controls the width of the regions of northward and southward flow that develop in order to produce the balance of potential vorticity at the steady state. (Development of these regions is described in section 3.2.2). The limiting width of these regions affects the propagation of planetary waves from the eastern boundary. With higher viscosities only a boundary current and a weak counter current develop, whilst with the lower viscosities a whole series of northward and southward flows develop associated with short planetary wave motion.

Close to the equator the flows with the lower viscosities are much stronger but at higher latitudes the currents produced are approximately equal $\sim 0.70ms^{-1}$. The maximum north-south pressure gradient across the boundary current is also unaffected by the value of A_H and in the region of -24m using the parameters of the initial experiment (section 3.2).

The changes in A_H do not effect the Poincare waves significantly and the amplitude of the initial coastal Kelvin wave remains the same throughout the experiments. The higher viscosities shorten the time taken to reach a steady state since they damp out the high frequency oscillations and the planetary waves.

3.3.7 Summary

The relaxation forcing condition produces and maintains a north-south difference in height. However, to produce a 60m pressure difference across the western boundary layer would require a pressure difference greater than 60m between the northern and southern forcing regions to be maintained. In the linear model it is this pressure gradient occurring across the boundary layer that controls the transport in the western boundary current.

The most practical boundary condition to use at the south of the channel is the relaxation condition used in the initial experiment. Implementation is straightforward and the boundary condition copes well with both wave motions and the resultant western boundary current.

Experiments with the lateral boundary conditions have shown that when lateral friction is the dominant mechanism for the decay of small scale energy the main difference between the no slip and free slip boundary conditions is the width of the western boundary layer.

The baroclinic model has reproduced the Munk type solution at the western boundary for a range of lateral viscosities.

3.4 THE LINEAR TWO LAYER MODEL

3.4.1 Introduction

The main difference between the two layer model and the baroclinic model is the inclusion of the free surface in the two layer model. A shorter timestep is required to resolve the faster ($\sim 120 \mathrm{ms}^{-1}$) surface mode. Introducing the free surface means that the north-south difference in sea surface elevation determined by Wyrtki (1987) can now be forced directly. To maintain the surface elevation in the northern forcing region requires a much faster relaxation rate than in the baroclinic model. Thus a barotropic relaxation rate α_1, is introduced. α_1 is set to (6 minutes)$^{-1}$ and α_2 is set to (30 minutes)$^{-1}$. In the northern forcing region the surface is forced to 20cm on a timescale of α_1. The surface and interface should come to hydrostatic equilibrium at steady state. In the southern forcing region the surface and interface are forced on timescales of α_1 and α_2 respectively to their unperturbed state. The two timescales are required to selectively remove the barotropic and baroclinic modes without reflection.

It was found that the linear two layer model produced numerical instabilities, which originated in the surface mode, for horizontal viscosities of less than 500m^{2}s^{-1}. Using a value of 500m^{2}s^{-1} the model was not stable beyond 100 days of integration. With higher viscosities the steady state was attained. The channel dimensions are identical to the initial experiment. The grid spacing is 20km and the timestep is 50 seconds. Experiments investigating the transient motions are carried out using a horizontal viscosity of 500m^{2}s^{-1} whilst in determining the steady state solution the higher value of 5000m^{2}s^{-1} is used.

3.4.2 Spin up of two layer linear model

There are two phases to the transitory motions, the very rapid passing of the surface mode (~5 hours) and the slow development of the baroclinic (internal) disturbance similar to that described in section 3.2.

Figures 3.4.1. and 3.4.2. show the instantaneous fields after 5 and 10 days respectively. After 5 days the baroclinic part of the adjustment can clearly be seen. The fields north of 5°S are similar to those of figure 3.2.1.a). To the south a western boundary layer has been formed by the rapid adjustment process of the surface mode. Currents in this boundary layer are equal both in magnitude (0.1ms^{-1}) anddirection (southwards) in the two layers.

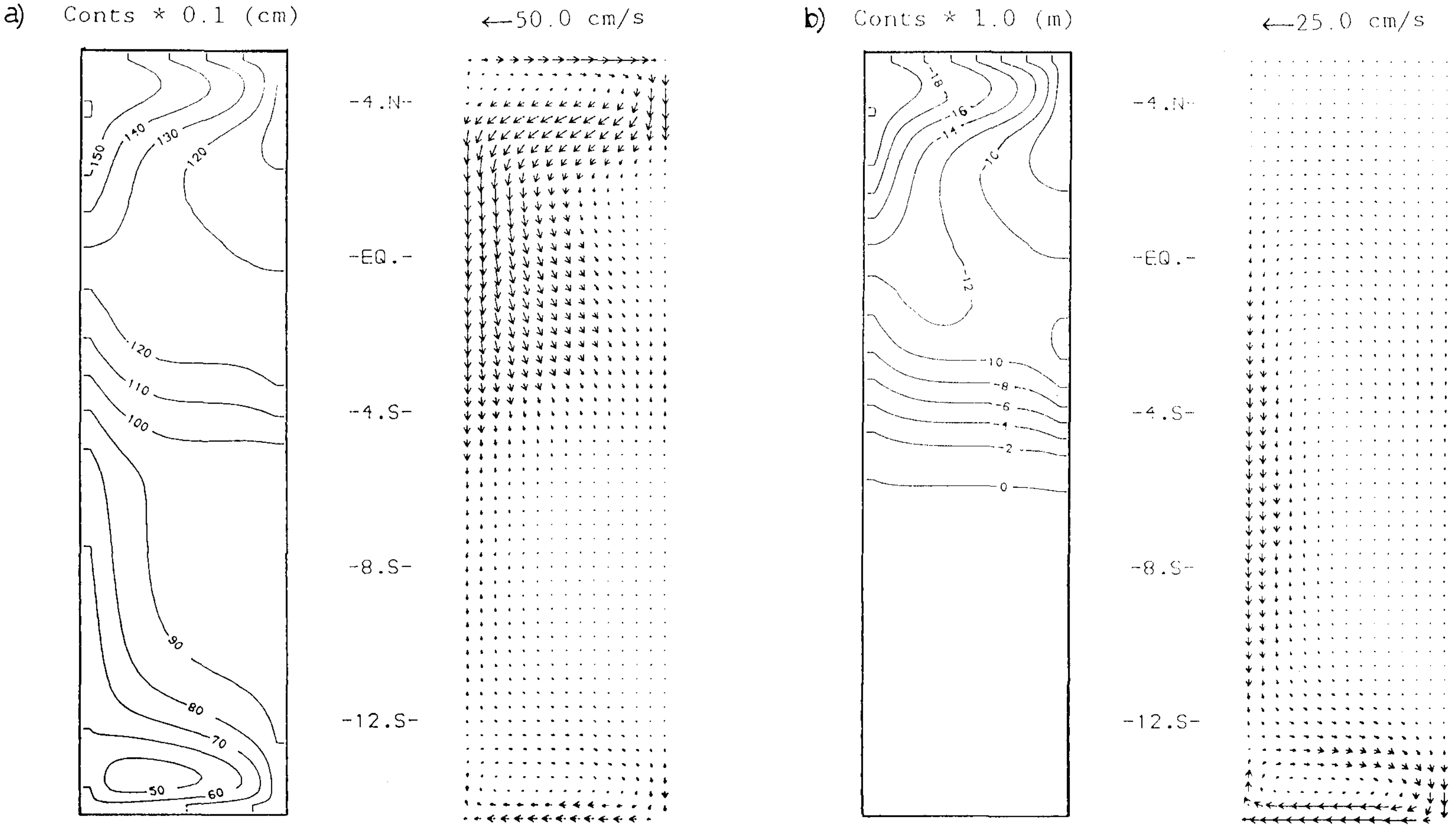

Figure 3.4.1 : Two Layer Linear Model, $A_H = 500m^2s^1$. Fields after 5 days a) Surface Elevation and Upper Layer Velocity, b) Interface Perturbation and Lower Layer Velocity.

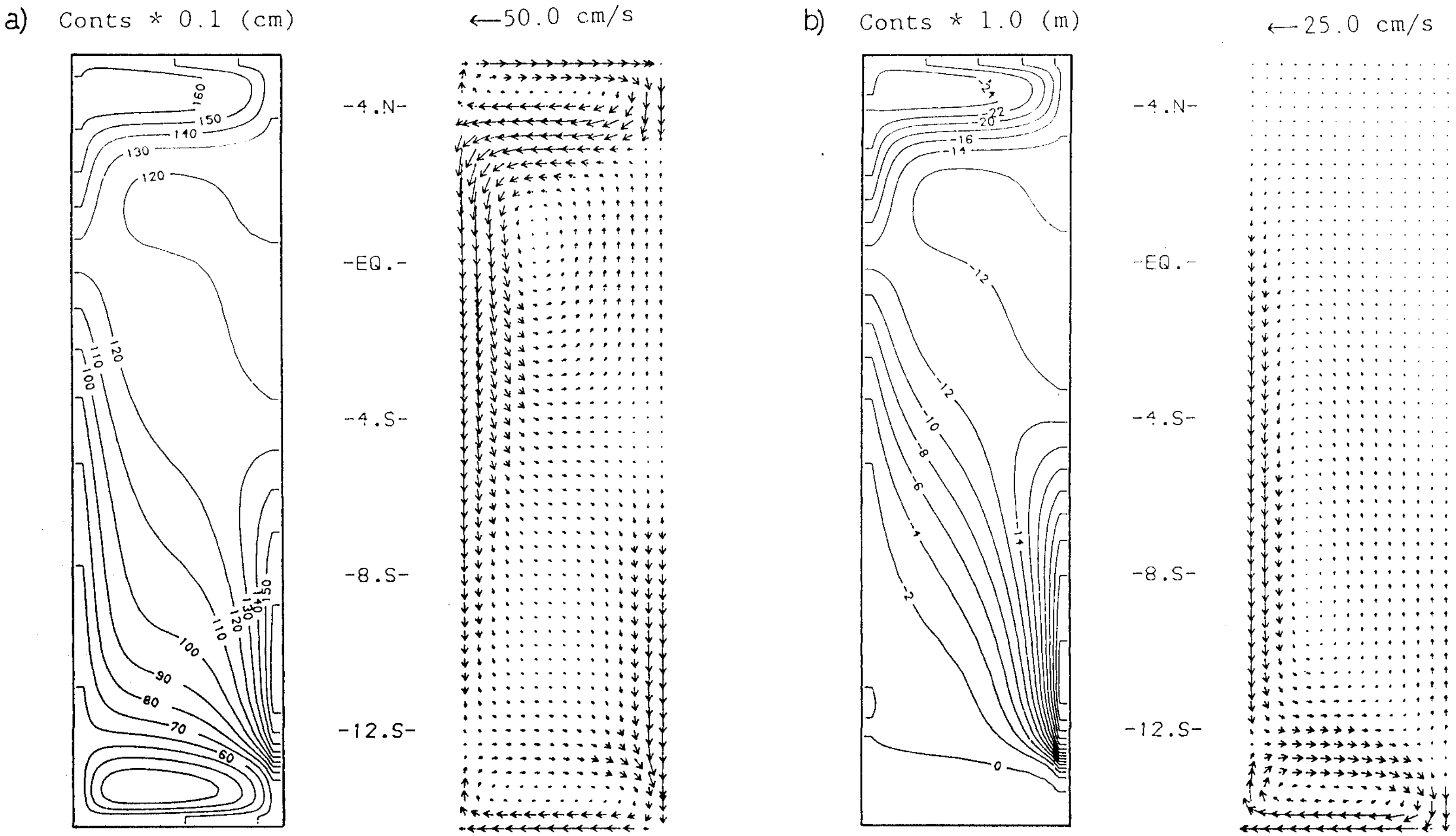

Figure 3.4.2 : Two Layer Linear Model, $A_H = 500m^2s^{-1}$, Fields after 10 days a) Surface Elevation and Upper Layer Velocity, b) Interface Perturbation and Lower Layer Velocity.

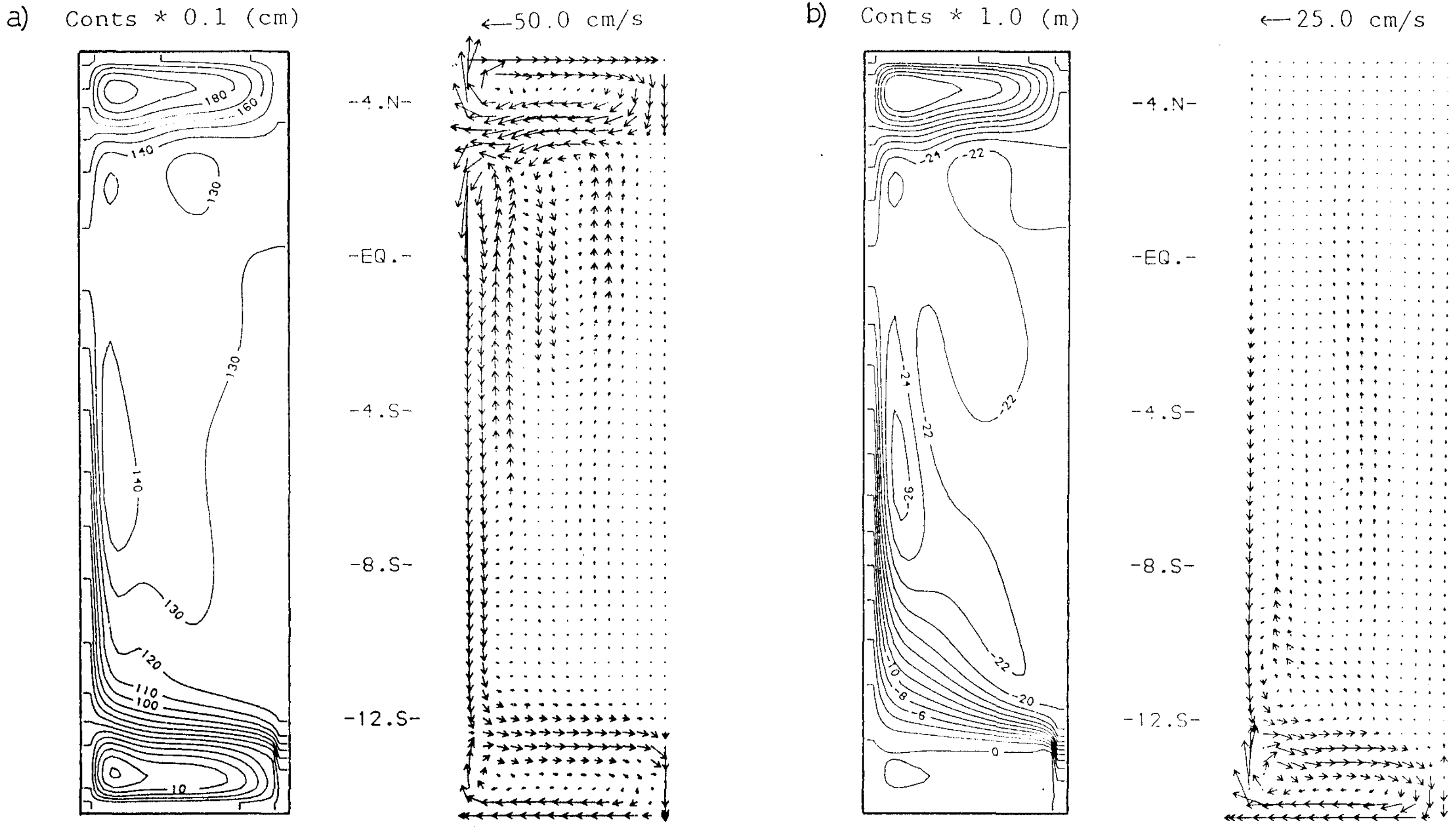

Figure 3.4.3 : Two Layer Linear Model, $A_H = 500m^2s^{-1}$, Fields after 50 days a) Surface Elevation and Upper Layer Velocity, b) Interface Perturbation and Lower Layer Velocity.

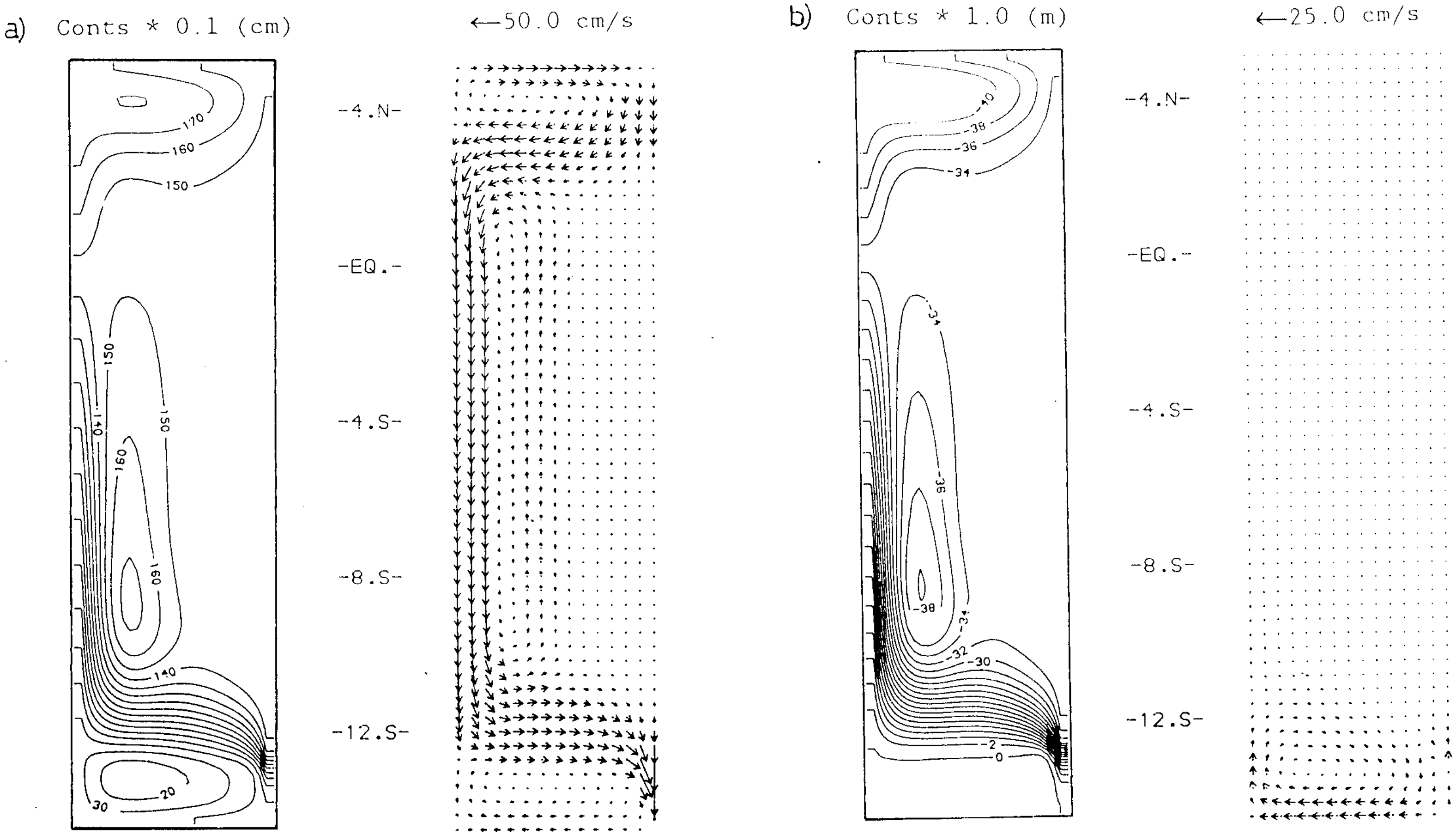

Figure 3.4.4 : Two Layer Linear Model, $A_H = 5000 m^2 s^{-1}$, Fields after 100 days, a) Surface Elevation and Upper Layer Velocity, b) Interface perturbation and Lower Layer Velocity.

After 10 days the baroclinic coastal Kelvin wave has reached the southern end of the channel and the equatorial planetary wave motions are evident. The baroclinic coastal Kelvin wave behaves in the same way as in the baroclinic model, with decay scale decreasing away from the equator. It is also apparent that the surface and interface are not in hydrostatic equilibrium at this time.

Figure 3.4.3. shows the fields after 50 days, comparison with figure 3.2.1.e) shows that the upper layer velocity field is similar to that in the baroclinic model. However in the lower layer the velocities are in the same direction as those in the upper layer and considerably stronger in the south of the channel than in the north. In the upper layer the enforced north-south pressure gradient of 20cm produces an actual difference of 14cm between the forcing regions.

When a horizontal viscosity of $5000 m^2 s^{-1}$ is used, (figure 3.4.4) the velocities in the lower layer are negligible and the upper layer velocities are the steady state Munk type solution. The surface and interface are close to the hydrostatic equilibrium. The width of the western boundary current (150km) and the ratio of the western boundary current to the counter current (18%) are the same as those of the linear baroclinic model with $A_H = 5000 m^2 s^{-1}$.

3.4.3 Balance of terms in energy equations

In this section the energetics as described in section 2.5.2 and the equations in Appendix B are used to compare the rates of conversion of energy in the two linear models.

Figures 3.4.5.a) - d) show the energetics for the complete integration of the linear baroclinic model described in section 3.2. At time zero the channel is at rest, the interface horizontal, the forcing commences and the adjustment process begins.

Initially the forcing in the north puts in 5.0×10^{-4} Wm^{-2} (figure 3.4.5.b)) directly into the potential energy. This energy is transferred to kinetic energy (figures 3.4.5.c) and d) and lost to horizontal dissipation. The forcing region in the south also removes

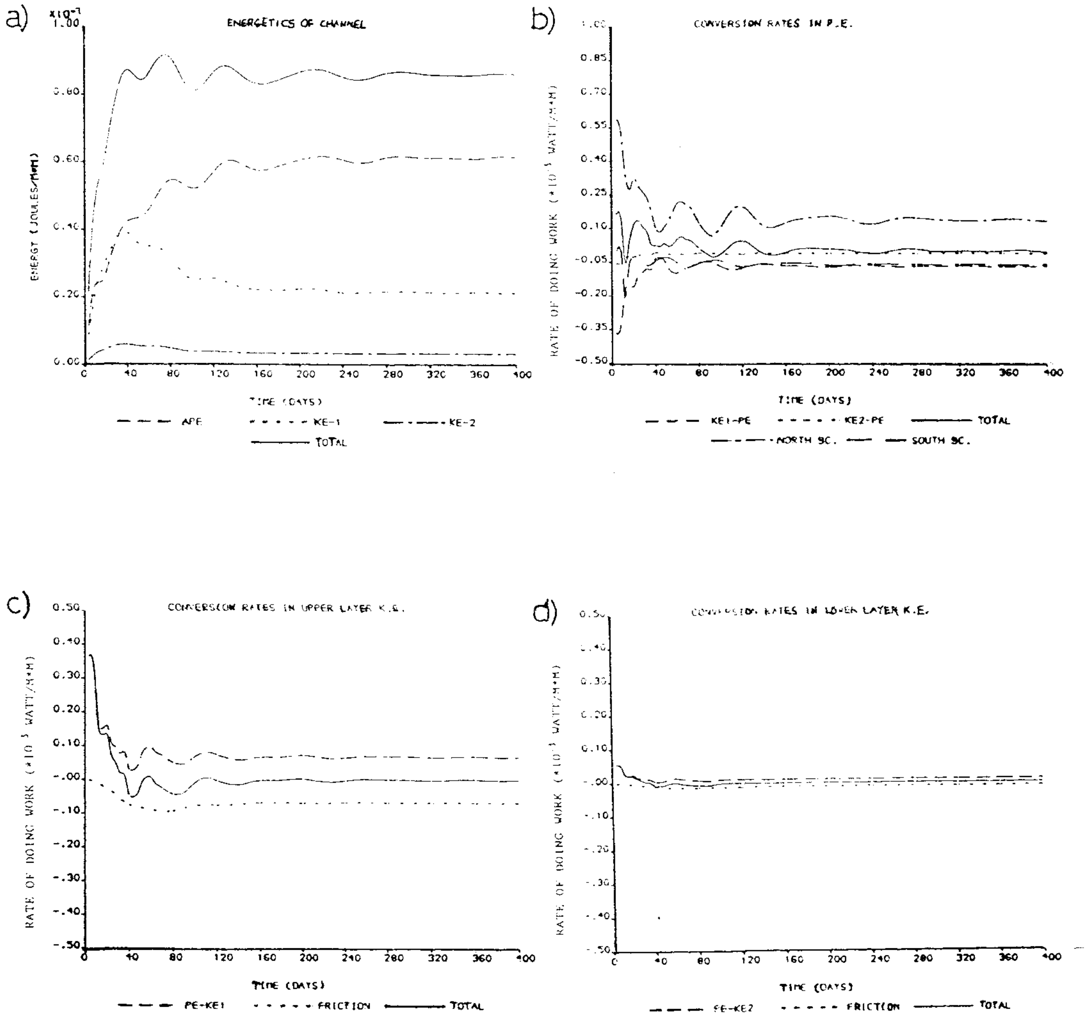

Figure 3.4.5 : Energy Budget for 400 day Integration of Linear Baroclinic Model a) Total Energy Budget, b), c) and d) Conversion Rates of Potential Energy and Upper and Lower Layer Kinetic Energy.

potential energy directly. The kinetic energy reaches a maximum after 40 days (figure 3.4.5.a) when the planetary wave action is strongest (see also figures 3.2.1.c) - f) . Thereafter the kinetic energy decreases and in the final steady state is associated with the western boundary region and the circulation in the two forcing regions. The oscillations in the total energy seen in figure 3.4.5.a) are due to oscillations in the input of potential energy in the northern forcing region, figure 3.4.5.b). These oscillations are due to feedback in interface perturbations in the northern forcing region caused by the wave motions present. The energetic properties of the steady state are summarised in table 3.4.1.

The energetics of the linear two layer model are not sufficiently different from the linear baroclinic model to merit figures showing the individual terms. Energy enters as surface potential energy in the northern forcing region. This energy can only be converted into kinetic energy in the two layers. The potential energy of the interface comes from the conversion of lower layer kinetic energy. The total energy is due almost entirely to the interface perturbation. The hydrostatic balance gives the surface potential energy to be 0.3% (g'/g) of the interface potential energy at steady state. Horizontal dissipation and the southern forcing region remove kinetic and potential energy respectively from both layers. The conversion rates of the linear two layer model with values of horizontal viscosity of $500m^2s^{-1}$ and $5000m^2s^{-1}$ after 100 days are summarized in table 3.4.2.

In table 3.4.2 the rates of input and output of energy in the linear two-layer model do not sum to zero shows that the steady state has not been attained after 100 days (within 5% of steady state).

TABLE 3.4.1 **Energy balance at steady state ***

Energy ($\times 10^{-3}Jm^{-2}$)

	P.E.		K.E.		TOTAL
baroclinic model	(PE)		(KE_1)	(KE_2)	
A_H=100m^{2}s^{-1}	61.5		21.5	3.5	86.5
two layer model	(PE_1)	(PE_2)	(KE_1)	(KE_2)	
A_H = 500m^{2}s^{-1}	1	89	56	14	160
A_H = 5000m^{2}s^{-1}	1	123	30	2	156

TABLE 3.4.2 **Rates of conversion of energy at steady state ***

Rates of Conversion of Energy (x10 Wm^{-2})

	INPUT			OUTPUT		CONVERSION		
	north	south		dissipation		potential-Kinetic		
baroclinic model	(PE)	(PE)		(F_1)	(F_2)	(PE-KE_1)	(PE-KE_2)	
A_H=100m^{2}s^{-1}	+14	-6		-7	-1	+7	+1	
two layer model	(PE_1)	(PE_1)	(PE_2)	(F_1)	(F_2)	(PE_1 -KE_1)	(PE_1 -KE_2)	(PE_2 -KE_2)
A_H = 500m^{2}s^{-1}	+68	-16	-9	-32	-4	+32	+20	-13
A_H = 5000m^{2}s^{-1}	+88	-18	-13	-48	-4	+48	+22	-17

* within 5% in two layer case.

The total energy of the two layer model is greater than that of the baroclinic model because of the difference between the enforced north-south sea level difference which was 20cm for the two layer models and the equivalent of 10cm for the baroclinic model.

3.4.4 Balance of terms in the momentum equations

Figure 3.4.6 shows the spatial distribution of the terms that make up the momentum balances after 10 days in the two layer linear model with a horizontal viscosity of $5000 m^2 s^{-1}$. The region displayed is that part of the channel between 2°N and 12°S avoiding the forcing regions. The momentum balances in the forcing regions are in geostrophic balance (section 3.2).

The zonal momentum is a geostrophic balance (ie. balance between the pressure term and the Coriolis term). At the Western boundary the barotropic adjustment shows up clearly, having produced a southward current where the terms in the balance are of the same sign in the two layers. At the eastern boundary the baroclinic Kelvin wave shows terms of opposite sign in the two layers.

The meridional momentum balance is more complicated. In the interior the balance is approximately geostrophic in both layers (opposite sign in the two layers). At the eastern and western boundaries the viscous terms become important.

After 100 days, with the fields close to steady state the velocities in the lower layer decrease and become negligible. Figure 3.4.7. shows that the zonal momentum remains in geostrophic balance, except at the equator where pressure term is zero. The meridional momentum balance is between the pressure and viscous terms on the western and eastern boundaries, again at the equator the meridional pressure term is zero. The steady state balances in the momentum equations of the linear baroclinic model are the same as those for the linear two layer model, with the exception that velocities in the lower layer are not negligible, but smaller and in opposite direction to those in the upper layer.

3.4.5 Balance of terms in the vorticity equation

The theory described in section 2.5.3 and the equations in Appendix C are now used to determine the balance of terms in the depth averaged vorticity equation of the linear two layer model.

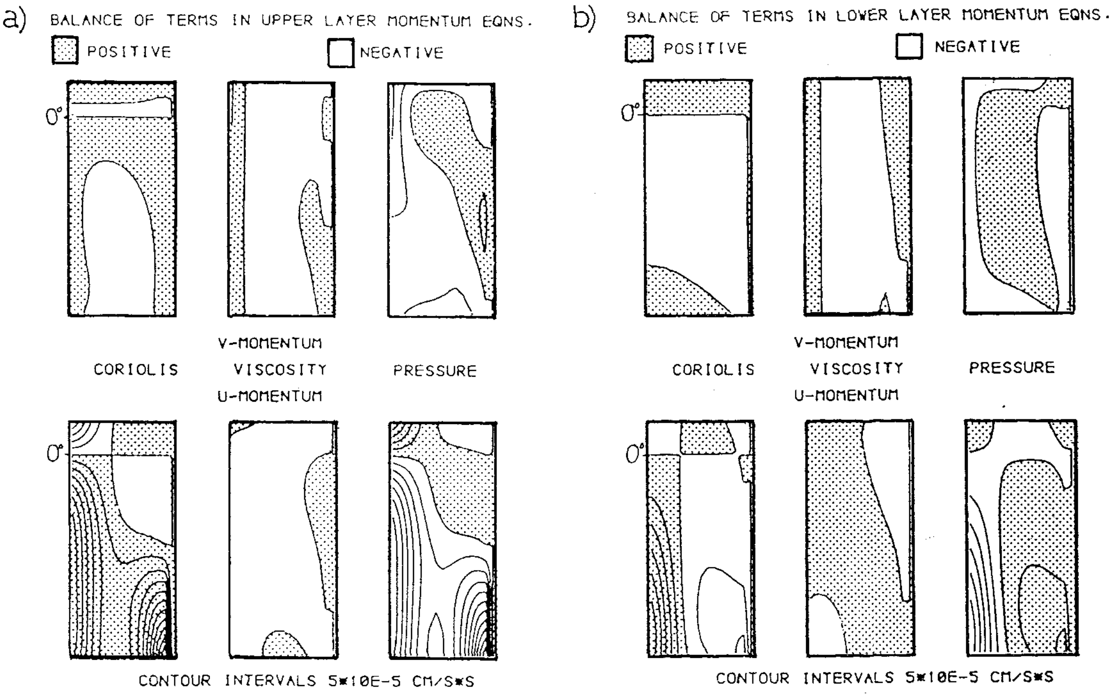

Figure 3.4.6 : Balance of terms in Momentum Equation of Two Layer Linear Model, $A_H = 5000 m^2 s^{-1}$, Fields after 10 days, a) Upper Layer, b) Lower Layer.

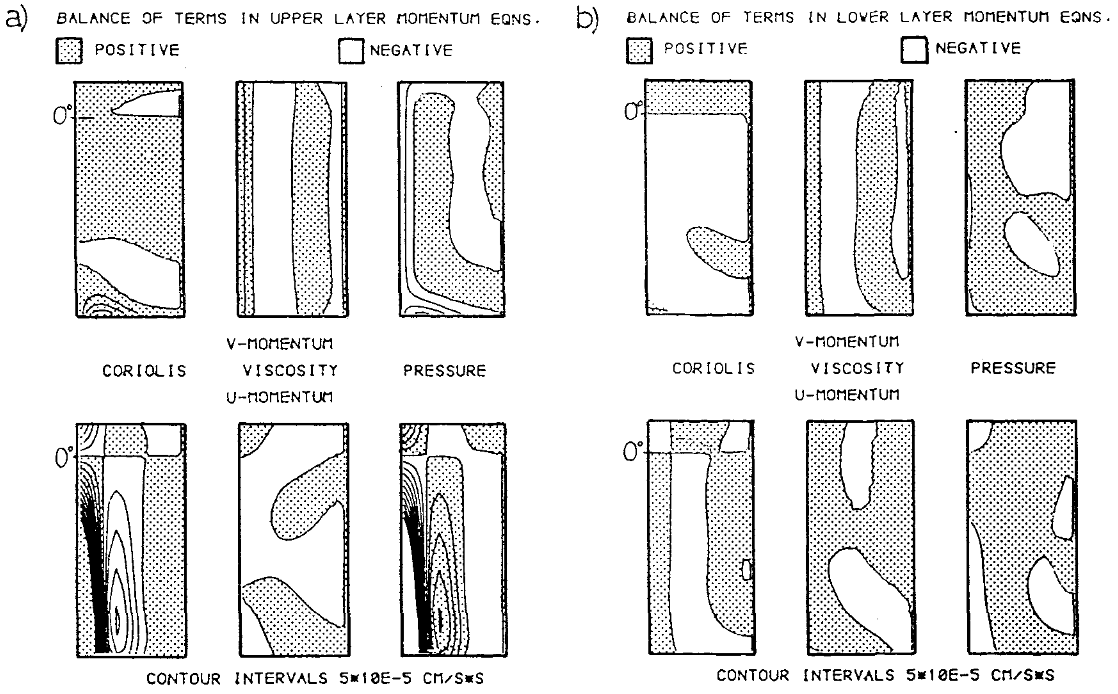

Figure 3.4.7 : Balance of terms in Momentum Equation of Two Layer Linear Model, $A_H = 5000 m^2 s^{-1}$, Fields after 100 days a) Upper Layer b) Lower Layer.

The spatial distribution of the terms in the vorticity equation after 10 days are shown in figure 3.4.8. Similar to the balance of terms in the momentum equations the fields show the initial barotropic western boundary current (signs the same in both layers) and the baroclinic Kelvin wave (signs opposite in the two layers). The planetary vorticity dominates initially. At the western boundary vorticity is removed by dissipation due to the viscosity. The viscous boundary layer width is 150km whilst the planetary vorticity boundary layer width in 180km.

After 100 days, figure 3.4.9. the steady state is almost attained (within 5%), the total rate of change of vorticity in the two layers being equal and opposite. The width of the planetary vorticity boundary layer has decreased to that of the viscous boundary layer (150km). The balance is that of the Munk solution, with planetary vorticity being lost to viscous dissipation. The region of the counter current is shown clearly and is required to conserve potential vorticity in the boundary region. The maximum rate of viscous dissipation of the vorticity is - 2.84 x 10^{-9} ms^{-2}.

As with the momentum balance, the terms in the lower layer are very much smaller than in the upper layer. However the magnitude of the total balance for each layer is comparable.

It should be noted that with the no slip boundary condition the individual terms in the balance at the boundaries must be zero at the boundaries and thus the planetary term must vanish at all boundaries. At steady state this forces the viscous term to be zero at the boundary to complete the balance. However for the free slip conditions (the case presented) the major terms in the balance assume maximum values at the boundary.

3.4.6 Transport through the channel

In this section the flow through the channel will be discussed and a simple theory based on the geostrophic balance in the western boundary layer developed.

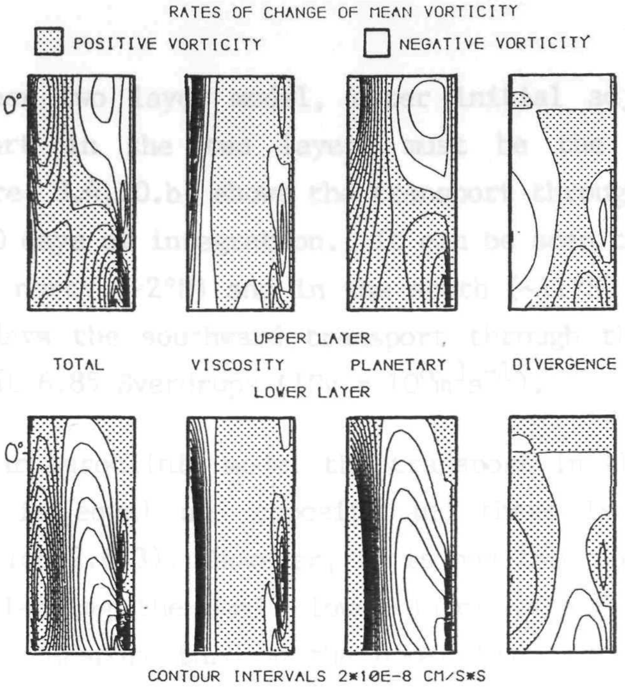

Figure 3.4.8 : Balance of terms in Vorticity Equation of Two Layer Linear Model, $A_H = 5000m^2s^{-1}$, Fields after 10 days

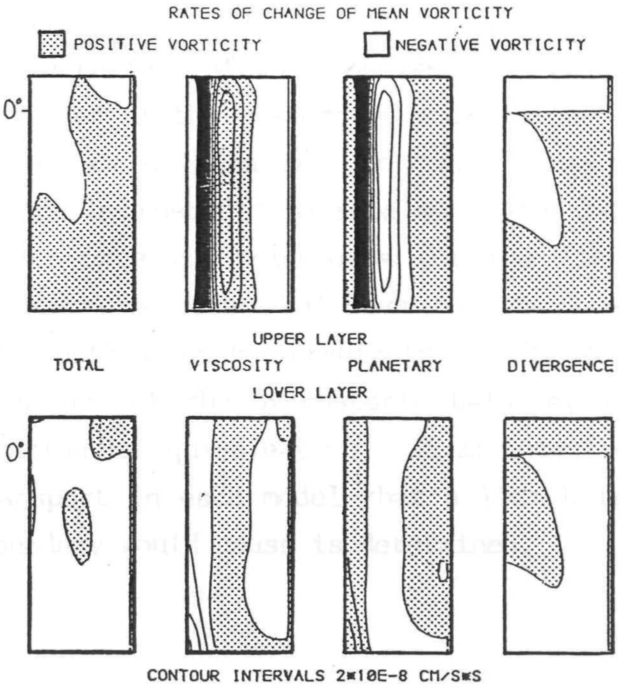

Figure 3.4.9 : Balance of Terms in Vorticity Equation of Two Layer Linear Model, $A_H = 5000m^2s^{-1}$. Fields after 100 days.

In the linear two layer model, after initial adjustment, the combined transport in the two layers must be the same at all latitudes. Figure 3.4.10.b) shows the transport through the channel for the first 100 days of integration. It can be seen that the total transport in the north (~2°N) and in the south (~11°S) is equal and that after 100 days the southward transport through the channel is almost constant at 6.85 Sverdrups (1Sv = $10^6 m^3 s^{-1}$).

In the linear baroclinic model the transport in the two layers at any latitude is equal and opposite and there is thus no net throughflow (section 2.6.3). However, it is possible to estimate the transport by neglecting the small lower layer velocities. At the steady state the transport through the upper layer at all latitudes should be equal. For the preliminary experiment this estimate of the throughflow is shown in figure 3.4.10.a). After 400 days a steady state has been attained and the southward transport in the upper layer is 2.63Sv.

In order to compare the transports between different integrations of the same model and between the two models it is necessary to compare the pressure gradients that caused the transport. For integrations of the same model scaling by the north-south pressure gradient at the western boundary between 3°N and 12°S allows direct comparison of results. To compare the baroclinic and two layer models the hydrostatic balance must also be used. Table 3.4.3 shows the steady state transports for the linear baroclinic model, and the transports after 100 days for the linear two layer model. The north-south pressure gradients at the western boundary are given. Making use of the hydrostatic balance, in this case a 10cm surface elevation is equivalent to a 28.2m interface depression, the effective transport in each model that a 10cm height difference at the western boundary would cause is determined.

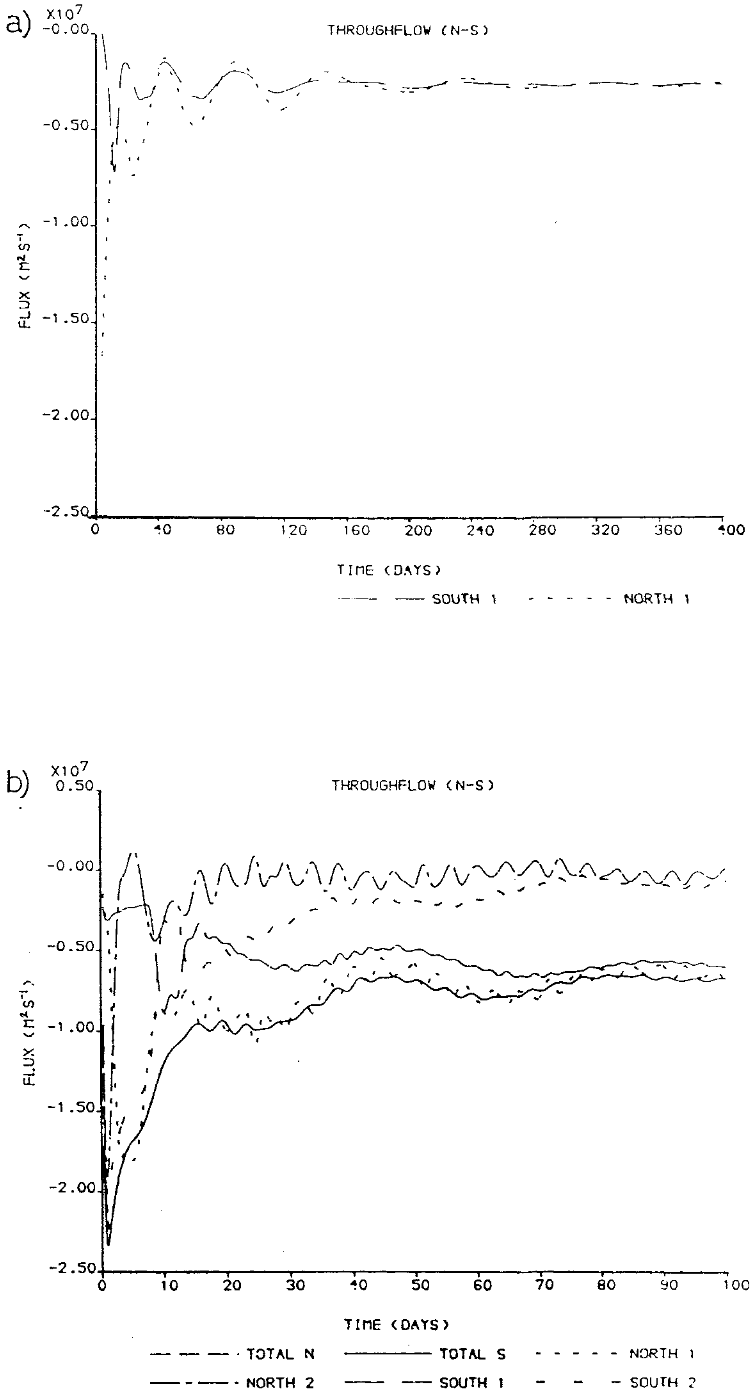

Figure 3.4.10 : Transport through Channel (Positive Northwards)
a) Linear Baroclinic Model, $A_H = 100m^2s^{-1}$ 400 days of integration,
b) Two Layer Linear Model, $A_H = 500m^2s^{-1}$, 100 days of integration.

TABLE 3.4.3 **Summary of Transport in the Linear Models**

	Transport (Sv)	3°N-12°S Pressure Difference (m)	10cm N-S gradient. Effective Transport (Sv)
Baroclinic Model		(interface)	
$A_H = 100 m^2 s^{-1}$ (freeslip)	2.63	11.0	6.7
$= 500 m^2 s^{-1}$ "	3.25	17.5	5.2
$= 5000 m^2 s^{-1}$ "	4.38	24.0	5.1
$= 100 m^2 s^{-1}$ (no slip)	2.63	11.0	6.7
Two Layer Model		(surface)	
$A_H = 500 m^2 s^{-1}$ (freeslip)	6.85	0.11	6.2
$= 5000 m^2 s^{-1}$ "	8.65	0.135	6.4

Table 3.4.3 gives a mean transport of 5.7Sv for the linear baroclinic model when the equivalent of a 10cm height difference occurs between 3°N and 12°S. In the linear two layer model this transport is greater, 6.3Sv.

The enforced height difference between the forcing regions in all the baroclinic models was -30m and in both the two layer models was 20cm. The effect of the horizontal viscosity in the channel is to control the north-south extent of the circulation in the forcing regions, this then affects the pressure gradient that forms between the two forcing regions. For the higher viscosities the circulation associated with the forcing regions extends south of 3°N and north of 12°S.

As first noted in section 3.2.2 and as clearly shown in figure 3.4.7.a) at steady state the meridional velocity at the western boundary is in geostrophic balance. It is thus possible to estimate the southward transport through the channel from the u-momentum equations.

$$fv = g'\frac{h}{x} \quad \text{and } fv = g\frac{\eta}{x} \qquad (3.4.6.1)$$

integrating across the channel to determine the transport gives

$$\text{transport} = \frac{g'}{f}\,\Delta h\,\frac{H_1H_2}{H_1+H_2} \text{ and } = \frac{g}{f}\,\Delta\eta H_1 \qquad (3.4.6.2)$$

respectively for the baroclinic and two layer model. It can be seen that for the equivalent of a zonal pressure gradient of 10cm at 12°S the transports estimated from equation 3.4.6.2 are 5.5Sv and 6.5Sv respectively for the baroclinic and two layer models. These values are in good agreement with the mean transports determined from table 3.4.3.

It is now possible to use Wyrtki's (1987) value of 16cm for the mean sea level difference between the Phillipines and the Indian Ocean south of Java to estimate the throughflow. The important sea level difference is that across the current in the south. Thus the sea level difference between New Guinea and the Indian Ocean south of Java is required to estimate the throughflow. However after passage of the initial Kelvin wave the sea level along the eastern boundary remains approximately level and the value of 16cm can be used. if the east-west pressure gradient is taken to occur at 10°S and with transport in the upper 200m only a value of 12.6Sv is obtained for the Pacific to Indian Ocean throughflow.

3.4.7 SUMMARY

Results from the linear two layer model show good agreement with the theory of section 1.5 and the results of the linear baroclinic model. It is necessary to use high horizontal viscosities ($A_H >$ $500m^2s^{-1}$) for stable integration. The initial rapid barotropic adjustment due to the free surface in the two layer model does not affect the steady state solution. Velocities in the lower layer at steady state are negligible.

The energy budget shows a conversion of potential energy from the northern forcing region into kinetic energy within the two layers. Some lower layer kinetic energy is converted into potential energy of the interface. Kinetic energy is lost to friction and the southern forcing region removes potential energy.

The vorticity balances of the linear models have been investigated and are found to be that of the Munk solution in the western boundary layer. Planetary vorticity being balanced by viscous dissipation in the western boundary current and a weak counter current.

The momentum balances show that the steady state is dominated by the geostrophic balance of the meridional velocity in the upper layer. It is possible to calculate transport through the channel based on this balance.

The similarity between the results of the linear baroclinic and linear two layer models suggest that there is little to be gained from experimenting with the computationally slower two layer model except where it is necessary to include the free surface when topography is included (eg. sills and shelves).

3.5 THE NON LINEAR BAROCLINIC MODEL

3.5.1 Introduction

The only difference between the nonlinear and linear baroclinic models are the inclusion of the advective terms in the momentum equations and the layer thickness which includes the perturbation of the interface in the continuity equation. In this section the results of the nonlinear baroclinic flux model developed in section 2.2.5 are presented and compared with the results of the linear baroclinic model.

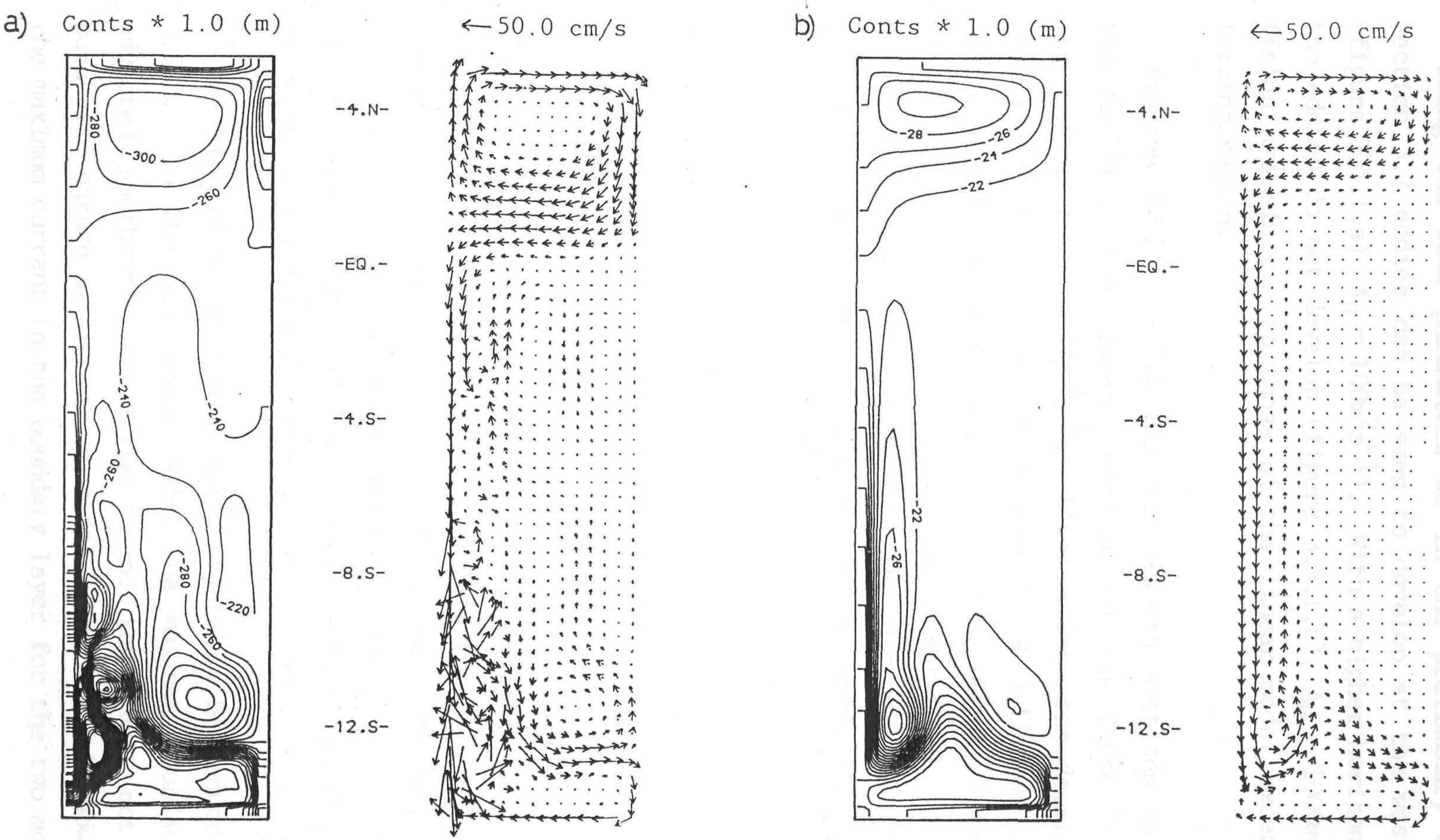

Figure 3.5.1 : Non Linear Baroclinic Model. Fields after 50 days, Interface Perturbation and Upper Layer Velocity a) $A_H = 100 m^2 s^{-1}$, b) $A_H = 1000 m^2 s^{-1}$.

3.5.2 RESULTS

Using the same parameters as in the preliminary experiment of section 3.2 eddies can be seen to develop at the western boundary (figure 3.5.1.a) $A_H = 100m^2s^{-1}$). With a higher horizontal viscosity the eddies do not develop (figure 3.5.1.b), $A_H = 1000m^2s^{-1}$) and the fields are similar to those of the linear model except within the forcing region.

Figures 3.5.2 - 3.5.4 show north-south sections in time through the fields at the western boundary for the first 50 days of the integration with $A_H=100m^2s^{-1}$. After 5 days the development of the western boundary current can be seen to be different and more rapid in the non linear model (figure 3.5.2.b). After 20 days eddies can be seen to develop at $\sim$6°S in the nonlinear model. The development of the eddies is associated with the narrowing of the region of southward flow at the western boundary southwards from the equator.

With the simple relaxation boundary condition at the south of the channel there is some reflection of the eddies as they enter the region. This reflection shows most clearly in the interface perturbation (figure 3.5.4.b)). The incident eddies partially reflect out the speed of the baroclinic coastal Kelvin wave. The reflection effects are small but show that the simple relaxation boundary condition does not work adequately when non linear effects are important. Possibilities for overcoming this effect are 1) the use of a well designed radiative boundary condition, 2) neglect of the non linear terms into the boundary region, 3) increasing the size of the region over which the damping occurs, or 4) increasing the friction in some manner in the forcing region.

The time of maximum boundary current can be deduced from figure 3.5.2. In the non linear model the maximum boundary current is advected southwards at $0.55ms^{-1}$ and thus does not display the parabolic nature of the linear model. Table 3.5.1 shows the time of the maximum current in the boundary layer for the two models.

3.5.2.

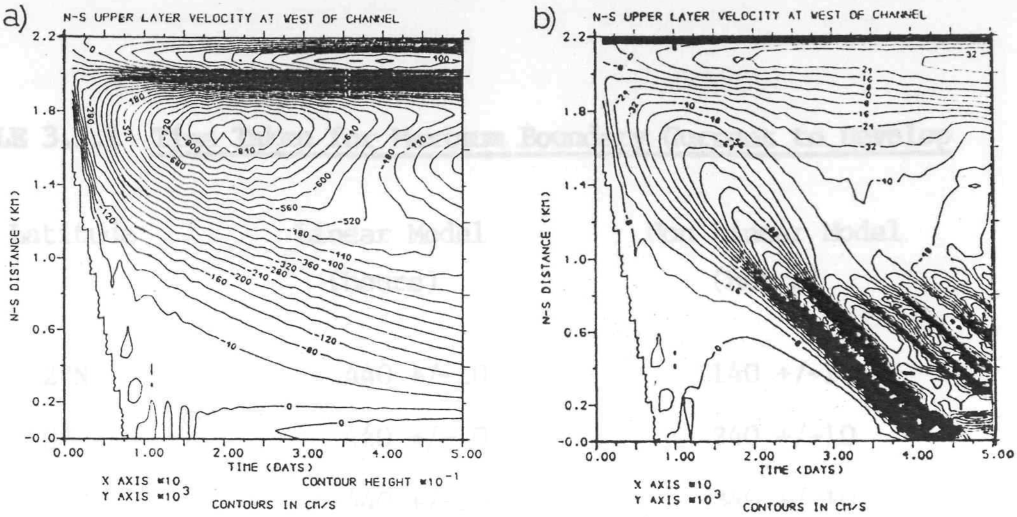

3.5.3.

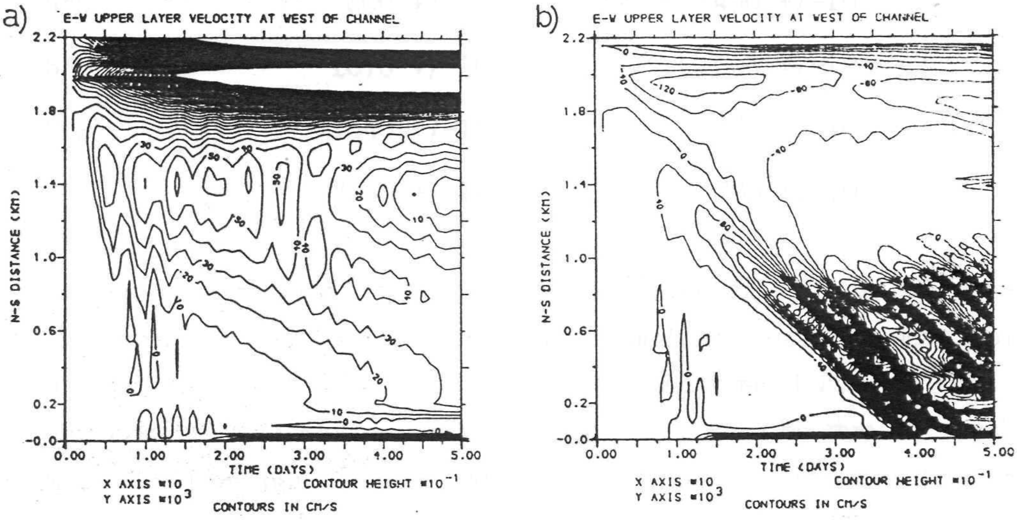

3.5.4.

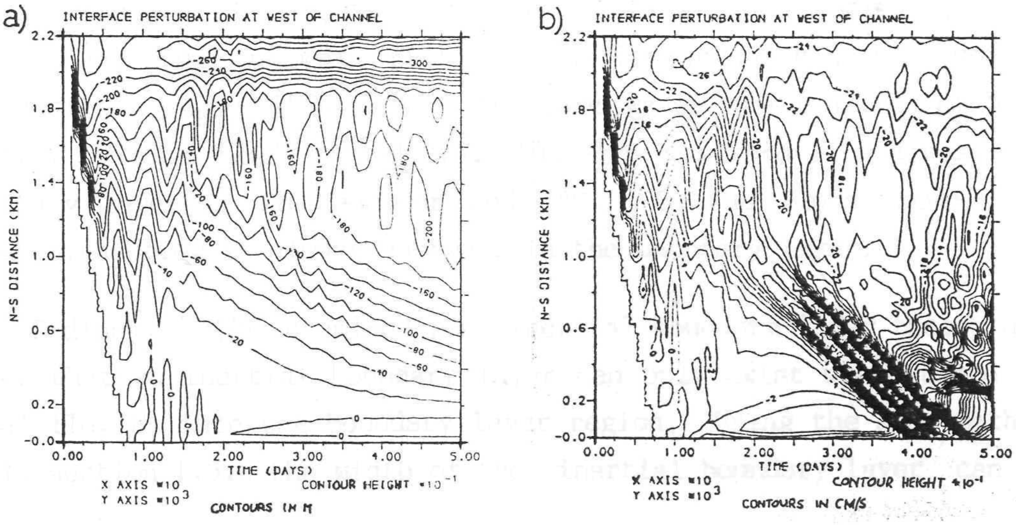

Figures 3.5.2 – 3.5.4 : North-South Sections in time through; (3.5.2), the Meriodional Velocity, (3.5.3), the Zonal Velocity and (3.5.4), the Interface Perturbation. a) The Linear Barolinic model b) The Non Linear Baroclinic Model.

TABLE 3.5.1 **Time Taken for Maximum Boundary Current to Develop**

Latitude	Linear Model (hours)	Non Linear Model (hours)
2°N	440 +/-10	140 +/-10
0°	440 +/-10	240 +/-10
2°S	440 +/-10	340 +/-10
4°S	800 +/-10	450 +/-10
6°S	1070 +/-10	560 +/-10
8°S	1540 +/-10	670 +/-10
10°S	2150 +/-10	780 +/-10

In the linear model the meridional trapping of the planetary waves can clearly be seen with the boundary current developing simultaneously at 2°N and 2°S (see also section 3.2.5). In the nonlinear case the formation is more rapid and must be due to another process. In the non linear model the time of maximum boundary current coincides with the time that the zonal current at the western boundary reverses. Figures 3.5.5 and 3.5.7 show east-west sections through the zonal velocity fields of the linear and nonlinear models respectively ($A_H = 100m^2s^{-1}$). Poincare waves are evident in both models. Figure 3.5.5 b) and 3.5.6.b), show westward flow across the boundary layer at the equator and 2°S. In the linear model, a) figures,the flow is always eastward in the boundary layer.

Pedlosky (1979) examined pure inertial boundary layer theory and shows that an inertial boundary layer can only exist where there is zonal flow U_I into the boundary layer region. Using the same method as in section 1.5.6 the width of the inertial boundary layer can be

3.5.5.

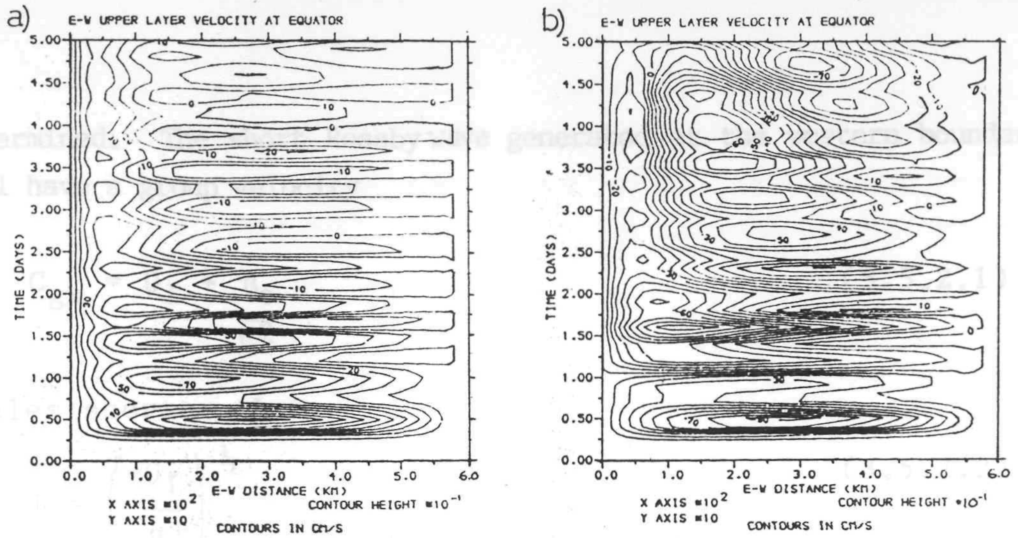

3.5.6.

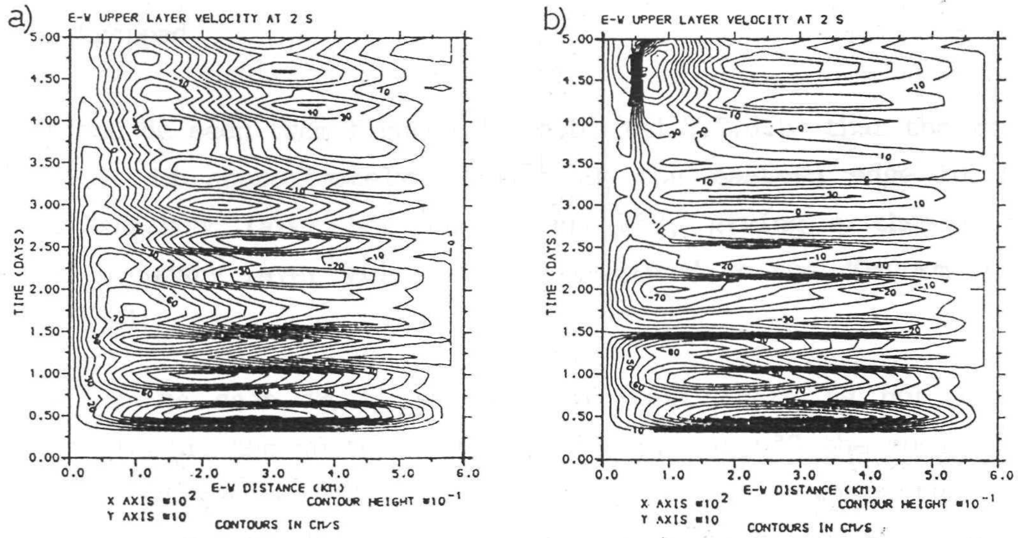

3.5.7.

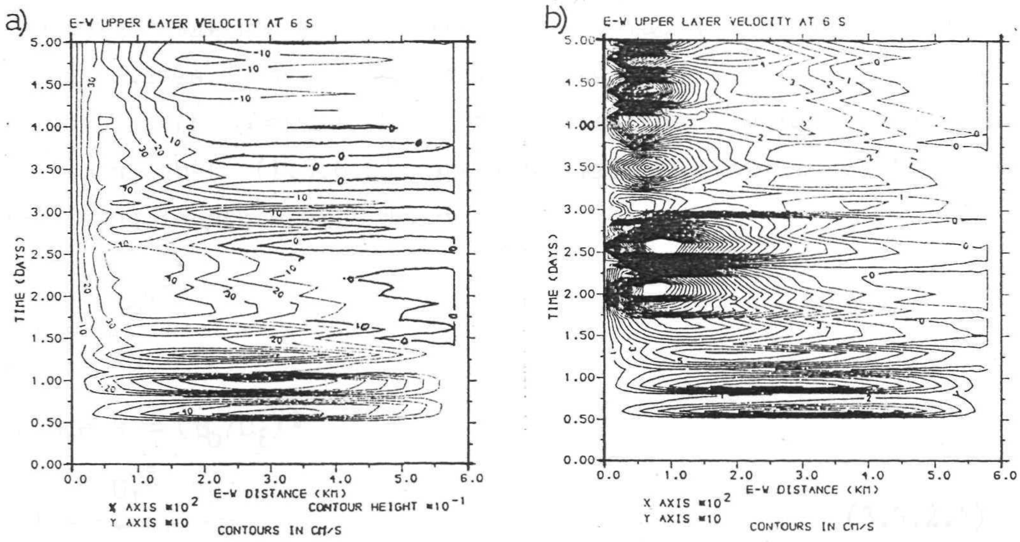

Figures 3.5.5 - 3.5.7 : East - West Sections in time through the Zonal Velocity. (3.5.5) At Equator, (3.5.6) At 2°S and (3.5.7) At 6°S. a) The Linear Baroclinic Model b) The Non Linear Baroclinic Model.

determined. The short Rossby wave generated at the western boundary will have a group velocity

$$C_{gx} = U_I + \frac{\beta_o}{K^2} \qquad (3.5.2.1)$$

scales shorter than

$$1 = \left(\frac{-U_I}{\beta_o}\right)^{\frac{1}{2}} \qquad (3.5.2.2)$$

will be trapped

It can be seen from figures 3.5.5.b) and 3.5.6.b) that the zonal current U_I is approximately -2cms^{-1} at the eastern edge of the western boundary layer between 0° and 2°S, giving a theoretical inertial boundary layer width of 30km compared to the 30–40km shown in the model.

It can be seen in figure 3.5.5.b) that there is not always westward flow at the western boundary layer. At 6°S the zonal flow periodically reverses (30–40 days). In the region where there is flow eastward out of the boundary layer the short waves generated at the western boundary are assisted and radiated towards the interior as Rossby waves. As they radiate they will decay by dissipative processes. If horizontal friction is the dominant dissipative mechanism so that (1.5.6.2) applies the scale over which the Rossby waves of wavelength k will decay is

$$1 = \frac{\beta_o k^{-4}}{A_H}$$

and since $k = (\beta_o/U_I)^{\frac{1}{2}}$

$$1 = \frac{U_I^2}{\beta_o A_H} \qquad (3.5.2.4)$$

Using the value of 2cms^{-1} for U_I a value of 174km is determined for the scale over which the Rossby waves leaving the western boundary decay. This scale is close to the diameter of the observed eddies.

3.5.3 Energy budget and transport

Figures 3.5.8 and 3.5.10 show the energy budget and transport of the channel for values of horizontal viscosity of $100\text{m}^2\text{s}^{-1}$ and $1000\text{m}^2\text{s}^{-1}$ respectively. The higher viscosity case is not significantly different from the linear case. (section 3.4.3). However a comparison of figure 3.5.8.a) and b) (or 3.4.5) shows that the total energy of the nonlinear model with $A_H = 100\text{m}^2\text{s}^{-1}$ is nearly double that of the linear model. The mean potential energy after 200 days in figure 3.5.8.a) (0.07Jm^{-2}) is comparable to the figure given in table 3.4.1 (0.062) for the linear case. The mean total kinetic energy (0.07Jm^{-2}) is three times that of the linear case. The explanation for this increase in kinetic energy is the length scale of the eddies. The average potential energy is proportional to the mean square displacement of the interface whilst the average kinetic energy is proportional to the mean square slope of the interface. If the potential energy of the mean flow (in the linear case) is converted into eddies the mean square displacement of the interface is not significantly changed but the mean square slope is increased if the scale of the eddies is small comparable to the scale of the mean flow (Gill et al, 1974).

In figures 3.5.8 - 3.5.10 and also figures 3.5.2 - 3.5.7 it can be seen that in the first 20 days the nonlinear, effects are not significant, there is little difference between the two experiments. After 20 days concurrent with the generation of eddies at 6°S the kinetic energy increases in the low viscosity case, the potential energy is unaffected. After 100 days a statistically steady state is attained in which eddies (wavelength 400km period 30-40 days) are superimposed on the mean circulation.

The mean transport for the two cases is summarised in table 3.5.2.

3.5.8.

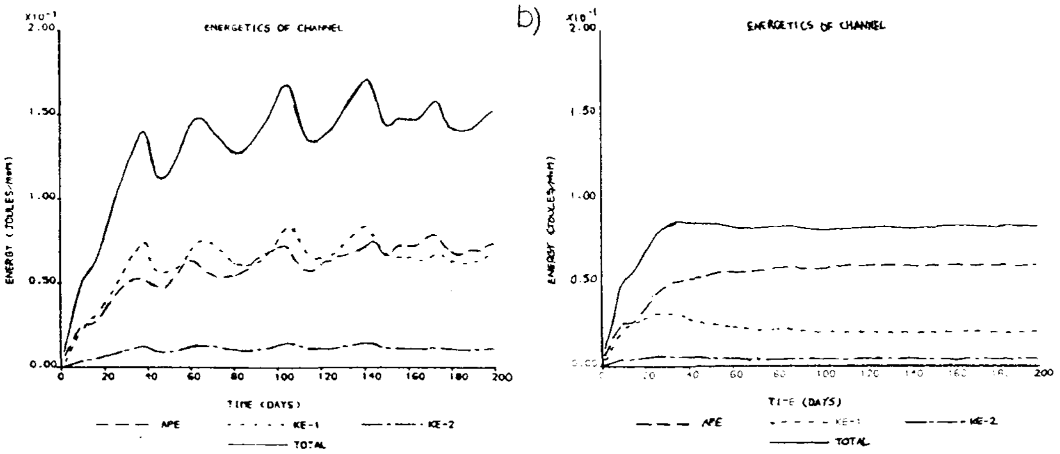
a) b)

3.5.9.

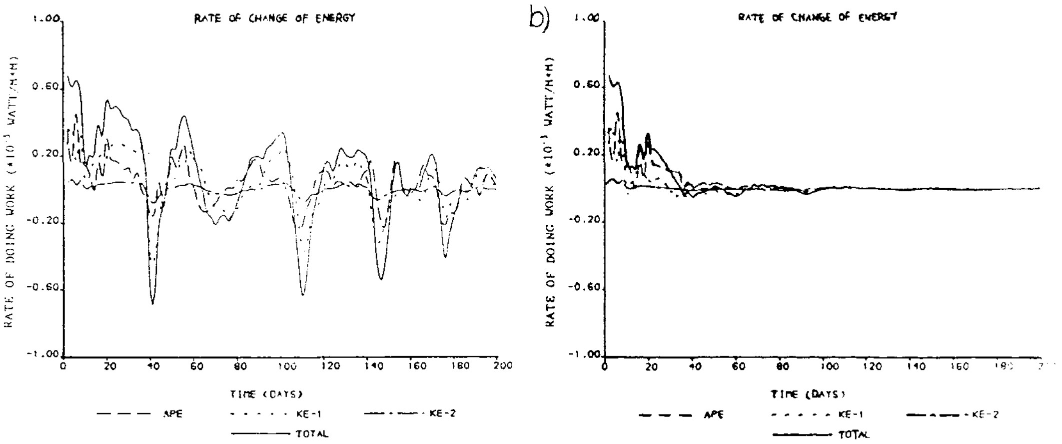
a) b)

3.5.10.

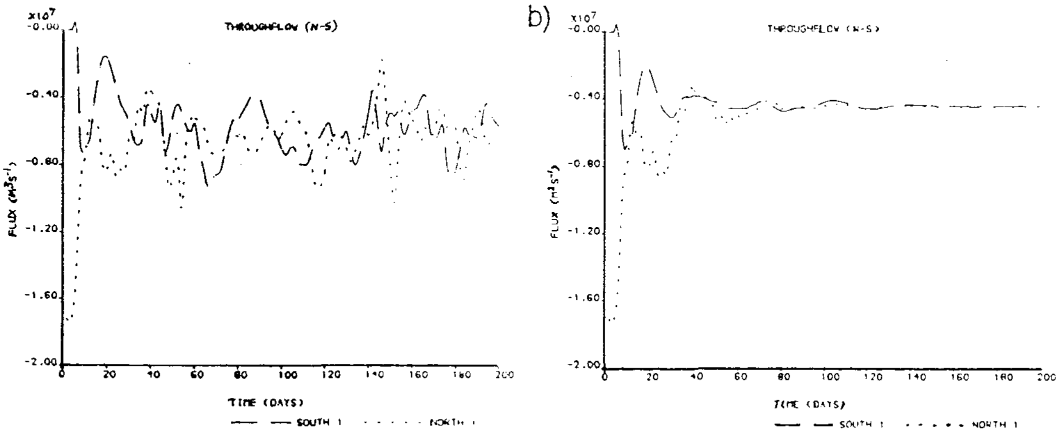
a) b)

Figures 3.5.8 - 3.5.10 : Energy Budget and Transport. (3.5.8) Total Energy Budget (3.5.9) Rate of Change of Energy (3.5.10) Transport through Channel (Positive Northwards) b) The Linear Baroclinic Model a) The Non Linear Baroclinic Model.

TABLE 3.5.2 <u>Steady State Mean Transport through non Linear Model</u>

Model	Transport (Sv)	Interface Gradient (m)	10 cm N-S gradient Effective Transport (Sv)
$A_H = 100 m^2 s^{-1}$	6.00	14.00	12.0
$A_H = 1000 m^2 s^{-1}$	4.40	21.5	5.8

3.5.4 Nature of instability

The eddies that develop must draw their energy from one of two sources. Either from the available potential energy (baroclinic instability) or from the available kinetic energy (barotropic instability).

The pure baroclinic problem is generally applicable only when the undisturbed flow has horizontal scales large compared with the Rossby radius. The condition is also the one for the energy of the undisturbed flow to be principally available potential energy rather than kinetic (Gill, 1982). Neither of these cases is met in this channel study. The linear model produces only a western boundary current with width dependent upon A_H, there is no large scale interior flow. In realistic cases (small A_H) the length scale of the western boundary region is less than the radius of deformation. The available potential energy in the linear models with small A_H is greater than the kinetic energy but not by three orders of magnitude as in the case of an oceanic gyre (Gill et al, 1974).

The opposite limit, pure barotropic instability, occurs when the velocity profile is dependent only on y and variations with height can be neglected.

Blandfield (1971) found that in a one layer model eddies formed due to the barotropic instability of the boundary current effectively increased the diffusion of vorticity so that the negative vorticity in the boundary current could be diminished and the fluid parcels could move into the interior region. It is proposed here that in the channel with low horizontal viscosity and inclusion of advective terms the eddies are a necessary process in the balance of vorticity at the western boundary.

3.5.5 SUMMARY

Results from the baroclinic nonlinear model show that nonlinear effects only become important when low values of horizontal viscosity are used. For $A_H = 100m^2s^{-1}$ the nonlinear baroclinic model produces an inertial boundary current. Eddies with a wavelength of 400km are generated south of 6°S due to the barotropic instability of the boundary layer.

The kinetic energy of the flow associated with the eddies increases the total energy of the channel to almost twice that of the linear case. Furthermore the transport is increased by inclusion of the nonlinear terms.

There was insufficient time to investigate the statistical properties of these eddies thoroughly or to compare their generation with wind forced mesoscale eddies (e.g. Holland and Lin, 1975 a,b). Further discussion of the eddies is outside the scope of this study.

4. RESULTS: EFFECTS OF ISLANDS, SILLS AND SHELVES IN THE CHANNEL

4.1 INTRODUCTION

The broad aim of this chapter is to determine the effects of islands, sills and shelves on the transport and flow in the north-south cross equatorial channel of chapter 3.

In the case of including islands in the channel the baroclinic models can quite satisfactorily be used and a series of island sizes and position and channel viscosities are modelled. The use of these models to study changes in channel depth has been discussed in section 2.6.4 and the computationally slower linear two layer model that includes the free surface is favoured. This limits the number of experiments that can practically be performed. Effort is therefore made to investigate specific bathymetric features of the Eastern Archipelago, namely the sills in the Lombok and Macassar Strait and the wide continental shelves to the south of the region.

In this chapter the discussion of the results is in terms of comparisons with the initial channel models of chapter 3. This allows the singular effects of an island, sill or continental shelf in the channel to be determined. In chapter 5 the production of a more realistic model representation of the Eastern Archipelago is discussed.

4.2 EFFECTS OF ISLANDS IN THE CHANNEL

4.2.1 Introduction

A series of experiments are presented with islands at different latitudes and at various distances from the meridional boundaries (A_H in the range 100-10000m^2s^{-1}). The size of the islands is also varied. For each experiment the meridional transport in the upper layer to the east and west of the island is determined. The experiments all involve the integration of the model for 100 days.

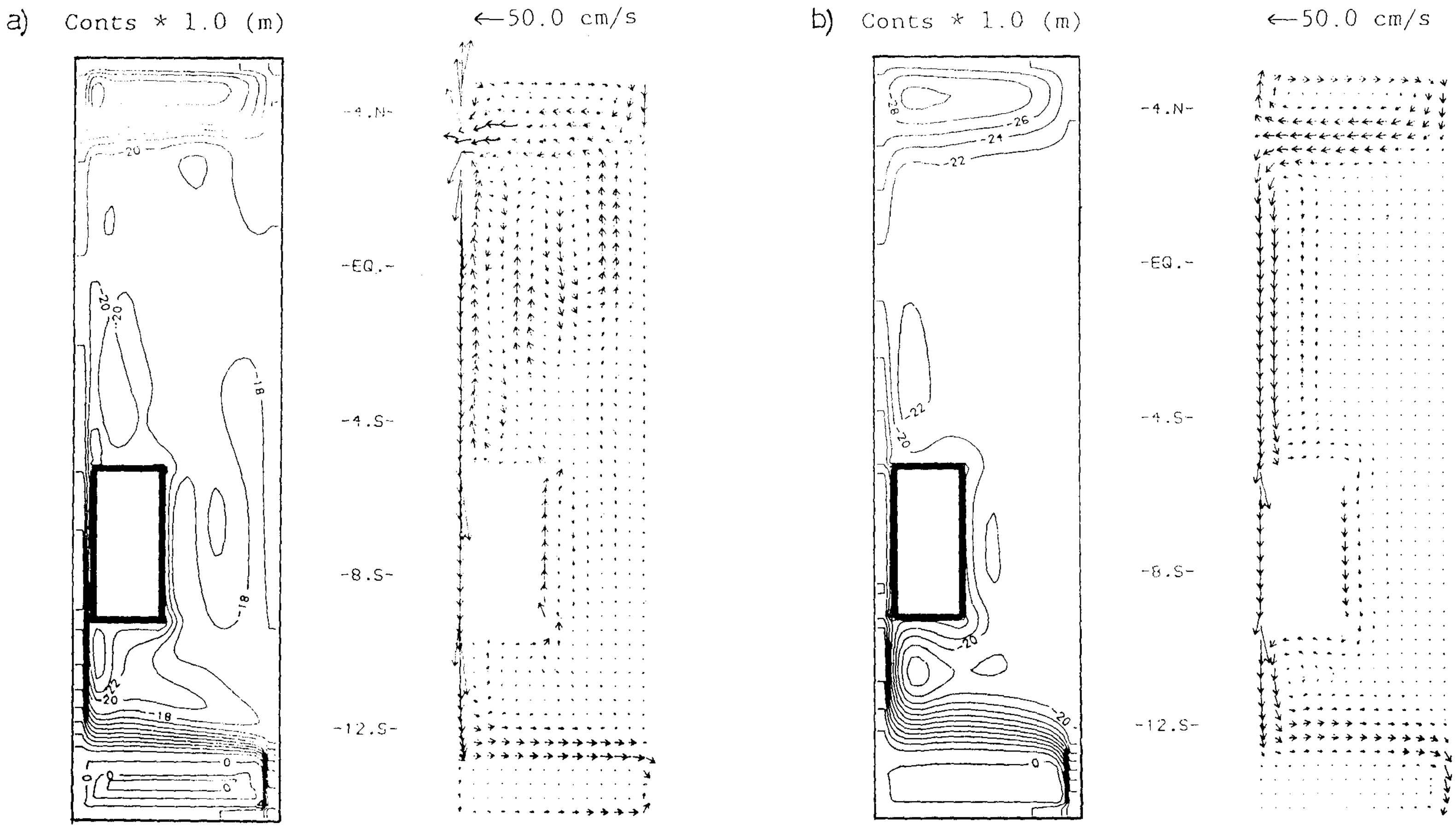

Figure 4.2.1 : Linear Baroclinic Model, Fields after 100 days, Interface Perturbation and Upper Layer Velocity, a) $A_H = 100 m^2 s^{-1}$, b) $A_H = 1000 m^2 s^{-1}$.

At high viscosities ($>500 m^2 s^{-1}$) this implies a steady state is attained whilst at lower viscosities transports are within 10% of the steady state value.

Islands can be represented by the use of free slip (or no slip) lateral boundary conditions at some interior points in the grid. (see also section 2.4.1). With the c-grid some care has to be taken at the corners of the island where both the meridional and zonal velocities are zero.

4.2.2 The Linear Model

A series of experiments were carried out using a rectangular island 400km in north-south extent and 200km in east-west extent. The position of the island was varied between integrations. The lateral viscosity was set at 100, 1000 and $10{,}000 m^2 s^{-1}$ to alter the thickness of the viscous boundary layer, 37, 90 and 180km respectively (from table 3.3.3). The forcing terms used were the same as for the baroclinic models of chapter 3, with the relaxation boundary condition enforcing a -30m difference between the interface north of 3°N and south of 12°S.

Figures 4.2.1.a) and b) show the instantaneous fields after 100 days for an island 40km from the western boundary (A_H = 100 and $1000 m^2 s^{-1}$ respectively). It can be seen that for the lower viscosity integration the steady state has not yet been attained as planetary wave motions are evident. The higher viscosity solution is close to the steady state. In both cases the effect of the island is to interrupt the meridional boundary flow and to force the flow to continue to the east of the island. Thus in figure 4.2.1.b) part of the western boundary current flows between the island and the western boundary whilst the remainder is forced to form to the east of the island.

Figure 4.2.2.a) shows the ratio of the flow to the west of the island compared to that to the east of the island after 100 days. The length scale, L_W, is the width of the western strait divided by the viscous boundary layer width (from table 3.3.3). There is little

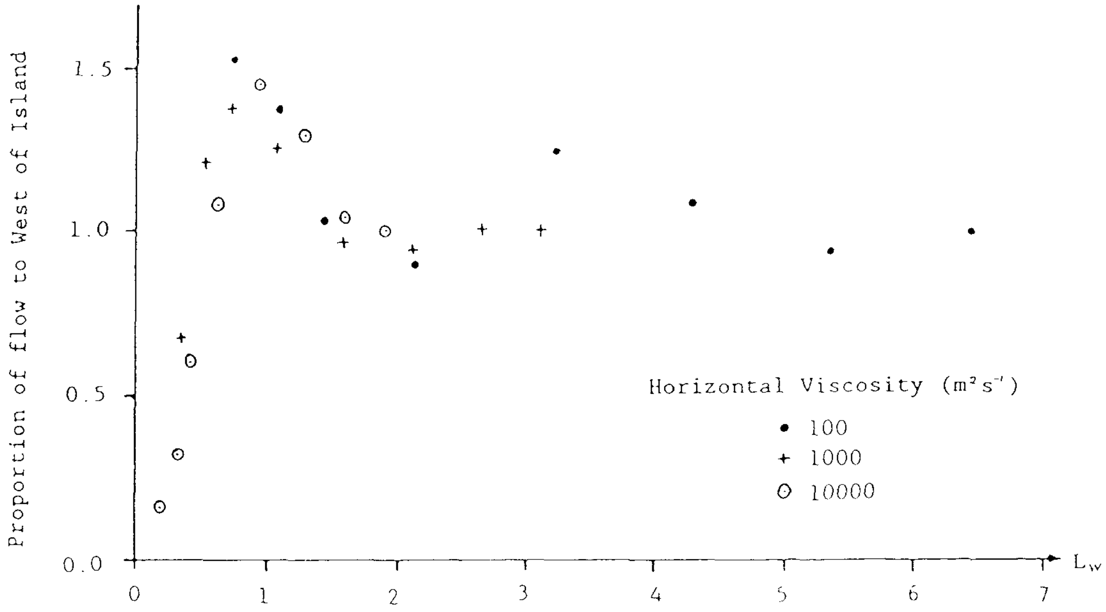

Figure 4.2.2.a) : Proportion of steady flow to west of island in linear baroclinic model.

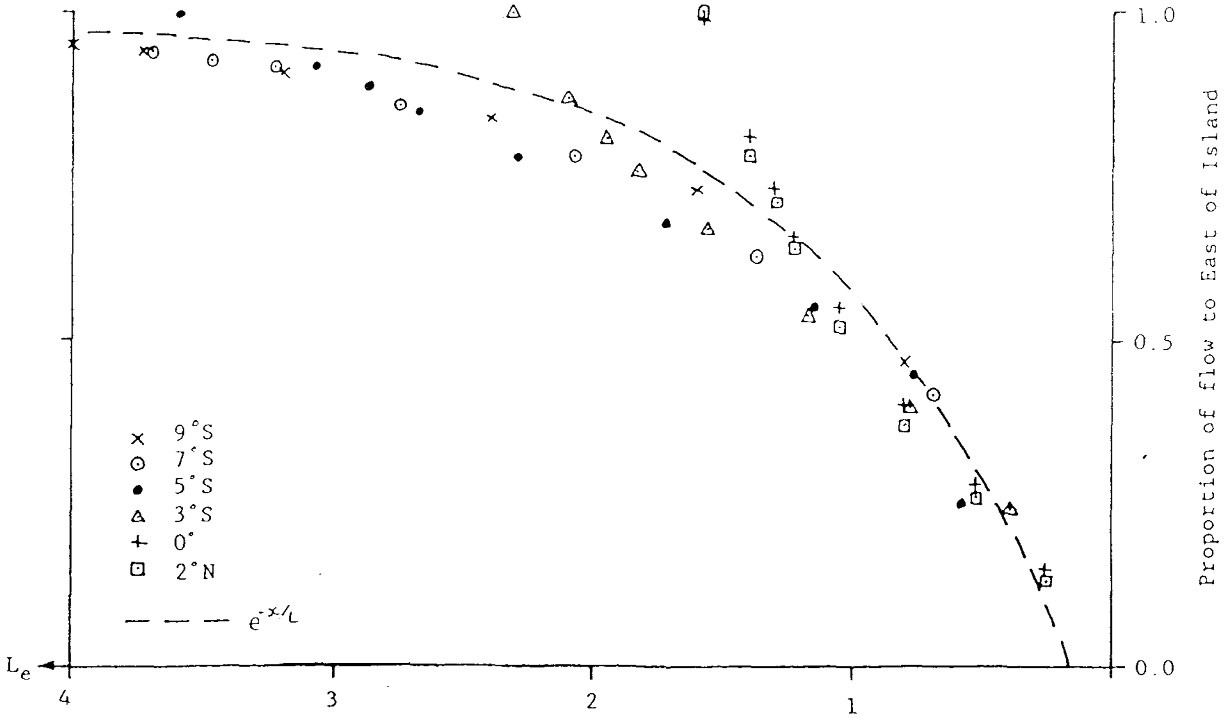

Figure 4.2.2.b) : Proportion of transient flow to east of island in linear baroclinic model.

difference ($\pm 5\%$) to the ratio with latitudinal position of the island or with the value of A_H although the higher viscosity experiments are closer to steady state and do not show evidence of planetary wave motions for values of $L_W > 3$. The ratio is altered by the width of the western strait. The main features of the model are the maximum transport through the western strait that occurs at $L_W \simeq 0{\cdot}7$ and the lower values of transport at $L_W \simeq 2{\cdot}0$.

No transport occurs through the strait until the strait is two grid points in width (40km). There is then an increase in transport through the strait until the width of the strait is the same width as the western boundary layer, which when using free slip boundary conditions is approximately two-thirds that of the Munk boundary layer thickness given in table 1.5.3. With increasing width of strait the transport decreases to a minimum value when both the western boundary current and counter current are within the strait. If there were no flow in the interior this minimum transport would be unaltered by increasing the width of the western strait. The proportion of flow to the west of the island to that to the east of the island would then be 100% in figure 4.2.2.a) this can be seen to be the case for viscosities greater than $100\text{m}^2\text{s}^{-1}$, where the steady state is attained.

Table 4.2.1 gives the transport determined in the models and the pressure gradient at the western boundary that caused the flow. The transport equivalent to a 10cm pressure gradient between 3°N and 12°S is also given for comparison with table 3.4.3.

TABLE 4.2.1 **Transport through linear channel**

		3°N - 12°S	10cm N-S gradient
Model	Transport	Interface Gradient	Equivalent
Transport			
	(Sv)	(m)	(Sv)
$A_H = 100\text{m}^2\text{s}^{-1}$	2.90 - 4.20	17.5 ± 0.5	4.5 - 6.8
$A_H = 1000\text{m}^2\text{s}^{-1}$	3.95 - 4.30	24	4.6 - 5.1

The range of transports given are due to the fact that transport increased the further north the island was positioned in the channel. The transport with $A_H = 100m^2s^{-1}$ is in reasonable agreement with the value in table 3.4.3. (6.7Sv).

The effect of an island on the coastal Kelvin wave can be seen in figure 4.2.2.b). The length scale, L_E, in this case is the width of the eastern strait divided by the radius of deformation of the latitude at which the meridional transports are determined. Similar to the western boundary current, that part of the Kelvin wave that cannot propagate through the eastern strait is forced to flow to the west around the island.

At low latitudes, <3°, the behaviour is more linear than exponential, this is because the deformation radius is not small compared to the width of the straits and non rotational (linear) effects become important. At higher latitudes the observations for both the linear and non linear cases (nonlinear case presented in section 4.3 figure 4.2.4.b) lie close to the theoretical curve for the decay of a Kelvin wave away from the eastern boundary ($e^{-x/L}$) (dashed line in figure 4.2.2.b)). Changes in lateral viscosity have no effect on this transient process.

Experiments were carried out to look at the effect of changing the zonal extent of the island. It was found that with an east-west width of 120-280km there were no significant differences (±5%) to the results described above. Similarly altering the meridional extent of the island by ±50% did not have any significant effect (±5%).

4.2.3 The non-linear Model

The experiments with the initial rectangular island (400km x 200km) were repeated with the non-linear baroclinic model to determine the effects of the island on the eddies that developed at the western boundary (see section 3.5).

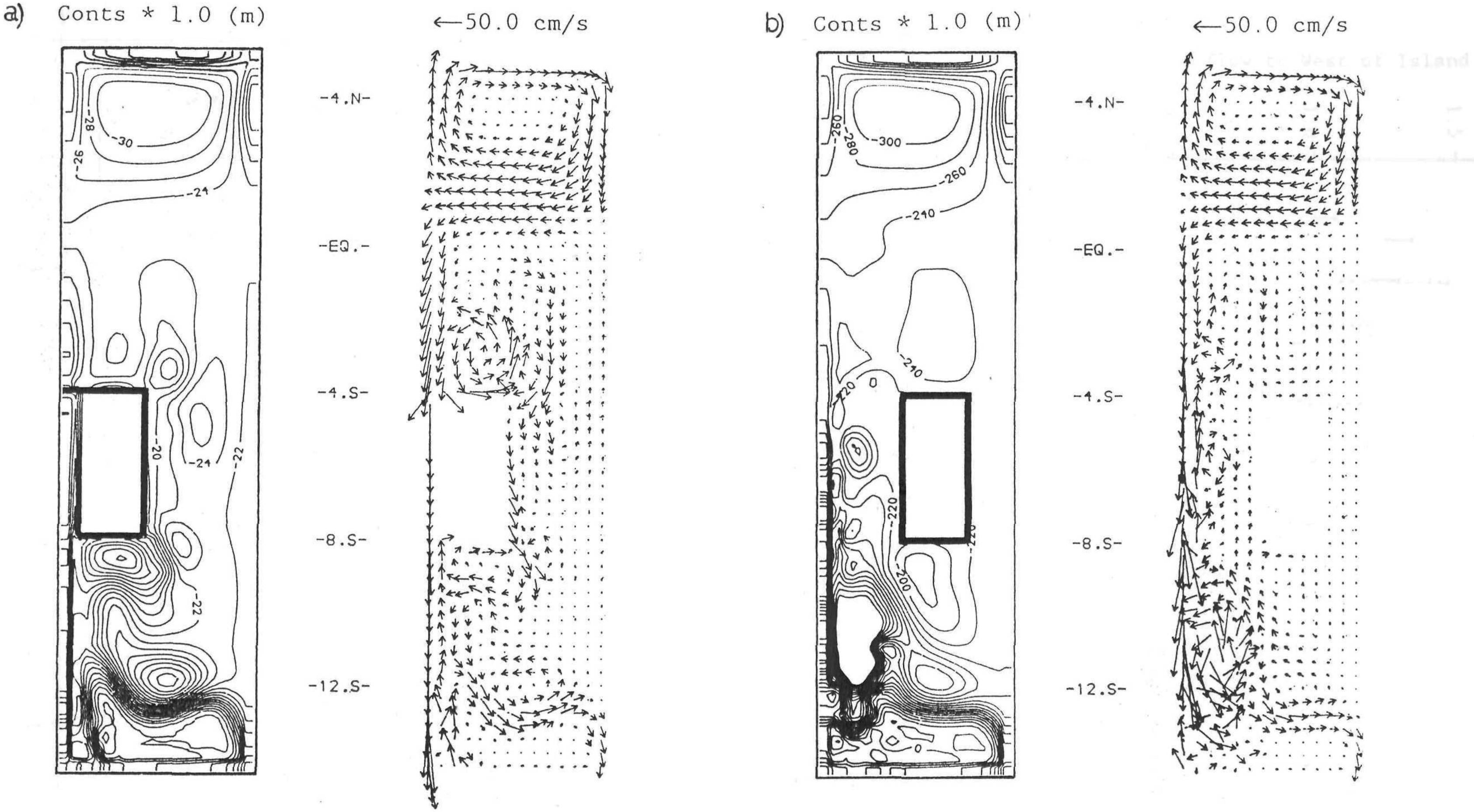

Figure 4.2.3 : Non Linear Baroclinic Model, Fields after 100 days, Interface Perturbation and Upper Layer Velocity, $A_H = 100m^2s^{-1}$
a) Island 60km from Western Boundary, b) Island 140km from Eastern Boundary.

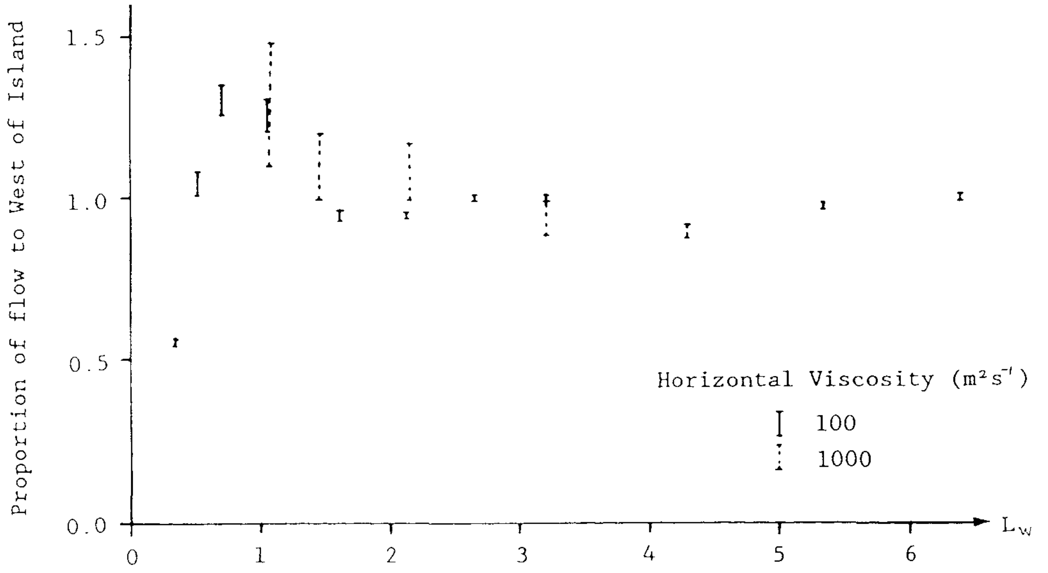

Figure 4.2.4.a) : Proportion of steady flow to west of island in non linear baroclinic model.

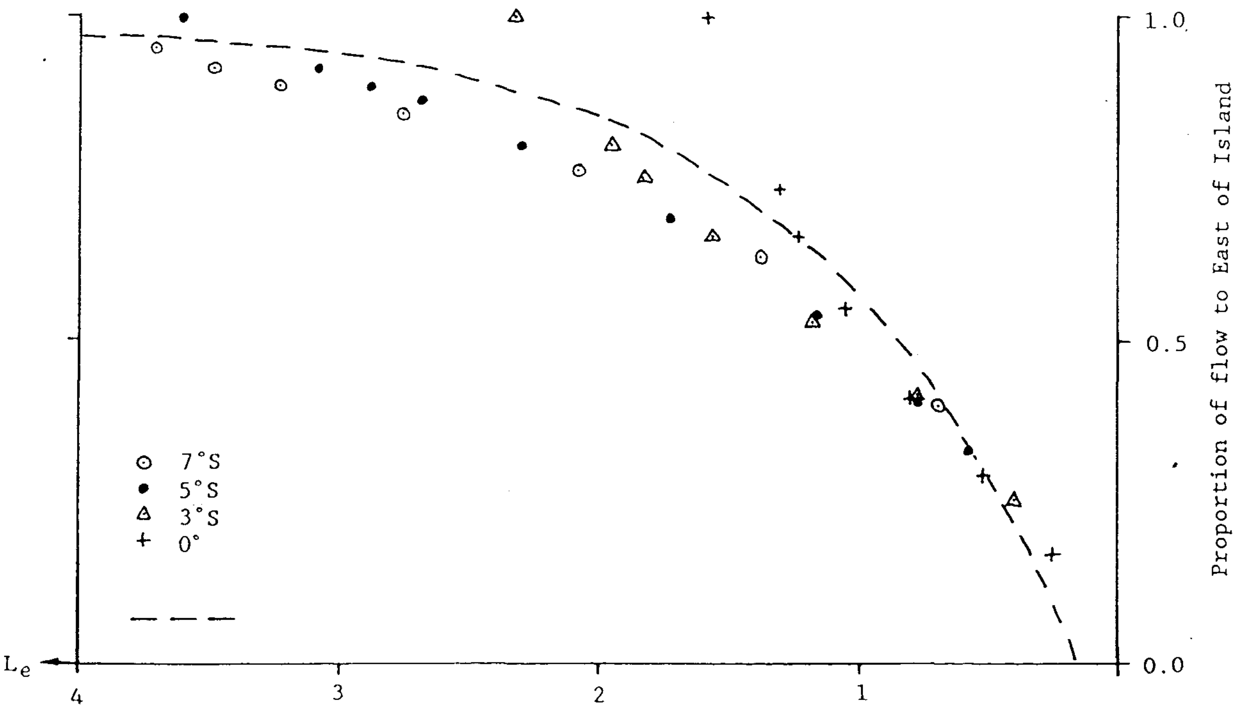

Figure 4.2.4.b) : Proportion of transient flow to east of island in non linear baroclinic model.

Figure 4.2.3.a) shows that there is no significant difference between the behaviour of the initial Kelvin wave response in the two models. This is because the initial response is dominated by linear dynamics. It is only after water has started to move large distances that advective effects become important.

When the island is close to the western boundary (figure 4.2.3.a)) the flow through the western strait is undistorted. To the east of the island and at the corners of the island eddies are formed. When the width of the western strait is increased (figure 4.2.3.b)) eddies develop in the western strait and not at the corners of the island or the eastern strait. In both cases there is a region of recirculation immediately south of the island.

The effect of the island is similar to that in the linear model. That part of the open channel western boundary solution (chapter 3) that cannot form in the western strait is forced to form to the east of the island. To the south of the island where the horizontal gradients in the h,u and v fields are large non linear effects also become important.

Figure 4.2.4.a) shows the ratio of the flow through the western strait compared to that through the eastern strait after 100 days. The flow has more variance than in the linear model (figure 4.2.2.a)) and the standard mean error $(\sigma/\sqrt{n})$ has been included in the plot. It can be seen however that there is good agreement with figure 4.2.2.a) with a maximum at $L_W < 0.7$ and the lower values at $L_W \simeq 2.0$. This suggests that after 100 days a viscous boundary layer has been formed in the nonlinear channel and that the inertial boundary layer (described in section 3.5) has decayed. The eddy field is superimposed on fields similar to the linear baroclinic model.

Table 4.2.2 gives the transport determined in the models and the pressure gradient at the western boundary for comparison with table 4.2.1 and table 3.5.2

TABLE 4.2.2 Transport through non linear channel

Model	Transport (Sv)	3°N - 12°S Interface Gradient (m)	10cm N-S gradient Equivalent Transport (Sv)
$A_H = 100m^2s^{-1}$	2.90 - 4.20	26 ± 3	5.4 - 8.6
$A_H = 1000m^2s^{-1}$	3.95 - 4.30	19	6.4 - 6.9

4.2.4 Summary

The inclusion of an island (200km x 400km) in the channel does not significantly alter the transport through the channel. The further north the island in the channel the closer the transport to that of the open channel model. The zonal position of the island has negligible effect on the total transport through the channel.

The effect of an island in the channel is to divert that part of the open channel solution (non-linear or linear, transient or steady) that would have formed in the region the island occupies to flow around the island. Thus both the western boundary layer and the initial Kelvin wave are affected by the zonal position of the island.

4.3 EFFECTS OF SILLS IN THE CHANNEL

4.3.1 Introduction

In this section attention is turned to modelling the effects of cross channel sills on the flow through the cross equatorial channel. Figure 1.2.1 shows that the Eastern Archipelago is composed of numerous sills and basins, of these, the sills in the Lombok strait and south of the Macassar Strait are the shallowest, both of which come within 500m of the surface.

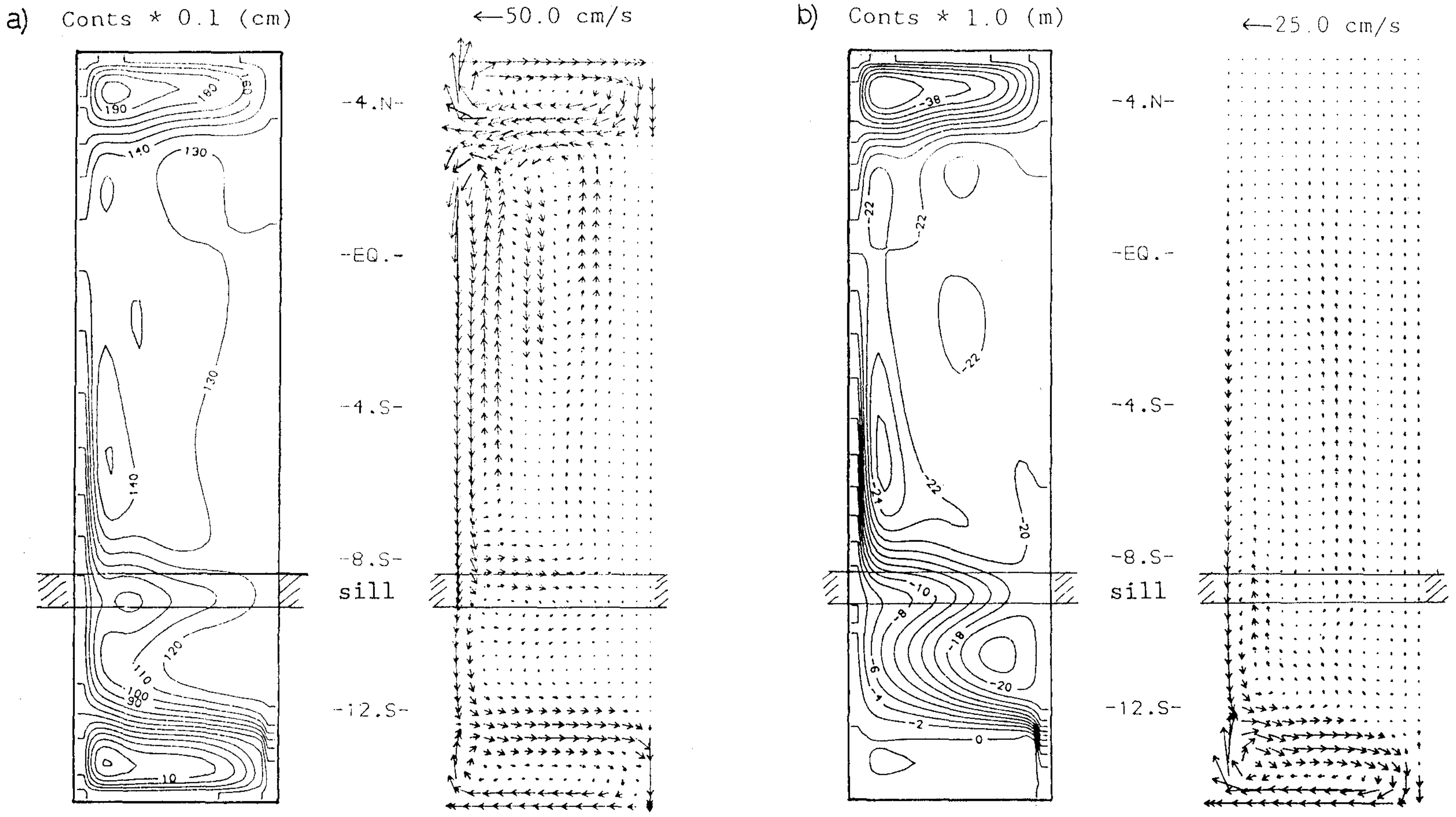

Figure 4.3.1 : Two Layer Linear Lombok Sill Model, $A_H = 500 m^2 s^{-1}$, Fields after 50 days, a) Surface Elevation and Upper Layer Velocity b) Interface Perturbation and Lower Layer Velocity. (Position of Sill Marked)

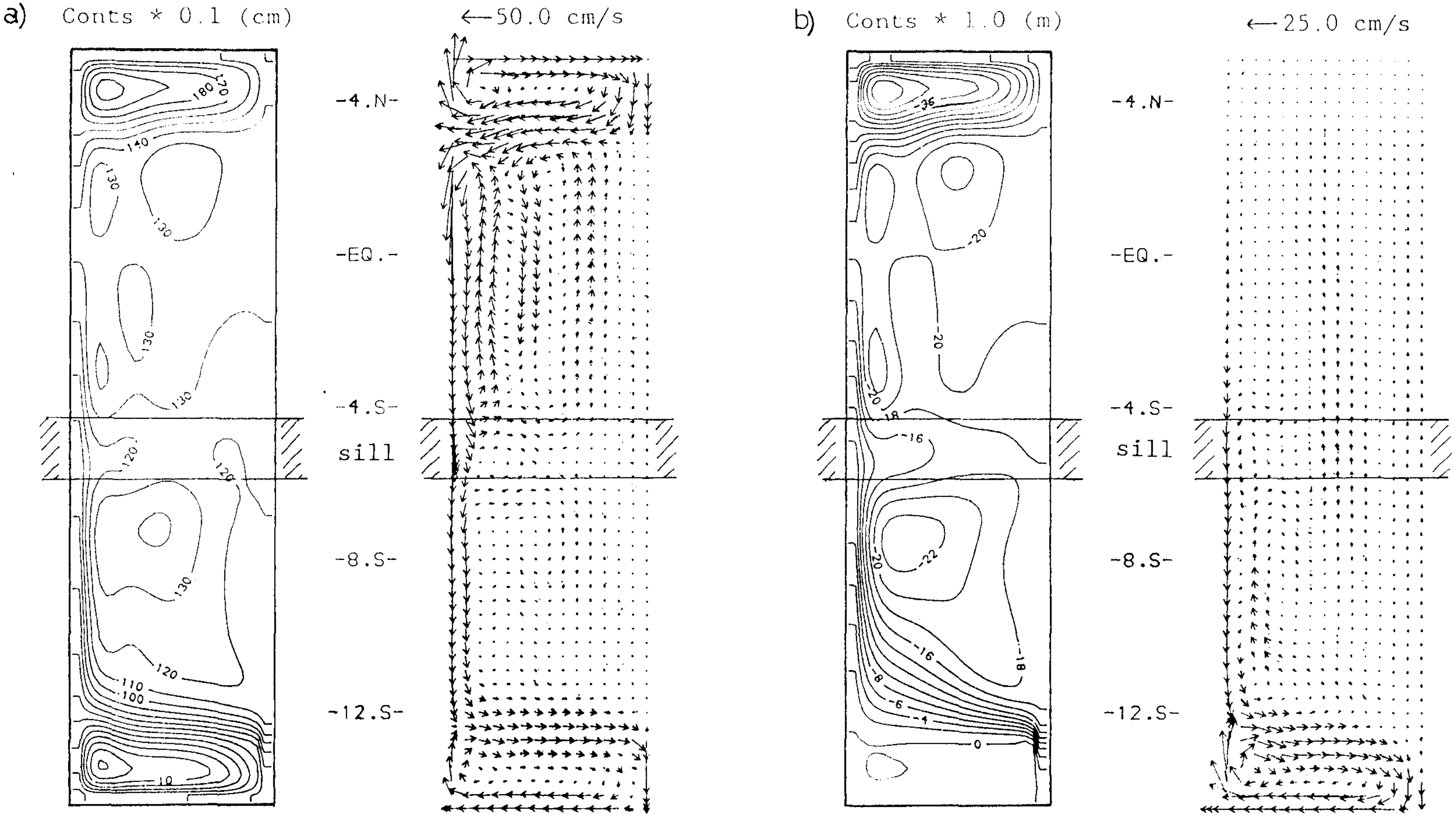

Figure 4.3.2 : Two Layer Linear Macassar Sill Model, $A_H = 500m^2s^{-1}$, Fields after 50 days, a) Surface Elevation and Upper Layer Velocity. (Position of Sill marked).

In the linear channel models topography can be represented by changing the lower layer thickness, H_2. Thus to represent a 500m sill H_2 is set equal to 300m. The main aim here is to determine the effects of the major sills on the transport through the channel. Thus the baroclinic model is not suitable for the purpose. Over the 500m sill the lower layer velocities would be 67% of those in the upper layer and neglect of these large velocities to determine the transport would be a very poor approximation (see section 3.4.6).It is also necessary to include the free surface in models with large scale topography in order to include the effects of the interaction between the baroclinic and barotropic modes. Hence the linear two layer model is used throughout this section.

The use of the two layer model necessitates a different approach to that of section 4.2 where many experiments were carried out to determine the general effects of an island in the channel. In this section the major concern is in the determination of the effects on transport and velocity fields of two specific sills with meridional extent and latitudinal position similar to the sills in the Lombok strait and south of the Macassar Strait. The Lombok sill occurs between the islands of Lombok and Bali and is approximately 60km in north-south extent centred on 9°S. The Macassar sill is approximately 160km in meridional extent and centred at 5°S. The zonal extent of both sills is taken to be 560km (the model channel width) for the two experiments.

4.3.2 **Results**

Figures 4.3.1 and 4.3.2 show the instantaneous fields after 50 days for the Lombok sill and Macassar sill. The flows are not at steady state value (see figure 3.4.10.b)), all parameters are the same as in section 3.4. Figure 4.3.3 shows that north of the sills all the fields are similar to the open channel solution, showing development of the western boundary layer and meridional flow associated with the planetary wave motion. South of the sills the lower layer velocity fields of figures 4.3.1.b), 4.3.2.b) and 3.4.3.b) are similar. In the vicinity of the sill the upper layer

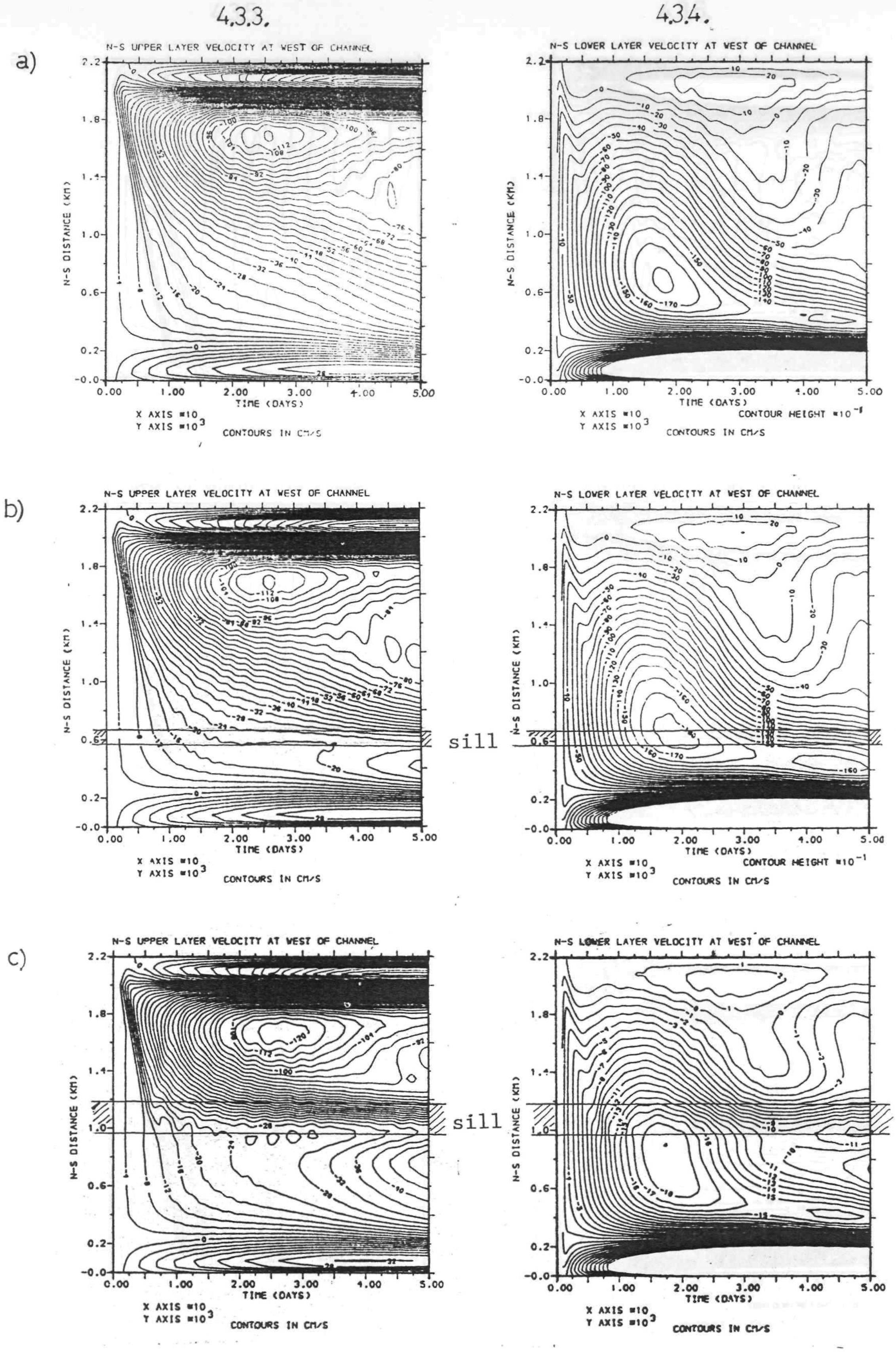

Figure 4.3.3 - 4.3.4 : North - South Sections in time through the Meridional Velocity. (4.3.3), Upper Layer, (4.3.4), Lower Layer. a) Open Channel Model, b) Lombok Sill Model and c) Macassar sill Model. (Position of Sills marked).

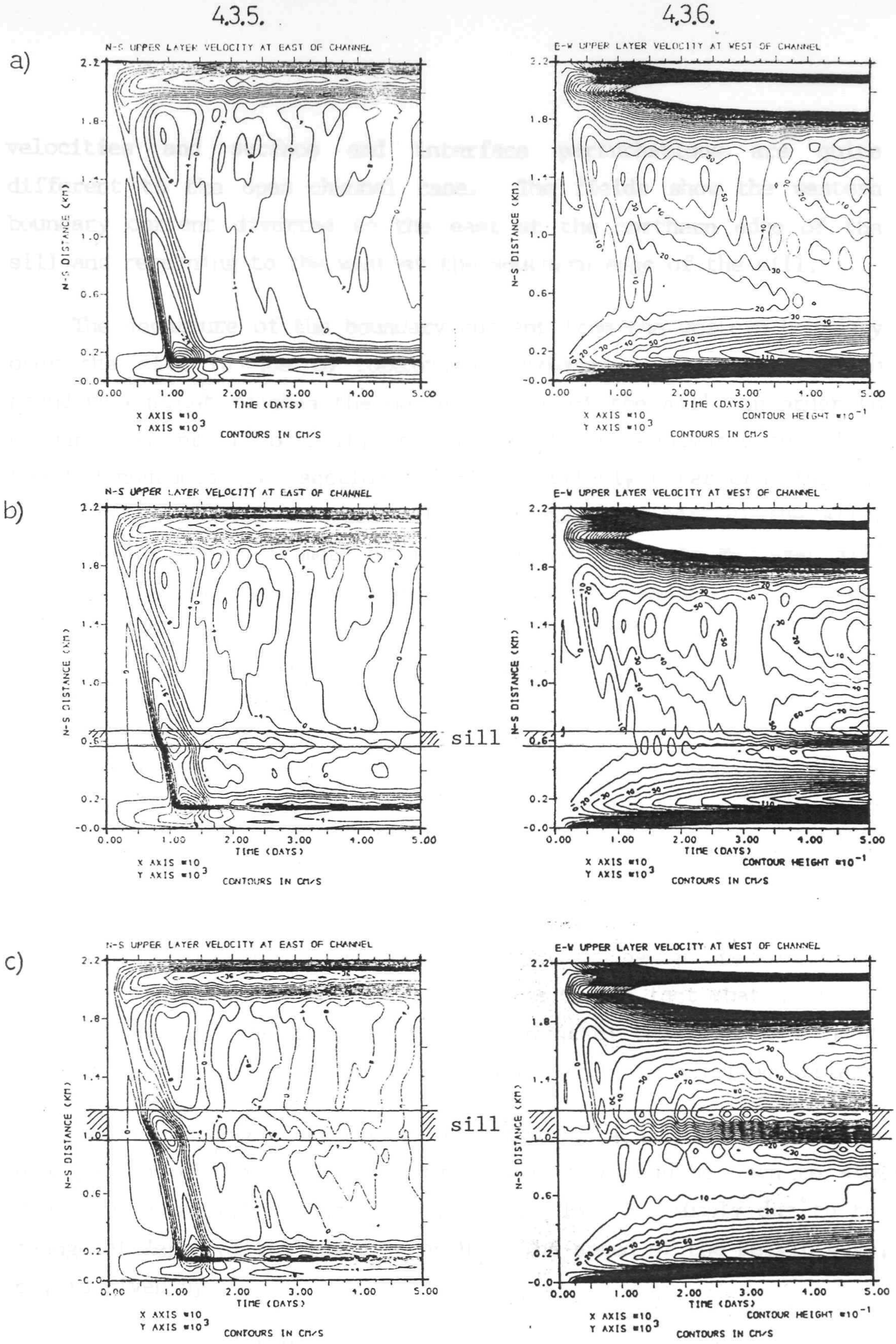

Figure 4.3.5 - 4.3.6 : North - South Sections in time through; (4.3.5), The Meridional Velocity at east of channel and (4.3.6). The Zonal Velocity at west of Channel. a) Open Channel Model, b) Lombok Sill Model and c) Macassar Sill Model. (Position of Sills Marked).

velocities and surface and interface perturbations are quite different to the open channel case. The fields show the western boundary current diverted to the east at the northern edge of the sill and returning to the west at the southern edge of the sill.

The departure of the boundary current from the western boundary over the sill is due to topographic steering. When the western boundary current reaches the northern edge of the sill, in order to conserve potential vorticity the flow is forced eastwards to follow the f/H contours (see section 1.5.3). Similarly after crossing the sill flow is forced westwards along the southern edge of the sill. The Lombok sill has a more pronounced effect than the Macassar sill on the velocity and height fields because the Lombok sill (in the model) is five radii of deformation in zonal width compared with the Macassar sill which being at a lower latitude is only three radii of deformation in zonal width.

Sections in time at the western and eastern boundaries of the upper and lower layer velocities are shown in figure 4.3.3 - 4.3.6 for the open channel and sill models. The effect of the sills shows up clearly in the upper layer meridional velocity at the western boundary (figure 4.3.3) but the lower layer velocities are not dramatically altered. The effects seem to be greater with the Macassar sill (figures c)) but this is due to the fact that after the first 50 days of integration the development of the western boundary current at 9°S (the latitude of the Lombok sill) is still occurring.

At the eastern boundary in figures 4.3.5 the southwards propagation of the initial coastal Kelvin wave can be seen to slow down over the sill (figures b) and c)). This is simply due to the change of depth of the lower layer H_2. The speed of the Kelvin wave, c_1, is given by

$$c_1^2 = g' \frac{H_1 H_2}{H_1 + H_2} \qquad (4.3.2.1)$$

The baroclinic phase speed, c_1 (with H_1 = 200m, H_2 = 1300m) is 2.4ms^{-1}, but with H_2 = 300m is reduced to 2.0ms^{-1}. The slowing down of the Kelvin wave over the sill is associated with an increase in the meridional velocity.

The upper layer zonal velocities at the western boundary (figure 4.3.6) clearly show the development of the regions of eastward and westward flow at the northern and southern edge of the sill associated with topographic steering. The edges of the sills also act as sources of high frequency waves. At the Lombok sill the waves generated have a period of 54±2 hours (frequency 3.2 x 10^{-5}s^{-1}) and at the Macassar sill the waves have period 71±2 hours (frequency 2.5 x 10^{-5}s^{-1}). The frequency of these waves is slightly higher than that of the waves generated at corresponding latitudes in the open channel (table 3.2.2).

4.3.3 **Transport and Energy budget**

Table 4.3.1 summarizes the energy balance after 50 days of integration for the open channel and sill models (see also section 3.4.3). The figures in parentheses are the percentage of the total energy.

TABLE 4.3.1 **Energy budget of open channel and sill models**

		Energy (x10^{-3}Jm^{-2})			
Model	Total	KE1	KE2	PE1	PE2
Open channel	141	59	20	1	61
		(42)	(14)	(1)	(43)
Lombok sill	137	61	21	1	54
		(45)	(15)	1	(39)
Macassar sill	132	61	23	1	47
		(46)	(17)	1	(36)

The total energy of the channel is reduced by the inclusion of a sill. This is due to the reduction in the potential energy of the interface. The rate of conversion of lower layer Kinetic energy to potential energy of the interface is given by

$$-\rho g' \, H_2 h \left(\frac{\partial u_2}{\partial x} + \frac{\partial v_2}{\partial y} \right) \qquad (4.3.3.1)$$

The reduction in the thickness of the lower layer over the sill and the area over which the sill extends are the important factors. Velocity gradients in the lower layer with the sills are not significantly different to the open channel case.

Table 4.3.2 gives the model transports after 50 days of integration for the three models. The north-south difference in surface elevation between 3°N and 12°S and the transport that would be produced by a 10cm height difference are also given to allow direct comparison between the experiments.

TABLE 4.3.2 **Transport through open channel and sill models**

Model	Transport (Sv)	3°N - 12°S Surface Gradient (cm)	10cm N-S Gradient Effective Transport (Sv)
Open channel	6.85	11.0	6.2
Lombok sill	7.15	11.0	6.5
Macassar sill	7.45	10.5	7.1

There is little difference (<5%) between the transport after 50 days in the open channel and that at steady state (table 3.4.3). With the sill models the transport appears to be increased but it would be necessary to integrate the model to steady state to confirm this and to see whether a counter current is formed south of the sill.

4.3.4 Summary

The inclusion of a cross channel sill in the linear two layer model increases transport through the channel by up to 15%. The effect is greater for a sill of meridional dimension similar to the Macassar Strait sill than the Lombok strait sill.

The main effect of the sills is localized topographic steering of the western boundary current over the northern and southern edges of the sills. This process appears to inhibit the formation of a counter current at the western boundary over the sill and south of the sill and may account for the increase in transport.

4.4 EFFECTS OF CONTINENTAL SHELVES IN THE CHANNEL

4.4.1 Introduction

The effects of continental shelves on either side of the channel are investigated using the two layer linear model. the South East Asian Waters contain many regions of shallow seas. The Eastern Archipelago is partially bounded by two regions of wide (>200km) continental shelf. The Torres Strait - Gulf of Carpenteria - North West Australian Shelf in the south east and the Java Sea in the west. Elsewhere the continental shelves surrounding islands are narrower (figure 1.2.1).

In section 1.5.3 it was noted that bottom dissipation of the vorticity in the water of the surface layers might be an important mechanism in the southward flow of water from the Pacific to the Indian Ocean. The aim of this section is to determine whether the additional dissipation of kinetic energy over the shelf regions by bottom friction effects the flow in the deep channel and/or the meridional transport through the channel.

The major feature of the shelf model is hence the inclusion of a bottom friction term (equation 2.6.5.1 - 2.6.5.2) over the shallow shelf regions on either side of the basic linear two layer channel model. Following the same approach as in section 4.3 a general study of shelves of various widths, depths and coefficients of bottom friction is not undertaken. An integration using a shelf width of 300km a shelf depth of 60m and a co-efficient of bottom friction of C_D = 0.002 (Csandy, 1982) with a horizontal viscosity of $500m^2s^{-1}$ is presented here.

4.4.2 Results

Figure 4.4.1 shows the instantaneous fields after 50 days of integration. Comparison with the open channel case shown in figure 3.4.3 shows some significant differences. The spatial extent of the forcing region is the same in both models (only over the deep channel in shelf model).

Currents in the upper layer are much weaker in the shelf model. Southward flow occurs in two regions; across the width of the western shelf and in a weak boundary current at the western edge of the deep channel. No counter current has developed adjacent to the boundary current and the current has developed only as far south as 6°S. In the open channel the western boundary current has developed the length of the channel within 50 days. Regions of meridional flow associated with planetary wave motions at low latitudes are very weak in the upper layer of the shelf model.

The surface elevation in the shelf model is similar to that in the open channel, except that the strong gradients in the open channel, which occur over the western boundary current, are now found over the western shelf. Over the eastern shelf the surface is level. Between 3°N and 12°S at the western edge of the deep channel the difference in height of the surface in the shelf model is 9.0cm compared to 11.0cm in the open channel.

In the lower layer velocity fields (figure 4.4.1.b)) there are no significant differences between the open channel and the shelf model. The interface perturbation of the shelf model reflects the surface perturbation hence the interface field at the western boundary is different to that of the open channel. Free slip boundary conditions are used at the shelf edge for the lower layer.

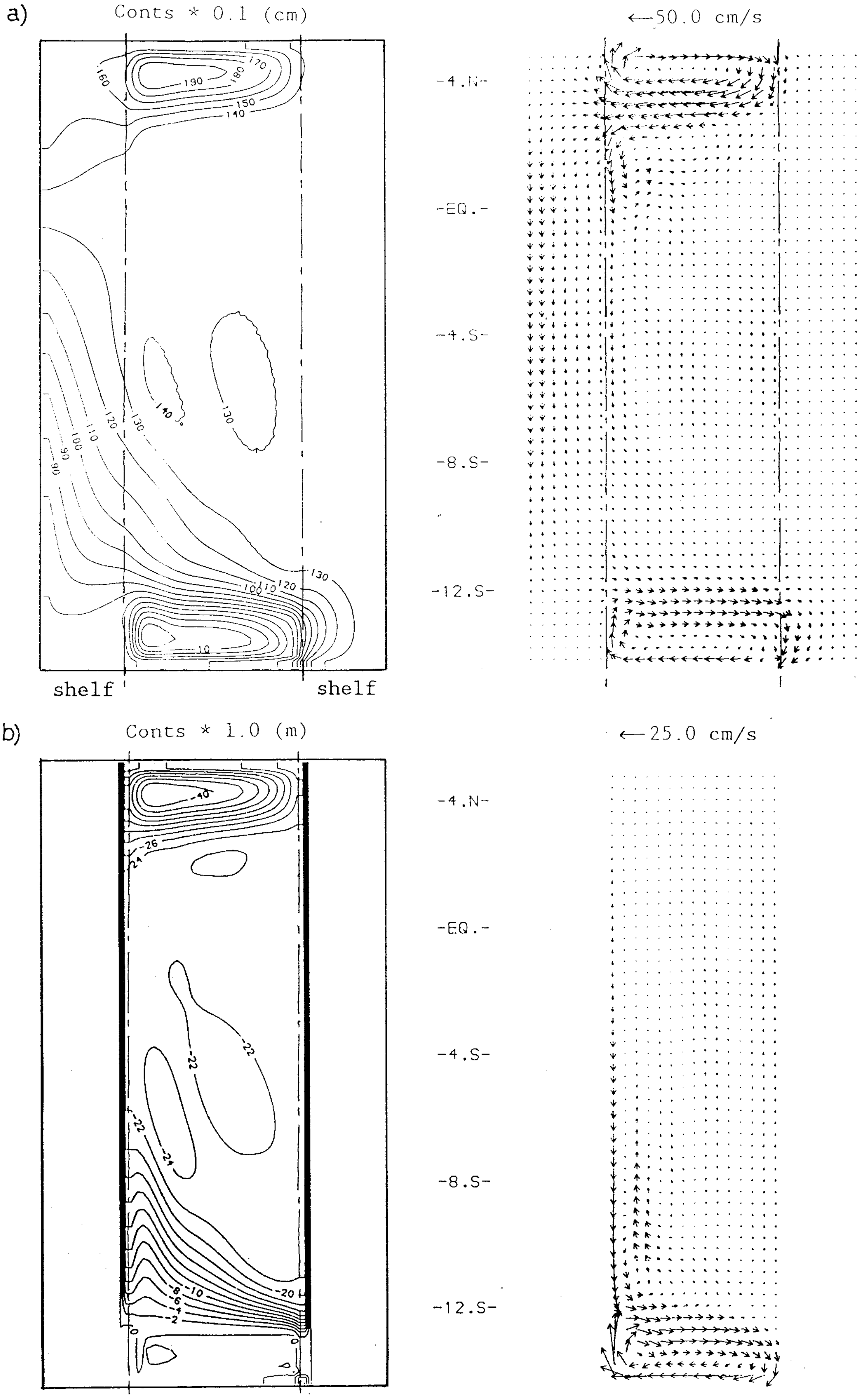

Figure 4.4.1 : Two Layer Linear Shelf Model, $A_H = 500 m^2 s^{-1}$, Fields after 50 days, a) Surface Elevation and Upper Layer Velocity b) Interface Perturbation and Lower Layer Velocity. (Position of Shelf edge marked).

The steep gradient at the western and eastern boundaries of the interface field is an artefact of the plotting and data handling routines. The true shelf edge is marked with the dashed line.

Figure 4.4.2 shows east-west sections in time through the meridional velocity field of the upper layer of the shelf model. Corresponding sections through the fields of the open channel are shown in figure 4.4.3. At 2°S the planetary wave amplitudes can be seen to be much weaker in the shelf model than the open channel (figures a)). The development of the viscous boundary layer that dominates the open channel is seen to be weaker in the shelf model. However the time that the maximum current develops in the boundary current is the same as in the open channel. The major difference in the shelf model is the broad southward current over the western shelf that can be seen to develop almost immediately.

Flow over the western shelf is dominated by bottom friction similar to that first investigated by Stommel (1948). In Stommel's model the characteristic time for the decay of small scale energy produced at the western boundary is

$$t_D = \frac{D}{2C_D V_*} \qquad (4.4.2.1)$$

where D is the depth of the water column, C_D as used in 2.6.5.1 and 2.6.5.2 and V_* an average velocity at the bottom of the water column. Similar to determining the width of the viscous boundary (section 1.5.6) and the width of the inertial boundary, (section 3.5.2) the distance that the small scale energy moves in time t_D is

$$l = C_{gx}\ t_D = \frac{\beta}{K^2}\ \frac{D}{2C_D V_*} \qquad (4.4.2.2)$$

and since $K = l^{-1}$ the width of the boundary layer when bottom dissipation of vorticity dominates is

$$l = \frac{2C_D V_*}{\beta\ D} \qquad (4.4.2.3)$$

4.4.2.a)

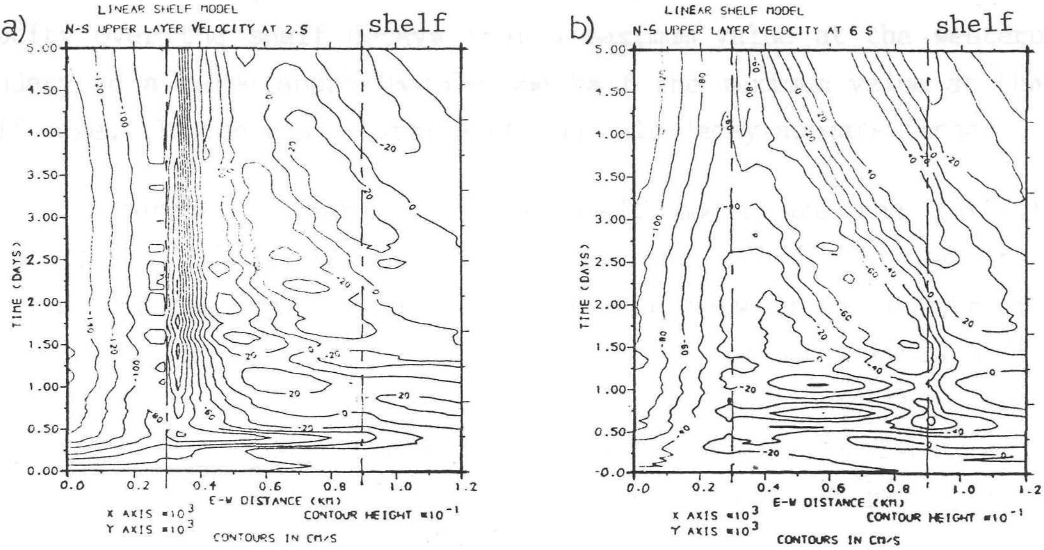

4.4.3.a)

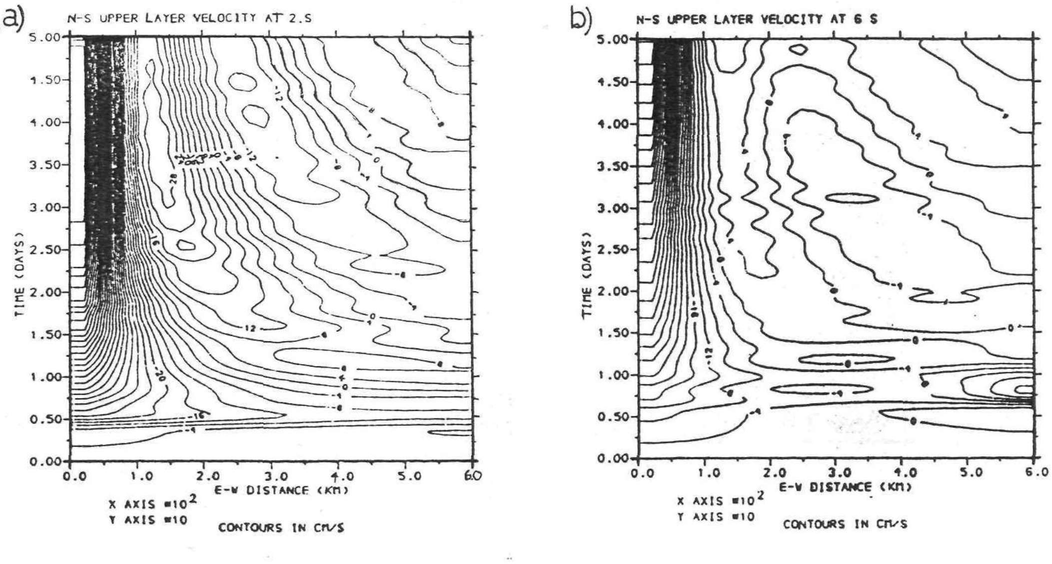

Figures 4.4.2 – 4.4.3 : East-West Sections in time through the Zonal Velocity (4.4.2) Shelf Model (4.4.3) Open Channel Model a) At 2°S b) At 6°S. (Position of Shelf edge marked).

From figure 4.4.2 a value of $V_* \simeq 0.1\text{ms}^{-1}$ is obtained. Using D = 60m and $C_D = 0.002$ the width of the boundary current expected is approximately 290km, which is similar to the width of the shelf. The velocity over the shelf decays from a maximum value at the western boundary to a value approximately one half the maximum value at the shelf edge. In the east - west sections this decay appears linear.

An interesting feature of the shelf model are the initial motions forced by the passage of the barotropic front. In the first few hours of the integration the difference between the barotropic speed in the deep channel ($\simeq 121\text{ms}^{-1}$) and over the shelf ($\approx 24\ \text{ms}^{-1}$) can clearly be seen in the reflections of the barotropic front from the western and eastern boundaries (figure 4.4.4). This front excites Poincare wave motions at the shelf edges which can be seen (figures 4.4.5) to propagate to and fro across the deep channel at $\approx 2.3\text{ms}^{-1}$. These gravity waves are rapidly damped out over the shelf where there is little zonal motion.

4.4.3 Transport and energy budget

Table 4.4.1 summarizes the energy balance of the shelf model and the open channel model after 50 days of integration. The figures in parentheses are the percentage of the total energy.

TABLE 4.4.1 Energy budget of open channel and shelf model

	Energy ($\times 10^{-3}\text{Jm}^{-2}$)				
Model	TOTAL	KE1	KE2	PE1	PE2
Open channel	141	59	20	1	61
		(42)	(14)	(1)	(43)
Shelf model	112	23	22	1	66
		(20)	(20)	(1)	(59)

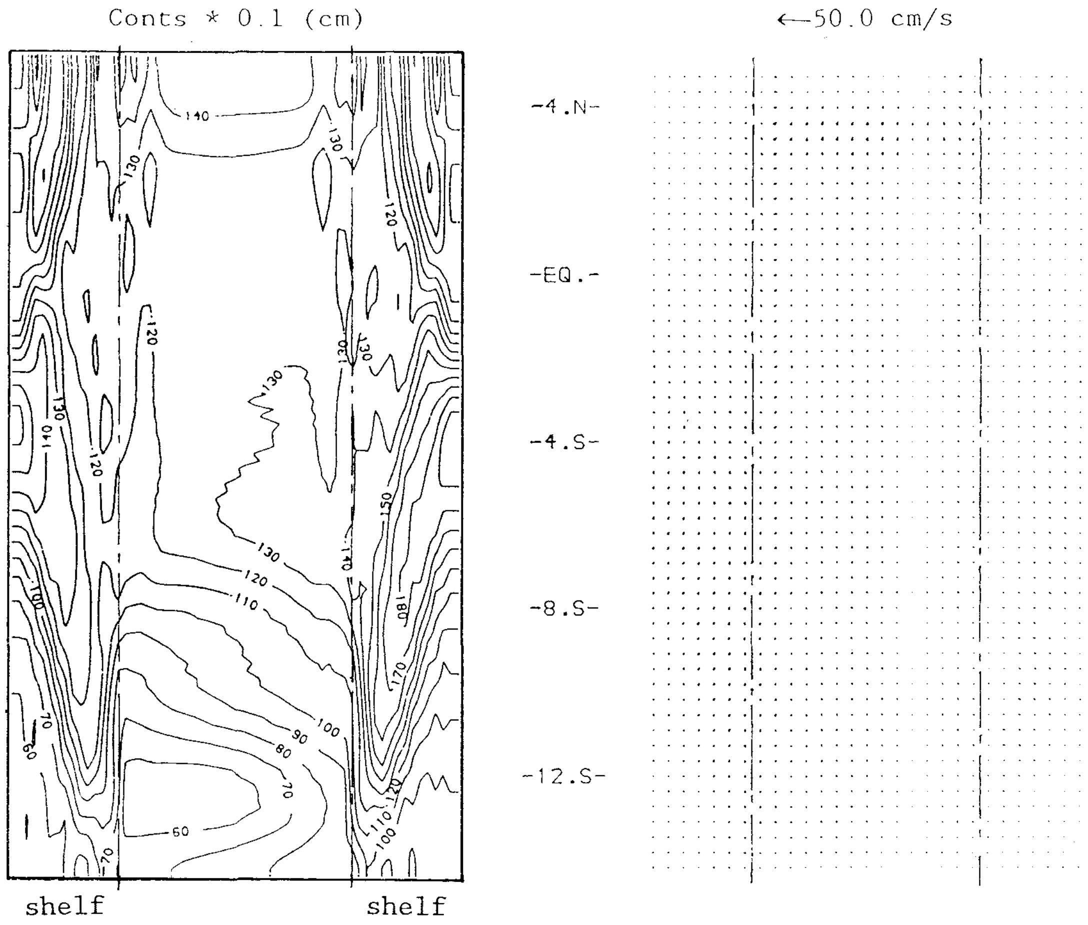

Figure 4.4.4 : Two Layer Linear Shelf Model, $A_H = 500m^2s^{-1}$, Fields after 12 hours, Surface Elevation and Upper Layer Velocity. (Position of Shelf edge marked).

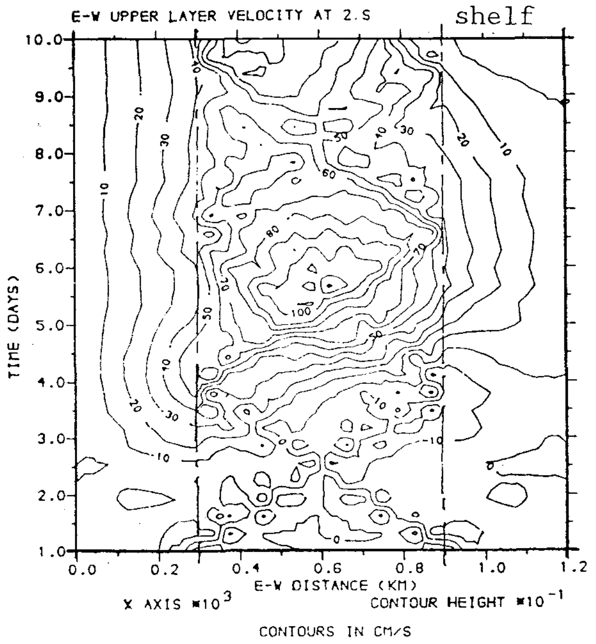

Figure 4.4.5 : East - West Section in time through the zonal velocity for first 10 days of integration. (Position of shelf edge marked).

The total energy of the channel is reduced by the effect of bottom friction over the shelves which reduces the Kinetic energy of the upper layer.

With a value of $C_D = 0.002$ the loss of upper layer kinetic energy to bottom friction is the same as the loss to horizontal viscosity. In the shelf model less surface potential energy is converted into kinetic energy. In the lower layer this is because the largest gradient of the surface elevation occurs over the western shelf. In the upper layer the reduction is because the largest gradients occur over the shallow water.

Table 4.3.2 gives the model transport for the shelf and open channel models after 50 days of integration.

TABLE 4.3.2 **Transport through open channel and shelf model**

Model	Transport (Sv)	3°N - 12°S Interface Gradient (cm)	10cm N-S Gradient Effective Transport (Sv)
Open channel	6.85	11.0	6.2
Shelf model	6.70	9.0	7.4

The effective transport appears to have increased in the above table due to the presence of shelves, however the effective cross-sectional area of the upper layer has increased by 30%. For this reason it cannot therefore be concluded that the transport in the shelf model is increased.

4.4.4 Summary

The inclusion of wide continental shelves in the linear two layer model increases the transport through the channel. There is some difficulty in directly comparing the transport in the shelf model with that in the other two layer models (table 4.3.2) because of the increase in channel area and effects due to the forcing regions interacting with shelf flow north of 3°N and south of 12°S.

The effect of bottom friction acting over the shelves is to reduce the kinetic energy of the upper layer. Additionally because large gradients in the surface elevation occur over the western shelf the conversion of surface potential energy to kinetic energy of the upper and lower layers is reduced.

The southward flow through the channel occurs in a broad region over the western shelf and in a weak viscous boundary layer at the western edge of the deep channel. The timescales for the development of these boundary layers are quite different, ~100 hours and ~1000 hours respectively.

Transient motions in the shelf model are similar to those of the open channel but wave amplitudes are generally weaker. Additional effects are caused by wave reflection and generation at the shelf edges and by the difference in the barotropic wave speed in the deep water and over the shelves.

The implications of these results on flow through the South East Asian Waters during the last ice age, when sea level would have been much reduced (100-200m) is that the throughflow would have been reduced because there would have been less dissipation of relative vorticity in the much reduced shelf sea areas. The magnitude of this reduction is dependent upon choice of values of A_H and C_D for the real ocean.

5. RESULTS: THE REALISTIC MODEL

5.1 INTRODUCTION

The aim of the first part of this chapter is to develop, by the process of building upon the basic models and the results of the two preceding chapters, a model capable of investigating the throughflow from the Pacific to the Indian Ocean through the Eastern Archipelago. This realistic model is then used to determine the transport forced by a constant north-south difference in sea surface elevation of 16cm. The effects of the seasonal variation of this pressure gradient (Wyrtki, 1987) are determined (section 5.4) and compared with the current meter observations made in the Lombok Strait by Murray and Arief (1988). The effects of a 30 day oscillation in the forcing is also investigated (section 5.5).

5.2 DESIGN OF REALISTIC MODEL

5.2.1 Geometry of Model

Figure 1.2.1 shows the complex geometry and bathymetry of the Eastern Archipelago. In most places the 1000m and 200m isobaths are close together. Two large regions of shallow water (<200m) exist, the Java Sea and the North West Australian Shelf - Torres Strait - Gulf of Carpenteria. The region also contains hundreds of islands of varying sizes.

In producing the model geometry the aim is to include the salient features that should affect the large scale circulation and throughflow but to avoid unnecessarily complicating the model and interpretation of results. The aim is to include the two deep channels through the Indonesian island peninsula (8°S-9°S), the Lombok Strait (~300m in depth) and the Timor Sea (~1500m in depth). Current meter data from the Lombok Strait (Murray and Arief, 1988) is one of the few direct observations of Pacific to Indian Ocean throughflow available.

The results of section 4.2 have shown that it is the large islands that are important in modifying the large scale open channel circulation. Accordingly the Celebes and Indonesian island peninsula (Lombok-Timor) are the only two islands included in the model.

As discussed in section 4.3 the two major sills in the region are those in the Lombok Strait and the southern Macassar Strait. Results of section 4.3 show that the effect of a sill on the circulation is localized, to the edges of the sill. The greater the length of a sill relative to the Rossby radius of deformation the larger is this effect. Throughout the entire region all sills are less than the radii of deformation in width.

The area to be modelled is approximately 110°-140°E, 10°N-20°S, and is shown in figure 5.2.1. Computational storage and data handling considerations permit the use of a 20km grid (175x170 points). Higher resolution would present storage problems and the results of chapters 3 and 4 have not suggested lack of resolution to be an area of concern using the 20km grid. Coarser resolution is not possible as the minimum size of features being modelled (2 grid points) would then be of similar size to the Rossby radius.

Although the region contains many deep basins (>4000m) the deepest direct pathway from the Pacific to the Indian Ocean is at 1500m. Thus the stratification of the realistic model is not changed from that of the preceding models (H_1=200m, H_2=1300m).

Solid lateral boundaries are applied at the edges of the model ocean. In the north the Sulu Archipelago between the Philippines and Borneo is taken as a solid boundary. In the east the island groups of Halmahera and Ceram are joined to New Guinea.

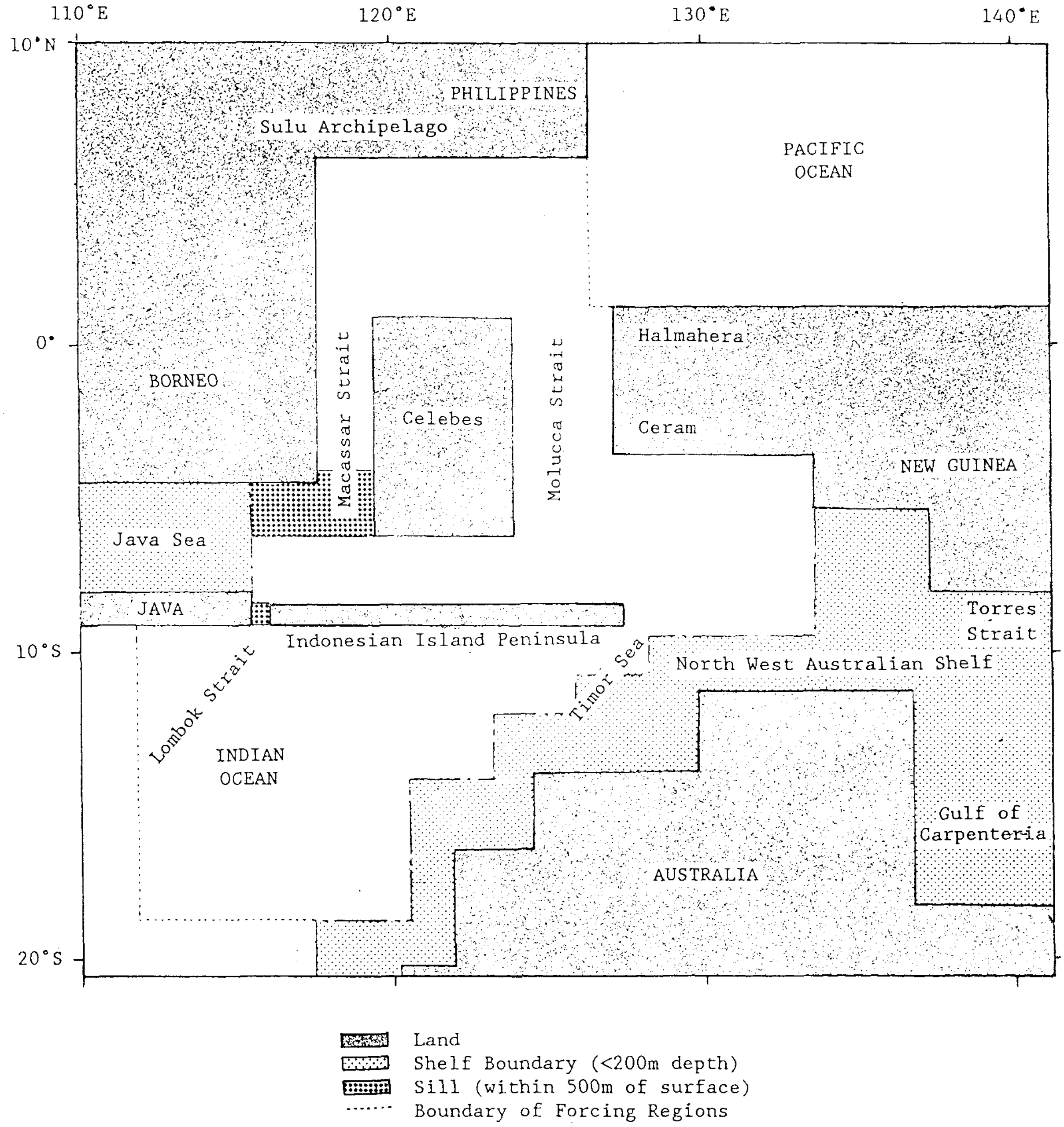

Figure 5.2.1 : Realistic Model geometry.

5.2.2 Choice of Model

Throughout this study a choice has been available as to whether to use the two layer model or the baroclinic model. The inclusion of large scale bathymetric features (sills or shelves) in the model requires the use of the two layer model (section 2.6.4). However computer time and the similarity between the results of the open channel models of chapter 3 suggest the use of the baroclinic model whenever possible. In this type of exploratory study the use of a computationally fast model aids interpretation and understanding of the model and ocean dynamics considerably. At this stage in the study the decision was made to use the baroclinic model for a series of integrations rather than aim to complete a single integration with the two layer model.

The model geometry shown in figure 5.2.1 is readily adapted for the linear baroclinic model. The ocean/land boundary is moved to the shelf edge where necessary and sills are neglected. This simplification of topography is supported by the results of chapter 4. The inclusion of sill, shelves and islands in the open channel did not increase transport through the channel by more than 20%. Sills had the most localised effect on the circulation in the channel (section 4.3.2). Shelves on the western boundary of the model ocean had the largest effect on transport. Shelves on the eastern boundary did not appear to significantly alter the propagation of the coastal Kelvin wave (section 4.4.2). Islands are required in the model to produce the two deep channels in the south, however, islands can be included in any of the models of chapter 3.

5.2.3 Forcing in the model

The aim of the forcing in the model is to produce a pressure gradient between the Pacific and Indian Ocean regions of the model that represents the difference in sea surface elevation between these oceans. The model is not intended to reproduce the circulation within the Western Pacific or the South East Indian Ocean. The forcing method used is the same as that used in the baroclinic models of chapters 3 and 4. However the difference in the forcing between the realistic model and the channel model is in the size of the forcing regions. In the north the interface in the whole of the region representing the Pacific Ocean is forced to h_p (-75.0m) whilst in the 10 grid points adjacent to the model boundary in the Indian Ocean the interface is forced to h_I(0.0m). In the Indian Ocean the forcing is at the boundary to avoid interference with the throughflow through either the Lombok Strait or Timor Sea. The forcing regions are shown in figure 5.2.1.

To model the mean throughflow caused by a north-south difference in surface elevation of 16cm using the same model parameters as in chapters 3 and 4 requires an interface gradient of approximately -46m across the region. In Section 3.3.2 it was found that setting h_p-h_I to the required difference, produced a difference in interface height between the forcing regions less than that prescribed. Throughout this chapter the pressure gradients have been set to -75m to produce the required pressure difference of approximately -46m. As in Chapters 3 and 4 transports caused by the pressure gradient are scaled so as to be equivalent to the transport caused by an interface difference of -46m. In the figures no scaling has been carried out, but in all currents and transports quoted in the text and tables the appropriate scaling has been applied.

5.3 RESULTS: STEADY FORCING

5.3.1 Introduction

The result of three integrations forced by the mean difference in sea level (~16cm) between the Pacific and Indian Ocean are presented. Two integrations are carried out with free slip boundary conditions forcing the model ocean to a steady state with lateral viscosities of $100m^2s^{-1}$ and $1000m^2s^{-1}$. Finally an integration with noslip boundary conditions and a lateral viscosity of $1000m^2s^{-1}$ is made.

Results are presented and analysed in the same manner as in chapters 3 and 4. In plots of the velocity fields the velocity at every fourth grid point is shown. This is because of the larger area represented by the model.

5.3.2 Transition to steady state

The initial response is the development of two coastal Kelvin waves. The first wave propagates southward through the Mollucca Sea, around the eastern boundary of the Banda Sea, through the Timor Sea and along the North West Australian Shelf. The Second Kelvin wave propagates through the Macassar Strait and anticlockwise around the Celebes (in accordance with section 1.5.5). Part of this wave is reflected in the Molluca Strait and then follows the same pathway as the first wave into the Indian Ocean. This Kelvin wave behaviour is seen throughout the earlier models in Chapters 3 and 4.

In figures 5.3.1-5.3.3 evidence of the Kelvin wave on the North West Australian shelf can be clearly seen. The subsequent development of a western boundary current after initial passage of the Kelvin wave in the Macassar Strait is identical to that in the channel models of Chapter 3. Transport through the Lombok Strait increases as this western boundary current develops. Not until the western boundary current is fully developed (figure 5.3.4) does the anticlockwise flow around the Celebes cease.

In the Indian Ocean flow through the Lombok Strait turns east as another coastal Kelvin wave until the development of the western boundary current through the Lombok Strait (figure 5.3.4). The perturbation on the Australian shelf propagates offshore by the action of long Rossby waves and weakens as less transport occurs through the Timor Sea because of the development of the western boundary current through the Lombok Strait.

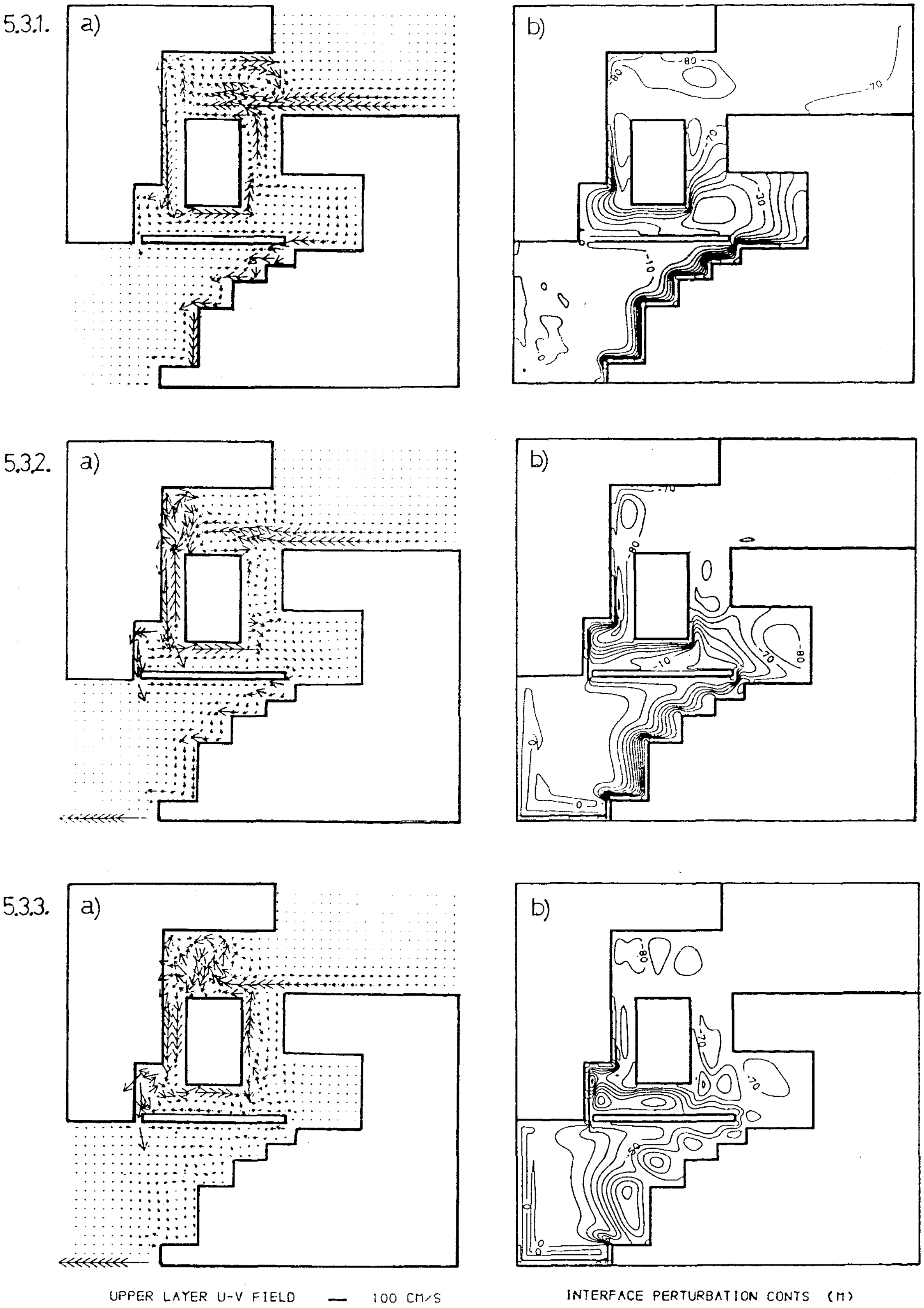

Figure 5.3.1 - 5.3.3 : Realistic Linear Baroclinic Model, Steady Forcing, $A_H = 100m^2s^{-1}$, Fields after (5.3.1) 25 days, (5.3.2) 50 days and (5.3.3) 100 days. a) Upper Layer Velocity, b) Interface Perturbation.

5.3.4.

5.3.5.

5.3.6.

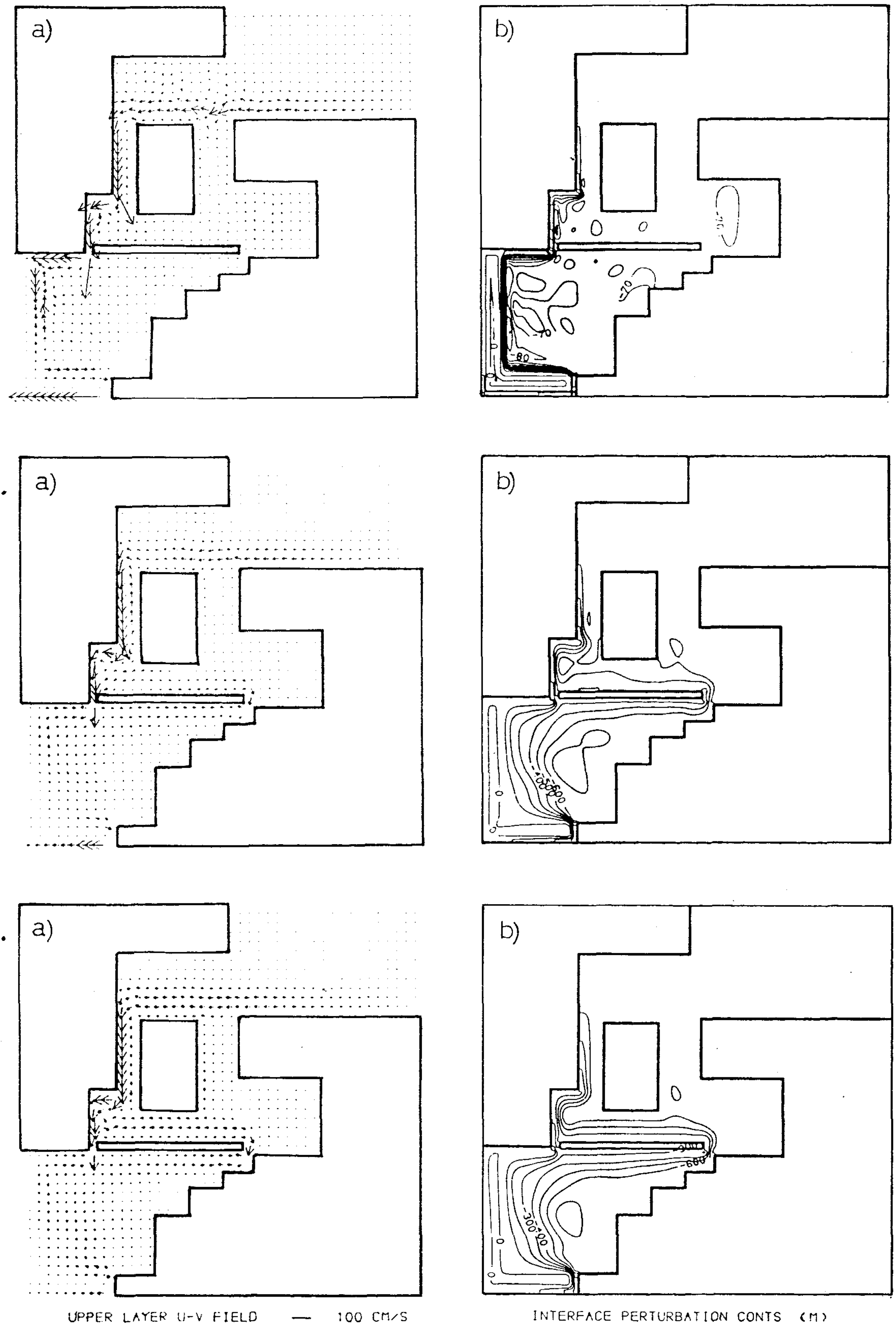

Figures 5.3.4 - 5.3.6 : Realistic Linear Baroclinic Model, Steady Forcing. a) Upper Layer Velocity, b) Interface Perturbation. (5.3.4) $A_H = 100m^2s^{-1}$, Fields after 300 days, (5.3.5) $A_H = 1000m^2s^{-1}$, Fields after 150 days (5.3.6) $A_H = 1000m^2s^{-1}$, Fields after 150 days, no slip boundary conditions.

In the Pacific Ocean transport into the Eastern Archipelago occurs along the southern boundary of the forcing region in the same way as in the earlier models. Maxima and minima in the interface fields and their associated regions of northward and southward flow can be seen north of the Celebes. These motions are due to planetary wave action as discussed in section 3.2.5.

Figure 5.3.4 shows the steady state solution. The throughflow can be seen to occur in a western boundary layer confined to the western margin of the model geometry. In the Indian Ocean the flow turns west south of Java and only turns south because of the forcing region. As in the earlier channel models there is negligible flow outside the western boundary layer at steady state.

To investigate the sensitivity of the numerical solutions to viscosity an additional 150 day integration with a viscosity of $1000 m^2 s^{-1}$ was made (figure 5.3.5). The solution is similar to that for the lower viscosity except for the increased width of the western boundary layer. The width of the southward flowing boundary current is now larger than the width of the Lombok Strait and as found in section 4.2 part of the southward flow is forced around the Lombok-Timor island into the Indian Ocean through the Timor Sea. Again the flow into the Indian Ocean, is seen to turn westward at steady state.

Similarly to section 3.3.4 an integration using noslip lateral boundary conditions was made. As expected the results, shown in figure 5.3.6, show increased transport at steady state through the Timor Sea because of the increased width of the western boundary current (see figure 3.3.5). The weak counter current at the western boundary is now forced around the Celebes to form in the Molucca Strait.

5.3.3 Energy and transport in the model

The balance between the kinetic and potential energy of the three integrations is given in table 5.3.1. The higher viscosity integrations attained a steady state after 150 days (when $\partial E/\partial t = 0$), the lower viscosity experiment was integrated for 300 days.

TABLE 5.3.1 **Energy balance at steady state**

Model	energy (Jm^{-2}) TOTAL	P.E	K.E
$A_H=100m^2s^{-1}$	3.08	2.68	0.40
$A_H=1000m^2s^{-1}$	2.38	2.24	0.14
$A_H=1000m^2s^{-1}$ (no slip)	2.28	2.20	0.08

As found in section 3.4.3. increasing the lateral viscosity reduces the kinetic energy of the circulation. The additional effect of no slip boundary conditions is to cause a slight reduction in both potential and kinetic energy.

The upper layer transport forced by the equivalent of a 16cm sea level difference through the various straits in the model is given in Table 5.3.2.

TABLE 5.3.2 **Transport at steady state**

Model	Pacific Inflow (Sv)	Macassar Strait (Sv)	Molucca Strait (Sv)	Lombok Strait (Sv)	Timor Sea (Sv)	Mean Throughflow (Sv)
$A_H=100m^2s^{-1}$	-8•1	-8•1	+0•1	-8•3	+0•6	-7•9+/-0•1
$A_H=1000m^2s^{-1}$	-7•5	-7•1	-0•4	-4•1	-3•4	-7•5
$A_H=1000m^2s^{-1}$ (no slip)	-7•2	-7•4	+0•2	-2•7	-4•5	-7•2

From the average of the three total transports (Pacific inflow, Macassar and Molucca Straits and Lombok Strait and Timor Sea) the mean throughflow is found. For the low viscosity case the standard mean error is given. In this case the model may not have quite attained steady state. The transport through the Lombok Strait is very sensitive to the dimensions of the western boundary layer.

The mean throughflow estimated in section 3.4.6 from equation (3.4.6.2) using a 16cm pressure gradient was 12.6Sv. This geostrophic approximation is much larger than the mean transports in table 5.3.2. In section 3.4.6 there was good agreement between the linear open channel models and the geostrophic estimate.

5.4 RESULTS: SEASONAL FORCING

5.4.1 Introduction

The effects of the strong seasonal variation in the north-south pressure gradient between the Pacific and Indian Ocean on the throughflow are investigated in this section. Wyrtki's (1987) data for the difference in sea level between the Phillipines and Darwin in the Indian Ocean is shown in figure 1.2.3. A simple sine wave can be used to represent the observed sea level differences.

The seasonal variation in the forcing is represented by a mean interface difference of -75m with the seasonal signal of +/-75m superimposed (forcing Pacific). As stated in section 5.2.4. This difference leads to enhanced transport throughout the region. Account has been taken of this in all the values quoted in the text.

Prior to using the realistic linear baroclinic model with seasonal forcing the linear baroclinic model of section 3.2 is used to obtain an initial understanding of the effects of the seasonal forcing. Finally the realistic linear baroclinic model with A_H=1000m^{2}s^{-1} is integrated from the steady state of section 5.3.3 for a further fifteen months with the seasonal forcing of figure 1.2.3. For simplicity one month is taken as thirty days in length. All integrations start in April when sea level difference is 16cm.

5.4.2 The open channel model

The linear baroclinic model described in section 3.2 is integrated for two years with the seasonal forcing described in section 5.4.1 Figures 5.4.1 - 5.4.4 show sections in time through the velocity fields of the channel.

The development of the western boundary current can be seen to occur even with the seasonal forcing (figures 5.4.1 and 5.4.3). Figures 5.4.2 and 5.4.4.a) show the strong southward flow at the western boundary reversing after six months at the equator. Further south (5.4.3, b) and c) the time at which the current is towards the north is shorter. At 8°S the reversal of the boundary current occurs approximately two months after that at the equator. This phase difference is equal to the difference in time between the initial formation of the western boundary current at the two latitudes found in section 3.2.5.

Figure 5.4.4 shows short planetary waves propagating eastward at approximately $1.5 cms^{-1}$. The waves are formed initially by the same process as those with the steady forcing (see section 3.2). Subsequent generation of the planetary waves coincides with the change in direction of the western boundary current. The inertia gravity waves formed by the initial disturbance decay within the first 100 days similar to those in the channel with steady forcing with $A_H=100m^2s^{-1}$ (section 3.2.4). In the second year of the integration the seasonal variation in the velocity fields is very smooth. The slow variation of the forcing term does not regenerate inertial period waves. The inertia-gravity waves are generated by the passage of the initial front.

Figures 5.4.5 - 5.4.7 show the energy balances and conversion rates in the channel. The seasonal cycle can clearly be seen, with maximum and minimum total energy occurring in August and February respectively. The rise and fall in energy in the channel is asymmetrical. The phase differences between the input of potential

5.4.1.

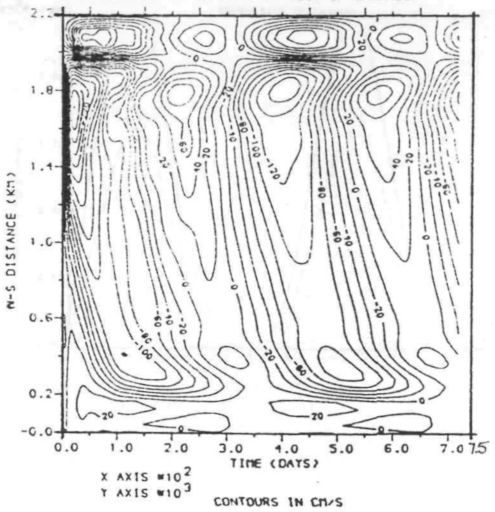

5.4.2.

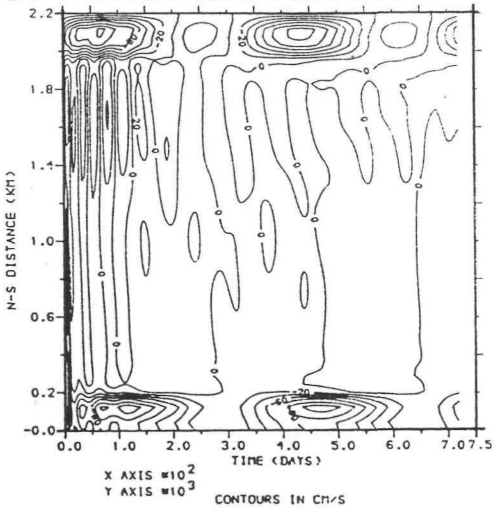

5.4.3.

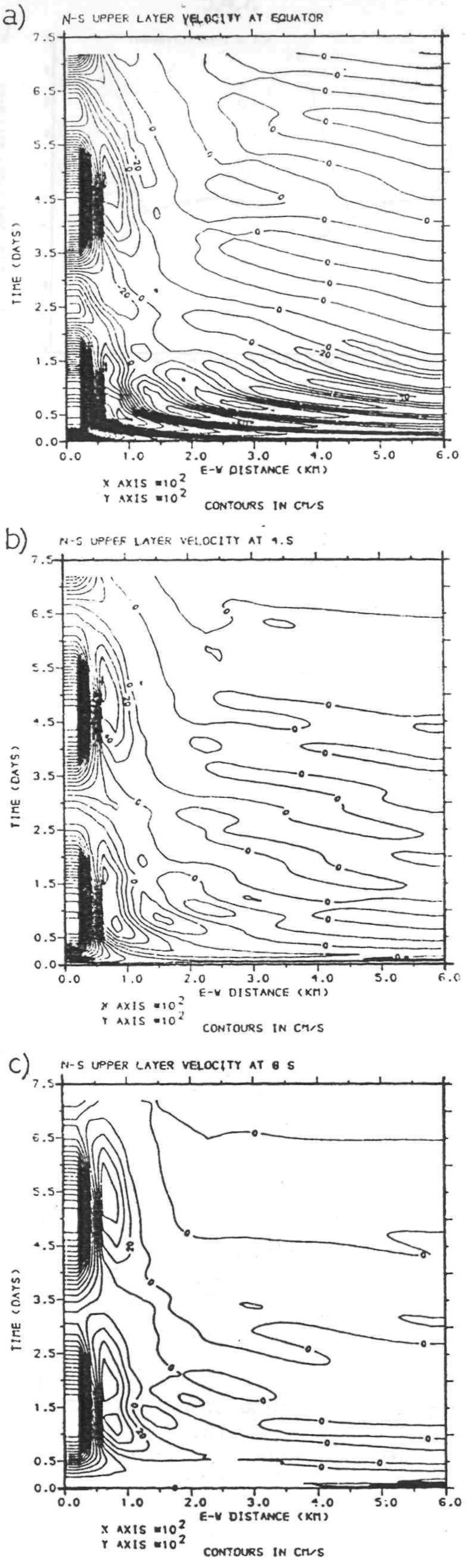

5.4.4.

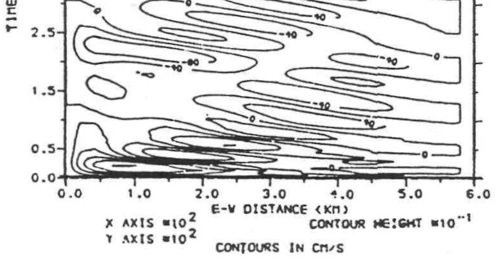

Figures 5.4.1 - 5.4.4 : Sections in time through the seasonally Forced Open Channel Model. (5.4.1), (5.4.2) North - South Sections through Meridional Velocity, (5.4.3) East-West section through Meridional Velocity, a) at Equator, b) at 4°S and c) at 8°S. (5.4.4) East-West Section through Zonal Velocity at 4°S.

5.4.5.

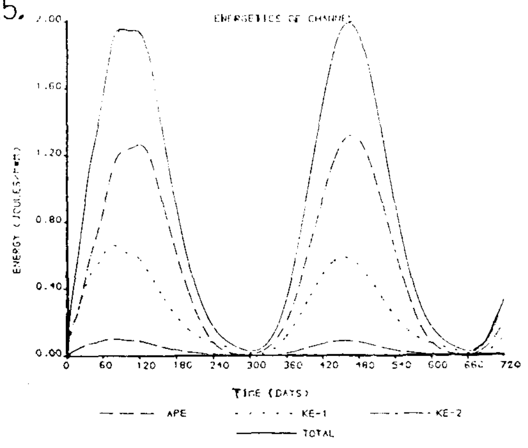

5.4.7.

a)

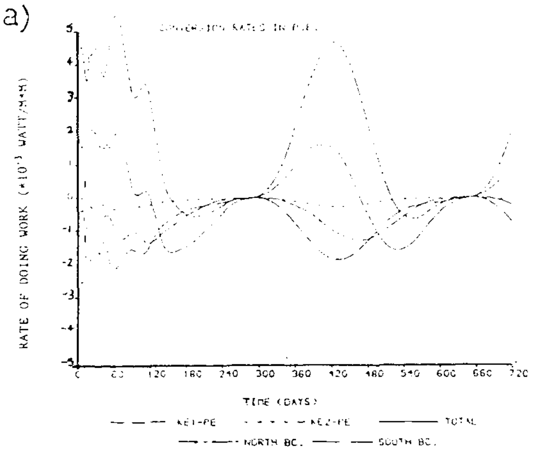

5.4.6.

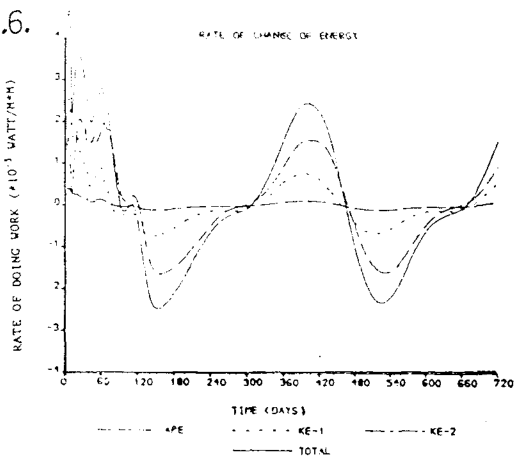

b)

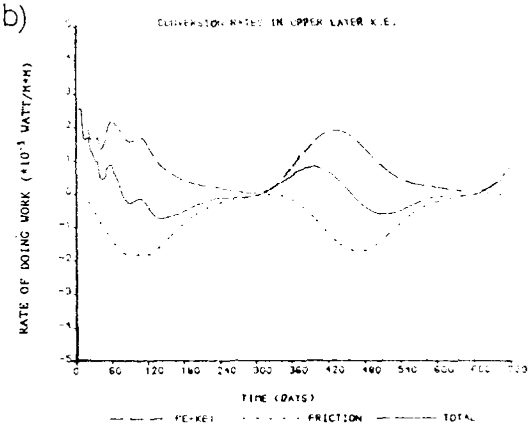

5.4.8.

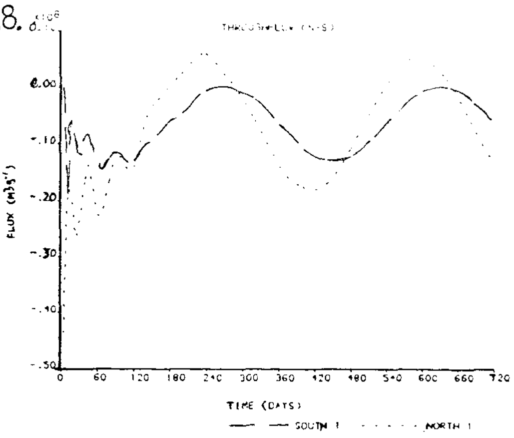

c)

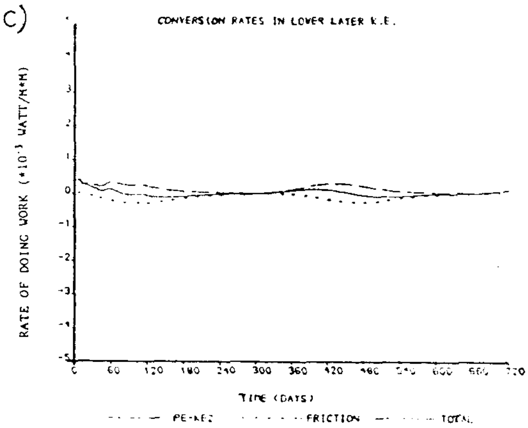

Figures 5.4.5 - 5.4.8 : Energy Budget and Transport in the Seasonally Forced Open Channel Model (5.4.5), Total energy, (5.4.6) Rate of Change of Energy (5.4.7), Conversion Rates of a) Potential Energy and b) Upper Layer and c) Lower Layer Kinetic Energy. (5.4.8). Transport through channel (Positive Northwards).

energy in the north and subsequent removal of this energy by the southern forcing region and the effect of viscous dissipation account for the faster rise in total energy (see figure 5.4.7 a) - c).

The transport through the upper layer of the channel is shown in figure 5.4.8. The seasonal signal is clearly displayed. The baroclinic model is never in a steady state so the transport at the north of the channel is not equal to that at the south of the channel. The transports are summarised in table 5.4.1.

TABLE 5.4.1 **Transport in channel model**

	Transport		Month of
	Mean (Sv)	Oscillatory (Sv)	max. transport
North	-6.35	11.55	June
South	-6.35	6.45	August

There is a phase difference between the transports in the north and south due to the time taken for the boundary current to form between these latitudes. In the South the ratio of the mean to the amplitude of the seasonal transport is similar as expected from the linear nature of the problem and the form of the seasonal pressure gradient (fig. 1.2.3). In the north the seasonal transport is larger due to partly to the accumulation of mass within the channel between 2°N and 11°S. To ascertain whether this is a real feature rather than an artefact of producing upper layer transports from the baroclinic model it would be necessary to repeat the experiment with the two layer model.

5.4.3 The realistic model: Results.

Figures 5.4.9 - 5.4.10 show the instantaneous fields of the realistic linear baroclinic model at two monthly intervals when forced by the seasonal pressure gradient of figure 1.2.3.

In February energy is at a minimum (figure 5.4.5 and figure 5.4.11) and there is little transport from the Pacific into the region (figure 5.4.14). Similarly there is little circulation in the Macassar and Molucca Straits (figure 5.4.9.a). There is a weak

5.4.9.

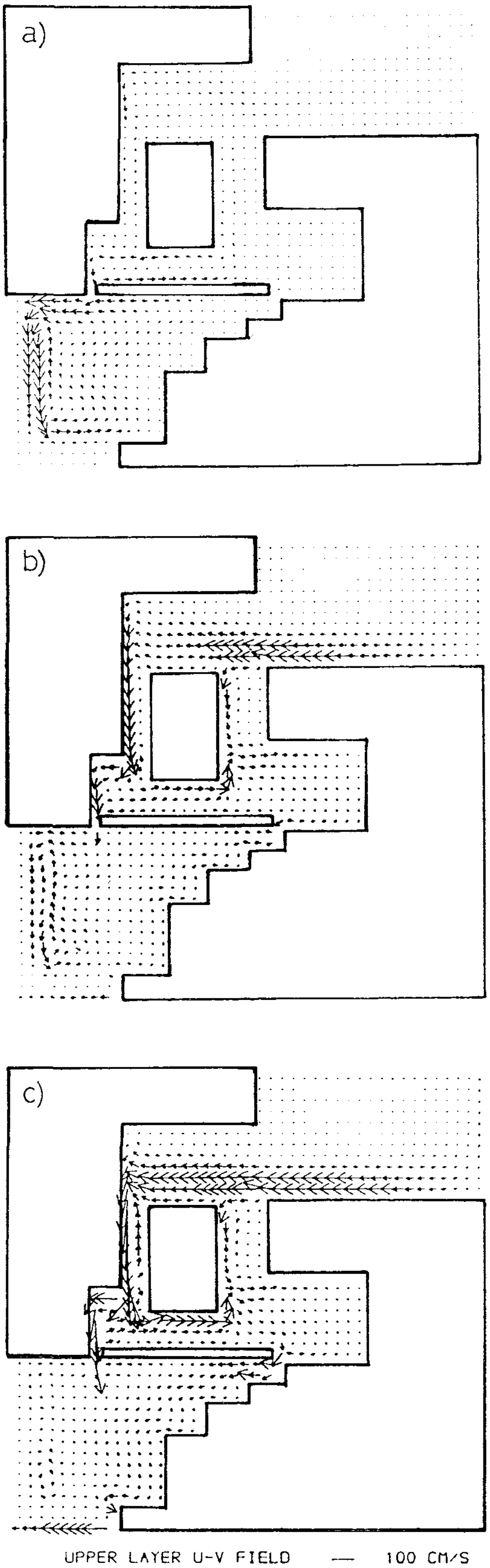

5.4.10.

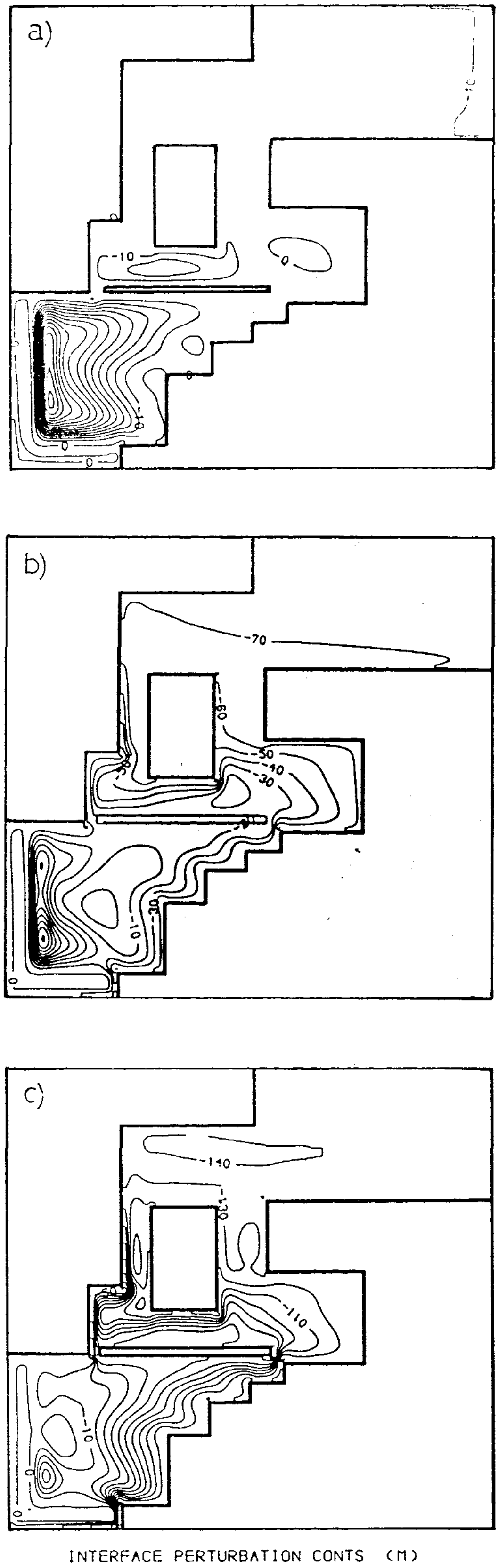

Figures 5.4.9 - 5.4.10: Realistic Linear Baroclinic Model, Seasonally forced , A_H=1000m^2s^{-1}, (5.4.9) Upper layer Velocity (5.4.10) Interface Perturbation. Fields in a) February, b) April and c) June.

5.4.9. 5.4.10.

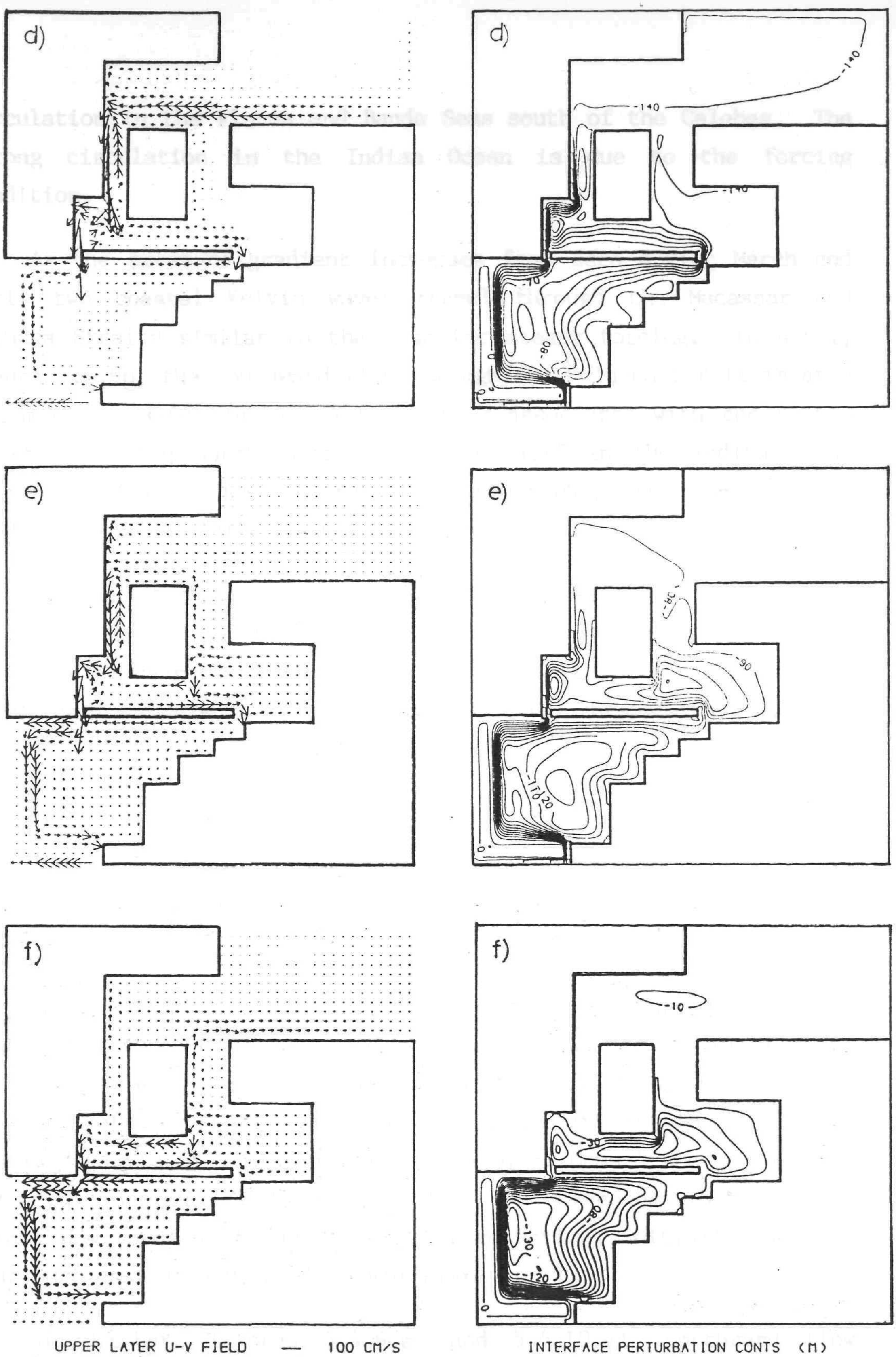

Figures 5.4.9 - 5.4.10: Realistic Linear baroclinic Model, Seasonally forced , A_H=1000m^2s^{-1}, (5.4.9) Upper layer Velocity (5.4.10) Interface Perturbation. Fields in d) August, e) October and f) December.

circulation in the Flores and Banda Seas south of the Celebes. The strong circulation in the Indian Ocean is due to the forcing condition.

As the pressure gradient increases from zero during March and April two coastal Kelvin waves travel through the Macassar and Molucca Straits similar to the case for steady forcing. In April, figure 5.4.9b, the southward flow through the Molucca Strait is at a maximum (see also figure 5.4.14). Flow associated with the Kelvin waves along the North West Australian Shelf in the Indian Ocean begins to destroy the recirculation associated with the boundary condition in the Indian Ocean.

In June the transport through the Macassar Strait is at a maximum. Circulation throughout the region is similar to that after 75 days of integration with the steady forcing in section 5.3.2. The development of the western boundary region through the Macassar Strait can clearly be seen with regions of southward and northward flow in the Strait. At this time the flow into the Indian Ocean is still that associated with the transitional Kelvin waves and does not turn west south of Java (figure 5.4.9.c)). The circulation in the India Ocean associated with the forcing region has now been destroyed.

In August, figure 5.4.9.d), circulation is similar to the steady state of figure 5.3.5.a). This circulation persists for a month until the pressure gradient across the Molucca Strait reverses and flow out of the Banda Sea occurs. In August transport into the Indian Ocean is at a maximum. Currents of ~$120cms^{-1}$ are produced in the Lombok Strait. Outflow into the Indian Ocean through the Lombok Strait now turns west due to Rossby wave action, initially the flow must turn east as a coastal Kelvin wave.

In October, figures 5.4.9.e) and 5.4.10.e), northward flow through the Molucca Strait occurs. This flow is forced by the interface gradient between the Banda Sea and the Pacific. The interface depression in the Banda Sea developed through the action of the initial Kelvin waves that caused the interface to be the Pacific returns to the unperturbed state so does the interface along the eastern boundary. The interface depression originally at the coast propagates west throughout September-February creating westward flow south of the Celebes.

In December, figure 5.4.9.f), there is northward flow through the Macassar and Molucca Straits. The flow associated with the interface depression in the Banda Sea is not significantly different to that in October. South of the Celebes the circulation has increased as pressure gradients develop. In the Indian Ocean the westward flow south of Java and the Lombok-Timor island remains until the March-April Kelvin waves destroy the circulation set up by the Rossby waves.

5.4.4 **The realistic model: Energy and transport**

The total energy balance shown in figure 5.4.11 shows the same ratio between potential and kinetic energy as for the steady forcing case given in table 5.3.1 in July and August. Kinetic energy being approximately 6% of the total energy at this time. In January to March this ratio has increased and the kinetic energy is approximately 17% of the total energy.

The asymmetry of the seasonal energy variation shown in figure 5.4.12 is similar to that of figure 5.4.7 and is again due to the phase difference between removal of energy and input of energy in the south and north respectively.

Figure 5.4.13 shows the upper layer transport through the various straits and is summarized in table 5.4.2. The transport through each strait is approximated by a sinusoidal seasonal oscillation superimposed upon a mean value. The month that the maximum transport occurs is also given.

Figure 5.4.14 shows the transport into the region from the Pacific compared with the combined transports through the Macassar and Molucca Straits and the Lombok Strait and the Timor Sea. The

5.4.11.

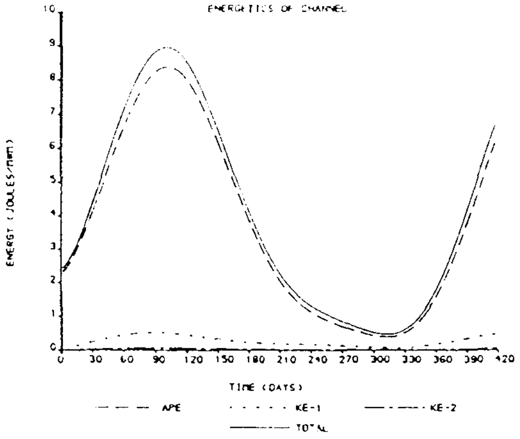

5.4.12.

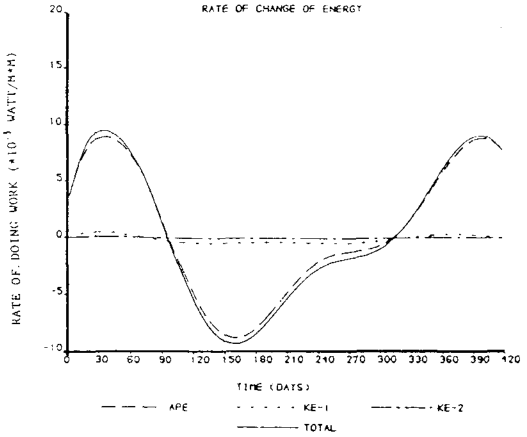

5.4.13.

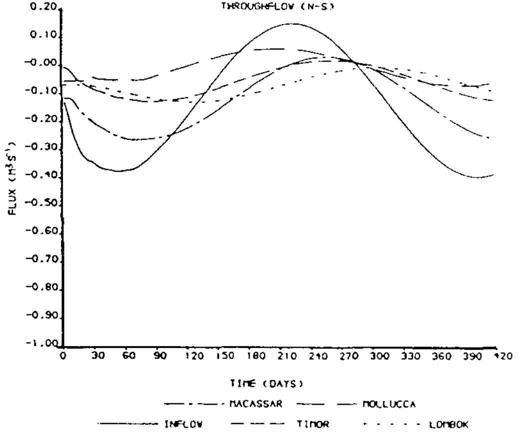

5.4.14.

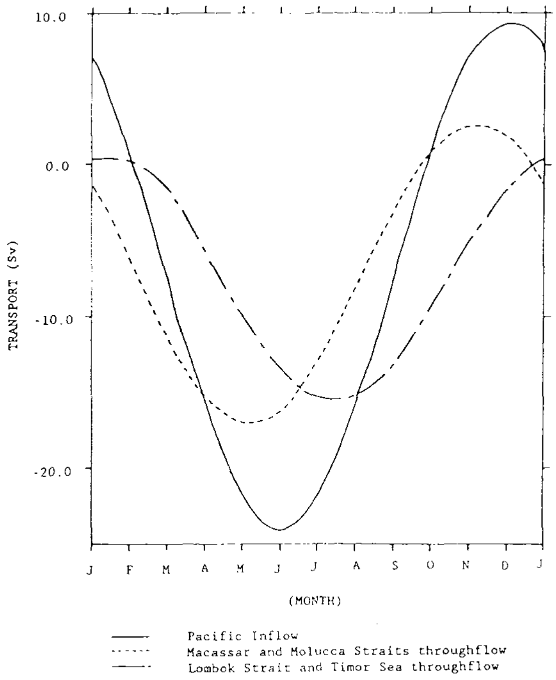

5.4.15.

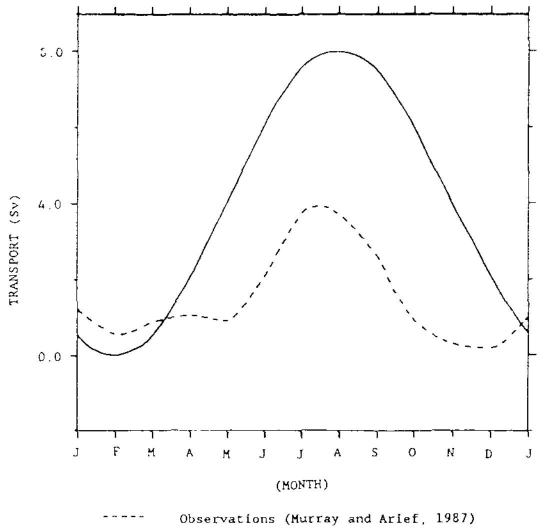

Figures 5.4.11 – 5.4.15 : Energy Budget and Transport in the seasonally Forced Realistic Model. (5.4.11). Total energy, (5.4.12) Rate of Change of Energy (5.4.13). Transport through the Channel. (5.4.14). Transport through Straits (5.4.15). Transport through Lombok Strait (Positive Southwards).

seasonal oscillation is greatest for the inflow and weakest for the flow into the Indian Ocean. This is similar to the situation in the open channel (Table 5.4.1).

TABLE 5.4.2 **Transport in Realistic Model**

	Transport		Month of
	Mean (Sv)	Oscillatory (Sv)	max. transport
Pacific inflow	-7.4	16.7	May-June
Macassar Strait	-7.0	9.0	June
Molucca Strait	-0.2	4.0	March
Timor Sea	-3.5	4.4	July
Lombok Strait	-4.0	4.0	August

The prediction for the total transport from the Pacific to Indian Ocean forced by the seasonal variation in sea level difference from this model is 7.5 +/- 7.9 Sv with the maximum throughflow occurring in July - August.

The mean transport through each strait in table 5.4.2 is approximately equal to the transport through each strait when the steady forcing of section 5.3 is used (see table 5.3.2).

5.4.5 The realistic model: Comparison with observations in the Lombok Strait.

In this section a preliminary comparison of the results of the realistic model with the current meter observations of Murray and Arief (1988) in the Lombok Strait is made.

The Lombok Strait is between 800-1000m in depth except in the south where a small island divides the Strait. On either side of the island divides the Strait. On either side of the island there are sills with a maximum depth of 350m. In the north of the strait the channel is 30km wide between the 200m isobaths (35km between Bali and Lombok). Murray and Arief found tidal currents of +/- 3.5ms^{-1} in the south of the channel. Drag forces here were too large for a line of moorings. In the north the tidal currents ranged between 20-50cms^{-1} over the spring neap cycle. Accordingly observations were made at two stations in the northern strait between January 1985 and February 1986.

Observations were made at 35m, 75m, 300m and 800m. Results showed a mean flow to the south with a strong decrease in speed between 75m and 300m. Reversals of the mean current lasting for approximately 10 days were observed in January - April and were associated with intense cyclones crossing the Timor Sea.

The annual time series of the low pass currents (periods below 60 hours removed) at 35m shows maximum southward velocities (85cms^{-1}) were attained between July and September. A minimum was found between October and January with speeds generally less than 10cms^{-1}. The linear baroclinic model gives a maximum velocity of 1.2ms^{-1} in the Lombok Strait in August and the velocities decrease sinusoidally to a minimum in February of zero.

Murray and Arief computed the volume transport through the Lombok Strait across 8°27'S for each month using the monthly means of the component of the low-pass currents from the mooring sites in the north of the channel. The shape of the velocity profile between the 75m and 300m levels was interpolated using data from the Snellius expedition (Lek, 1938). The cross sectional area of the strait at 8°27'S was determined and found to be $13.3 \times 10^6 m^2$ above the 400m depth level.

Murray and Arief found that 80% of the net transport was contained in the upper 200m, in good agreement with Wyrtki (1987) who concluded that the pressure gradient that drives the throughflow is concentrated in the upper 200m. Murray and Arief neglected the transport in the lateral frictional wall layers of thickness 1km that arise when the Lombok Strait is considered a narrow (non rotating) channel. Results of the transport computation are shown in figure 5.4.15 for comparison with the transport determined in the model.

The model transport is in phase with the observations of Murray and Arief. However the mean transport of the model, 4.0Sv, is more than twice that of the observations, 1.7Sv. The model transport is too large because the resolution in the Lombok Strait is inadequate (require 15km grid for 30km channel). The mean transport through the Lombok Strait in the model is also sensitive to the choice of lateral boundary condition and horizontal viscosity (table 5.3.2).

5.5 RESULTS: 30 DAY FORCING

5.5.1 Introduction.

The effects of a shorter period oscillation of +/-15m at the interface superimposed on the mean north-south interface difference of -75m are investigated in this section. The aim is to represent the 30 day equatorial wave in the Pacific Ocean of Semtner and Chervins (1989) model. The 30 day oscillation is due to the westward propagation of long Rossby waves, discussed by Weisberg (1980). As with the experiments with seasonal forcing an integration is first carried out with the open channel model.

5.5.2 The open channel model

The linear baroclinic model described in section 3.2 is integrated for 300 days with the 30 day oscillation with the arbitrarily chosen amplitude of (±20%) in the steady forcing. Figures 5.5.1-5.5.3 show sections in time through the meridional velocity fields.

The development of the western boundary layer can clearly be seen in figure 5.5.1. Oscillations due to the 30 day signal can be seen in the strength of the western boundary current. The 30 day forcing is not of sufficient amplitude to cause reversal of the boundary current.

The oscillations are strongest at the equator (figure 5.5.3a), where after 200 days the emission of westward propagating Rossby waves with a speed of $25 \mathrm{cms}^{-1}$ occurs every 30 days. The Rossby wave is generated at the time a coastal Kelvin wave passes. Comparison of figure 5.5.3a with figure 3.2.3.e) shows how, after 200 days, the zonal wave motion becomes less dominated by the short Rossby waves when the continual generation of long Rossby waves at the eastern boundary occurs. Away from the equator the amplitude of the 30 day oscillation decays (figure 5.5.3.b)-d). The 30 day oscillation produces a coastal Kelvin wave that can clearly be seen in figures 5.5.2 and 5.5.3.d).

The oscillation of the western boundary at the equator is in part due to the Kelvin wave. At the equator the Rossby radius is 228km so the Kelvin wave is effective across the entire channel width. This is also the case at 4°S. At 12°S, figure 5.5.3.d), the Kelvin wave can be seen decaying away from the eastern boundary and does not affect the western boundary.

The budget of energy in the channel (figure 5.4.4.a)) shows the 30 day oscillation about a mean value. The mean value is attained after approximately 150 days as in the case with steady forcing. There is a lag of 5 days between the potential energy and the kinetic energy of the channel. Similarly there is a lag of 5 days between the maximum transport in the north and that in the south

5.5.1.

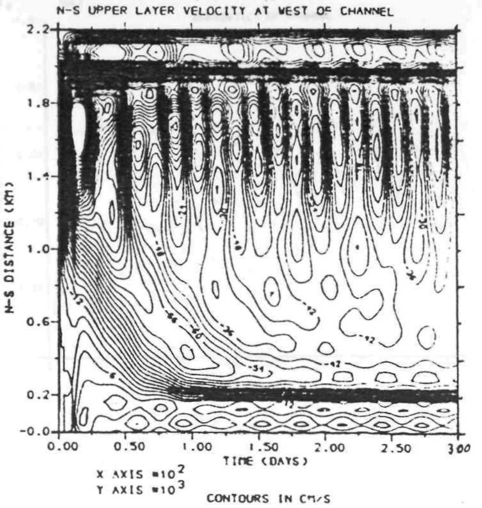

5.5.2.

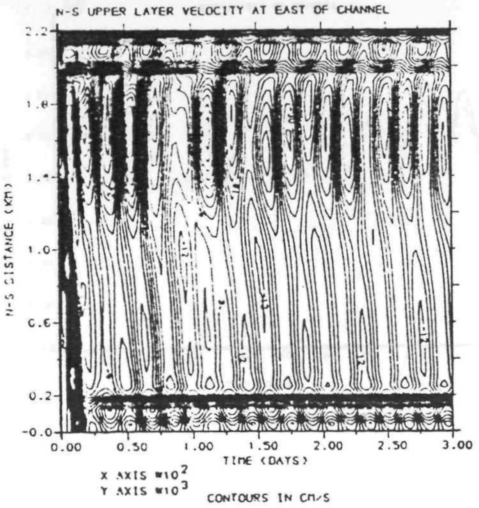

5.5.3.

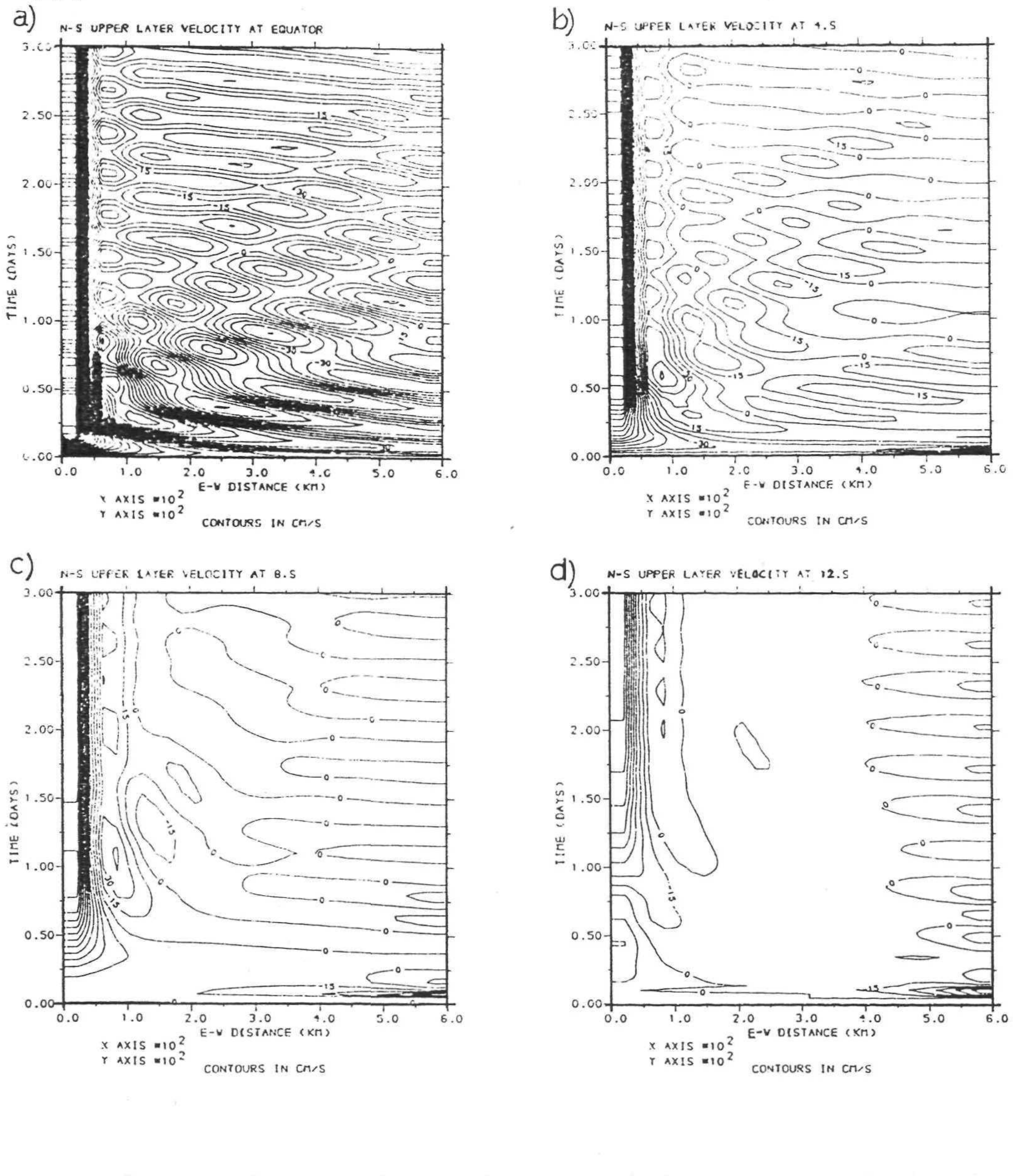

Figures 5.5.1 - 5.5.3 : Sections in time through the 30 day Forced Open Channel Model. (5.5.1), (5.5.2) North - South Sections through Meridional Velocity. (5.5.3) East - West Sections through Meridional Velocity a) at Equator, b) at 4°S c) at 8°S and d) at 12°S.

5.5.4.

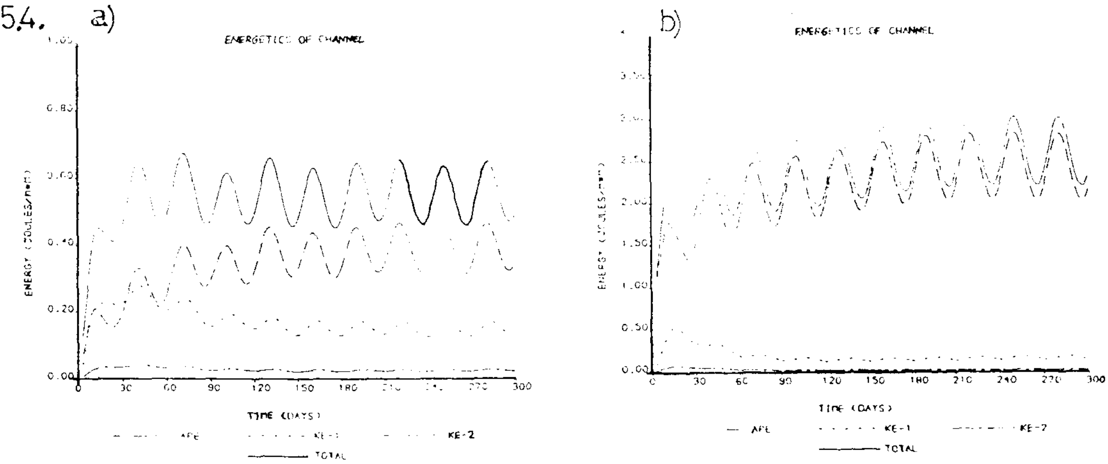

5.5.5.

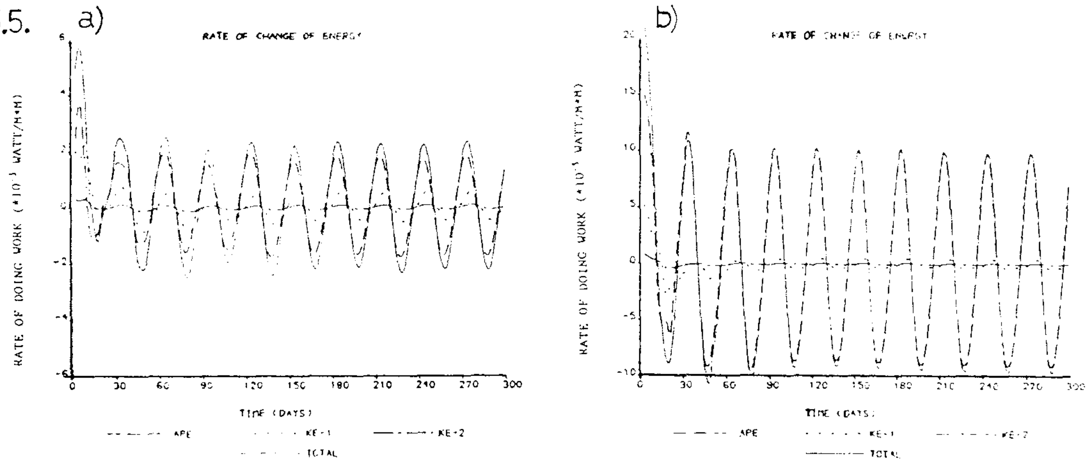

5.5.6.

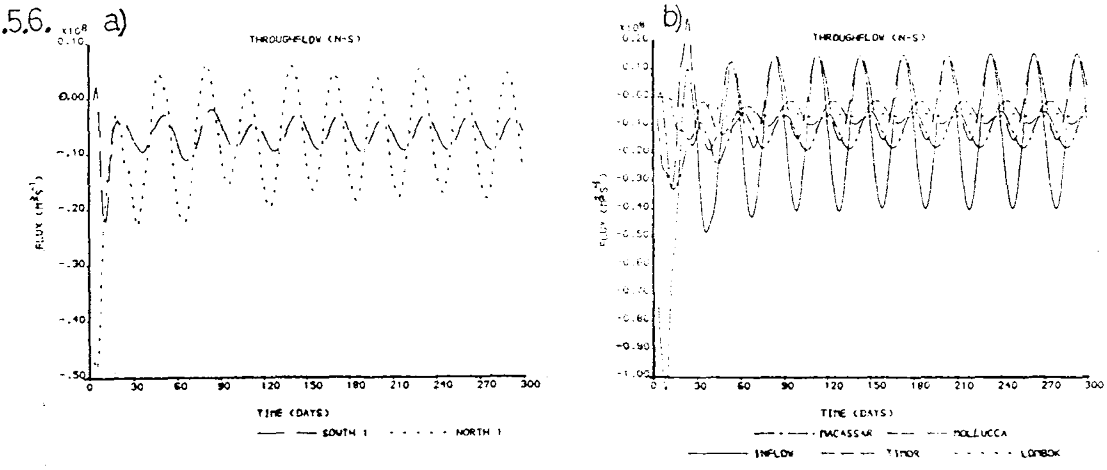

Figures 5.5.4 - 5.5.6 : Energy Budget and Transport in 30 day Forced Models. (5.5.4) Total Energy, (5.5.5) Rate of Change of Energy, (5.5.6) Transport (Positive Northwards) a) Open Channel Model b) Realistic Model,

(figure 5.5.6.a)). It can be seen that there is a greater difference between the amplitude of oscillatory transport in the north and south than in the seasonally forced model (table 5.4.1). This may be due to resonance associated with the timescale of the forcing. This could be established with a series of further experiments. The time sequence of the maximum energy and transport in the channel is summarized in table 5.5.1.

TABLE 5.5.1 **Timing of maximum energy and transport in channel model.**

	(day)
maximum P.E.	280
maximum K.E.	285
maximum transport (N)	290
maximum transport (S)	295

The time delay between the passage of a Kelvin wave from the north of the channel to the south of the channel accounts for the phase difference between transport in the north and south. The lag between the kinetic and potential energy maximums is due to the conversion rate of potential to kinetic energy. Potential energy is added to the channel in the northern forcing region, this has then to be converted to kinetic energy.

The mean transport in the upper layer is 6.35Sv. The mean transport is the same as in section 5.4.2 in the seasonally forced model.

5.5.3 The realistic model: Results.

Figure 5.5.7 - 5.5.8 show the instantaneous fields of the realistic linear baroclinic model at 10 day intervals after 300 days of integration. Forcing is by a mean pressure gradient with a 30 day oscillatory component equal to 20% of the mean gradient. The fields are similar to the steady state solution of figure 5.3.5.a) but show

increased circulation in the Molucca strait and Banda Sea due to the passage of two coastal Kelvin waves that are generated every 30 days.

Figure 5.5.7.b) shows the passage of the Molucca Strait Kelvin wave. Comparison with figure 5.3.5.a) shows enhanced flow out of the Pacific associated with the increase in pressure gradient. Figure 5.5.7.c) shows eastward flow through the Flores Sea and northward through the Molucca Strait. This northward flow is due to the change in sign of the pressure gradient across the Strait (see figures 5.5.8.b) and c) caused by the Macassar Strait Kelvin wave. Figure 5.5.7.a) shows the fields at the time of maximum rate of change of potential energy. (ie. when forcing is instantaneously the mean value -75m.). As with the open channel case of section 5.5.2 the western boundary current is not significantly altered by the 30 day oscillation. However the counter current in the Macassar Strait is affected by the propagation of Kelvin waves around the Celebes. In figure 5.5.7.a) the current is enhanced and in figure 5.5.7.b) the current is reduced.

5.5.4 The realistic model: Energy and transport.

The balance between the kinetic and potential energy is shown in figure 5.5.4.b). The same ratio between potential and kinetic energy as in the steady state is found with kinetic energy being approximately 6% of the total energy.

As with the open channel of section 5.5.2 the maximum in the kinetic energy is found to lag the maximum in the potential energy by approximately five days.

Figure 5.5.6.b) shows that the transport through the Lombok Strait is largely unaffected by the Kelvin waves. Table 5.5.2 summarizes the transport through the different straits giving the mean and oscillatory transports and the phase difference between the maximum transports relative to the Pacific inflow.

5.5.7.

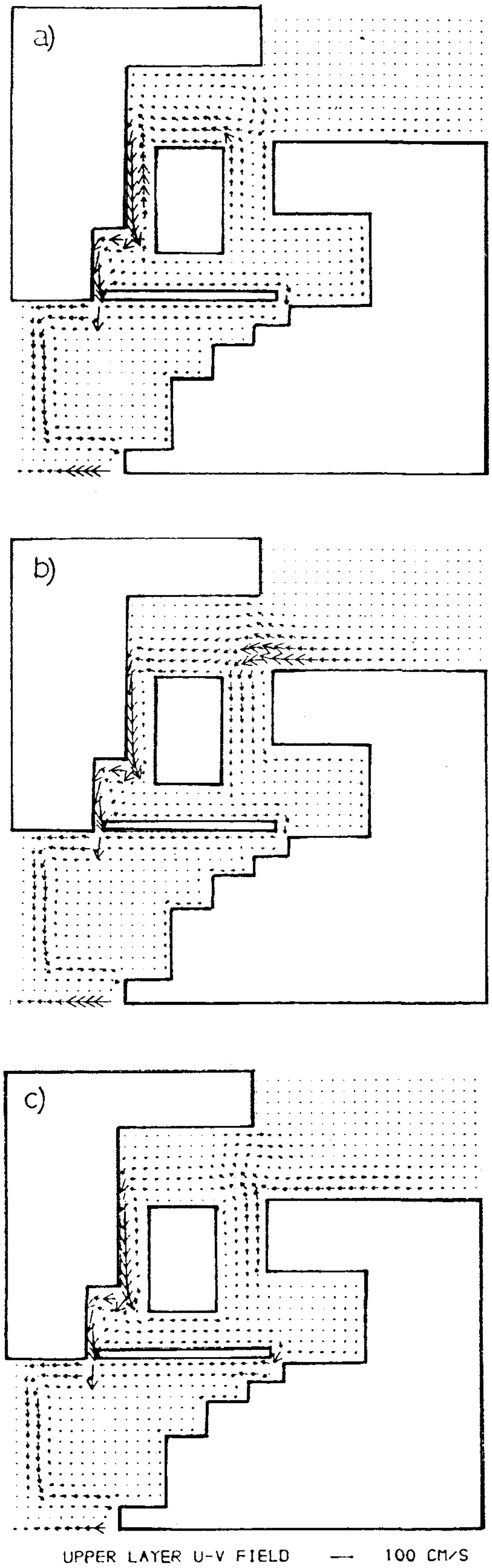

5.5.8.

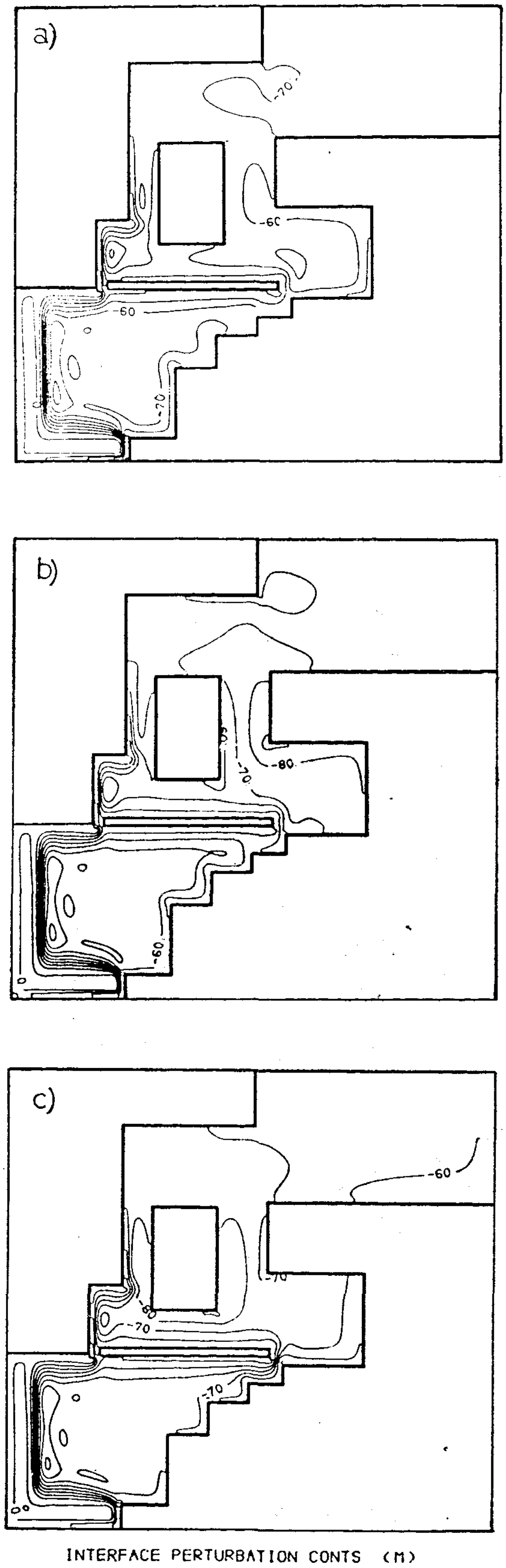

Figures 5.5.7 - 5.5.8 : Realistic Linear Baroclinic Model, 30 day Forcing, A_H=1000m^2s^{-1}. (5.5.7). Upper Layer Velocity, (5.5.8) Interface Perturbation. Fields a) at 300 days, b) at 310 days and c) at 320 days.

TABLE 5.5.2 Transport Through Realistic Model.

	Mean Transport (Sv)	**Oscillatory Transport (Sv)**	**Phase Difference (days)**
Pacific inflow	-7.6	16.8	0
Macassar Strait	-7.2	4.0	-8
Molucca Strait	-0.4	9.0	-1
Timor Sea	-3.4	2.4	-11·5
Lombok Strait	-3.9	0.4	-17

The phase differences are associated with the time for the Kelvin waves to propagate around their respective paths. The mean throughflow from the Pacific to Indian Ocean is -7.5Sv the same as for the model with seasonal forcing (table 5.4.2) and for the steady state solution with $A_H = 1000m^2s^{-1}$ and freeslip boundary conditions (table 5.3.2).

6. DISCUSSION

6.1 CONCLUSIONS

In this section the main conclusions of the results in chapters 3,4, and 5 are summarized. The conclusions are numbered in chronological order and will be discussed further in the following sections.

1) Transitional motions forced by a north-south pressure gradient within a cross equatorial channel are dependent on the width of the channel. Initially a front travels southwards through the channel and becomes confined to the eastern boundary as a Kelvin wave away from the equator. Passage of the front excites both westward (long) and eastward (short) propagating Rossby waves at the corresponding boundaries of the channel. Initially all wavelengths of Rossby wave may be generated. After the waves have been reflected by the boundaries a few times constructive and destructive interference occurs and the finite width of the channel causes only certain channel modes to exist. No evidence is found for long westward propagating Rossby waves reflecting at the eastern boundary.

2) At the steady state southward flow through the channel occurs in a western boundary layer where the required change in planetary vorticity is balanced by dissipation of vorticity. When viscous dissipation of vorticity is the dominant process the thickness of the boundary current is dependent upon the value of the horizontal viscosity and the choice of lateral boundary condition. The solution with no slip boundary conditions is similar to that predicted by Munk (1950). Free slip boundary conditions give a boundary current width of approximately two-thirds of that produced by the no slip boundary condition.

3) Meridional flow through the channel at steady state is found to be largely due (>80%) to a balance between the cross channel pressure gradient and the coriolis term in the zonal momentum equation.

4) When nonlinear terms were included in the model equations it was found that for low values of horizontal viscosity ($A_H < 500m^2s^{-1}$) an inertial boundary layer was formed. Associated with this boundary layer was the generation of eddies of wavelength 100-200km similar to the Rossby radius.

5) The effect of islands in the channel was to divert parts of the boundary solutions (steady or transient) around the island. Thus at steady state part of the boundary current might occur to the east and west of an island if the island was positioned within a boundary layer width of the western boundary. The further north the island was positioned in the channel the closer the transport through the channel was to the open channel case.

6) Inclusion of zonal sills within a free surface model appeared to increase the transport throughout the channel by up to 15%. The steady state flow was partially diverted to the east at the northern edge of the sill and returned westward to rejoin the southward flowing western boundary current at the southern edge of the sill. This localised effect was due to the flow following contours of f/H. There was no evidence of reflected northward flow north of the sill.

7) The addition of regions of shallow (60m) shelves, where bottom dissipation of vorticity could occur, on either side of the channel increased the transport through the channel by 20%. At steady state transport occurred over the western shelf in a broad Stommel type boundary layer and in a weakened Munk type boundary layer that formed at the western shelf edge in the deep channel.

8) A realistic linear baroclinic model (20km grid) of the Eastern Archipelago forced by a north-south gradient on the interface equivalent to the mean difference in sea level (16.3cm) between the Western Pacific and South Eastern Indian Ocean predicted values for the mean transport from the Pacific to the Indian Ocean of 7.2-7.9Sv.

9) The initial response of the realistic model to switched on forcing was the development of two coastal Kelvin waves. The first wave propagated southwards through the Molucca Sea, around the eastern boundary of the Banda Sea, through the Timor Sea and along the North West Australia Shelf. The second Kelvin wave propagated through the Macassor Strait and anticlockwise around the Celebes;

eastwards through the Flores Sea and northwards through the Molucca Strait and follows the same pathway as the first wave into the Indian Ocean.

10) The steady state transport took 150–200 days to develop depending on the value of the horizontal viscosity, A_H. Outflow into the Indian Ocean through the model representations of the Lombok Strait and Timor Sea was dependent on the choice of A_H and the lateral boundary conditions.

11) Forcing the regional model with the seasonal north–south pressure gradient and using a horizontal viscosity A_H of $1000 m^2 s^{-1}$ gave a mean throughflow of 7.5Sv with a seasonal oscillation of +/-7·9Sv. Maximum throughflow occurred in August and minimum in January. Flow through the Lombok Strait accounted for 53% of the total transport into the Indian Ocean.

12) The seasonal forcing produced a quasi steady state, similar to 10) above, in August. This quasi steady state circulation decreased in strength to zero during the period September to February as the north–south pressure gradient decreased to zero. In March–April as the pressure gradient begins to increase the transient motions in 8) above were produced followed by the adjustment back to quasi steady state in August. The seasonal forcing thus produced a pulse of outflow confined to the North West Australian shelf during March-July. During the remainder of the year outflow from the Lombok Strait and Timor Sea turned westwards along 10°S.

13) Changes in the Pacific sea level reached the North West Australian Shelf with the Kelvin wave. Changes in the Indian Ocean sea level south of Java occur only after Rossby waves have had time to propagate.

14) The use of a 30 day oscillation equivalent to ± 3cm in addition to the mean pressure gradient of 16cm gave a mean transport of 7·5Sv and an oscillatory transport of +/- 2.5Sv. The oscillatory transport occurred entirely through the Timor Sea. 30 day forcing is of too high a frequency for the western boundary response of 12), 13) above to develop.

6.2 DISCUSSION OF RESULTS

6.2.1 Introduction

In this section the results presented in chapters 3,4 and 5 are discussed with reference to other work. The aim and spirit of the experiments has been discussed in section 1.6.1. In section 6.2.2 lack of suitable analytic solutions and other similar modelling studies keeps the discussion short. In section 6.2.3 the results of the experiments with islands, sills and shelves which were largely preliminary to the development of the realistic model are briefly discussed, extensive discussion is not merited and would not be within the aims of this study.

6.2.2 The cross equatorial channel

The results of chapter 3 show that initially the transition to steady state circulation in a narrow cross equatorial channel is the same as that for an equatorial ocean scale basin (>2000km in width). Namely the rapid propagation of Kelvin waves away from the equator along the eastern boundary followed by subsequent development of poleward flow in a western boundary layer due to the trapping of eastward propagating short Rossby waves. The timescale for the development of the western boundary layer is dependent on the speed of these Rossby waves.

Reviews of equatorial wave motions (Cane and Sarachik, 1983 and McCreary, 1985) describe the reflections that occur at the equator in equatorial ocean basins after reflection of the initial waves. Fast eastwards travelling Kelvin waves are reflected at the western boundary as a series of westward travelling long Rossby waves. Westward travelling Rossby waves are subsequently reflected at the eastern boundary as another fast eastward travelling Kelvin wave and a series of slow eastward travelling short Rossby waves. The short Rossby waves can become trapped at the western boundary to form a boundary layer.

In a narrow channel, the width of the channel becomes important in determining the subsequent transitional motions that occur after generation of the initial waves. In chapter 3 no fast ($\sim 2.4\text{ms}^{-1}$) eastward travelling Kelvin waves are ever observed at the equator. This is because the width of the channel (560km) is less than three equatorial radii of deformation (228km) and the equatorial Kelvin wave is never able to develop. The initial waves that are generated interfere constructively and destructively in the channel. After a few reflections have occurred the wave motions are dominated by scales dependent upon the channel width (section 1.5.5). In the channel of width 560km the fastest westward propagating Rossby wave that can eventually occur has a group velocity of 10cms^{-1} (see figure 1.5.3.a)). In an equatorial ocean basin with the same baroclinic phase speed ($\sim 2.4\text{ms}^{-1}$) the fastest westward travelling Rossby wave would have a group velocity close to 80cms^{-1}.

The transitional motions that occur in the channel after 200 days are found to be dominated by eastward propagating Yanai and Rossby waves. (section 1.5.4). This motion is equatorially confined, away from the equator transitional motions after initial passage of the coastal Kelvin wave and decay of inertial-gravity waves are very small.

Analytic work on equatorial waves (e.g. Cane and Sarachik, 1976, 77, 79) has used wind forcing to induce motion. The formulation of an analytic solution for motion forced by a north-south pressure gradient is not straightforward (section 1.5.7). Thus no analytical solution for the transient motion within the channel is available.

In the model, where viscous effects are included, the shortest of the Rossby waves produced at the western boundary are trapped by the action of lateral viscosity dissipating small scale energy. As shown in section 3.4.5. the steady state vorticity balance at the western boundary shows planetary vorticity being balanced by viscous dissipation of vorticity. This balance is similar to that shown in Munk's (1950) solution. When free slip boundary conditions are used the width of the viscous boundary layer is less than that predicted by Munk's solution. When no slip boundary conditions are used (section 3.3.4) the boundary layer is similar to that predicted by Munk. With no slip boundary conditions additional dissipation of vorticity through the western boundary can occur because of the velocity shear at the boundary. The western boundary acts as a source of negative vorticity, to balance this the width of the viscous boundary layer (source of positive vorticity) must increase.

Munk's (1950) solution is for wind driven circulation, there is no net transport through his ocean basin. The western boundary transport is balanced by the counter current and an interior Sverdrop flow. In the channel at steady state there is negligible interior flow and no eastern boundary layer is necessary to close the circulation. Flow is only possible at the western boundary where potential vorticity is balanced by diffusion.

The use of the nonlinear baroclinic model was primarily to see whether instabilities would develop in the channel when advective terms were included in the model. As described in section 3.5.2 an inertial boundary layer and eddies were formed when the horizontal viscosity was less than $500m^2s^{-1}$. This value for the upper limit of horizontal viscosity for eddy formation is similar to that of Holland and Lin (1975b). The nature of the instabilities, has been discussed in section 3.5.4. The wavelength of the eddies (100-200km) is related to the wavelength of the short Rossby waves (174km) that would be generated where the inertial boundary layer rejoins the interior flow.

6.2.3 Islands, sills and shelves

Previous studies of islands in an equatorial ocean basin (reviewed by McCreary, 1985) have looked at the interactions of islands with long equatorial waves. The islands in these studies were of similar simple geometries to those used in section 4.2. In equatorial ocean basins islands close to the equator interact with zonal currents. In this study, as seen in the results of section 4.2, the islands in the narrow channel are interacting with a strong meridional flow. Thus a direct comparison with the results of the previous studies is not valid.

Some discussion of Yoon's (1981) study is useful. Yoon used zonal wind forcing in a shallow water model and found that the eastward energy flux of equatorial Kelvin waves was almost unaffected by an island. Coastal Kelvin waves could develop to propagate the energy around the island. Yoon observed that because of this propagation around an island care has to be taken with interpretation of sea level data at equatorial islands. The westward propagation of energy by long Rossby waves is greatly altered by equatorial islands with meridional extent equal to or greater than the radius of deformation. At the island no coastal waves can exist, instead a western boundary current is formed. Higher order meridional modes that are less equatorially confined may propagate past the island.

In this study with strong meridional flow it is found that the initial coastal Kelvin wave is unaffected by an island. Kelvin waves propagate around the island in agreement with Yoon (1981). Transport through the western boundary current is also unaffected by the imposition of an island. The development of the western boundary layer occurs only to the east of an island when the island is within a boundary layer width of the western boundary.

The results of the experiments with sills in the linear two layer model 6), (section 4.3) show that transport through the channel is slightly increased by the inclusion of a sill. Southward transport occurs in a western boundary current as in the open channel. The major effect of a sill is the localised topographic steering of the western boundary current. Killworth (1989) considers the interaction between an internal coastal Kelvin wave and a smooth ridge extending away from the coastline. Killworth shows that ridges of north-south extent of one or two radii of deformation reduce the amplitude of the Kelvin wave by approximately the ratio of the undisturbed layer over the top of the ridge to the depth of the layer away from the ridge. Scattering of the Kelvin wave along the ridge accounts for the reduction in amplitude and energy. The effect of a ridge of north-south extent less than the radius of deformation on the coastal Kelvin wave is negligible in the limit of vanishing width. The results of section 4.3 agree with Killworth's work in so far as the initial Kelvin wave crosses the sill with negligible reduction in amplitude, sills used are less than a radius of deformation in north-south extent. Reference to figure 1.2.1 shows that all the major sills in the Eastern Archipelago are less than the equatorial radius of deformation in width.

The experiments with shelves in the linear two layer model were made in the same spirit as those with the sills. The choice of 60m depth over the shelves was based on the mean depth of the South China Sea, Java Sea and Arafura Sea. The choice of value for the coefficient of bottom friction was made in the range 10^{-4} - 10^{-3} suggested by Gill (1982). The purpose of the experiment was to determine whether or not dissipation of vorticity over the shelves could be an important mechanism (section 1.5.3) and whether a simple representation of shelf seas in the model could adequately represent the effects of bottom friction. The results of section 4.4 show that this was indeed the case. Total transport through the region was increased by the addition of shelves. Transport occurred in a broad Stommel type boundary layer over the western shelf and a viscous boundary layer at the western edge of the deep channel. The viscous boundary layer was weaker than in the open channel and there was negligible counter current development. The implication of this result on transport through the Eastern Archipelago during the last ice age when sea level was 100m lower is that transport from the Pacific to the India Ocean would be reduced. However throughflow could still occur in the deep channels where viscous diffusion of potential vorticity at the western boundary occurs.

6.2.4 Realistic model and forcing

The estimates of the mean throughflow from the Pacific to the Indian Ocean through the Eastern Archipelago of the South East Asian Waters in this study (7.2 - 7.9 Sv) agree with the range of recent observational estimates that suggest a throughflow of 6-8Sv (discussed in section 1.3.3 and summarised in table 1.3.1)

Results from the NORDA global model, first used to investigate the Pacific to Indian Ocean throughflow by Kindle et al (1987), have been reported by Wyrtki (1987) and Murray and Arief (1988). The model is described in section 1.4.2. In the initial model (Kindle et al, 1987) the region representing the Eastern Archipelago did not include the Macassar Strait or Lombok Strait. In the results of the model reported by Wyrtki (1987) the Macassar Strait is included in the model. Following the observations of Murray and Arief (1988) it has been decided to incorporate the Lombok Strait in the model.

The results of the NORDA model reported by Murray and Arief (1988) are compared with the results of section 5.4.4 in figure 6.2.1. It can be seen that there is good agreement in the predicted phase between the two models. Both models exhibit a phase difference between inflow from the Pacific and outflow into the Indian Ocean (figure 5.4.15 and Kindle et al, 1987) implying that a steady transport through the whole region is never attained in the seasonal cycle. The path of the throughflow in the integrations of the NORDA model described by Wyrtki (1987) shows the development of a strong western boundary current through the Macassar Strait, Flores Sea and into the Indian Ocean via the Timor Sea. This is similar to the model results shown in sections 5.3.2 and 5.4.3 particularly if the Lombok Strait was closed. Neither Wyrtki (1987) or Murray and Arief (1988) discuss the seasonal variability of the pathway of the throughflow in the NORDA model.

The flow through the Lombok Strait produced by the model has been compared with the observations of Murray and Arief (1988) in section 5.4.5. The over estimation of flow through the Lombok Strait by the model is in part due to the resolution of the model. The model strait does not include any topography. A sill of 350m depth exists in the Lombok Strait. Experiments in section 4.3 do not determine the affects of such a narrow sill on the local circulation in the Strait. Observations show no deep reflected flow away from the sill (Murray and Arief, 1988). The results of section 4.3 also produced no northward flow reflected from sills. It has also been

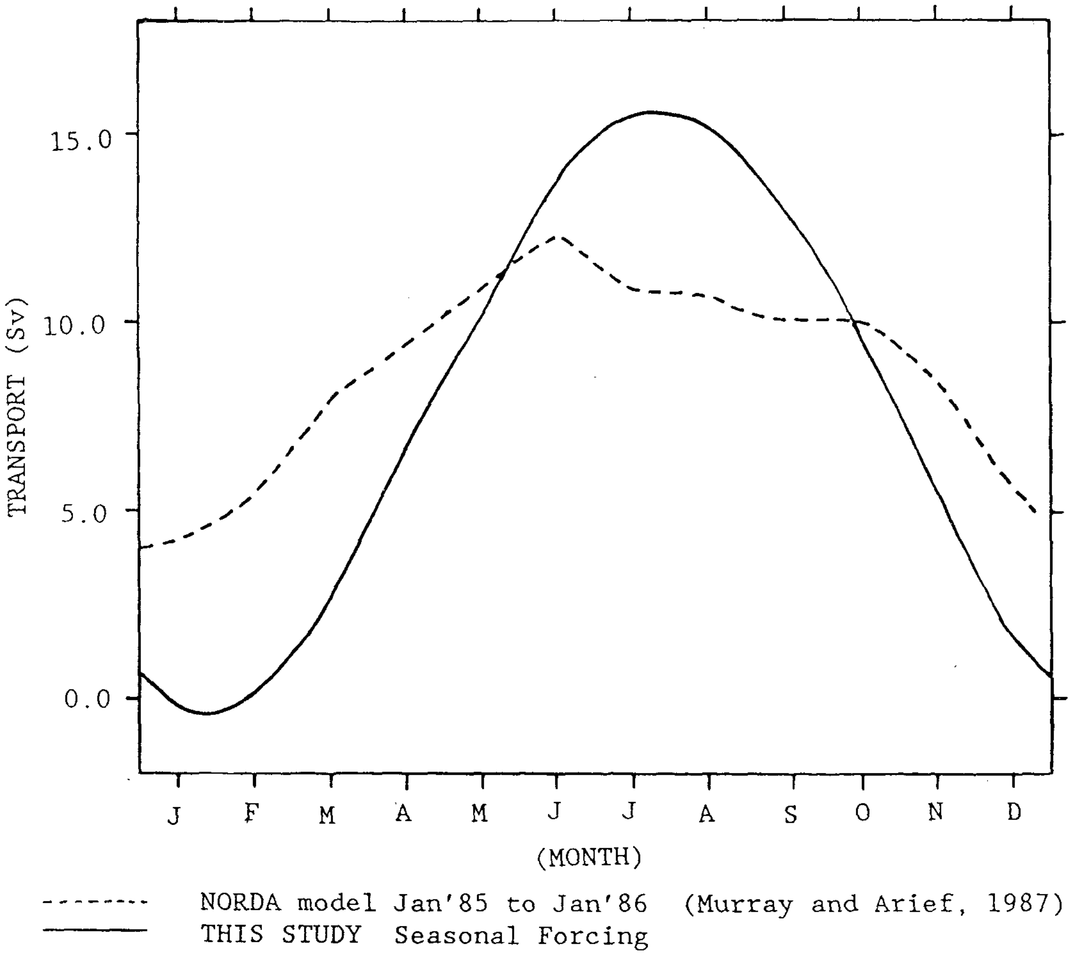

Figure 6.2.1 : Comparison of realistic model results with the NORDA model.

shown, table 5.3.2, that the mean transport through the Lombok Strait is sensitive to the choice of lateral boundary condition and horizontal viscosity in the model.

The model results for the Macassar Strait are in good agreement with the current meter observations of the Snellius Expedition. The model produces a maximum current of $1ms^{-1}$ cf. observations of $0.84ms^{-1}$. Wyrtki (1961) shows reversal of surface flow occurring in the Macassar Strait in October with development of a northward current at the western boundary. Hughes (1981) uses the reversal of the monsoon wind system to account for this asymmetry. In this study the model predicts a steady circulation in the Macassar Strait from May to November with a southward western boundary current and a weaker northward counter current. The width of this feature is dependent upon the horizontal viscosity in the model (see table 3.3.3). In December to February the flows are very weak and reverse due to the weak north-south pressure gradient. The flow at this time is forced by the interface depression in the Flores and Banda Seas. In March-April the flow in the Macassar Strait is in a transitional state as the western boundary current is reformed.

The nature of the outflow into the Indian Ocean 12), 13) through the Timor Sea is similar to that found by Kundu and McCreary (1986) when their steady forcing was switched on. Initially outflow occurs as a coastal Kelvin wave along the North West Australia Shelf. Subsequently westward propagating Rossby waves carry the outflow offshore and ultimately a westward jet is formed at 10°S. In this study outflow also occurs through the Lombok strait. This outflow initially turns east as a coastal Kelvin wave. The quasi steady state outflow is a westward jet at 10°S formed by the flow through the Lombok Strait turning west due to Rossby wave motion. Kundu and McCreary (1986) showed that this adjustment process could not be completed when there was vertical mixing in their model. Barotropic waves were unaffected by vertical mixing and thus adjusted to form a westward jet. Baroclinic waves however were damped in the direction of their group velocity by vertical mixing. In this case the coastal current initially formed did not move completely offshore and the steady state comprised some southward coastal flow. Kundu and

McCreary concluded that this was not the major source of mass for the Leeuwin current that flows clockwise around the coast of Western Australia.

In contrast to Kundu and McCreary (1986) this study has shown that using a forcing term representing the seasonal variation in the north-south pressure gradient across the Eastern Archipelago no steady state outflow is attained. From March to July there is outflow along the North West Australia shelf of the model associated with the Kelvin waves that develop as the pressure gradient increases from its minimum in January and February. From August to December the outflow through the Timor Sea turns westward at 10°S due to the development of the coastal jet by Rossby waves. Outflow also occurs throughout the Lombok Strait but since this outflow develops by Rossby waves forming a western boundary current through the Eastern Archipelago the timescale for this development is similar to that of the coastal jet at 10°S. This study concludes that the throughflow from the Pacific to the Indian Ocean can provide a major source of mass for the Leeuwin Current and that this source has a seasonal variation in phase with the development of the Leeuwin Current. The Leeuwin Current is a seasonally varying current that is seen to develop off North West Australia in April and ends in October (Thompson, 1984).

The experiment with the 30 day forcing, section 5.5, was to investigate the effect of a higher frequency oscillation (long equatorial waves) in the forcing. Because the amplitude of the oscillation was not equal to the mean pressure gradient the outflow through the Lombok Strait is unaffected by the oscillatory forcing. The flow through the Timor Sea is seen to be a series of Kelvin waves caused by the oscillating pressure gradient. Changes in the Pacific sea level reach the North West Australia Shelf with the Kelvin waves. With the 30 day forcing Rossby waves do not have time to develop hence changes in the sea level south of Java are negligible (figure 5.5.8).

To compare the model with the global model of Semtner and Chervin (1988) would require the use of the nonlinear baroclinic model (section 3.5). It is then possible that the 30 day forcing might propagate through the western boundary region in the form of an eddy. But it seems more likely from the result of sections 5.5.3 and 3.5.2 that an oscillation in the forcing would only produce an oscillation in the circulation at the eastern boundary.

The poor resolution of Semtner and Chervin's model has been suggested by them as a reason why the predicted mean throughflow in their model (15-18Sv) is too high. The eddies produced by their model in the eastern Pacific are seen to propagate across the equatorial Pacific and through the Macassar Strait. The eddies have a wavelength of approximately 200km. The eddies are seen to reorganize after passage through the models submerged Lombok Strait (100km wide, 710m deep). If the Lombok Strait were fully resolved then this mechanism might be quite different with eddies possibly unable to propagate through a strait of 30-40km width and 350m depth. Semtner and Chervin do not give details of other circulation in the Eastern Archipelago and do not discuss the nature of the outflow into the Indian Ocean.

The north-south forcing used throughout this study is based upon the observations collated by Wyrtki (1987). The observed difference in sea level between the Pacific and Indian Oceans is due to the effects of global wind forcing driving oceanic circulation and the more localised effects of monsoonal wind forcing. This form of forcing allows the regional model to be compared with the results of wind forced global models. The aim of this study has not been to predict or represent the circulation in the Pacific and Indian Oceans because this is not possible with the forcing condition used. However effects of the throughflow on the sea level in the Indian Ocean can be determined.

In the model, changes in Pacific sea level reach the North West Australia Shelf (Darwin) with the Kelvin wave. Changes in sea level south of Java only occur after Rossby waves have had time to propagate from the North West Australian Shelf. Wyrtki (1987) gives data for the monthly mean sea level at Darwin and at Cilacap on the south coast of Java. The data for Cilacap comes from only a 7 year long record (1925-1931). There is general agreement between the sea level record at the two sites which led Wyrtki to consider the sea level difference between Davao in the Philippines and Darwin to be representative of the difference in sea level between the Pacific and the Indian Ocean (shown in figure 1.2.2). Closer examination of the monthly mean sea level data for Cilacap and Darwin (figure 1.2.2) shows that between March and October there appears to be a phase difference between the sea level elevation at Darwin and Cilacap of approximately two months. This phase difference may be related to the time taken for Rossby waves to propagate from the North West Australian shelf to Java.

6.3 SUGGESTIONS FOR FURTHER WORK

6.3.1 Modelling Studies

The use of the nonlinear realistic baroclinic model and a horizontal viscosity less than $500 m^2 s^{-1}$ would allow a closer comparison with the results of Semtner and Chervin (1988). The results of section 3.5 suggest that eddies at the western boundary would increase the transport through the region. Prior to the use of a nonlinear realistic model it would be worthwhile investigating in more detail the nonlinear baroclinic channel model of section 3.5 to determine the exact nature of the instability and the energy and vorticity balances of the flow. Further work on producing an open boundary condition that allowed passage of an advected eddy would be required. Ross and Orlanski (1982) use an Orlanski type scheme with the local advection velocity normal to the boundary replacing the local phase speed of the variables at the boundary.

The linear two layer model could be used to include the major bathymetric features of the Eastern Archipelago in the realistic model. However to compute the seasonal forcing experiment of section 5.4 would require approximately 40 hours of computing time as opposed to 35 minutes when the baroclinic model was used. It would thus be imperative that the parameters used for horizontal viscosity and coefficient of bottom friction were suitable.

Preliminary to an experiment with a realistic two layer model it would be useful to further investigate the inclusion of sills and shelves in the channel. It would also be useful to look at the flow through a realistic representation of the Lombok Strait in order to determine whether the high transports of chapter 5 are only due to poor resolution of the strait.

6.3.2 Other Studies

The formulation of analytic solutions on the lines of Cane and Sarachik (1976, 77, 79) for the transient motion, and Munk (1950) for the steady state solution would be useful additions to the study. This problem is complicated (section 1.5.7) by the fact that the forcing (the north-south pressure gradient) in the problem is via the continuity equation rather than the momentum equation.

Other useful work would involve a comparison of the monthly velocity fields and transports within the region of this study and recent integrations of the NORDA model (Wyrtki, 1987 and Murray and Arief, 1988) and Semtner and Chervin's model when their proposed seasonal forcing is carried out. It would be interesting to see whether the global models produce a seasonal outflow along the North West Australian Shelf. It is possible that the resolution within the global models is insufficient for this.

Finally of utmost importance are the observational studies within the region. Fine resolution, sophisticated models are of limited use without a background of observational data for comparison with predicted fields. The observations to be made in the WOCE and INSTEP programs (see chapter 1) are of great interest, as is the observation of sea level variation throughout the Eastern Archipelago.

REFERENCES

Andreyev, O.A., B.A. Kagan, and L.A. Oganesyan, 1976: On the Global Circulation in a two layer Model. Oceanology, 16, 1-51.

Bennet, A.F., and P.C. McIntosh, 1982: Open Ocean Modelling as an Inverse Problem: Tidal Theory. J. Phys. Oceanogr., 1004-1018.

Blandford, R.R., 1971: Boundary conditions in Homogeneous Ocean Models. Deep-Sea Res., 18, 739-751.

Boland, F.M., and B.V. Hamon, 1970: The East Australian Current, 1965-1968. Deep-Sea Res., 17, 777-751.

Bryan, K., 1969: A Numerical Method for the study of the Circulation of the World Ocean. J. Comp. Phys., 347-376.

Bryan, K., S. Manabe, and R.C. Pacanowski, 1975: A Global Ocean-Atmosphere Climate Model: II The Ocean Circulation. J. Phys. Ocenogr., 5, 30-46.

Camerlengo, A.L., and J.J. O'Brien, 1980: Open Boundary Conditions in Rotating Fluids. J. Comp. Phys., 35, 12-35.

Cane, M.A., and E.S. Sarachik, 1976: Forced Baroclinic Ocean Motions: I. The Linear Equatorial Unbounded Case. J. Mar. Res., 34, 629-665.

Cane, M.A., and E.S. Sarachik, 1977: Forced Baroclinic Ocean Motions: II. The Linear Equatorial Bounded Case. J. Mar. Res., 35, 395-432.

Cane, M.A., and E.S. Sarachik, 1979: Forced Baroclinic Ocean Motions: III. The Linear Equatorial Basin Case. J. Mar. Res., 37, 355-398.

Cane, M.A., and E.S. Sarachik, 1983: Equatorial Oceanography. Rev. Geophys and Space Phys., 21, 1137-1148.

Chapman, D.C., 1985: Numerical Treatment of Cross-Shelf Open Boundaries in a Barotropic Coastal Ocean Model. J. Phys. Oceanogr., 15, 1060-1075.

Cox, M.D., 1975: A Baroclinic Numerical Model of the World Ocean: Preliminary Results. In: Numerical Models of Ocean circulation, 107-118, Nat. Acad. Sciences, Washington D.C.

Cresswell, G.R., and T.J. Golding, 1980: Observations of a South flowing current in the South East Indian Ocean. Deep-Sea Res., 27, 449-466.

Csanady, G.T., 1982: Circulation in the Coastal Ocean. D. Reidel Publishing Co., 279 pp.

Fine, R.A., 1985: Direct Evidence using Tritium Data for throughflow from the Pacific into the Indian Ocean. Nature, 315, 478-480.

Fu, L.L., 1986: Mass, Heat and Freshwater Fluxes in the South Indian Ocean. J. Phys. Oceanogr., 16, 1683-1693.

Gill, A.E., 1976: Adjustment under gravity in a Rotating Channel. J. Fluid Mech., 77, 603-621.

Gill, A.E., 1982: Atmosphere-Ocean Dynamics. Academic Press, 662 pp.

Gill, A.E., J.S.A. Green, and A.J. Simmons, 1974: Energy Partition in the Large-Scale Ocean Circulation and the production of Mid-Ocean Eddies. Deep-Sea Res., 21, 499-528.

Godfrey, J.S., 1989: A Sverdrup Model of the Depth Integrated Flow for the World Ocean allowing for Island Circulations. J. Geophys. Astrophys. Fluid Dyn., 45, 89-112.

Godfrey, J.S., and T.J. Golding, 1981: The Sverdrup Relation in the Indian Ocean and the Effect of Pacific - Indian Ocean Throughflow on Indian Ocean Circulation and on the East Australian Current. J. Phys. Oceanogr., 11, 771-779.

Godfrey, J.S., and K.R. Ridgway, 1985: The Large-Scale Environment of the Poleward flowing Leeuwin Current, Western Australia: Longshore Steric Height Gradients, Wind Stresses and Geostrophic flow. J. Phys. Oceanogr., 15, 481-495.

Gordon, A.L., 1986: Inter Ocean Exchange of Thermocline Water. J. Geophys. Res., 91, 5037-5046.

Holland, W.R., and L.B. Lin, 1975a: On the Generation of Mesoscale Eddies and their Contribution to the Oceanic General Circulation. I. A Preliminary Numerical Experiment. J. Phys. Oceanogr., 5, 642-657.

Holland, W.R., and L.B. Lin, 1975b: On the Generation of Mesoscale Eddies and their Contribution to the Oceanic General Circulation. II. A Parameter Study. J. Phys. Oceanogr., 5, 658-669.

Horel, J.D., and J.M. Wallace, 1981: Planetary-Scale Atmospheric Phenomena associated with the Southern Oscillation. Month. Weath. Rev., 109, 813-829.

Hughes, R.L., 1981: On Cross-Equatorial flow within a channel with application to the Macassar Strait. Dyn. Atmos. Ocean. 6, 103-120.

Killworth, P.D., 1989: How much of a Baroclinic Coastal Kelvin Wave Gets over a Ridge? J. Phys. Oceanogr., 19, 321-341.

Kindle, J.C., G.W. Heburn, and R.C. Rhodes, 1987: An Estimate of the Pacific to Indian Ocean Throughflow from a Global Numerical Model. In: Further Progress in Equatorial Oceanography (E.J. Katz and J.M. Wilte eds.) 317-321, Fort Lauderdale, F.A: Nova University Press, 450pp.

Kundu, P.K., and J.P. McCreary, 1986: On the Dynamics of the Throughflow from the Pacific into the Indian Ocean. J. Phys. Oceanogr., 16, 2191-2198.

Lek, L., 1938: Die Ergebnisse der Strom und Serienmessungen, Snellius Exped. East. Part, Neth. East Indies 1927-1930, 2, 169 pp.

Levitus, S., 1982: Climatological Atlas of the World Oceans. NOAA Prof Pap. 13, U.S. Government Printing Office, Washington D.C., 173 pp.

Lilly, D.K., 1965: On the Computational Stability of Numerical Solutions of time dependent non-linear Geophysical Fluid Dynamics Problems. Month. Weath. Rev., 93, 11-26.

McCreary, J.P., 1985: Modelling Equatorial Ocean Circulation. Ann. Rev. Fluid Mech., 17, 359-409.

Mesinger, F., and A. Arakawa, 1976: Numerical Methods used in Atmospheric Models. WMO/ICSU Joint Organizing Committee, GARP Publications Series No.17, 64 pp.

Miller, M.J. and A.J. Thorpe, 1981: Radiation Conditions for the Lateral Boundaries of Limited Area Numerical Models. Quart. J. Roy. Met. Soc., 107, 615-628.

Moore, D.W., 1968: Planetary-Gravity Waves in an Equatorial Ocean, Ph.D. Thesis. Harvard University. Cambridge, Massachusetts.

Munk, W.H. 1950: On the Wind-driven Ocean Circulation. J. Met., 7, 79-93.

Murray, S.P., and D. Arief, 1988: Throughflow into the Indian Ocean through the Lombok Strait, January 1985 - January 1986. Nature, 333, 444-447.

Orlanski, I., 1976: A Simple Boundary Condition for Unbounded Hyperbolic Flows. J. Comp. Phys., 21, 251-269.

Pedlosky, J., 1979: Geophysical Fluid Dynamics. Springer-Verlag, Berlin and New York, 624 pp.

Piola, A.R. and A.L. Gordon, 1984: Pacific and Indian Ocean Upper-Layer Salinity Budget. J. Phys. Oceanogr., 14, 747-753.

Postma, H., 1958: The Snellius Expedition - In the Eastern Part of the East Indian Archipelago 1929-1930. Volume II, Oceanographic Results - part 8. Chemical Results and a Survey of Water Masses and Currents, 116 pp.

Prell, W.L., W.H. Hutson, D.F. Williams, A.W.H. Be, K. Geitzenauer, and B. Molfino, 1980: Surface Circulation of the Indian Ocean during the last Glacial Maximum, Approximately 18,000 BP. Quat. Res., 14, 309-336.

Rochford, D.J., 1964: Hydrology of the Indian Ocean. III Water Masses of the Upper 500m of the South Eastern Indian Ocean. Aust. J. Mar. Freshw. Res., 15, 25-55.

Rochford, D.J., 1966: Distribution of Banda Intermediate Water in the Indian Ocean. Aust. J. Mar. Freshw. Res., 17, 61-76.

Rochford, D.J., 1969: Seasonal Variations in the Indian Ocean along 110°E. I Hydrological Structure of the Upper 500m. Aust. J. Mar. Freshw. Res., 20, 1-50.

Ross, B.B., and I. Orlanski, 1982: The evolution of an Observed Cold Front. Part I: Numerical Simulation. J. Atmos. Sciences, 39, 196-327.

Semtner, A.J., and R.M. Chervin, 1988: A Simulation of the Global Ocean Circulation with Resolved Eddies. J. Geophys. Res., 93, 15502-15522.

Sommerfeld, A., 1949: Partial Differential Equations in Physics. Academic Press, New York, 335 pp.

Stommel, H., 1948: The Westward Intensification of Wind Driven Ocean Currents. Trans. Am. Geophys. Union, 99, 202-206.

Takano, K., 1975: A Numerical Simulation of the World Ocean Circulation: Preliminary Results. In: Numerical Models of Ocean Circulation, 121-129, Nat. Acad. Sciences, Washington D.C.

The Shipboard Scientific Party, 1974: Site 258. In: Initial Reports of the Deep Sea Drilling Project, Vol. 26. (T.A. Davies, B.P. Luyendyl et al. eds.), U.S. Government Printing Office, Washington D.C., 359-414.

Thompson, R.O.R.Y., 1984: Observations of the Leeuwin Current off Western Australia. J. Phys. Oceanogr., 14, 623-628.

TOGA Scientific Steering Group, 1985: Scientific Plan for the Tropical Ocean and Global Atmosphere Programme. WCRP Pulications Series No.3, WMO/TD No.64.

Veronis, G., 1973 : Model of World Ocean Circulation: I. Wind-driven two layer. J. Mar. Res., 31, 228-289.

Veronis, G., 1976: Model of the World Ocean Circulation. II Thermally-driven, two layer. J. Mar. Res., 34, 199-216.

Webb, D.J., and R.J. Morris, 1984: DSDP Site 258: Evidence for Recent Nutrient-rich Upwelling off Western Australia. Deep Sea Res., 31, 1265-1272.

Webb, D.J., et al., 1989: Institute of Oceanographic Sciences Deacon Laboratory, Cruise Report, No.207, 34 pp.

Weisberg, R.H., 1980: Equatorial Waves during GATE and their relation to the Mean Zonal Circulation. Deep-Sea Res., 26, Supplement 2, 179-198.

WOCE Scientific Steering Group, 1986: Scientific Plan for the World Ocean Circulation Experiment. WCRP Pulications Series No.6, WMO/TD No.122.

Wolanski, E., P. Ridd, and M. Inoue, 1988: Currents through Torres Strait. J. Phys. Oceanogr., 18, 1535-1545.

Wunsch, C., 1978: The General Circulation of the North Atalantic west of 50°W determined from Inverse Methods. Rev. Geophys. Space Phys., 16, 583-620.

Wyrtki, K., 1961: Physical Oceanography of the South East Asian Waters. NAGA Report, 2, Scientific Results of Maritime Investigations of the South China Sea and Gulf of Thailand 1959-1961. Scripps Institute of Oceanography, 195 pp.

Wyrtki, K., 1987: Indonesian Throughflow and the Associated Pressure Gradient. J. Geophys. Res., 92, 12941-12946.

Wyrtki, K., E.B. Bennet, and D.J. Rochford, 1971: Oceanographic Atlas of the International Indian Ocean Expedition. National Science Foundation, Washington D.C., 531 pp.

Yoon, J.H., 1981: Effects of Islands on Equatorial Waves. J. Geophys. Res., 86, 10913-10920.

APPENDIX A. FINITE DIFFERENCE EQUATIONS

A.1 Notation.

In the finite difference equations, the variables (u_i, v_i, h and η) are not continuous functions of x and y but are defined only at discrete values of these co-ordinates. These points are shown in figure A.1. The indices i and j define the relative position of a point in the x - y plane.

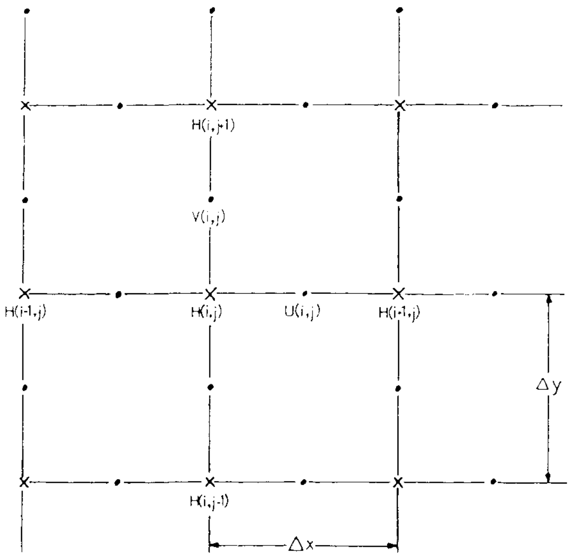

Figure A.1 : The Arakawa C-grid.

Using the operators described in section 2.3.3 and the temporal schemes of section 2.3.2 the finite difference equations for the foursets of predictive equations are given in section A.2 - A.5.

A.2. The Two layer equations.

Equations (2.2.2.8) - (2.2.2.13) in finite difference form become.

$$(U_1)^{n+1} = (U_1)^{n-1} - 2\Delta t[(H_1+\eta-h)(g\delta_x\eta)-\beta y\overline{\overline{V_1}^{x}}^{y}$$
$$+ \delta_x(\overline{u_1}^{x}\overline{U_1}^{x}) + \delta y(\overline{u_1}^{y}\overline{V_1}^{x})]^n$$
$$+ 2\Delta t[(H_1+\eta-h)A_H\nabla^2 u_1 + u_1\alpha_1(\eta_o-\eta) - u_1\ \alpha_2(h_o-h)]^{n-1} \qquad (A.2.1)$$

$$(V_1)^{n+1} = (V_1)^{n-1} - 2\Delta t[(H_1+\eta-h)(g\delta_y\eta)+\beta y\overline{\overline{U_1}^{x}}^{y}$$
$$+ \delta_x(\overline{v_1}^{x}\overline{U_1}^{X}) + \delta_y(\overline{v_1}^{y}\overline{V_1}^{y})]^n$$
$$+ 2\Delta t[(H_1+\eta-h)A_H\nabla^2 v_1 + v_1\alpha_1(\eta_o-\eta) - v_1\alpha_2(h_o-h)]^{n-1} \qquad (A.2.2)$$

$$(U_2)^{n+1} = (U_2)^{n-1} - 2\Delta t[(H_2+h)(g\delta_x\eta+g'\delta_x h)-\beta y\overline{\overline{V_2}^{x}}^{y}$$
$$+ \delta_x(\overline{u_2}^{x}\overline{U_2}^{x}) + \delta_y(\overline{u_2}^{y}\overline{V_2}^{x})]^n$$
$$+ 2\Delta t[(H_2+h)A_H\nabla^2 u_2 + u_2\alpha_2(h_o-h)]^{n-1} \qquad (A.2.3)$$

$$(V_2)^{n+1} = (V_2)^{n-1} - 2\Delta t[(H_2+h)(g\delta_y\eta+g'\delta_y h) + \beta y\overline{\overline{U_2}^{x}}^{y}$$
$$+ \delta_x(\overline{v_2}^{x}\overline{U_2}^{y}) + \delta_y(\overline{v_2}^{y}\overline{V_2}^{y})]^n$$
$$+ 2\Delta t[(H_2+h)\ A_H\nabla^2 v_2 + v_2\alpha_2(h_o-h)]^{n-1} \qquad (A.2.4)$$

$$(\eta)^{n+1} = (\eta)^{n-1} - 2\Delta t[\delta_x U_1 + \delta_y V_1 + \delta_x U_2 + \delta_y V_2]^n$$
$$+ 2\Delta t[\alpha_1(\eta_o-\eta) + \alpha_2(h_o-h)]^{n-1} \qquad (A.2.5)$$

$$(h)^{n+1} = (h)^{n-1} - 2\Delta t[\delta_x U_2 + \delta_y V_2]^n + 2\Delta t\alpha_2(h_o-h)\ ^{n-1} \qquad (A.2.6)$$

A.3. The Linear two layer equations

Equations (2.2.4.1) - (2.2.4.6) in finite difference form become

$$(u_1)^{n+1} = (u_1)^{n-1} - 2\Delta t(g\delta_x\eta - \beta y\overline{\overline{v_1}^x}^y)^n + 2\Delta t A_H\nabla^2(u_1)^{n-1} \qquad (A.3.1)$$

$$(v_1)^{n+1} = (v_1)^{n-1} - 2\Delta t(g\delta_y\eta + \beta y\overline{\overline{u_1}^x}^y)^n + 2\Delta t A_H\nabla^2(v_1)^{n-1} \qquad (A.3.2)$$

$$(u_2)^{n+1} = (u_2)^{n-1} - 2\Delta t(g\delta_x\eta + g'\delta_x h - \beta y\overline{\overline{v_2}^x}^y)^n + 2\Delta t A_H\nabla^2(u_2)^{n-1} \qquad (A.3.3)$$

$$(v_2)^{n+1} = (v_2)^{n-1} - 2\Delta t(g\delta_y\eta + g'\delta_y h - \beta y\overline{\overline{u_2}^x}^y)^n + 2\Delta t A_H\nabla^2(v_2)^{n-1} \qquad (A.3.4)$$

$$(\eta)^{n+1} = (\eta)^{n-1} - 2\Delta t[H_1(\delta_x u_1+\delta_y v_1)+H_2(\delta_x u_2+\delta_y v_2)]^n + 2\Delta t[\alpha_1(\eta_o-\eta)+\alpha_2(h_o-h)]^{n-1} \qquad (A.3.5)$$

$$(h)^{n+1} = (h)^{n-1} - 2\Delta t[H_2(\delta_x u_2+\delta_y v_2)]^n + 2\Delta t\alpha_2(h_o-h)^{n-1} \qquad (A.3.6)$$

A.4. The non linear baroclinic equations

Equations (2.2.5.4, 2.2.5.6 and 2.2.5.7 in finite difference form become.

$$(U)^{n+1} = (U)^{n-1} + 2\Delta t\left[\frac{(H_2+h)(H_1-h)}{H_1+H_2}\, g'\delta_x h + \beta y \overline{\overline{V}^{x}}^{y}\right.$$

$$\left. + \frac{H_1-H_2}{H_1+H_2}\left(\delta_x(\overline{u}^{x}\overline{V}^{x}) + \delta_y(\overline{u}^{y}\overline{V}^{x})\right) - \frac{2hu}{H_1+H_2}\left(\delta_x U + \delta_y V\right)\right]^{n}$$

$$+ 2\Delta t\left[\frac{(H_2+h)(H_1-h)}{H_1+H_2} A_H \nabla^2 u - u\frac{(H_1-2h-H_2)}{H_1+H_2}\alpha_2(h_o-h)\right]^{n-1}$$

(A.4.1)

$$(V)^{n+1} = (V)^{n-1} + 2\Delta t\left[\frac{(H_2+h)(H_1-h)}{H_1+H_2}\, g'\delta_y h - \beta y \overline{\overline{U}^{x}}^{y}\right.$$

$$\left. + \frac{H_1-H_2}{H_1+H_2}\left(\delta_x(\overline{v}^{x}\overline{U}^{y}) + \delta_y(\overline{v}^{y}\overline{V}^{y})\right) - \frac{2hv}{H_1+H_2}\left(\delta_x U + \delta_y V\right)\right]^{n}$$

$$+ 2\Delta t\left[\frac{(H_2+h)(H_1-h)}{H_1+H_2} A_H \nabla^2 v - v\frac{(H_1-2h-H_2)}{H_1+H_2}\alpha_2(h_o-h)\right]^{n-1}$$

(A.4.2)

$$(h)^{n+1} = (h)^{n-1} + 2\Delta t(\delta_x U + \delta_y V)^{n} - 2\Delta t\,\alpha_2(h_o-h)^{n-1} \qquad (A.4.3)$$

where $U=U_1-U_2$, $V=V_1-V_2$, $u=u_1-u_2$ and $v=v_1-v_2$.

A.5. The linear Baroclinic equations

Equations (2.2.6.1) - (2.2.6.3) in finite difference form become.

$$(u)^{n+1} = (u)^{n-1} + 2\Delta t(g'\delta_x h + \beta y\overline{\overline{v}^{x}}^{y})^{n} + 2\Delta t A_H \nabla^2 (u)^{n-1} \tag{A.5.1}$$

$$(v)^{n+1} = (v)^{n-1} + 2\Delta t(g'\delta_y h - \beta y\overline{\overline{u}^{x}}^{y})^{n} + 2\Delta t A_H \nabla^2 (v)^{n-1} \tag{A.5.2}$$

$$(h)^{n+1} = (h)^{n-1} + 2\Delta t\left[\frac{H_1 H_2}{H_1+H_2}(\delta_x u + \delta_y v)\right]^{n} - 2\Delta t\,\alpha_2(h_o - h)^{n-1} \tag{A.5.3}$$

APPENDIX B ENERGETICS

B.1 Notation

As described in section 2.5.2 the energy equations can be written in terms of the work done on each layer by the various forces acting upon that layer (the boundary forcing, friction and potential to kinetic energy exchanges). These terms are determined for each set of predictive equations in sections B.2 - B.5.

(Notation is the same as in chapter 3.)

APPENDIX B.2 The two layer equations

$$\langle \partial/\partial t(PE_1)\rangle = \langle P_1+N_1+S_1\rangle \qquad (B.2.1)$$

$$\langle \partial/\partial t(PE_2)\rangle = \langle P_2+N_2+S_2\rangle \qquad (B.2.2)$$

$$\langle \partial/\partial t(KE_1)\rangle = \langle P_3+F_1+O_1\rangle \qquad (B.2.3)$$

$$\langle \partial/\partial t(KE_2)\rangle = \langle -(P_1+P_2+P_3)+F_2+O_2\rangle \qquad (B.2.4)$$

where

$$P_1 = -\rho g\ \eta\left(\frac{\partial U_1}{\partial x}+\frac{\partial V_1}{\partial y}+\frac{\partial U_2}{\partial x}+\frac{\partial V_2}{\partial y}\right) \qquad (B.2.5)$$

$$P_2 = -\rho g'h\left(\frac{\partial U_2}{\partial x}+\frac{\partial V_2}{\partial y}\right) \qquad (B.2.6)$$

$$P_3 = \rho g\left(\frac{U_1\partial\eta}{\partial x}+\frac{V_1\partial\eta}{\partial y}\right) \qquad (B.2.7)$$

$$F_1 = \rho A_H(U_1\nabla^2u_1 + V_1\nabla^2v_1) \qquad (B.2.8)$$

$$F_2 = \rho A_H(U_2\nabla^2u_2 + V_2\nabla^2v_2) \qquad (B.2.9)$$

$$N_1 = \rho g\eta(\alpha_1(\eta_\rho-\eta) + \alpha_2(h_\rho-h)) \qquad (B.2.10)$$

$$N_2 = \rho g'h(\alpha_2(h_\rho-h) \qquad (B.2.11)$$

$$S_1 = \rho g\eta(\alpha_1(\eta_I-\eta) + \alpha_2(h_I-h)) \qquad (B.2.12)$$

$$S_2 = \rho g'h(\alpha_2(h_I-h)) \qquad (B.2.13)$$

$$O_1 = \rho(u_1{}^2+v_1{}^2)(\alpha_1(\eta_\rho-\eta)+\alpha_1(\eta_I-\eta)\ -\alpha_2(h_\rho-h)\ -\alpha_2(h_I-h)) \qquad (B.2.14)$$

$$O_2 = \rho(u_2{}^2+v_2{}^2)(\alpha_2(h_\rho-h) + \alpha_2(h_I-h)) \qquad (B.2.15)$$

APPENDIX B.3 The linear two layer equations

$$\langle \partial/\partial t(PE_1)\rangle = \langle P_1+N_1+S_1\rangle \tag{B.3.1}$$

$$\langle \partial/\partial t(PE_2)\rangle = \langle P_2+N_2+S_2\rangle \tag{B.3.2}$$

$$\langle \partial/\partial t(KE_1)\rangle = \langle P_3+F_1\rangle \tag{B.3.3}$$

$$\langle \partial/\partial t(KE_2)\rangle = \langle -(P_1+P_2+P_3) + F_2\rangle \tag{B.3.4}$$

where

$$P_1 = -\rho g \left(H_1 \eta \left(\frac{\partial u_1}{\partial x} + \frac{\partial v_1}{\partial y} \right) + H_2 \eta \left(\frac{\partial u_2}{\partial x} + \frac{\partial v_2}{\partial y} \right) \right) \tag{B.3.5}$$

$$P_2 = -\rho g' h \; H_2 h \left(\frac{\partial u_2}{\partial x} + \frac{\partial v_2}{\partial y} \right) \tag{B.3.6}$$

$$P_3 = \rho g H_1 \left(u_1 \frac{\partial \eta}{\partial x} + v_1 \frac{\partial \eta}{\partial y} \right) \tag{B.3.7}$$

$$F_1 = \rho H_1 A_H (u_1 \nabla^2 u_1 + v_1 \nabla^2 v_1) \tag{B.3.8}$$

$$F_2 = \rho H_2 A_H (u_2 \nabla^2 u_2 + v_2 \nabla^2 v_2) \tag{B.3.9}$$

$$N_1 = \rho g \eta (\alpha_1 (\eta_\rho - \eta) + \alpha_2 (h_\rho - h) \tag{B.3.10}$$

$$N_8 = \rho g' h (\alpha_2 (h_\rho - h)) \tag{B.3.11}$$

$$S_1 = \rho g \eta (\alpha_1 (\eta_I - \eta) + \alpha_2 (h_\rho - h)) \tag{B.3.12}$$

$$S_2 = \rho g' h (\alpha_2 (h_I - h)) \tag{B.3.13}$$

B.4 The non linear baroclinic equations

$$\langle \partial/\partial t(PE)\rangle = \langle -M+N+S\rangle \qquad (B.4.1)$$

$$\langle \partial/\partial t(KE)\rangle = \langle M+F+O\rangle \qquad (B.4.2)$$

where

$$M = -\rho g h\left(\frac{\partial U}{\partial x} + \frac{\partial V}{\partial y}\right) \qquad (B.4.3)$$

$$F = \rho A_H \quad (U\nabla^2 u + V\nabla^2 v) \qquad (B.4.4)$$

$$N = -\rho g' h\alpha_2(h_\rho - h) \qquad (B.4.5)$$

$$S = -\rho g' h\alpha_2(h_I - h) \qquad (B.4.6)$$

$$O = -\rho(u^2+v^2)\frac{(H_1-2h-H_2)}{H_1+H_2}(\alpha_2(h_\rho-h)+\alpha_2(h_I-h)) \qquad (B.4.7)$$

$$M_1 = \frac{(H_2+h)}{H_1+H_2} M \quad , \quad M_2 = \frac{(H_1-h)}{H_1+H_2} M$$

$$F_1 = \frac{(H_1-h)}{H_1+H_2} F \quad , \quad F_2 = \frac{(H_2+h)}{H_1+H_2} F$$

where $U = U_1-U_2$, $V=V_1-V_2$, $u_4=u_1-u_2$ and $v=v_1-v_2$

B.5 The linear baroclinic equations

$$\langle \partial/\partial t(PE) \rangle = \langle -M+N+S \rangle \tag{B.5.1}$$

$$\langle \partial/\partial t(KE) \rangle = \langle M+F \rangle \tag{B.5.2}$$

where

$$M = -\rho g \frac{H_1 H_2}{H_1 + H_2} h \left(\frac{\partial u}{\partial x} + \frac{\partial v}{\partial y} \right) \tag{B.5.3}$$

$$F = \rho \frac{H_1 H_2}{H_1 + H_2} A_H \left(u \nabla^2 u + v \nabla^2 v \right) \tag{B.5.4}$$

$$N = -\rho g' h \alpha_2 (h_\rho - h) \tag{B.5.5}$$

$$S = -\rho g' h \alpha_2 (h_I - h) \tag{B.5.6}$$

$$M_1 = \frac{H_2}{H_1+H_2} M \quad , \quad M_2 = \frac{H_1}{H_1+H_2} M$$

$$F_1 = \frac{H_2}{H_1+H_2} F \quad , \quad F_2 = \frac{H_1}{H_1+H_2} F$$

where $u = u_1 - u_2$ and $v = v_1 - v_2$

APPENDIX C VORTICITY BALANCE

C.1 Notation

As described in section 2.5.3 the local rate of change of depth averaged vorticity in the upper or lower layer at points away from the forcing regions can be written.

$$\frac{\partial \zeta_i}{\partial t} = \text{ADVECTION} + \text{BETA} + \text{DIVERGENCE} + \text{VISCOSITY}$$

These terms are determined for each set of predictive equations in sections C.2 - C.5.

APPENDIX C.2 The two layer equations

The depth averaged vorticity equation for each layer from equations (3.2.2.10) - (3.2.2.14) is

$$\frac{\partial \zeta_i}{\partial t} = \mathrm{ADVECTION} + \mathrm{BETA} + \mathrm{DIVERGENCE} + \mathrm{VISCOSITY}$$

where

$$\mathrm{ADVECTION} = -\frac{\partial^2}{\partial x^2}(v_i U_i) - \frac{\partial^2}{\partial x \partial y}(v_i V_i - u_i U_i) + \frac{\partial^2}{\partial y^2}(u_i V_i) \qquad \text{(C.2.1)}$$

$$\mathrm{BETA} = -\beta V_i \qquad \text{(C.2.2)}$$

$$\mathrm{DIVERGENCE} = -\beta y \left(\frac{\partial U_i}{\partial x} + \frac{\partial V_i}{\partial y} \right) \qquad \text{(C.2.3)}$$

$$\mathrm{VISCOSITY} = (H_1 + \eta - h) A_H \nabla^2 \left(\frac{\partial v_1}{\partial x} - \frac{\partial u_1}{\partial y} \right) + A_H \nabla^2 v_1 \left(\frac{\partial \eta}{\partial x} - \frac{\partial h}{\partial x} \right) - A_H \nabla^2 u_i \left(\frac{\partial \eta}{\partial y} - \frac{\partial h}{\partial y} \right) \text{ for upper layer} \qquad \text{(C.2.5)}$$

$$= (H_2 + h) A_H \nabla^2 \left(\frac{\partial v_2}{\partial x} - \frac{\partial u_2}{\partial y} \right) + A_H \nabla^2 v_2 \frac{\partial h}{\partial x} - A_H \nabla^2 u_2 \frac{\partial h}{\partial y} \text{ for lower layer} \qquad \text{(C.2.5)}$$

The total local rate of change of vorticity can be found by adding the contribution of the two layers.

C.3 The linear two layer equations

The depth averaged vorticity equation for each layer from equations (3.2.4.1) - (3.3.4.4) is

$$\frac{\partial \zeta_i}{\partial t} = \text{BETA} + \text{DIVERGENCE} + \text{VISCOSITY}$$

where

$$\text{BETA} = \quad - H_i \beta v_i \qquad (C.3.1)$$

$$\text{DIVERGENCE} = - \beta y H_i \left(\frac{\partial u_i}{\partial x} + \frac{\partial v_i}{\partial y} \right) \qquad (C.3.2)$$

$$\text{VISCOSITY} = H_i \; A_H \; \nabla^2 \left(\frac{\partial v_i}{\partial x} \; \frac{\partial u_i}{\partial y} \right) \qquad (C.3.3)$$

The total rate of change of local vorticity can be found by adding the contribution of the two layers.

APPENDIX C.4. The non linear baroclinic equations

The depth averaged vorticity equation from equations (3.3.5.7) - (3.3.5.8) is

$$\frac{\partial \varsigma}{\partial t} = \text{ADVECTION} + \text{BETA} + \text{DIVERGENCE} + \text{VISCOSITY}$$

where

$$\begin{aligned}\text{ADVECTION} = {} & \frac{H_1-H_2}{H_1+H_2}\left(\frac{\partial^2}{\partial x^2}(vU) + \frac{\partial^2}{\partial x \partial y}(vV-uU) - \frac{\partial^2}{\partial y^2}(uV)\right) \\ & + \frac{2}{H_1+H_2}\left[\left(\frac{\partial U}{\partial x} + \frac{\partial V}{\partial y}\right)\left(h\left(\frac{\partial u}{\partial y} - \frac{\partial v}{\partial x}\right) + u\frac{\partial h}{\partial y} - v\frac{\partial h}{\partial x}\right)\right. \\ & \left. + hu\left(\frac{\partial^2 U}{\partial x \partial y} + \frac{\partial^2 V}{\partial y^2}\right) - hv\left(\frac{\partial^2 U}{\partial x^2} + \frac{\partial^2 V}{\partial x \partial y}\right)\right] \qquad \text{(C.4.1)}\end{aligned}$$

$$\text{BETA} = -\beta V \qquad \text{(C.4.2)}$$

$$\text{DIVERGENCE} = -\beta y\left(\frac{\partial U}{\partial x} + \frac{\partial V}{\partial y}\right) \qquad \text{(C.4.3)}$$

$$\begin{aligned}\text{VISCOSITY} = {} & \frac{(H_2+h)(H_1-h)}{H_1+H_2} A_H \nabla^2 \left(\frac{\partial v}{\partial x} - \frac{\partial u}{\partial y}\right) \\ & + A_H \nabla^2 v\left(\frac{H_1-H_2-2h}{H_1+H_2}\right)\frac{\partial h}{\partial y} \\ & + A_H \nabla^2 u\left(\frac{H_1-H_2-2h}{H_1+H_2}\right)\frac{\partial h}{\partial x} \qquad \text{(C.44)}\end{aligned}$$

and $U=U_1-U_2$, $V=V_1-V_2$, $u=u_1u_1-u_2$ and $v=v_1-v_2$

To separate into the vorticity for the upper and lower layers multiply by $(H_2+h)/(H_1+H_2)$ and $-(H_1-h)/(H_1+H_2)$ respectively.

C.5. The linear baroclinic equations

The depth averaged vorticity equation from equations (3.3.6.1) - (3.3.6.2) is

$$\frac{\partial \zeta}{\partial t} = \text{BETA} + \text{DIVERGENCE} + \text{VISCOSITY}$$

where

$$\text{BETA} = -\frac{H_1 H_2}{H_1+H_2} \beta v \qquad \text{(C.5.1)}$$

$$\text{DIVERGENCE} = -\frac{H_1 H_2}{H_1+H_2} \beta y \left(\frac{\partial u}{\partial x} + \frac{\partial v}{\partial y} \right) \qquad \text{(C.5.2)}$$

$$\text{VISCOSITY} = \frac{H_1 H_2}{H_1+H_2} A_H \nabla^2 \left(\frac{\partial v}{\partial x} - \frac{\partial u}{\partial y} \right) \qquad \text{(C.5.3)}$$

and $u=u_1-u_2$ and $v=v_1-v_2$.

To separate into the vorticity for the upper and lower layers multiply by $H_2/(H_1+H_2)$ and $-H_1/(H_1+H_2)$ respectively.